Investigations on the distribution of tropospheric carbon monoxide over India and surrounding oceanic region

Thesis submitted to

Cochin University of Science and Technology

in partial fulfilment of the requirements for the award of

Doctor of Philosophy
in
Physics

Under the Faculty of Sciences

by

Girach Imran Asatar

Space Physics Laboratory
Vikram Sarabhai Space Centre
Indian Space Research Organisation
Thiruvananthapuram – 695022
India

April 2019

DECLARATION

I hereby declare that the work presented in this thesis titled, ***"Investigations on the distribution of tropospheric carbon monoxide over India and surrounding oceanic region"*** was carried out by me at Space Physics Laboratory (SPL), Vikram Sarabhai Space centre (VSSC), Indian Space Research Organisation (ISRO), Thiruvananthapuram, India under the supervision of **Dr. Prabha R Nair**. This work was carried out for the award of the degree of **Doctor of Philosophy** in **Physics** from the Cochin University of Science and Technology (CUSAT), Cochin, India. This thesis is the outcome of the original work done by me, and the work did not form part of any dissertation submitted for the award of any degree, diploma, associateship or any other title or recognition from any University or Institution.

30 April 2019   Girach Imran Asatar
Thiruvananthapuram   (Author)

अन्तरिक्ष भौतिकी प्रयोगशाला
SPACE PHYSICS LABORATORY

डॉ प्रभा आर नायर / Dr. Prabha R Nair,
Scientist/Engineer - G & Head, ACTG

30 April 2019

<u>CERTIFICATE</u>

Certified that the thesis titled "**Investigations on the distribution of tropospheric carbon monoxide over India and surrounding oceanic region**" submitted by Mr. Girach Imran Asatar (Ph. D. Registration Number: 4629) in partial fulfilment of the requirements for the Degree of Doctor of Philosophy in Physics to the Cochin University of Science and Technology, Cochin, India embodies the original results of the investigations carried out under my supervision at the Space Physics Laboratory, Vikram Sarabhai Space Centre, Thiruvananthapuram. The work presented in this thesis has not been submitted for the award of any other degree, diploma or associateship to any other University or Institution.

Dr. Prabha R Nair

(Thesis Supervisor)

Thiruvananthapuram

भारतीय अंतरिक्ष अनुसंधान संगठन इसरो Indian Space Research Organisation

अन्तरिक्ष भौतिकी प्रयोगशाला
SPACE PHYSICS LABORATORY

डॉ प्रभा आर नायर / Dr. Prabha R Nair,
Scientist/Engineer - G & Head, ACTG

30 April 2019

CERTIFICATE

Certified that all the relevant corrections and modifications suggested by the audience during the Pre-synopsis seminar and recommendations of the Doctoral Committee of the candidate, Mr. Girach Imran Asatar (Ph. D. Registration Number: 4629), have been incorporated in this thesis.

Dr. Prabha R Nair

(Thesis Supervisor)

Thiruvananthapuram

भारतीय अंतरिक्ष अनुसंधान संगठन इसरो isro Indian Space Research Organisation

Acknowledgements

In this journey, I am deeply indebted to those who motivated, encouraged, helped, and supported me in every aspect of learning, researching, and exploring the boundaries of knowledge. With pleasure, I take this opportunity to express my gratitude.

Firstly, I express my sincere gratitude and respect to Dr. Prabha R. Nair, my supervisor and mentor, for her continuous and wholehearted support, immense patience and encouragement at each stage of my Ph.D. work. It is her efforts and hard work which made a platform to conduct the research on trace gases and helped to form this thesis. I am indebted to her for all the experience that I have gained from her during this work. I am very thankful to her for exonerating my mistakes and peacefully allowing myself to improve.

I am grateful to Dr. Radhika Ramachandran, Director, Space Physics Laboratory (SPL) for her advices and support for the research work carried out. I also extend my gratitude to former directors of SPL, Dr. Anil Bhardwaj, Dr. K. Krishna Moorthy, and Prof. R. Sridharan for their valuable suggestions and constant encouragement.

Besides my advisor and present and former Directors of SPL, I would like to express my sincere thanks to the members of the doctoral, and the research and academic committees for their feedbacks and advices which was helpful to improve the approach towards the research topic. I thank each and every member of these committees — Dr. Radhika Ramachandran, Dr. K. Rajeev, Dr. Tarun Kumar Pant, Dr. Geetha Ramkumar, Dr. K. Kishore Kumar, Dr. S. Suresh Babu, Dr. C. Suresh Raju, Dr. D. Bala Subrahmanyam, Dr. Siddharth Shankar Das, Dr. Siji Kumar, Dr. K. N. Uma, Dr. N.V.P. Kiran Kumar, Dr. Mukunda M. Gogoi, Dr. Prashanth Hegde, Dr. S. V. Sunil Kumar, Dr. P. Sreelatha, Dr. Vipin Kumar Yadav, Dr. G. Manju, and Dr. Sandhya K. Nair, for their feedbacks, advices and criticism especially during the annual reviews which helped me in shaping my thesis better. Special thanks to Dr. K. Rajeev for his constructive criticism and questions on lacuna and to Dr. Tarun Kumar Pant for providing broader view to the various aspects of the research topic. I am thankful to Dr. Andrea Pozzer and Dr. Lelieveld for their constructive feedback on the research paper. I also thank Dr. C. Vineeth, Dr. D. Bala Subrahmanyam, Dr. Siddharth Shankar Das, Dr. N.V.P. Kiran Kumar for their genuine feedback on the presentations, advices and making these moments joyful during evening tea.

I am thankful to the doctoral and research committee members from CUSAT, Prof. B. Pradeep, Prof. K Mohan Kumar, Prof. C. A. Babu, Prof. Godfrey Loius, Prof. Kurian

Publications in Journals

1. **Girach I. A.**, Ojha N., Nair P. R., Tiwari Y. K., Ravi Kumar K., **2018**, "Variations of trace gases over the Bay of Bengal during the summer monsoon", **Journal of Earth System Science**, 127, 15. (http://dx.doi.org/10.1007/s12040-017-0915-y).

2. **Girach I. A.**, Ojha N., Nair P. R., Pozzer A., Tiwari Y. K., Ravi Kumar K., Lelieveld J., **2017**, "Variations in O_3, CO, and CH_4 over the Bay of Bengal during the summer monsoon season: shipborne measurements and model simulations", **Atmospheric Chemistry and Physics**, 17, 257-275. (http://dx.doi.org/10.5194/acp-17-257-2017)

3. **Girach I. A.** and Nair P. R., **2014**, On the vertical distribution of Carbon monoxide over Bay of Bengal during winter: Role of water vapour and vertical updrafts, **Journal of Atmospheric and Solar-Terrestrial Physics**, 117, 31–47. (http://dx.doi.org/10.1016/j.jastp.2014.05.003)

4. **Girach I. A.**, Nair V. S., Babu S. S., Nair P. R., **2014**, Black Carbon and Carbon Monoxide over Bay of Bengal during W_ICARB: Source characteristics, **Atmospheric Environment**, 94, 508-517. (http://dx.doi.org/10.1016/j.atmosenv.2014.05.054)

5. **Girach I. A.** and Nair P. R., **2014**, Carbon monoxide over Indian region as observed by MOPITT, **Atmospheric Environment**, 99, 599-609. (http://dx.doi.org/10.1016/j.atmosenv.2014.10.019)

Publications in Proceedings

1. **Girach I. A.**, Nair P. R., **2016**, Long-term trend in tropospheric carbon monoxide over the globe, Proceeding of SPIE 9876, Remote Sensing of the Atmosphere, Clouds, and Precipitation VI, 987624. (http://dx.doi.org/10.1117/12.2223380)

2. **Girach I. A.**, Nair V. S., Babu S. S., Nair P. R., **2014**, Black carbon and Carbon monoxide over bay of Bengal during W_ICARB, Proceeding of IASTA (Indian Aerosol Science and Technology Association) – 2014, IASTA bulletin vol. 21, ISSN 09714510.

Conference Presentations

International

1. **Girach I. A.**, Nair P. R., Pozzer A., Ojha N., Subrahmanyam K. V., Koushik N., Mohammed Nazeer M., Kiran Kumar N. V. P., Surface ozone over the coastal Antarctica during Austral summer, 14th iCACGP (The international Commission on Atmospheric Chemistry and Global Pollution) Quadrennial Symposium/15th IGAC (International Global Atmospheric Chemistry) Science Conference at Takamatsu, Kagawa, Japan during 25–29 September **2018**. **('Honourable Mention')**

2. **Girach I. A.** and Nair P. R., Global long-term trend in tropospheric carbon monoxide, International Conference on Climate Change and Disaster Management at Thiruvananthapuram, India during 26–28 February **2015**. **(Best paper award)**

3. **Girach I. A.** and Nair P. R., Seasonal variations of surface Ozone and Carbon monoxide over the Bay of Bengal: Synthesis of multi-campaign measurements, Predicting and Projecting Climate change over Asian Region (UPCAR) conference at Sri Venkateswara University, Tirupati and National Atmospheric Research Laboratory (NARL), Gadanki, India during 26–28 June **2017**.

4. **Girach I. A.** and Nair P. R., Long-term trend in tropospheric carbon monoxide over the globe, SPIE Asia-Pacific Remote Sensing conference at Vivanta by Taj-Dwarka, New Delhi, India during 4–7 April **2016**.

5. Ojha N., **Girach I. A.**, Saha S., Sharma S. K., Singh N., Tropospheric Ozone over South Asia: Climatology and Long-term Trend, URSI AP-RASC 2019, New Delhi, India during 09–15 March **2019**.

6. Phanikumar D.V., Niranjan Kumar K., Bhattacharjee S., Naja M., **Girach I. A.**, Enhancement of Tropospheric and Surface Ozone Observed During Orography Induced Gravity Waves Over Himalayan Region, AS41-D4-PM2-334-007, AS41-A014, 14th Annual Meeting of the Asia Oceania Geosciences Society (AOGS - 2017) at Singapore during 6–11 August **2017**.

National

1. **Girach I. A.**, Tripathi N., Ojha N., Nair P. R, Sahu L. K., Trace gases in the marine boundary layer of the Arabian Sea and Indian Ocean during winter, 20th National Space Science Symposium at Savitribai Phule Pune University (SPPU), Pune during 29-31 January 2019. **(Lead Talk)**

2. **Girach I. A.**, Nair P. R., Subrahmanyam K. V., Koushik N., Shreedevi P. R., Mohammed Nazeer M., Kiran Kumar N. V. P., Surface ozone variation during summer season at Bharati station, Antarctica, NCPS – 2017 National Conference on Polar Sciences at National Centre for Antarctic and Ocean Research (NCAOR), Ministry of Earth Sciences (MoES), Goa during 16 –17 May 2017.

3. **Girach I. A.**, Ojha N., Nair P. R., Tiwari Y. K., Ravi Kumar K., Variations of trace gases over the Bay of Bengal during the summer monsoon, TROPMET 2016 – National Symposium on Tropical Meteorology : Climate Change and Coastal Vulnerability at SOA university, Bhubneswar during 18-21 December 2016.

4. **गिराच इमरान** और प्रभा आर नायर**,** तटीय स्टेशन थुम्बा पर विभिन्न परिवेशी अनुरेख गैसों का विचरण**,** केंद्र स्तरीय तकनीकी हिन्दी संगोष्ठी**,** विक्रम साराभाई अंतरिक्ष केंद्र**,** तिरुवनन्तपुरम, 19–20 जुलाई **2016**.

5. **Girach I. A.**, Nair P. R., Hegde P., Carbon monoxide over Indian region as observed by MOPITT, PS1A_237, National Space Science Symposium, Space Physics Laboratory, Vikram Sarabhai Space Centre, ISRO, Thiruvananthapuram during 9–12 February 2016.

6. **Girach I. A.**, Nair P. R., Ojha N., Hegde P., Aryasree S., Variations in near-surface Ozone over Bay of Bengal during summer-monsoon, PS1A_236, National Space Science Symposium, Space Physics Laboratory, Vikram Sarabhai Space Centre, ISRO, Thiruvananthapuram during 9–12 February 2016.

7. **Girach I. A.**, Nair V. S., Babu S. S., Nair P. R., Black carbon and Carbon monoxide over bay of Bengal during W_ICARB, Indian Aerosol Science and Technology Association (IASTA) at Banaras Hindu University, Banaras during 11–13 November 2014.

8. Ojha N., **Girach I. A.**, Saha S., Sharma S. K., Singh N., Spatio-temporal distribution of tropospheric ozone over South Asia: Model results versus Observations, 20th National Space Science Symposium at Savitribai Phule Pune University (SPPU), Pune during 29–31 January 2019.

9. Nair P. R., **Girach I. A.**, Kavitha M., Revathy S. A., Aryasree S., Systematic seasonal pattern of tropospheric trace species over Indian region, TROPMET 2016 – National Symposium on Tropical Meteorology : Climate Change and Coastal Vulnerability at SOA university, Bhubaneswar during 18–21 December 2016.

10. Hegde P., **Girach I. A.**, Nair P. R., Molecular composition of organic aerosols, Indian Aerosol Science and Technology Association (IASTA) at Banaras Hindu University, Banaras during 11–13 November 2014.

11. Kavitha M., Nair P. R., **Girach I. A.**, and Renju, R., "Diurnal and seasonal variation of trace gases over the tropical coastal station, Thumba, Thiruvananthapuram, 13th Kerala Environmental Congress, Thiruvananthapuram during 6–8 December 2017.

12. Aryasree S., Nair P. R., **Girach I. A.**, Salu Jacob, Seasonal variation of aerosol chemical characteristics over Bay of Bengal: A Multi Campaign Analysis, Indian Aerosol Science and Technology Association (IASTA) at Banaras Hindu University, Banaras during 11–13 November 2014.

13. Lakhima C., N. Ojha, M. Kumar, A. Kumar, **Girach I. A.**, Pathak B., Bhuyan P. K., Regional scale modeling of secondary organic aerosols over Indian subcontinent using WRF-chem during winter, 20th National Space Science Symposium, Savitribai Phule Pune University (SPPU), Pune during 29–31 January 2019.

Preface

With the rising concern about global warming and climate change; the studies on chemistry and composition of the atmosphere have gained a great attention in the last two decades. Trace species such as ozone (O_3), carbon monoxide (CO), nitrogen oxides (NOx), sulphur dioxide (SO_2) and aerosols play extremely important role in the atmospheric chemistry and climate, despite of the fact that they constitute less than 0.1% of the atmospheric volume. Carbon monoxide is one of the most abundant air pollutants and an indirect greenhouse gas which has adverse health effects when its concentration exceeds certain threshold. Indirect radiative forcing due to CO is estimated to be 0.23 (0.18–0.29) Wm^{-2} through the production of ozone, methane and carbon dioxide. In addition, CO is also an important trace gas playing key role in the tropospheric chemistry as it consumes a large fraction of hydroxyl radical (OH) and is a precursor for tropospheric ozone, which is another greenhouse gas. CO is a by-product of incomplete combustion. Fossil fuel, biomass and biofuel burning; and oxidation of hydrocarbons are the major anthropogenic sources of CO whereas the ocean, volcanoes, soil and plants (oxidation of biogenic hydrocarbon from plants) are weak natural sources of CO.

In view of the rapid growth in the anthropogenic activities which lead to emissions of various trace gases and aerosols, the intense tropical solar radiation, high water vapour content, and the unique tropical meteorological conditions conducive for rapid mixing and transport; Indian landmass and the surrounding oceanic regions have been of interest for conducting scientific studies on these species and to assess their environmental impacts. Even though several studies are available on O_3 and NOx, CO remained the least addressed species in this region and a comprehensive picture of the tropospheric distribution of CO over the region is lacking. This study addresses the spatio-temporal characteristics of CO over the Indian region including the surrounding oceans, combining in-situ measurements, satellite observations and modelling.

The thesis work focuses mainly on the characterisation of CO distribution over the oceanic regions of the Bay of Bengal (BoB) and the northern Indian Ocean (IO), and the Indian landmass. The ship-based in-situ measurements of CO were carried out over the oceanic environments of the BoB and the northern IO during different seasons form the major data for this study. The in-situ observations of near-surface CO at the coastal station, Thumba, Thiruvananthapuram also have been made use in this study. Also, the satellite-based observations from the Measurements of Pollution in the Troposphere (MOPITT) validated against the in-situ surface observations were utilised for the characterisation of seasonal and long-term changes in CO on regional basis. The observed variations in the tropospheric distribution of CO were examined in the light of various atmospheric processes like horizontal advection, vertical transport and chemistry. The photochemical box-model simulations were carried out to understand the role of chemistry and the regional chemistry

transport model was used to delineate anthropogenic contributions in the surface CO over the oceanic regions.

Chapter - 1 provides a brief introduction to CO in the atmosphere, its heterogeneous sources and sinks, atmospheric chemistry of CO, its role as an air pollutant, and as an indirect green house gas influencing the climate. The various experimental techniques used for CO measurements both in-situ and remote sensing, and brief accounts of the models used for the simulations of trace gases are also included. This chapter also presents a brief overview of the of various studies on CO reported from all over the globe with emphasis on the science outcome followed by an account of CO measurements and studies from the Indian region. The chapter ends by listing the major objectives of the thesis.

Chapter - 2 gives the detailed descriptions of (1) the measurement technique of the CO analyser utilised for in-situ measurements of surface CO and (2) the satellite based technique for retrieval of CO from the MOPITT. In addition to the main data set (in-situ measured and satellite retrieved CO), various supporting data sets are used in the study; their details and sources are described in this chapter along with their uncertainties, spatial resolutions, etc.

The results of the in-depth study on the distribution of tropospheric CO over the marine environment of the BoB during different seasons, the source regions and transport pathways are presented in Chapter - 3. Both in-situ measurements and satellite-based MOPITT data have been utilised in this study along with airflow pattern, back trajectory analysis, fire count data and MACC-reanalysis (Monitoring Atmospheric Composition and Climate) data. The satellite-retrieved vertical distribution of CO also was analysed. The in-situ measurements of near-surface CO were carried out over the BoB as part of ICARB-2009 (Integrated Campaign for Aerosols, gases and Radiation Budget; January-February 2009) and CTCZ-2009 (Continental Tropical Convergence Zone; July-August 2009) during winter and monsoon seasons respectively. This analysis showed presence of significant amount of CO over marine environment of BoB, where no prominent sources exist. Winter-time characteristic showed distinctly different regional features and transport pathways of CO over different parts of BoB. The CO mixing ratio was high (~302±68 ppbv) over northern BoB due to transport from eastern Indo Gangetic Plains (IGP) under the influence of northerlies as revealed by back-trajectory analysis. The highest CO values ~340±89 ppbv were observed over the eastern BoB where easterlies/north-easterlies prevailed which brought pollutants like CO from the Southeast Asian courtiers where higher biomass burning events were seen. The lowest mixing ratios ~168±37 ppbv were observed over southern BoB which is under the influence of marine airmass. During monsoon season, surface CO mixing ratios were lower being 50–200 ppbv compared to the winter season. The westerlies/south-westerlies transport the CO from central/southern Indian region to the BoB during monsoon season. MOPITT retrieved surface CO and CO from MACC-reanalysis were compared with the in-situ observations and found to be in good agreement. An analysis of the role of chemistry and the long residence time (transit time) of airmass over the marine region is also presented in

this chapter. The altitude distribution of CO also was investigated based on the satellite-based vertical profiles along with the role of horizontal and vertical transport in their seasonal changes.

Chapter - 4 discusses the spatial variability of surface CO and upper-tropospheric CO (at ~ 300 hPa) over northern IO, specifically, southeast Arabian Sea and equatorial IO during winter. The in-situ measurements of surface CO were carried out as part of ICARB-2018 (during January-February 2018). The comparisons of surface CO from satellite-based MOPITT and CAMS (Copernicus Atmosphere Monitoring Service) model data with the in-situ observations were also carried out. Back-trajectory analysis and residence time estimates in conjunction with CAMS reanalysis were used to identify the source characteristics and the transport processes. Based on analysis of O_3/CO ratio, the ozone production efficiency in different airmasses was studied. The CO measurements conducted during ICARB-2018 were compared with those measured during INDOEX-1999; which showed the reduced level, indicating the long-term decreasing trend in CO over this oceanic region. A detailed analysis of upper tropospheric CO is carried out, which revealed an unusual enhancement in upper tropospheric CO during February 2018 which was investigated in terms of atmospheric dynamics.

The results of a comprehensive study on the spatio-temporal changes in the tropospheric CO focusing on lower-tropospheric, upper-tropospheric and columnar CO over the Indian region are presented in the Chapter - 5. The latest satellite retrievals from MOPITT over the Indian region were utilised to investigate the seasonal variations in the vertical distributions and the long-term trends. The seasonal variation in surface CO at Trivandrum and few other sites (as available in literature) were compared with MOPITT surface retrievals and found that MOPITT could capture the seasonal changes reasonably well and this data can be used to understand the temporal changes over the broad regions. The regional differences in the seasonal amplitudes are also presented. The seasonal patterns of upper-tropospheric CO differ from that of the lower tropospheric CO. The association of the observed changes with biomass burning activities (assessed in terms of fire count), anthropogenic activity and meteorology (synoptic winds and convective activity) is investigated in this study. The regional differences in the association of columnar CO with biomass burning are also presented. The higher vertical extent of CO seen during pre-monsoon and monsoon were examined in the context of convective activities and associated updrafts. The altitude dependent long-term trends of CO over the Indian region as well as over the globe are also discussed in this chapter. The trends in lower-tropospheric and columnar CO were examined using in-situ observations from NOAA (National Oceanic and Atmospheric Administration) network stations and multiple satellite data.

In the chapter - 6, a photochemical box model, NCAR-MM [NCAR's (National Center for Atmospheric Research) - Master Mechanism] is used to understand the role of water vapour, NO_2 and/or O_3, and hydrocarbons on the CO variation over the study region. The model simulations were carried out under different background/initial conditions of various

trace gases and water vapour, and their effects are studied. Simulations of the spatial distribution of CO in the oceanic environments of the BoB and the IO were carried out using the regional chemistry transport model, WRF-Chem (Weather Research and Forecasting model coupled with Chemistry). The WRF-Chem model simulations were inter-compared with in-situ observations. In addition, WRF-Chem was used to delineate the contribution of anthropogenic emission from Indian region over to the oceanic region.

The summary of the thesis work, the major scientific outcome and the future scope of this study are presented in Chapter - 7.

Contents

List of Acronyms

ABL	Atmospheric Boundary Layer
ACE-FTS	Atmospheric Chemistry Experiment - Fourier Transform Spectrometer
Agl	above ground level
AIRS	Atmospheric Infrared Sounder
Amsl	above mean sea level
AOD	Aerosol Optical Depth
AS	Arabian Sea
AWS	Automatic Weather Station
BoB	Bay of Bengal
BOBEX	Bay of Bengal Experiment
BOBPS	Bay of Bengal Processes Studies
CAMS	Copernicus Atmosphere Monitoring Service
CARIBIC	Civil Aircraft for the Regular Investigation of the Atmosphere Based on an Instrument Container
CPCB	Central Pollution Control Board
CRDS	Cavity Ring-Down Spectroscopy
CSIRO	Command wealth Scientific and Industrial Research Organisation
CTCZ	Continental Tropical Convergence Zone
DOAS	Differential Optical Absorption Spectroscopy
DOF	Degree of Freedom
ECCAD	Emissions of atmospheric Compounds and Compilation of Ancillary Data
ECMWF	European Centre for Medium-Range Weather Forecasts
EDGAR	Emissions Database for Global Atmospheric Research
ENSO	El Niño Southern Oscillation
ENVISAT	Environmental Satellite
EOS	Earth Observing Systems
EPA	Environmental Protection Agency
EPS	EUMETSAT Polar System
ERA	ECMWF Re-Analysis
ERF	Effective Radiative Forcing
ESRL	Earth System Research Laboratory
EUMETSAT	European Organization for the Exploitation of Meteorological Satellites
FFP	First Field Phase
FTIR	Fourier Transform Infrared

NCAR	National Center for Atmospheric Research
NCEP	National Center for Environmental Prediction
NDIR	Non-Dispersive Infrared
NIR	Near Infrared
NMHC	Non-Methane Hydrocarbon
NMVOC	Non-Methane Volatile Organic Compounds
NOAA	National Oceanic and Atmospheric Administration
ORV	Oceanic Research Vessel
PBL	Planetary Boundary Layer
PMC	Pressure Modulator Cell
Ppbv	parts per billion by volume
Ppmv	parts per million by volume
Pptv	parts per trillion by volume
PTFE	Polytetrafluoroethylene
QA	Quality Assurance
RADM2	second-generation Regional Acid Deposition Model
REAS	Regional Emission inventory in Asia
RF	Radiative Forcing
RH	relative humidity
Rpm	rotation per minute
SAFAR	System of Air Quality Forecasting And Research
SCIAMACHY	SCanning Imaging Absorption spectroMeter for Atmospheric CartograpHY
SSA	single scattering albedo
TES	Tropospheric Emission Spectrometer
TH	Time Horizon
TIR	Thermal Infrared
TUV	Tropospheric Ultraviolet Visible
UV	Ultraviolet
UVRF	Vacuum Ultraviolet Resonance Fluorescence
V7-TIR	Version 7 - Thermal Infrared (Note: This is MOPITT data version)
VMR	Volume Mixing Ratio
VOCs	Volatile Organic Compounds
WDCGG	WMO World Data Centre for Greenhouse Gases
WHO	World Health Organization
WMO	World Meteorological Organization
WRF-Chem	Weather Research and Forecasting model coupled with Chemistry

List of Molecular formulae

C_5H_8	Isoprene
C_2H_6	Ethane
C_2H_4	Ethene OR Ethylene
C_3H_8	Propane
C_3H_6	Propene OR Propylene
CH_2O	Formaldehyde
CH_4	Methane
CO	Carbon Monoxide
CO_2	Carbon Dioxide
H_2O	Water
HO_2	Hydroperoxyl OR perhydroxyl
N_2	Nitrogen
N_2O	Nitrous Oxide
NO	Nitric Oxide
NO_2	Nitrogen Dioxide
O_2	Oxygen
O_3	Ozone
OH	Hydroxyl
SO_2	Sulfur Dioxide
NOx	Oxides of Nitrogen ($NOx = NO + NO_2$)

List of Figures

List of Tables

<div align="right">

Chapter - 1

</div>

<u>Atmospheric Carbon Monoxide: An Introduction</u>

1.1   Carbon monoxide: A trace constituent

Carbon monoxide (CO) is one of the trace gases in the earth's atmosphere, contributing only parts per billion or million of the atmospheric volume and mainly residing below 10–18 km of the atmosphere. Though the CO was first prepared by the French chemist de Lassone in 1776, by heating zinc oxide with coke, it was identified as a compound containing carbon and oxygen by the Scottish chemist William Cruikshank in the year 1800 (Cruikshank, 1801). CO is a colourless, odourless, tasteless and toxic gas. It is a diatomic molecule connected by a triple bond (as illustrated in the figure 1.1) characterized by a bond length of 0.1128 nm. 4 electrons of oxygen and 2 electrons of carbon participate in the bonding, leading to the $C \leftarrow O$ polarization of the molecule, with a small negative charge on carbon and a small positive charge on oxygen. This results in a small dipole moment. It has a molar mass of 28.0, making it slightly less dense than air.
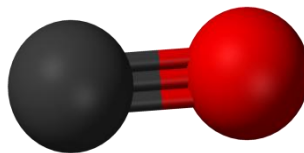
Figure 1.1: Illustration of CO molecule, representing the carbon and oxygen atoms by black and red balls respectively (curtsey: https://commons.wikimedia.org/wiki/File:Carbon-monoxide-3D-balls.png)

CO is produced by both natural and anthropogenic processes. The direct emission of CO occurs from anthropogenic activities like burning of fossil fuel and biomass (man-made forest fires and burning of wood/bush, savanna, agricultural waste, bio fuel, etc); naturally occurring events like volcanoes and forest fires; and from oceans, vegetation as well as biological processes in the soils. The indirect emission of CO is from oxidation of hydrocarbons (mainly methane and Isoprene), which includes both natural and anthropogenically emitted hydrocarbons. CO is also formed by the oxidation of several Volatile Organic Compounds (VOCs). Combining the direct and indirect emissions, the anthropogenic activities are responsible for about 60% of total CO in the atmosphere (WHO report, 2004; Seinfeld & Pandis, 2006). In the process of direct emission of CO, it is produced by incomplete combustion of carbon containing compounds as a by-product

of combustion. In the complete combustion carbon dioxide (CO_2) is released, but when sufficient oxygen is not available to mix with fuel while burning, it results in incomplete combustion releasing CO and soot particles instead of CO_2. In addition, smoke (aerosols) and other gases also get released in the incomplete combustion.

CO plays a major role in atmospheric chemistry involving hydroxyl (OH) radical (Finlayson-Pitts and Pitts, 2000; Seinfeld and Pandis, 2006). It is a precursor gas for tropospheric ozone (O_3), which is a greenhouse gas and air pollutant in the troposphere. The radiative forcing due to direct absorption of infrared radiation by CO is insignificant to consider it as a greenhouse gas. But it produces greenhouse gases like O_3, methane (CH_4) and CO_2 by photochemical reactions in the troposphere and thus considered as indirect greenhouse gas. The indirect radiative forcing due to CO is estimated to be 0.23 (0.18–0.29) Wm^{-2} through the production of O_3, CH_4 and CO_2 (IPCC 2013). It is also estimated that the short-term cumulative radiative forcing due to the direct anthropogenic emission of CO is larger than that due to anthropogenically emitted Nitrous oxide (N_2O; Daniel and Solomon, 1998; Finlayson-Pitts and Pitts, 2000).

CO is one of the most abundant air pollutants and it has significant impacts on regional air quality. It is a good tracer for primary pollution sources and transport of horizontal/vertical pollution due to its long lifetime of about 2 months (Seinfeld and Pandis, 2006). In presence of sufficient oxides of nitrogen (NOx = NO + NO_2), Hydroperoxyl radical (HO_2) produced from oxidation of CO (by OH radical) initiates photochemical reactions which result in the net production of O_3 (Fishman and Seller, 1983; Cros et al., 1988). CO is having adverse effect on humans and animals under long term exposure or short term exposure under high concentration. CO molecules are capable of forming strong bond with the haemoglobin molecule, forming carboxyhaemoglobin, which impairs the oxygen carrying capacity of the blood, thus causing serious health issues. The effects of CO exposure vary from person to person depending on age, general health, the concentration of CO and length of exposure. It has toxic effects to humans when exposed to mixing ratios above approximately 35 ppmv (0.0035%; WHO report, 2004). Due to aforesaid reasons, it is important to have detailed study on tropospheric CO.

Due to the large heterogeneity in sources and production mechanisms, variations in the strength of CO emissions, and shorter lifetime as compared to other greenhouse gases, CO varies significantly in space (region/location) and time (daily/seasonal/annual). This demands an in depth study on the tropospheric CO, its

horizontal and vertical variations and the role of various atmospheric processes (dynamical and chemical/photochemical) controlling the variations. This thesis work aims at a comprehensive study on CO over the Indian region making use of in-situ and satellite-based observations.

Though the global mean lifetime of CO is around 2 months against oxidation by the OH radical (Sze, 1977; Crutzen and Zimmermann, 1991), the lifetime is shorter over the tropics and in the lower and mid troposphere due to higher concentration of OH. This spatial and temporal variability of CO is higher for near-surface CO as compared to that over upper-troposphere. However, over the Indian region, the studies on spatial and temporal variability on CO and processes controlling those variations are limited except for a few in-situ measurements from selected locations which are treated as point measurements. But these observations could not bring out a comprehensive picture of CO distribution on regional scales along with seasonal changes. For this, the most widely accepted technique is the satellite-based remote sensing. The present study utilises (1) in-situ measurements of surface CO mixing ratios carried out over the Bay of Bengal, and northern Indian Ocean (2) limited observations at tropical coastal station, Thumba, Thiruvananthapuram (3) satellite-based observations of vertical profiles and columnar CO over the Indian region and (4) box-model and regional chemistry transport model. Utilising these approaches, India and surrounding oceanic region are characterised in terms of CO and associated atmospheric processes governing the spatial as well as temporal (seasonal and long term) variations are studied in the thesis.

The following sections starts with a brief introduction to atmospheric structure in terms of pressure, temperature and composition followed by an overview of the atmospheric CO in terms of its mean concentration levels in the troposphere, sources and sinks of CO, its role in the chemistry and global warming, various techniques for the measurement of CO mixing ratio in the atmosphere, and the literature survey of the CO studies in the global and Indian scenario.

1.2   Atmospheric pressure variation

At any point in the atmosphere, the pressure (P) is caused by the weight of the air above. The standard atmospheric pressure at mean sea level is 1013.25 hPa. The pressure decreases exponentially with altitude and the pressure at a given height (z) in the atmosphere is given by (Wallace and Hobbs, 2006)

$$P = P_0 \, e^{-z/H}$$

where, P_0 is the surface level pressure and H is the scale height of the atmosphere. $H = \frac{RT}{mg}$ where, R is gas constant (8.314 J mol^{-1} K^{-1}), T is temperature, m is mean molecular weight of air (28.97 g mole^{-1} for dry air) and g is the acceleration due to gravity (9.8 m s^{-2}). H is the thickness of a layer over which the pressure decrease by a factor of e (i.e., 2.7182). Considering the near-surface temperature of the air as 288 K, the scale height of the atmosphere near the ground is equal to 8.4 km. Thus, at a height of 8.4 km in the earth's atmosphere, the pressure is only 1/2.7 ($\sim$37%) of its value at the ground. As clearly seen, scale height is a function of temperature and since air temperature varies with altitude, it is in fact a function of altitude. As H depends on molecular weight, it is also species dependent.

Following the ideal gas equation, i.e., $PV = nRT$, where P=Pressure, V=volume, n=number of mole, R=gas constant and T=temperature), density of air, ρ, can be written as

$$\rho = \frac{Pm}{RT}$$

For the near surface, P = 1.013×10^5 Pa, T = 288 K, mass density of air is $\sim$1.2 kg m^{-3}.

Similarly, number density, n, can be written as following.

$$n = \frac{PN_A}{RT}$$

where, N_A is the Avogadro number, 6.023 x 10^{23} molecules mole^{-1}. For the near surface, P = 1.013×10^5 Pa, T = 288 K, and number density n = 2.4×10^{19} molecules cm^{-3}. As seen in the above equations, mass density or number density follows the altitude variation as that of air pressure.

Figure 1.2a shows that the vertical profile of air pressure, which decrease exponentially. The atmospheric pressure drops by $\sim$50% at a height of about 5 km above the earth's surface. At an altitude of 50 km the pressure is about 1 hPa so that only about 0.1% of the mass of the atmosphere lies above that level as marked in the figure 1.2a. The altitudinal pressure variation on the logarithmic scale is shown in the figure 1.2b along with air density. Since the x-axis in figure 1.2b is logarithmic, the curve appears linear. The deviation from linearity is due to temperature changes with altitude. Temperature profile of the atmosphere is discussed in the following section.
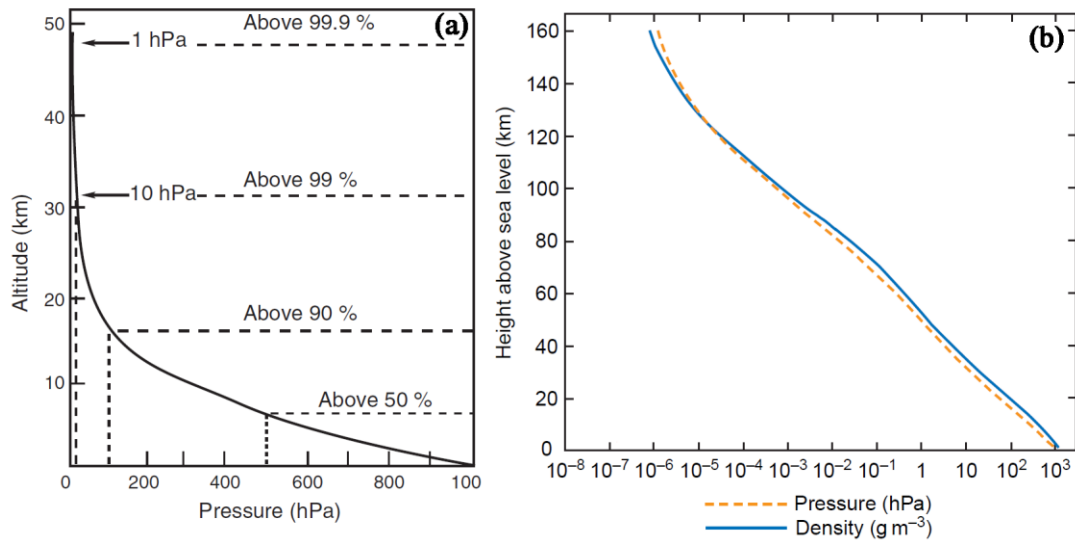
Figure 1.2: Vertical profile of atmospheric pressure on linear scale (a) and the same but on the logarithmic scale along with air density (b) above the earth surface. These figures are adapted from Mohanakumar, 2008; and Wallace and Hobbs, 2006.

1.3   Thermal structure of the atmosphere

Based on the nature of temperature variation (thermal structure), the atmosphere can be divided into different layers. The variations in the vertical structure of the temperature are mainly due to absorption of solar radiation by atmospheric constituents as well as the earth's surface. These layers are named as troposphere, stratosphere, mesosphere, and thermosphere. Figure 1.3 shows the vertical profile of temperature along with enlarged view over lower-stratosphere and upper-troposphere.
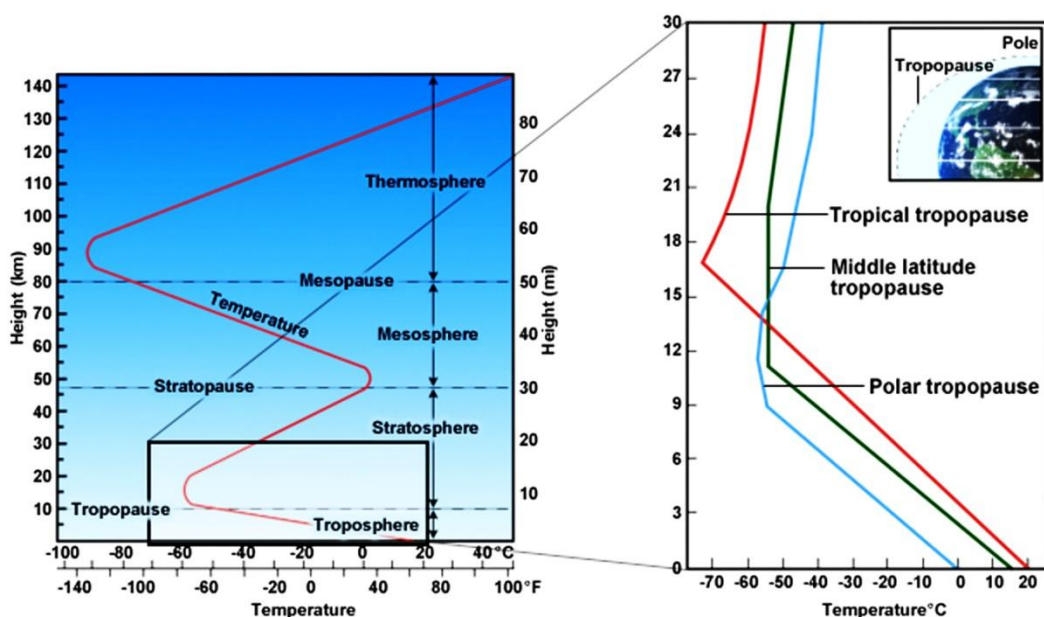
Figure 1.3: Vertical profile of air temperature above the earth surface upto ~120 km. This figure is adopted from Laing and Evans, 2011.

Troposphere is the lower most part of the atmosphere where temperature decreases (~ 6.5 ℃ for every 1km) upto about 17 km (8–10 km for higher latitudes) from the earth surface. It is the most turbulent part of the atmosphere in which the most of the weather phenomenon takes place. The shortwave solar radiation reaching the earth surface heats the ground, which in turn emits infrared radiation upward in to the atmosphere. The troposphere is heated from below by the terrestrial longwave (Infrared) radiation.

The lowest layer of the troposphere, close to the earth's surface, is known as the planetary boundary layer (PBL) or Atmospheric boundary layer (ABL), generally defined based on temperature inversion. The air parcels which are in the contact of earth surface gets heated up and rises in the atmosphere generating eddies or the turbulent motion. This turbulent motion or eddies cause well-mixing of air molecules including water vapour as well as other trace constituents. The height upto which turbulent mixing prevails defines the height of the boundary layer. The height of boundary layer varies from a few hundred meters over tropical oceans to few kilometers (may be upto 5 km over the hot and dry region like Sahara desert). It is the layer through which heat, moisture, and momentum are exchanged between the atmosphere and the surface. In view of the well-mixed nature within the boundary layer, the measurements of trace gases made near to the surface are considered to represent the concentration/mixing ratio of boundary layer. The ABL undergoes significant diurnal changes and correspondingly affects the near-surface concentration/mixing ratio of trace gases.

The tropospheric temperature reaches a minimum of about -80 ℃ (195 K) over the tropics, beyond which it increases. This region of increasing temperature is the stratosphere (stratified layer) and the region separating the troposphere and stratosphere is called the tropopause.

The stratosphere extends up to ~50 km. The temperature varies from -80 ℃ (near tropical tropopause) to 0 ℃ (273 K) at about 50km. The stratospheric increase is caused by the O_3 layer existing within it. O_3 molecules in this layer absorb the ultraviolet radiation from the incoming solar radiation and cause the heating in this region of the atmosphere. Such a temperature profile creates very stable atmospheric conditions, and the stratosphere lacks the air turbulence that is so prevalent in the troposphere. The boundary separating the stratosphere from the mesosphere is called the stratopause which occurs at an altitude of 50–55 km (with temperature ~ 0 ℃).

The mesosphere is the layer between ~50 to 80–85 km above the surface of the earth, where temperature again decrease with increasing altitude, reaching about -90 °C (180 K, the coldest point) at 80 km. In the mesosphere, the thin air and the small amounts of O_3 prevent the air from warming much. CO_2 molecules present in the mesosphere makes this layer cold due to radiative cooling. The boundary separating the mesosphere and the thermosphere is called the mesopause which occurs at an altitude of 80–85 km. Thermosphere is region above the mesopause; where temperature increases and characterized by very high temperatures (of the order of 500–2000 K) as a result of absorption of short ultraviolet radiation by N_2 and O_2.

1.4   Atmospheric Composition

The earth's atmosphere comprises of various gases and very small amount of particles (aerosols). The ways in which the gases interact with the electromagnetic radiation (incoming solar radiation) predominantly determine the radiation budget of the atmosphere. If the relative abundance of gases changes in the atmosphere, the radiative equilibrium of earth-atmosphere system shifts leading to change in the climate. This perspective defines the importance of the composition of the atmosphere and the changes occurring in it.

1.4.1   Units of gas abundance

There are many ways by which abundance of any constituent is expressed, like mass density (e.g., kg m^{-3}), number density (e.g., molecules cm^{-3}) and mixing ratios by mass (so-called mass mixing ratio) or mixing ratio by volume (so-called volume mixing ratio). In addition, columnar density expressed in the unit of molecules per cm^2 (or molecules per m^2) of the atmosphere is another widely used parameter.

As discussed above, the mass density or the concentration of any species can be written as

$$\rho_i = \frac{P_i m_i}{RT}$$

where, ρ_i is the mass density of species 'i', P_i is the partial pressure of species i, and m_i is the molecular weight of species i. It is used in to express the concentration (µg m^{-3}) of various pollutants. The emission inventories of any species are basically the flux of the species getting emitted which is in turn the surface density per unit time. Here, the surface density is expressed in terms of mass density in the unit of kg m^{-2} or similar to it.

Similarly, number density, n_i of species i can be written as following.

$$n_i = \frac{P_i N_A}{RT}$$

where, P_i is the partial pressure of species i.

Note that the sum of the number densities of the individual components of the atmosphere must sum to the total number density, just as the sum of the partial pressures must be the total pressure (Dessler, 2000). In the model simulations (box-model simulation discussed in chapter - 6), or in the estimation of the chemical yield under certain chemical reactions, number densities are used. In addition, spectroscopic technique for the measurement abundance of trace gases basically estimates the concentration in terms of number density.

Another unit of representation of the trace gas abundance in the atmosphere is the column density which is the integral of the number density along a certain path in the atmosphere. Generally, column density n_{column} is the integration of number density n_i along the altitude, h. Since, the number density is function of altitude, it can be written as followings.

$$n_{column} = \int_{path} n_i\ (h) \times dh$$

The volume mixing ratio (VMR) is a widely used unit of expressing the abundance of an atmospheric constituent. The VMR of a given constituent is the fraction of number of molecules in a given volume (of course, with respect to total number of molecules considering all constituents). It can be expressed as following.

$$X_i\ (or\ VMR) = \frac{n_i}{n_{total}}$$

where, X_i is the VMR of gas i, n_i is the number density of gas i, and n_{total} is the total number density (i.e., air number density). Therefore, volume mixing ratio is the ratio of number density of i to the total number density. Since VMR being a ratio, it is dimensionless quantity. Generally, for the trace gases, VMR is very small number and it is usually multiplied by 10^6, 10^9 and 10^{12} and represented as parts per million by volume (ppmv), parts per billion by volume (ppbv) and parts per trillion by volume (pptv), respectively (Dessler, 2000). These units are also expressed as ppm, ppv or ppt, omitting "v". However, in view of the fact that unit of numerator corresponding to the molecules i, whereas it is of all constituents (i.e., air) in the denominator, sometimes,

VMR is represented as μmol mol^{-1}, nmol mol^{-1}, or pmol mol^{-1} (Seinfeld and Pandis, 2006; Ojha et al., 2016).

VMR is the conserved quantity for the changes in pressure and temperature (Dessler, 2000). Similar to VMR, mass mixing ratio (MMR) is another unit for abundance representation. MMR is the ratio of mass density of 'i' to the total mass density of air. In case of simulations using chemistry-transport model or reanalysis data, the output data of various trace gases are represented in MMR. The difference between VMR and MMR is of molecular weight of the gas under consideration and the mean molecular weight of air. The MMR can be converted to VMR using following formula.

$$VMR_i = MMR_i \; \frac{mean\ molecualr\ weight\ of\ air}{molecular\ weight\ of\ gas\ i}$$

Based on this, VMR of CO is obtained from MMR as,

$$VMR_{CO} = MMR_{CO} \; \frac{28.97}{28.01}$$

The partial pressure, itself is a unit to represent the abundance. The partial pressure P_i of a gas 'i' in the mixture of gases is defined as the pressure exerted by the molecules of the gas 'i', if all the other components are excluded in the mixture. The relation between the partial pressure and the VMR is given as following.

$$P_i = VMR_i \times P$$

However, the usage of this unit is limited and generally used in the representation of vertical profile of O_3.

1.4.2 Chemical constituents in the atmosphere

The major constituents of the dry atmosphere include Nitrogen (N_2), contributing 78.084% and Oxygen (O_2) contributing 20.946% by volume. N_2, O_2 and Argon (Ar) account for ~99.96% of total composition of dry air and correspondingly the mean molecular weight of dry air is 28.97 g mole^{-1} (considering molecular weight of N_2, O_2, Ar and CO_2: 28.02, 32.0, 39.94 and 44.01 g mole^{-1} respectively). Other gases which include CO_2, CH_4, CO, O_3, N_2O, NOx ($NO+NO_2$), Sulfur dioxide (SO_2), Chloro Fluro Carbons (CFCs), and other Oxygen-bearing, Hydrogen-bearing, Nitrogen-bearing, Carbon-bearing, Sulphur-bearing, Halogen-bearing and the noble gases together contributing to <1% of atmospheric volume are known as trace gases. However, water vapour (molecular weight: 18.02 g mole^{-1}) accounts for 0–4% (i.e., 0–40,000 ppmv) depending on the region. The mean molecular weight of moist air is ~28.6 g mole^{-1} considering 4%

of water vapour. Figure 1.4 and Table 1.1 depicts the various constituents of our atmosphere and the relative concentrations. Aerosols, smoke, ash and cloud droplets, as suspended particles or liquids account for very small mass of the atmosphere too. Carbon monoxide, the species addressed in this thesis, has a global average mixing ratio of ~100 ppbv (Seinfeld and Pandis, 2006), which corresponds to 1×10^{-5} % of atmospheric volume.
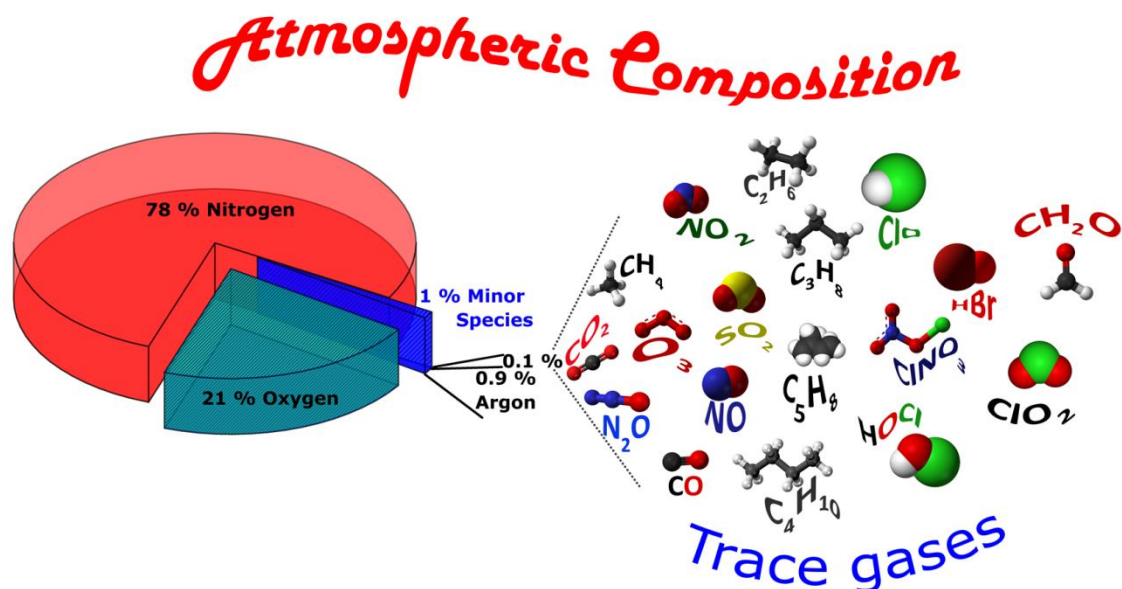
Figure 1.4: Composition of the earth's dry atmosphere by volume. Schematic representations of some of trace gases with their molecular structure are also shown along with.

Table 1.1: Composition of dry air by volume along with molecular weight (molar mass) of each constituent as adapted from Wallace and Hobbs, 2006; Seinfeld and Pandis, 2006; and http://elte.prompt.hu/sites/default/files/tananyagok/AtmosphericChemistry/ch01s03.html)

Constituent	Volume mixing ratio in dry air	Molecular Weight (g mole^{-1})
Nitrogen (N_2)	78.084%	28.02
Oxygen (O_2)	20.948%	32.00
Argon (Ar)	0.934%	39.94
Carbon dioxide (CO_2)	~400 ppmv	44.01
Neon (Ne)	~18 ppmv	20.18
Helium (He)	~5 ppmv	4.00
Methane (CH_4)	~1.8 ppmv	16.04
Hydrogen (H_2)	~0.5 ppmv	2.02
Krypton (Kr)	~1.1 ppmv	83.80

Nitrous oxide (N_2O)	~0.3 ppmv	44.01
Carbon monoxide (CO)	~50-250 ppbv	28.01
Xenon	~90 ppbv	131.3
Tropospheric ozone (O_3)	10-500 ppbv	48.0
Stratospheric O_3	0.5-10 ppmv	48.0
Nitrogen dioxide (NO_2)	1 pptv-50 ppbv	46.00
Ammonia (NH_3)	10 pptv-10 ppbv	17.03
Sulfur dioxide (SO_2)	10 pptv-10 ppbv	64.06
Hydroxyl (OH)	0.1-10 pptv	17.01
Other trace gases and aerosols	Trace and variable amounts	-

1.4.3 Homosphere and Heterosphere

Based on the mixing state, the atmosphere is divided into homosphere and heterosphere. The condition of mixing and the vertical distribution of atmospheric constituents are controlled by two competing processes namely (1) molecular diffusion and (2) mixing due to fluid motions/eddy diffusion. Upto ~100km, collisions between molecules are so frequent that all constituents are well mixed and no separation is possible. This well-mixed region (upto ~100 km) is known as the homosphere, where the mixing ratios remain fairly steady. The effectiveness of mixing depends on the mean free path (D) between collisions, which is a function of the mean velocity of molecules, which in turn is a function of temperature and pressure. Above 100 km, the molecular or atomic collisions are infrequent due very less density, and hence diffusion takes over. Diffusion separates the molecules based on their molecular weight (lightest on top). The scale height (H) which is a function of the molecular weight can be defined for each molecule. The mean free path rapidly increases with altitude, because the pressure decreases and D=H near 100 km. When H=D, the layer is not any longer mixed and the various constituents get separated. The region above 100 km to the top-of-the atmosphere is called the heterosphere. The region of transition from homosphere to heterosphere is called turbopause.

1.5 Sources of Carbon monoxide

CO is produced by both natural processes and anthropogenic activities. Almost half of the total emissions in the atmosphere is the from direct emissions due to anthropogenic activities, i.e., incomplete combustion of various fuels (biomass as well as fossil) [1350 Tg year^{-1} (IPCC, 2001)]. In the urban areas, motor vehicles are the main

source of CO pollution as exhaust of motor vehicles contains CO from incomplete burning of fuel (petrol, diesel, or gas) in the engine. Apart from the direct anthropogenic emissions, Weinstock, 1972 estimated that 5×10^{15} g of CO is emitted into the troposphere per year due to photochemical reaction, however, later the study by Logan et al., 1981 and Bergamaschi et al., 2000 showed $\sim 0.8–1.4 \times 10^{15}$ g year^{-1} from the oxidation of hydrocarbons (mainly methane and Isoprene), which was further fine tuned to 1.2×10^{15} g year^{-1} (1200 Tg year^{-1}) as reported in the IPCC 2001. Thus, about half of the CO in the earth's atmosphere is from the burning of fossil fuels and biomass (such as agricultural waste burning, forest fires and bushfires) and less than half is from the indirect emissions i.e., oxidation of hydrocarbons. This includes hydrocarbons emitted by human activities also. Thus, about 60% of the total CO emissions are of anthropogenic origin. The chemical reactions of VOCs, other than methane and Isoprene also contribute to CO formation.

Though ambient CO is known as a pollutant today, it has been present in the atmosphere due to volcanic eruptions. It is present in dissolved molten volcanic rock at high pressures in the earth's mantle. CO contents of volcanic gases vary from less than 0.01% to as much as 2%. CO is also emitted directly from other natural sources like, oceans and soil, with minor contributions to the total emissions (Finlayson-Pitts and Pitts, 2000). Moreover, since the natural source of CO, forest fires, is highly variable from year to year, it is difficult to make accurate estimates of natural emissions of the gas. The photolysis of chromophoric dissolved organic matter is one of the sources of CO in the open ocean (Ohta, 1997; Stubbins et al., 2006). Oceanic sources of CO contribute to $\sim 5\%$ of that produced through burning of fossil fuel (Stubbins et al., 2006). Model based estimate of open-ocean CO photo production was 47 ± 7 Tg CO yr^{-1} (Stubbins et al., 2006). Small amounts of CO are produced by vegetation and soil. Seed germination and seedling growth of higher plants produce very small quantities of CO (Siegel et al., 1962).

About 75% of atmospheric CO is produced by surface sources which are located predominantly in the northern hemisphere. Over half of the current CO emissions originate from anthropogenic activities, and the northern hemispheric burden is roughly twice that of the southern hemisphere. Despite many evaluations of the global CO budget, its global burden is less certain than those of methane and nitrous oxide (IPCC, 2001).

1.6 Sinks of Carbon monoxide

The reaction of CO with hydroxyl radicals is the major sink (~85%) of CO in the atmosphere (Logan et al., 1981).

$$CO + OH \rightarrow CO_2 + HO_2$$
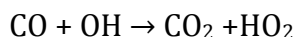
where, reaction rate constant, k= 1.5×10^{-13} ($1+0.6$ P_{atm}) cm^3 molecule^{-1} s^{-1}; The reaction cycle of the OH reactions is coupled with the cycles of CO, CH_4, H_2O, and O_3. As seen from the rate constant, the loss rate of CO is dependent upon the atmospheric pressure, in addition to its dependence on the abundance and distribution of OH in the troposphere.

Soil is a natural sink of atmospheric CO (Inman et al., 1971). CO in contact with soil may get oxidized and converted by methane-producing soil microorganisms in the presence of moisture under anaerobic conditions. The removal by soil uptake is very small about ~10% (Bartholomew & Alexander, 1981). The large scale atmospheric motions often move a fraction of tropospheric CO to upper altitudes. Under the deep convective activity, most of the CO molecules entering to the stratosphere gets depleted though CO + OH reaction (Pressman, J. and P. Warneck, 1970). Haemoglobin is also a sink for a small fraction of the ambient CO which is inhaled by humans. However, this contribution is small and estimate of the sink of ambient CO in haemoglobin is not available (Jaffe et al., 1968).

1.7 Global budget of Carbon monoxide

Understanding CO sources also places constraints on emissions of other pollutants released during combustion and whose emissions are often referenced to CO (Andreae and Merlet, 2001). It is also important as a correlative constraint for inverse analyses of CO_2 surface fluxes (Palmer et al., 2006).

Table 1.2: Budget (in Tg year^{-1}) of global tropospheric CO. Values are adapted from various reference.

[a] Corresponding to oxidation of Methanol and Acetone only.

Reference	Logan et al., 1981	Hauglustaine et al., 1998	Bergamaschi et al., 2000	IPCC, 2001	Duncan et al., 2007	Yin et al., 2015
Source						
Fossil and domestic fuel	500 (400-1000)	-	641	700	464–487	588
Biomass burning	680 (335-	-	768	650	640–762	327

	1400)					
Oceans and vegetation	140 (70-280)	-	49	200	-	54
Total direct emission	**1320**	**1219**	**1458**	**1550**	**-**	**969±180**
Oxidation of CH4	600	-	795	800	778–861	885±92
Oxidation of isoprene	690	-	268	270	170–184	-
Oxidation of terpenes		-	136	0	68–71	-
Oxidation of NMHC		-	203	160	116–124[a]	335±43
Total due to oxidation	**1290**	**881**	**1402**	**1230**		**1220**
Total Source	*2600 (2000-3000)*	*2100*	*2860*	*2780*	*2236–2489*	*2189±180*
Sink						
OH reaction	-	1920	-	-	-	2197
Surface deposition	-	190	-	-	-	

The annual global emissions of CO are estimated to be about 2600 ± 600 Tg, of which about 60% are from human activities including combustion of fossil fuels and oxidation of hydrocarbons including methane (Khalil & Rasmussen, 1990). The remaining 40% of the emissions are from natural processes, mostly from the oxidation of hydrocarbons and also from plants and the oceans. Major part of the CO emitted into the atmosphere each year is removed by reactions with OH radicals (85%), by soils (10%), and by diffusion into the stratosphere and subsequent oxidation.

As seen from the table 1.2, globally ~50% of CO is from direct emissions from fossil and biomass burning. It is also reported that ~60% of total CO is of anthropogenic origin after excluding the natural contribution of biomass burning, like naturally occurring forest fire events (Logan et al., 1981; WMO, 2004). The oxidation of methane

is corresponding to 23-30% to the total emission. The remaining amount is from direct emission from oceans as well as vegetation and oxidation of NMHCs including Isoprene. Almost half of the CO from CH_4 oxidation is of anthropogenic origin which corresponds to anthropogenic emission of CH_4 (Logan et al., 1981). It is to be noted that above budget is for global CO and percentage contribution to the total CO would vary depending upon the region. The region where forest fire or agricultural waste burning are dominant, the contribution from biomass burning to the total regional level CO would be larger. The urban region where higher fossil fuel consumption prevails, contribution from fossil fuel burning would be larger than other sources (Finlayson-Pitts and Pitts, 2000).

1.7.1 Indian CO emission budget

The studies on CO emission budget specifically focusing the Indian region are few, i.e., Dalvi et al., 2006. However, regional and global emission inventories provide the estimates on CO emission from the Indian region. As per the various emission inventories, total emission of CO from India is estimated to be 61.1 (base year -2006; INTEX-B; Zhang et al., 2009), 61.80 (base year -2008; REASv2.1; Kurokawa et al., 2013), 63.34 (base year - 2000; Streets et al., 2003), 66.7 (base year - 1999; Dickerson et al., 2002), 69.37 (base year - 2001; Dalvi et al., 2006) Tg CO year^{-1}. The differences among these estimations are due to uncertainty in the inventories and difference in the base year. The anthropogenic activities have increased over the year as seen in the increase in population and energy requirement and hence the base year under consideration for emission inventory is important. Aforementioned estimates are for the year 2008 or before. EDGAR v4.3 has the latest estimates of emissions from various sectors, total of 76.84 Tg CO year^{-1}. Though it includes the biomass burning like crop residue burning, however, biomass burning corresponding to the forest fires is excluded and hence total estimation is on its lower side.

1.8 Air quality standard for Carbon monoxide

CO is a highly toxic air pollutant having serious adverse health impacts on humans and animals. Increased levels of CO in the blood reduce the amount of oxygen carried by haemoglobin around the body and hence the vital organs (i.e., brain, nervous tissues and the heart) do not receive enough oxygen to work properly. Depending upon the CO level being inhaled, it can cause headache, dizziness, vomiting, nausea, unconscious or even death. Due to its toxicity and because it is colorless, odorless,

tasteless and non-irritating, it is called the "silent killer". The abundance of 0.16% (i.e., 1600 ppmv) can cause death in less than 2 hours (Goldstein, 2008).

The governments, health and environment organisations around the world have set up Air quality standards. The National Ambient Air Quality Standards (NAAQSs) for CO, established by the U.S. Environmental Protection Agency (EPA), are 9 parts per million (ppmv) measured as an annual second-maximum eight-hour average concentration and 35 ppmv averaged over a one-hour period. Though the carbon monoxide levels in ambient air in urban residential areas are unlikely to cause significant health effects, indoor sources such as poorly ventilated gas appliances and wood heaters pose risk to human health. Significant contribution of indoor air pollutants are made from the outdoor environments. Indoor environments also contain their own sources of pollution originating from activities such as cooking, fabrics, building materials, indoor smoking, combustion, and application of household chemicals (WHO, 2004).

In India, under the Air (Prevention and Control of Pollution) act, 1981, CPCB (Central Pollution Control Board) has defined NAAQS for 12 different pollutants in year 2009. The CO standard is 2 and 4 mg m^{-3} corresponding to ~1.7 and ~3.5 ppmv, respectively for the averaging interval of 8 and 1 hour. It is to be noted that 8 or 1 hourly values shall be complied with 98% of time in a year. The recommended measurement technique for monitoring the CO is NDIR as discussed in the section 2.2. In the megacities, it is likely that CO levels exceed the 1.7 ppmv (8 hourly) leading to the poor air quality. The Air quality monitoring stations are established over mega cities (like Delhi, Mumbai, Pune, and Ahmedabad) under SAFAR (System of Air Quality Forecasting And Research) project of IITM, MoES (Indian Institute of Tropical Meteorology, Pune; Ministry of Earth Sciences). In addition, monitoring of pollutants, including CO, is being carried out by Pollution Control Board over major cities in India. The measurement of CO and other air pollutants (O_3, NO, NO_2, PM10 and PM2.5) at multiple measurement sites across Delhi shows that levels of these pollutants frequently exceed the NAAQS (Peshin et al., 2017).

1.9   Lifetime of Carbon monoxide

The lifetime of a species is the average time that a molecule of that species resides in the atmosphere before removal either through chemical transformation to another species or any other processes (Seinfeld and Pandis, 2006). The average

lifetime of a gas molecule in the atmosphere can range from seconds to millions of years, depending on the effectiveness of the removal processes (Seinfeld and Pandis, 2006).

There are two ways by which lifetime of a species is defined based on the spatial scale. (1) Global lifetime (Dessler, 2000) or sometimes referred as "turn over time" (Bolin and Rodhe, 1973). This is estimated bases on the total global burden and total loss rate of the species. (2) The "local" lifetime (Dessler, 2000) or sometimes referred as "chemical lifetime" (Seinfeld and Pandis, 2006) or just as lifetime. This is estimated based on effectiveness of removal processes or lose rates.

The global lifetime is defined as following.

$$\tau_{global} = \frac{total\ atmospheric\ burden\ of\ the\ species}{total\ loss\ rate\ of\ the\ species}$$

Note that total atmospheric burden considers entire atmosphere. Alternatively,

$$\tau_{global} = \frac{Steady\ state\ abundance\ the\ species}{global\ emission\ rate}$$

Total global emission of CO = 2.78×10^{12} kg year^{-1} (IPCC, 2001; Seinfeld and Pandis, 2006)

Global mean columnar concentration of CO is 1.8×10^{18} molecules cm^2 (from multiple satellite observations). Thus, global CO abundance = Surface Area of earth × global Mean columnar concentration = $4 \times 3.14 \times (6370 \times 100000)^2 \times 1.8 \times 10^{18} = 9.1 \times 10^{36}$ molecules $= 9.1 \times 10^{36} \times 28.01/(1000 \times 6.023 \times 10^{23})$ kg CO $= 4.27 \times 10^{11}$ kg CO and

$$\tau_{global} = \frac{4.27 \times 10^{11}}{2.78 \times 10^{12}} \times 12\ months = 1.84\ months$$

Thus, the global mean lifetime of atmospheric CO is ~2 months. However, uncertainty in the emission value, global mean concentration and variation sink strength, this number would be in the range of 1–3 months.

For the estimation of atmospheric/chemical lifetime, multiple processes involved in the removal of the species need to be considered. In case of CO, there are two processes which are responsible for loss of CO, i.e., its reaction with OH and surface deposition. The lifetime can be estimated based on sink processes as following.

$$\tau = \frac{1}{\tau_1} + \frac{1}{\tau_2}$$

where, τ_1 is the lifetime corresponding to process 1 (i.e., OH-reaction) and τ_2 is corresponding to process 2 (i.e., surface deposition). Since surface deposition of CO is

corresponding to only ~10% (or less) of total sink of CO and hence second term can be neglected in the above equation. Thus, lifetime of CO is mainly due to its reaction with OH radical. Thus, $\tau = \tau_1$.

$$CO + OH \rightarrow CO_2 + HO_2$$
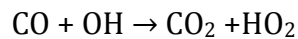
where, reaction rate constant, k= 1.5×10^{-13} (1+0.6 P_{atm}) cm^3 $molecule^{-1}$ s^{-1}

The above reaction is second-order reaction as two reactants are involved in the reaction. This means that the rate of the product depends on (1) rate constant and (2) concentrations of both reactants. However, In the case of atmosphere the concentration of CO (~10^{12} molecules cm^{-3}) is much higher than that of OH concentration (10^6 or 10^7 molecules cm^{-3}) and hence the above reaction is considered as pseudo-first order reaction. In the first order reaction, the concentration of species falls exponentially.

If the initial CO concentration is $[CO]_0$, then CO concentration at time t is defined by following equation. $[CO]_t = [CO]_0 e^{-kt}$

Thus, the lifetime is given by following equation, which is the e-fold time over which CO reduced by 1/e from its initial concentration.

$$\tau = \frac{1}{k\,[OH]}$$

Thus, the lifetime of CO depend on OH concentration and since k is depends on the atmospheric pressure, it depends on the atmospheric pressure also.

Considering the value of k=2.4×10^{-13} for pressure = 1 atmosphere, OH concentration of 1 x 10^6 molecules cm^{-3}, lifetime is calculated to be 48 days (~2 months). However, there exist large variability in the OH concentration (higher concentration over tropics and lower over polar region) and hence lifetime of CO would vary depending upon the region and the altitude. The various studies on the estimation of OH concentration shows the range from 0.6 to 1.33 x 10^6 molecules cm^{-3} (Lawrence et al., 2001 and reference therein) and hence accordingly lifetime would be in the range of 1 to 3 months. The lifetime is relatively shorter than other greenhouse gases like CH_4, N_2O, etc. and its heterogeneous distribution of sources produce large temporal and spatial CO variations. The recent estimation of OH made by Lelieveled et al., 2018 over Asian summer monsoon region in the upper and lower troposphere gives lifetime of 15 days in lower-troposphere and 42 days in the upper-troposphere as shown in the table 1.3. However, CO has a relatively short atmospheric lifetime, ranging from 10 days in

summer in the tropics to more than a year over the polar regions in winter (WMO, 2018; Novelli et al., 1992).

Table 1.3: OH concentration and corresponding lifetime of CO over Asian summer monsoon region. (OH values are adopted from Lelieveled et al., 2018)

Region/Description	OH concentration (molecules cm^{-3})	Rate constant for CO + OH reaction	Lifetime of CO
Lower troposphere (1000-800 hPa)	3.1×10^6	2.31×10^{-13} considering pressure 900 hPa	15 days
Upper troposphere (100-200 hPa)	1.7×10^6	1.64×10^{-13} considering pressure 150 hPa	42 days

The estimation of lifetime can be useful in estimating how far from its source a species is likely to remain in the atmosphere before it is removed from the atmosphere. The term "removed" would mean the significant reduction ($\sim$63%) from its value at the source. This is because of the way lifetime is defined; accordingly, the time over which the concentration of species of interest falls $1/e$ ($\sim$37%) of its initial value.

1.10 Greenhouse effect, Radiative forcing and Global warming potential of Carbon monoxide

The incoming shortwave solar radiation (peaking around 0.5 μm) heats up the earth's surface after partially getting absorbed by the atmosphere and reflected back to space. The earth surface emits the longwave/thermal radiation (peaking around 10 μm) which passes through the atmosphere. The presences of certain gases like CO_2, N_2O, CH_4, O_3 and H_2O, in the atmosphere, so-called greenhouse gases, absorb the infrared radiation blocking the outgoing radiation as they have absorption bands falling in the infrared regime. Much of this thermal radiation emitted by the land and ocean is absorbed by the atmosphere, including clouds, and radiated back to the earth. This makes the earth's atmosphere warmer by 33 K (Coakley and Yang, 2014) than that it would have been without such gases. This is called the greenhouse effect. Greenhouse gases are of natural origin or man-made which absorb and emit the radiation at specific wavelengths within the spectrum of thermal infrared radiation emitted by the earth's surface, the atmosphere itself, and by clouds. In addition to CO_2, CH_4, N_2O, O_3 and H_2O, there are man-made greenhouse gases such as chlorofluorocarbons (CFCs), hydrochlorofluorocarbons (HCFCs), hydrofluorocarbons (HFCs), and perfluorocarbons (PFCs) which are called the primary greenhouse gases. However, the excess amount of greenhouse gases enhances the greenhouse effect leading to global warming and

consequent climate change. Apart from the primary greenhouse gases, CO, Non-Methane Volatile Organic Compounds (NMVOC) and NOx are secondary or indirect greenhouse gases, which produce the primary greenhouse gases (i.e., CO_2, CH_4 and O_3) through chemical reactions.

There exists a radiative equilibrium for the earth-atmosphere system. If the amount of greenhouse gases increases in the atmosphere, the total energy absorbed by the earth-atmosphere system increases. In other words, an additional energy is getting added to the earth-atmosphere system which forces the system to achieve a new equilibrium. Such forcing is envisaged as radiative forcing (RF). The RF is defined as a change in the average net radiation at the tropopause or at the top of the atmosphere due to a particular perturbation or change of species of interest (greenhouse gases or aerosols, or clouds) (IPCC, 2013). RF is also defined as the change in net downward flux (shortwave + longwave) at the tropopause after allowing for stratospheric temperatures to readjust to radiative equilibrium, while holding other state variables such as tropospheric temperatures, water vapour and cloud cover fixed at the unperturbed values (IPCC, 2013). CO has two absorption/emission bands around 2.3 and 4.6 μm in the infrared regime and hence it can contribute directly to greenhouse effect by absorbing and emitting the radiation. The earlier work done by Evans and Puckrin, 1995; and Sinha and Toumi, 1996 shows that direct forcing of CO is relatively small in the global average, implying a 20-year global warming potential of much less than 1. Thus, CO does not directly contribute significantly to the greenhouse effect (IPCC, 1996; WMO, 2018). However, it contributes indirectly to the greenhouse effect or radiative forcing (1) through the oxidation of CO to produce CO_2, a green house gas and (2) by increasing the concentration of CH_4 and tropospheric O_3 (both are green house gases) by removing the OH radical which would otherwise destroy them. CO is also a precursor for the formation of tropospheric O_3 which is another greenhouse gas (IPCC, 2103; Seinfeld and Pandis, 2006). Thus, CO is known as indirect greenhouse gas.

The indirect RF due to CO is 0.23 (0.18–0.29) Wm^{-2} which is significantly smaller than that of CO_2, CH_4 and Black carbon aerosols, but higher than that of N_2O, HFCs, PFCs, SF_6, NMVOCs. The effects due to the greenhouse gases depend not only on the emissions but also on their lifetimes in the atmosphere. Global warming potentials (GWP) is defined as the time-integrated radiative forcing due to the instantaneous emission of a fixed amount (generally, it is with respect to 1 kg) of a reference gas most commonly, CO_2.

As per the definition of relative GWP, the GWP of CO_2 is 1. While CH_4 and N_2O have GWP of 21 and 310 over TH of 100 years, the indirect GWP for CO is in the range of 1 to 4.4 (Table 1.4).

Table 1.4: Indirect global warming potentials of carbon monoxide adopted from Daniel and Solomon, 1998.

Indirect effect	Time-Horizon: 20-Years	Time-Horizon: 50-Years	Time-Horizon: 100-Years
CH_4 response (includes CH_4 IR absorption, stratospheric H_2O, and O_3 production from CH_4)	2.8	1.6	1.0
Tropospheric O_3 production (from CO, lower and upper limits)	0.0-11.2	0.0-5.6	0.0-3.4
Total	2.8-14.0	1.6-7.2	1.0-4.4

1.11 Role of Carbon monoxide in the tropospheric chemistry

CO is a reactive gas that plays an important role in the chemistry of the atmosphere. The CO influences the concentrations and distributions of the atmospheric oxidants, O_3, HO_2, and OH. Most of the air pollutants get removed from the atmosphere by OH radical, which is the primary tropospheric oxidant and also known as "detergent" of the atmosphere. The oxidizing capacity of the troposphere depends on trends and variability CO because CO is a major sink for OH radical. While reaction between CO and OH represents ~90% of the CO sink (Logan et al., 1981), the same is responsible for 75% of the removal of OH (Thompson, 1992). However, recent study by Lelieveld et al., 2016 shows that ~40% global tropospheric OH is consumed by CO +OH reaction.

The reactions involving CO as well as OH are as followings.

(1) Photolysis of O_3 by ultraviolet radiation in the presence of water vapor.

$$O_3 + h\nu \ (\lambda < 330 \ nm) \rightarrow O \ (^1D) + O_2$$

$$O \ (^1D) + H_2O) \rightarrow 2 \ OH$$
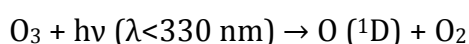
(2) $CO + OH \rightarrow CO_2 + HO_2$

Above reaction occurs in the presence of an air molecule that removes excess energy from reaction intermediates by collisions.

(3) $HO_2 + HO_2 \rightarrow H_2O_2 + O_2$

(4) $NO + HO_2 \rightarrow NO_2 + OH$
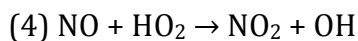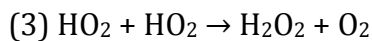
This reaction is known as NOx recycling process for OH. In addition, this leads to ozone production through photodissociation of NO_2 by ultraviolet and visible radiation.

$NO_2 + h\nu$ ($\lambda < 430nm$) $\rightarrow NO + O$ (^3P)

O (^3P) $+ O_2 \rightarrow O_3$
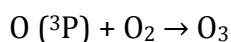
In the polluted environment where NO_2 is higher, NO_2 would be a sink for OH.

$NO_2 + OH \rightarrow HNO_3$

(5) $O_3 + HO_2 \rightarrow 2O_2 + OH$

(6) $H_2O_2 + h\nu$ ($\lambda < 550nm$) $\rightarrow OH + OH$

(7) $CH_4 + OH \rightarrow CH_3O_2 + H_2O$

(8) $HCHO + OH \rightarrow HO_2 + CO + H_2O$
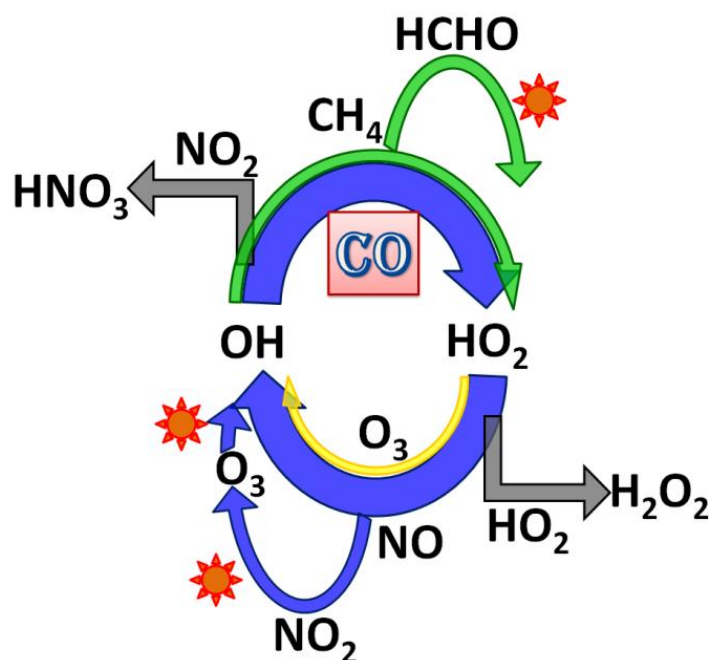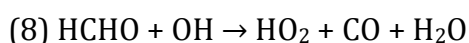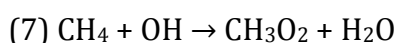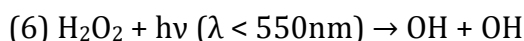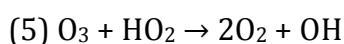
Figure 1.5: Thematic representation of prevailing tropospheric chemistry involving CO. The reaction which terminates the reaction cycle is shown by the gray arrows.

These set of reactions are important in tropospheric chemistry of CO and OH and it is represented thematically in the figure 1.5. These are the main reactions decides the production as well loss of the OH in the troposphere. It is interesting to note that NOx produced during the lightening (which occurs mainly during convective activities) recycles the OH, helping in the removal of CO, CH_4 and other pollutants in the free and

upper troposphere (Lelieveld et al, 2018). Two reactions (HO_2 +HO_2 and OH+HNO_3) shown by the gray arrows in the figure 1.5 are those which terminates the chain reaction. Since OH is crucial in the chemistry of CO (as well as other gases), its distribution is discussed briefly.

Figure 1.6 shows the distribution of zonally mean OH concentration based on the model simulations. More or less the distribution is in agreement with each other. Similar distribution but extending up to 10 hPa is reported by Lelieveld et al., 2016. The higher concentration of OH over the tropics is mainly due to higher solar radiation and higher water vapour. The mid-tropospheric high in the OH concentration is due to higher availability of add oxygen. It is important to note that ~63% of OH in the troposphere is from two reactions, $O(1D)$ +H_2O and NO+HO_2 (Lelieveld et al., 2016).
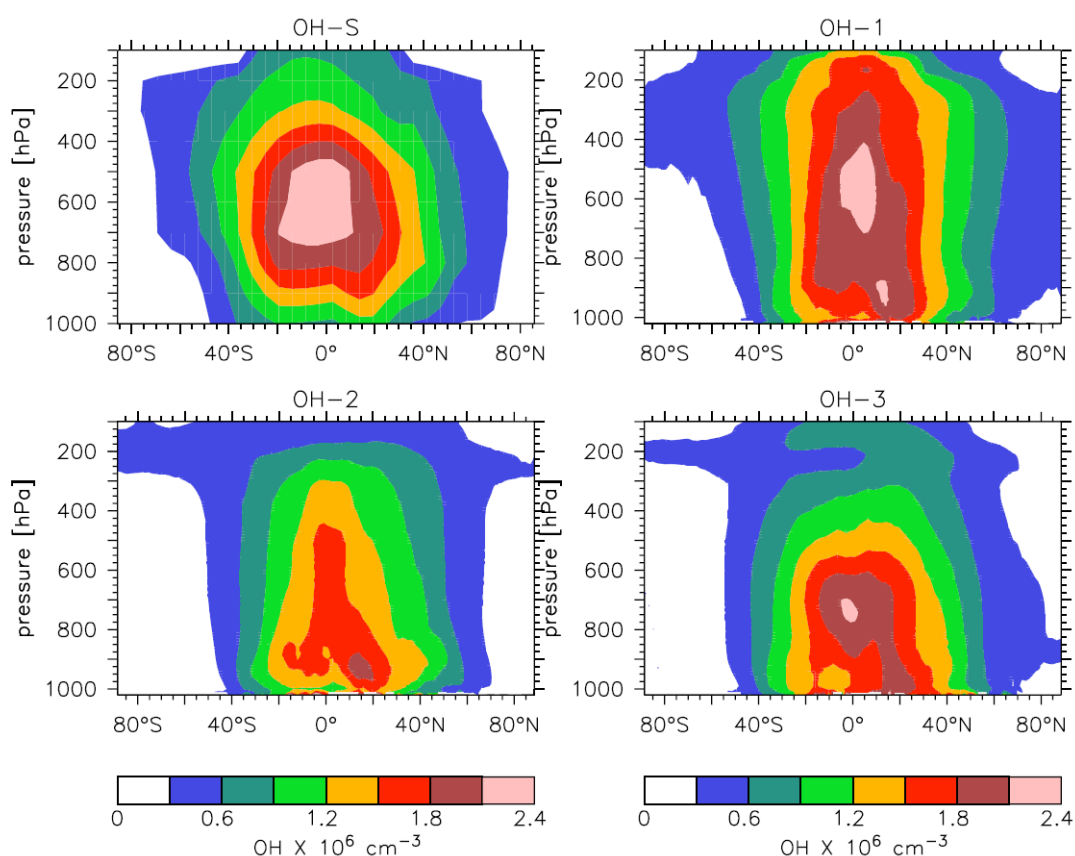
Figure 1.6 : The annual zonal mean OH fields based on, (a) OH-S (Spivakovsky et al., 2000); (b) OH-1 (Lawrence, 1996); (c) OH-2 (Lawrence et al., 1999); and (d) OH-3 (von Kuhlmann, 2001). The figure is adopted from Lawrence et al., 2001.

1.12   Stratospheric - Mesospheric Carbon monoxide

Very small quantity of CO exists in stratosphere and mesosphere (Hays and Olivero, 1970; Forkman et al., 2005). The distribution of CO in the stratosphere and the mesosphere has been used to infer the dynamical processes and study the transport of

trace gas (Hays and Olivero, 1970). Mixing ratios and its variation are important for understanding the large-scale mesospheric circulations (de Zafra and Muscari, 2004) and vertical motions in the stratosphere and mesosphere (Forkman et al., 2005). Utilising the satellite observations, the study by Minschwaner et al., 2010 has mapped the CO net production and loss indicating that photochemical loss dominates over production for nearly all conditions. Stratosphere acts as a sink for atmospheric CO based on the CO + OH reaction, which is also a sink mechanism in the troposphere. The OH radical produced photochemically in the stratosphere with a time constant several orders of magnitude less than the CO oxidation rate constant, so that, all the CO entering to the stratosphere will be destroyed/removed (Pressman, J. and P. Warneck, 1970). The rate limiting factor is the transport of CO rich air through tropopause. Both the deep convections and anticyclones affect CO in the tropical troposphere and lower stratosphere (Li et al., 2014).

1.13   Measurement techniques for Carbon monoxide concentration

The techniques for the measurements of concentration or mixing ratios can be divided into two broad categories, namely, in-situ measurements and remote sensing measurements.

1.13.1 In-situ methods

There are several measurement techniques for the measurements of CO mixing ratios. The widely accepted and used techniques are described in brief below.

1.13.1.1 Gas Chromatography

Gas Chromatography is the popular technique for the separation of different components in a given composite sample (gas or liquid solution). In the gas chromatograph, there exists a column (a very thin wire like tube with length of meters) of a specific material known as stationary phase (a solid or a heavy non-volatile and non-soluble liquid phase). Depending on the target species which needs to be separated from a mixture, the column (or the material of stationary phase) is selected. A mobile phase comprising of a liquid or gas, also called the carrier gas/liquid, keeps moving through the stationery phase. The mobile phase is inert (e.g., nitrogen gas) in nature and doesn't react with the sample. The sample which is subjected to analysis is taken through the column by the mobile phase. While sample passes through the column, the interactions of the components of the sample with the stationary phase lead to separation of different components based on the selective adsorption and desorption on

the surface area of the stationary phase. Based on the molecular weights, boiling points, Coulomb force between sample molecules and molecules of stationary phase, different components retains in the stationary phase (or column) for different times. The stronger the interaction with the stationary phase, the slower the components will move in the column and come out of the column (elutes) later. Thus, each component moves at different rates and emerge from the column with varying time of emergence to reach a suitable detector.

Depending upon the application and target species, suitable detectors need to be employed for identifying and quantifying the different components. There are various detectors, used in GC technique, like Thermal Conductivity Detector (TCD), Reduction Gas Detector (RGD) and Flame Ionization Detector (FID). For the detection of CO, RGD and FID detectors are widely used.

The FIDs detect hydrocarbons only; detection of CO using this detector requires an additional attachment known as Methaniser. The methaniser is basically a catalytic convertor, in which CO is converted to methane in the presence of nickel catalyst following to the reaction, $2CO + 4H_2 \leftrightarrow 2CH_4 + O_2$. The CO coming out from the column is swept through Methaniser and converted to methane. The methane, then, is fed to the FID. The FID has hydrogen flame at very high temperature and there exists an arrangement of anode and cathode around the flame. While hydrocarbon gets in to the flame, molecules are broken due to high temperature and ionized. Hence the positive and negative ions are generated and detected by the anode and cathode giving rise to the current in the circuit. Depending upon the amount of methane, a current is proportional to the amount of CO in the sample. As mentioned above, CO concentration is quantified based on calibration coefficient defined using the standard reference of CO.

RGD detector uses a mercuric oxide (HgO) reaction tube and UV cell (UV lamp and UV photodiode). CO coming out from the column is allowed to pass through this tube, the reaction $CO + HgO \rightarrow CO_2 + Hg$ (vapor) produces mercury vapor. The mercury vapor is then swept into the UV cell. Since mercury absorbs the UV light emitted from the lamp, the change in transmittance is detected by the UV detector depending upon the amount of mercury vapour in the cell. This signal is linearly proportional to the amount of CO and it is qualified based on calibration coefficient defined using the standard reference of CO. However, usage of RGD detector has become almost obsolete because of usage of Mercury in it which has environmental hazards.

1.13.1.2 Gas filter Correlation Non-Dispersive Infrared (GFC NDIR) absorption

GFC NDIR technique is the most commonly used for the measurements of CO mixing ratios. In the GFC NDIR technique, the infrared radiation coming from the source does not get dispersed and a band of infrared radiation around the CO absorption wavelengths is used for the measurement of CO mixing ratio/concentration. In order to eliminate the spectral contamination from the unwanted gases present in the sample, the target gas (i.e., CO) itself used as a filter for selective absorption of wavelengths corresponding to CO absorption features. In this study, the in-situ measurements were performed using the GFC NDIR based analyser. The detailed description of the technique, calibration, etc. is given in section 2.2. The instrument utilising this technique is less expensive than the gas chromatograph, and requires lesser efforts for its operation. However, due to the relatively higher value of detection limit of analysers, it is not very effective for the measurements over pristine locations like Antarctica where CO mixing ratios falls below 50 ppbv.

1.13.1.3 Vacuum Ultraviolet Resonance Fluorescence

At ground level, where CO mixing ratios does not change significantly over time scale of few minutes, techniques which offer slow response for measurement are well acceptable and being used widely. However, the in-situ measurement of vertical profile of CO measurement in general employs aircraft or balloons which moves much faster than the response time of instruments mentioned above. For such measurements, Vacuum Ultraviolet Resonance Fluorescence is one of the techniques which offer fast-response (~2 seconds) and high-precision measurements (Takegawa et al., 2001). The radiation around 150 nm is obtained by the discharge in CO_2/Ar mixture. This radiation is passed through a monochromator to obtained specific wavelengths where the CO absorption band (in UV) lies. The radiation excites the CO molecules and fluorescence from the excited molecules is detected using the photomultiplier tube. The signal at the PMT is proportional to the number of CO molecules present in the measurement chamber. In this technique, fluorescence from the H_2O present in the sample air could contaminate the measurements and hence optical filtering corresponding to the H_2O fluorescence is required.

1.13.1.4 Fourier Transform Infrared spectroscopy

Fourier Transform Infrared (FTIR) spectroscopy utilises Michelson-type interferometer. The infrared radiation from an IR source or the sun is passed though

sample gas or may be atmosphere and the received IR radiation is split into two beams by a beam-splitter. One beam is reflected from a fixed mirror and other from a moving mirror, which generates the path difference. When these beams interfere, the inference fringes are generated and the intensity of the light is measured at different time intervals. By making measurements of these signals at many discrete positions of the moving mirror, the source spectrum can finally be reconstructed using the inverse Fourier transform. The analysis of the FTIR spectrum provides simultaneous, continuous and multi-species analysis with high accuracy and precision. Since FTIR resolve the spectral features to very high resolution, interference from unwanted species is eliminated easily. However, this technique requires perfect optical alignments.

1.13.1.5 Cavity ring-down spectroscopy

Similar to Vacuum Ultraviolet Resonance Fluorescence technique, high precision with fast response is possible using Cavity Ring-Down Spectroscopy (CRDS) or off-axis Integrated Cavity Output Spectroscopy (OA-ICOS) techniques. CRDS technique uses the laser (highly monochromatic source) for specific wavelength where one of the CO absorption lines lies. The wavelength is so chosen that absorption due to unwanted species is zero or negligibly small. The light enters the cavity (i.e., measurement chamber which is filled with sample air) through a semi-transparent mirror. The cavity has arrangements of high reflective mirrors and the light beam bounces between mirrors and the light intensity in the cavity enhances with time. The mirror near to the detector is semi-transparent and the rise in the intensity is recorded. When intensity reaches to certain level, laser source is switched off and intensity falls exponentially. The time over which intensity falls to 1/e of its initial values (the values at the time of switching off the laser) is recorded. This time is known as ring-down time. If the concentration of target species is higher, the intensity would fall faster and hence ring-down time would be smaller. Thus, the ring down time is proportional to the concentration of target species in the cavity. Since the light beam travels great distance in the cavity (due to multiple reflections), very low concentration is detectable with high precision. The optical alignment is crucial part of the measurement.

1.13.1.6 Off-axis Integrated Cavity Output Spectroscopy (OA-ICOS)

This technique also utilises the laser as light source, but wavelength is made to vary over small range so that absorption line (or line shape) is scanned. The cavity has high reflecting and semi-transparent mirror with parallel arrangement. The laser enters

to the cavity at small angle to optical axis of the cavity (so-called, off-axis) though one of the mirrors. Due to high reflectivity, the beam travels a great distance in the cavity due to multiple reflections before leaking to the detector though the mirror near to the detector. The intensity is recorded with respect to the wavelength. As mention, wavelength varies to scan the absorption line. According to the Beer-Lambert's law, intensity falls exponentially from its initial value depending upon the concentration present in the cavity. The intensity falls at the absorption line but intensity remains unaffected at the edge of the absorption line. The magnitude of intensities at the edge of absorption line and peak of the absorption line allows calculating the concentration of target species. Both the techniques, CRDS and Off-axis ICOS, are also useful for the measurement of the isotopes of CO due to the use of laser and measurement at precise wavelength.

Zellweger et al., 2009 has made extensive inter-comparison of CO measurements corresponding to various measurement techniques discussed above. In general, the measurement agrees among various techniques.

1.13.1.7 Network of surface CO measurements
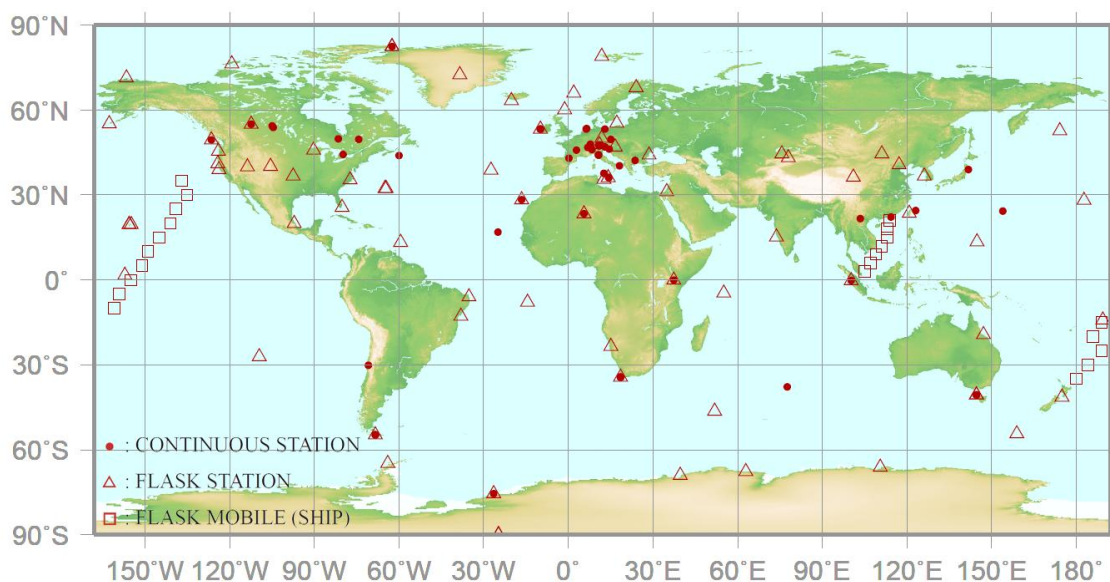
Figure 1.7: Network of observational sites where of surface CO measurements are being carried out by WDCGG/NOAA. The figure is adapted from WMO report (October 2018).

Surface CO is currently measured by a series of ground station networks spread across the globe. Specifically, the Global Atmosphere Watch (GAW) programme has a global network for monitoring the atmospheric greenhouse gases and other trace gases including CO. Observations are being made by Global Monitoring Division of the National Oceanic and Atmospheric Administration (NOAA). Currently, there are about

150 sites complemented by continuous flux tower, balloon, aircraft, and ship observations (figure 1.7). CO concentrations are reported by WMO World Data Centre for Greenhouse Gases (WDCGG) in WMO (October 2018) that is run by the Atmospheric Environment Division in Japan Meteorological Agency. Measurements are made either continuously by infrared analyzers or from air samples captured in the flasks which are later analyzed in the laboratory [WMO, October 2018; https://gaw.kishou.go.jp/static/publications/summary/sum42/sum42.pdf].

1.13.1.8 Aircraft-based measurements
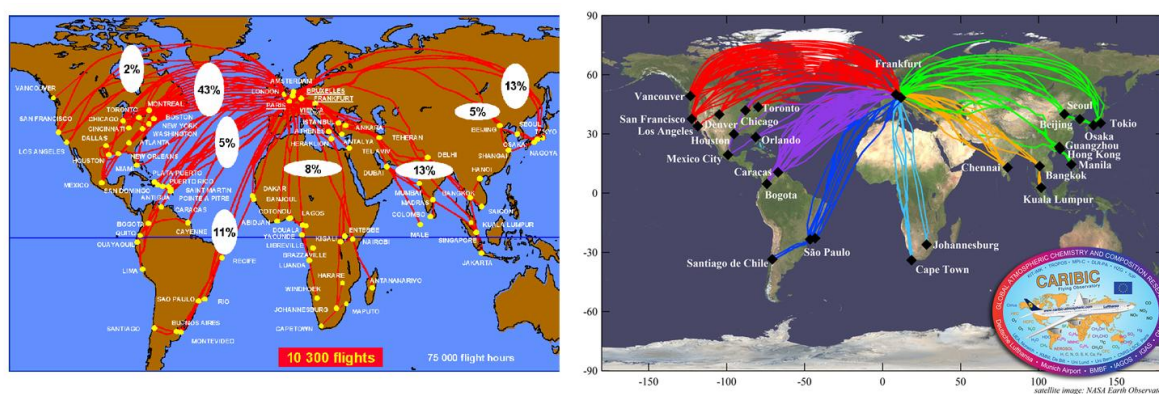
Figure 1.8: Schematic flight routes of MOZAIC (left) and CARIBIC (right) programs showing the global coverage (Image curtsey: http://web.mit.edu/jync/www/eos/ and https://www.caribic-atmospheric.com/Flight.php). The percentages shown for MOZAIC program are of total flights from the various global sectors.

The air traffic is getting increased day by day, and hence aviation affects the troposphere significantly, changing the chemistry of the upper troposphere. The remote sensing measurements from satellite give broader pictures (as discussed in various part of thesis) with continuous global coverage but it lacks small scale variations. The accurate and detailed measurements of the vertical profile and upper tropospheric CO can be achieved by aircraft based in-situ measurements which are also used for validation of satellite data. The observations of various trace gases including CO are being carried out by two projects, namely, 'Civil Aircraft for the Regular Investigation of the Atmosphere Based on an Instrument Container' (CARIBIC; Brenninkmeijer et al., 2007; https://www.caribic-atmospheric.com/Home.php) and Measurement of Ozone and Water Vapour by Airbus In-service Aircraft (MOZAIC; Marenco et al., 1998; https://www.umr-cnrm.fr/dbfastex/datasets/moz.html#moz_data). Various flight tracks form CARIBIC and MOZAIC are shown in figure 1.8, which shows the global coverage over which in-situ measurements are being performed. These programs provide valuable observations of various trace gases including CO. In addition to the detailed studies on the upper-tropospheric chemistry and variabilities of trace gases,

these measurements are also important for validation of satellite retrieved (Jiang et al., 2013) as well as model simulated parameters (e.g., Ojha et al., 2016). In addition, the program, "In-service Aircraft for a Global Observing System" (IAGOS; Petzold et al., 2015 https://www.iagos.org/) IAGOS builds on the framework of the European Research Infrastructure projects MOZAIC and CARIBIC, and provides essential climate variables (temperature, water vapor, and ozone, and other species) on a global scale.

1.13.2 Remote sensing methods

Both ground-based and space-based remote sensing techniques are used for the measurements of columnar CO and vertical profile of CO.

In the ground based remote sensing, sun is used as a source of radiation. Since CO absorption bands are around 2.3 and 4.7 μm, thermal radiation from the sun and emitted from the atmosphere are utilised for the retrieval of CO profile or columnar concentration. Ground based high spectral resolution (~0 .002 cm^{-1} or higher) solar spectral irradiance obtained using FTIR is also used for CO measurements. A modified Chahine-Twomey iterative inversion algorithm described by Liu et al., 1996 is used to retrieve the profiles of CO. Basically, line-by-line and layer-by-layer atmospheric transmission calculation is carried out. The vertical profile of CO is estimated by adjusting an initial profile (so-called a priori profile, which could be a climatologically mean profile of CO) to best fit the observed spectrum. The magnitude of change in the profile depends how large the averaging kernel used the retrieval. The magnitude of kernel depends on the amount of CO present in the atmosphere, sensitivity of detection of signal, signal to noise ratio or the configuration of the instrument. The Spectral window is selected such that it contains the information of vertical profile of CO and wavelengths which are corresponding to the interference from other species which are to be discarded. Zhao et al., 1997 and Yurganov et al., 2011 have described the methodology and the procedures for the retrieval of vertical profile of CO and columnar CO.

FTIR technique as discussed briefly above is used for ground and space-based remote sensing. TES aboard Aura satellite and IASI aboard MetOp-A are Fourier Transform Spectrometer (FTS).

Figure 1.9 depicts the process which the radiation emitted from the earth surface undergoes and before reaching the space based sensor/satellite. Figure 1.9 includes various equations corresponding to the intensity of the radiation emitted from the earth surface, scattering cross section in the Rayleigh regime, intensity reduction due to

absorption following to the Beer-Lambert's law, and radiative transfer equation which need to be solved for the retrieval of CO (This is applicable to any other gas whose absorption in the infrared region, specifically thermal infrared).

Considering the retrieval from thermal IR, the component of solar radiation reflected from the earth surface is neglected due its smaller contribution. Intensity of thermally emitted radiation from the earth surface (or atmosphere) depends upon the temperature and the emissivity of the earth surface. The emission of radiation is governed by Planck's law and since earth surface and the atmosphere are not the ideal black body, the radiation gets multiplied with the wavelength dependent emissivity factor or the coefficient. The terms in the equation shown for the thermal emission are following. dI_{th} is the intensity of thermal radiation emitted from a layer of dz thickness, h=6.626×10^{-34} Js (Planck's constant), k=1.38×10^{-23} JK^{-1} (Boltzmann constant), c = 3×10^{8} ms^{-1} (speed of light) and λ = wavelength of the radiation, and $\varepsilon_a(\lambda)$ is absorption coefficient. The similar equation would be applied for the earth's surface for the emitted radiation. Thus, thermally emitted radiation from earth's surface and atmosphere passes through the atmosphere.

While thermal IR passes through atmosphere, it undergoes absorption and scattering of two types, Rayleigh scattering (size of molecules/particles << wavelength) and Mie scattering (size of molecules/particles comparable to wavelength). The effect of Mie scattering is not significant in the thermal Infrared region of the spectrum and can be neglected. The intensity $I_{(\lambda)}$ after the radiation with its initial intensity $I_{0(\lambda)}$ passed through the absorbing medium of thickness dz is given by the Beer-Lambert's law as shown in the figure 1.9. The other terms are as followings. $\sigma_{a(\lambda)}$ is the absorption cross section and N is the number of absorbing molecules per unit volume. Similarly, The equation for the change in intensity dI_{th} in $I_{(\lambda)}$ due to Rayleigh scattering after passing through a layer of thickness dz is also shown in the figure 1.9 (d is the size of the particle and $\varepsilon_{s(d,\lambda)}$ is the scattering coefficient). The scattering coefficient is defined by number density times the scattering cross section. The cross section ($\sigma_{R(\lambda)}$) corresponding to Rayleigh scattering involves the parameters like, the real part of the refractive index ($n_{o(\lambda)}$), the number density of air (N_{air}), and the correction for anisotropy $F_{k(\lambda)} \sim 1.061$.

Considering the above three processes namely (1) emissions from earth's surface and atmosphere, (2) absorption by the atmosphere and (3) scattering by the atmosphere, radiative transfer (RT) equation need to be solved to estimate the concentration of target species. The RT equation is shown at the top in the figure 1.9. The terms in the RT equations are corresponding to the description above, except the

term $SC_{\lambda(\theta,\phi)}$, which is scattering function (a dimensionless quantity), to calculate the intensity added to the outgoing radiation by the scattering. Note that RT equation shown in the figure 1.9 is simplified version, as at the short wavelength region of the spectrum the contribution from the emission processes are neglected. Since it is impossible to solve the RT equation using analytical methods, numerical techniques are used. These methods would require knowledge on surface temperature, vertical profile of temperature of the atmosphere, emissivity of the earth surface and the atmosphere, and a priori knowledge of CO profile. The calculation becomes complicated when cloud is present in the atmosphere. Also, the complexity and the limitation of measurement made by the satellite sensors are crucial in the retrieval methodology. In addition, if measured signal have spectral contamination from the unwanted species, the correction would require the knowledge on the concentration of those species.

Satellite

$$\frac{dI_{(\lambda)}}{dz} = -[\varepsilon_{a(\lambda)} + \varepsilon_{s(\lambda)}] \times I_{(\lambda)} + \varepsilon_{s(\lambda)} \int_0^{\pi}\int_0^{2\pi} I_{(\lambda,\theta,\phi)}\left[\frac{SC(\theta,\phi)}{4\pi}\right]\sin\theta\, d\theta d\phi$$

Radiative transfer equation

Atmosphere

$$dI_s = I_{(\lambda)} \times \varepsilon_{s(d,\lambda)} \times dz$$

Intensity change due to scattering

$$\sigma_{R(\lambda)} = \frac{8\pi^3}{3\lambda^2 N_{air}^2} \times \left(n_{0(\lambda)}^2 - 1\right)^2 F_{k(\lambda)}$$

Scattering cross section (Rayleigh)

$$+$$

$$I_{(\lambda)} = I_o(_\lambda)\exp\left(-\sigma_{a\,(\lambda)} \times \int_0^z N\, dz\right)$$

Absorption

$$dI_{th}\,(\lambda, T) = \varepsilon_{a(\lambda)} \times \frac{2hc^2}{\lambda^5} \times \frac{1}{\exp\left(\frac{hc}{\lambda kT}\right) - 1} \times dz$$

Intensity of thermal emission

Earth Surface
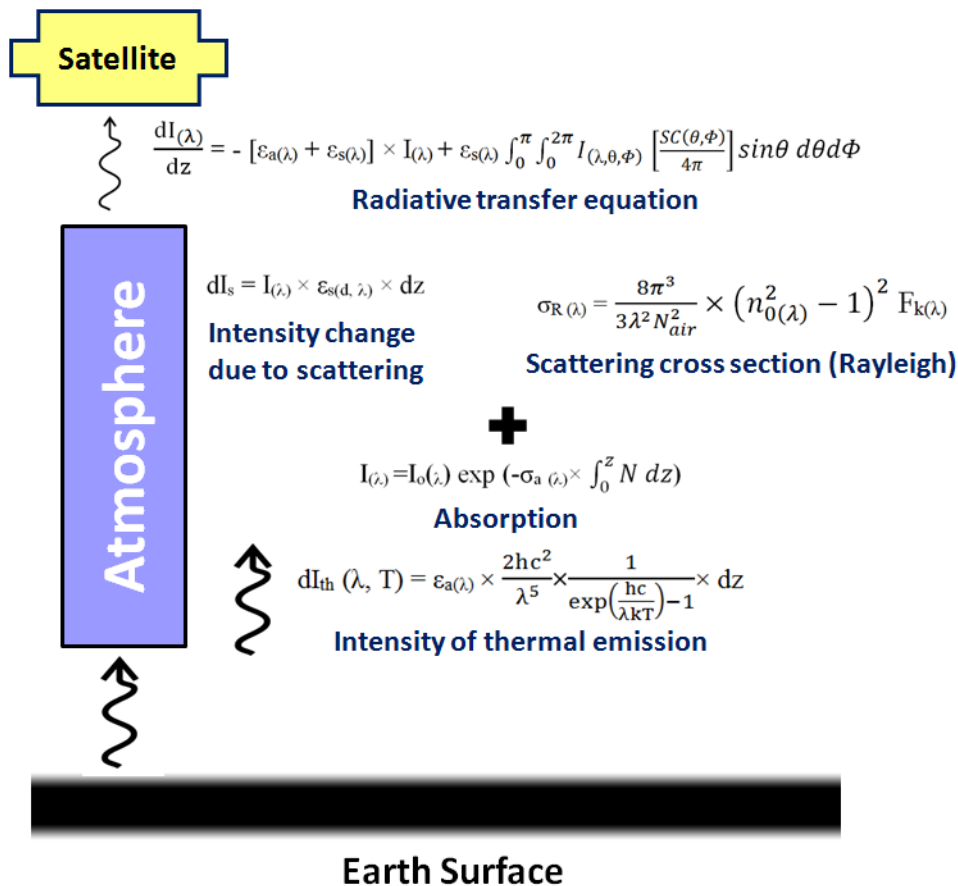
Figure 1.9: Schematic diagram along with various equations for radiative transfer calculation for retrieval of CO (or other gas) whose absorption lies in the Infrared regime. The equations are taken from Burrows, 2001.

1.13.2.1 Satellites in orbit measuring Carbon monoxide
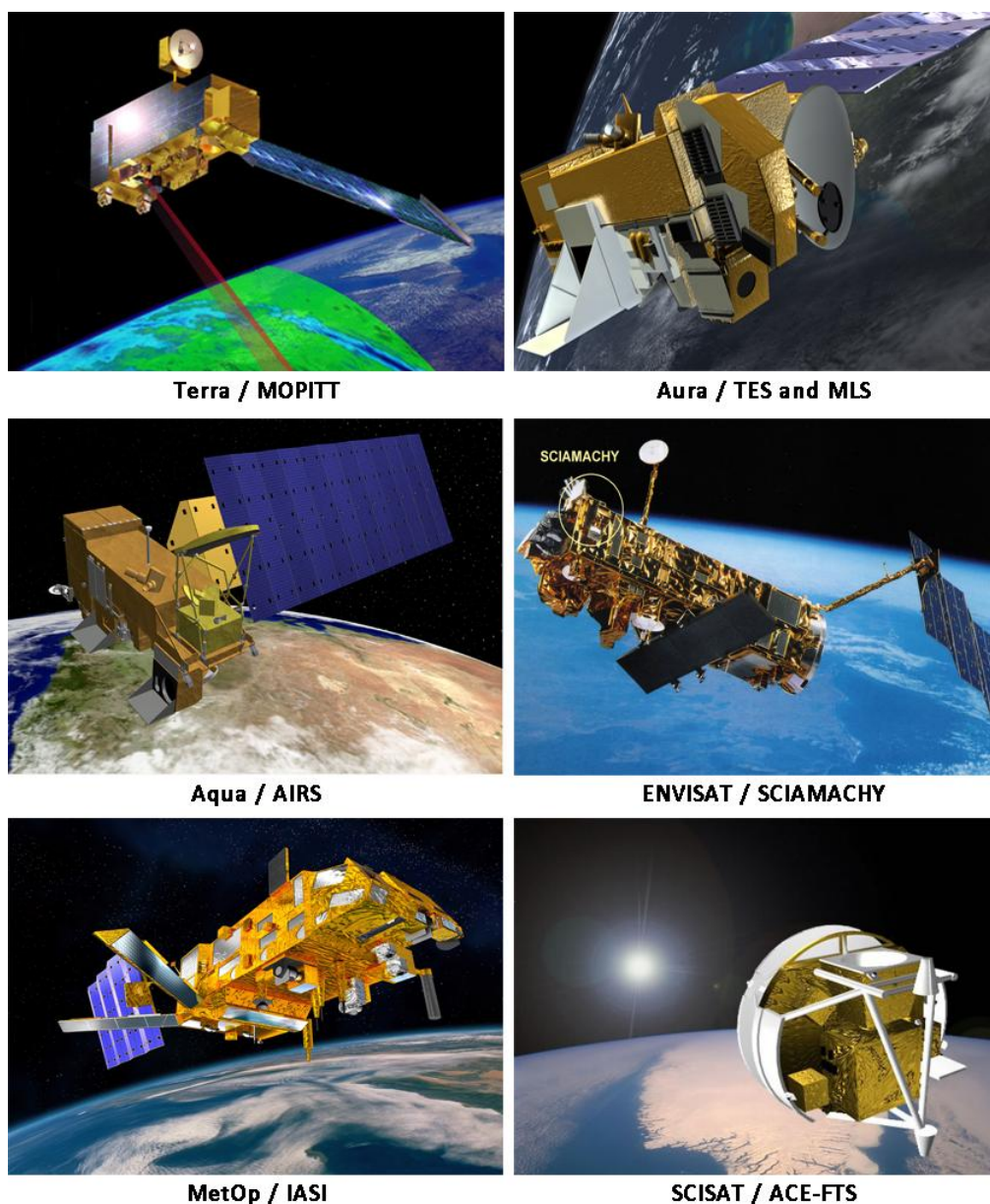
Figure 1.10: Various satellite carrying payloads for measurements of CO (Image curtsey: http://www.asc-csa.gc.ca/eng/satellites/mopitt.asp for Terra/MOPITT, https://tes.jpl.nasa.gov/mission for Aura/TES and MLS, https://airs.jpl.nasa.gov/mission_and_instrument/mission for Aqua/AIRS, https://atmos.eoc.dlr.de/projects/scops/sciamachy_book/sciamachy_book_figures_springer/chapter_2 for ENVISAT/SCIAMACHY, https://iasi.cnes.fr/en/IASI/index.htm for MetOp / IASI, and http://www.ace.uwaterloo.ca/mission.php for ACE-FTS/SCISAT).

There are six different instruments on different satellites performing space-based remote sensing for the measurements of columnar and/or vertical profile of CO. Figure 1.10 shows the images (artist's view) of different satellites as obtained from respective websites of different organisations/agencies. The measurement of tropospheric CO is being carried out by Measurements of Pollution in the Troposphere (MOPITT) on board Terra (Drummond, 1989; Drummond et al., 2010;

https://terra.nasa.gov/about/terra-instruments/mopitt), Atmospheric Infrared Sounder (AIRS) on board Aqua (Aumann et al., 2003; www.airs.jpl.nasa.gov), Tropospheric Emission Spectrometer (TES) on board Aura (Beer et al., 2001; www.tes.jpl.nasa.gov) under NASA's Earth Observing Systems (EOS) programme, and Infrared Atmospheric Sounding Interferometer (IASI) on MetOp-A (George et al., 2009; https://iasi.cnes.fr/en/IASI/GP_satellite.htm) under EPS (EUMETSAT Polar System) programme. The Scanning Imaging Absorption Spectrometer for Atmospheric Cartography (SCIAMACHY) instrument onboard the ENVISAT satellite (Bovensmann et al., 1999) has also provided measurements of CO till the mission ended in 2012. While Atmospheric Chemistry Experiment - Fourier Transform Spectrometer (ACE-FTS) on board the Canadian satellite SCISAT (http://www.asc-csa.gc.ca/eng/satellites/scisat/default.asp) provide profile from mid troposphere and above, the Microwave Limb Sounder (MLS) on board Aura (https://mls.jpl.nasa.gov/) provides profile of CO upper troposphere and above.

MOPITT uses correlation radiometry (Drummond, 1989) and the terrestrial thermal emission to retrieve the tropospheric CO profile and columnar CO using a maximum a posteriori method that incorporates a priori information of the physical and statistical variability. The detailed description about MOPITT measurement technique, algorithm and its data product are given in the Chapter-2. TES is basically a Fourier Transform Spectrometer (FTS) and measure the thermal radiation. It retrieves CO profile using optimal estimation retrieval (Rodgers, 2000) considering the region and season dependent a priori profiles. TES global coverage is available during global survey mode only and has no cross-track scanning capability, yielding a much sparser dataset than MOPITT or AIRS (Rinsland et al., 2006). Similar to TES, IASI is also a FTS and profiles are retrieved using an optimal estimation approach (Hurtmans et al., 2012). AIRS is a grating spectrometer which also measures radiation at 4.7 μm (McMillan et al., 2005) and obtain the CO profile using perturbation functions. However, unlike MOPITT, AIRS can retrieve profile in partially cloudy sky (Susskind et al., 2003). SCIAMACHY is a spectrometer and it measures radiation at 2.3 μm (mainly solar backscattered). It has uniform sensitivity in the tropospheric (Buchwitz et al., 2004). Due to low reflectivity of ocean water (in IR), it provide lesser coverage. MLS is radiometer, works at 1.3 mm spectral line of CO. CO in the upper troposphere and above is retrieved using optimal estimation algorithm (Livesey et al., 2006). The ACE-FTS is in a high-inclination (74°), circular low-earth (650 km) orbit launched in 2003. ACE-FTS (http://www.ace.uwaterloo.ca/index.php) has high spectral resolution and retrieves

the CO profile during solar occultation from the mid troposphere and above up to 100 km (Clerbaux et al., 2005). Further details about aforementioned instruments are given in Chapter -2.

All these satellite-based measurements provide near daily coverage of tropospheric CO over the globe. The comparison studies have shown that retrievals from these instruments are more or less in agreement among themselves. However, the MOPITT retrievals are for the longest period (~19 years), since March 2000 and mainly these retrievals are used in the study. The satellite or instruments mentioned here are corresponding to time frame after year 2000. However, prior to year 2000, there were three space-based instruments which had made measurement of CO. The MAPS (Measurements of Air Pollution from Satellites; Reichle et al., 1999) was flown on shuttle during 1981, 1984 and 1994. The Interferometric Monitor for Greenhouse Gases (IMG; Kobayashi et al., 1999) was a Japanese FTIR instrument on the ADEOS-1 mission launched in 1996. The Atmospheric Trace Molecules Observed by Spectroscopy (ATMOS; Gunson et al., 1996) was a shuttle-based solar occultation Fourier Transform Spectrometer flown during 1985, 1992, 1993 and 1994 (Drummond et al., 2010). ACE-FTS is similar in some respects to the ATMOS experiment.

1.14   Trace gas modelling scenario

Atmospheric models present the quantitative understanding about various physical, chemical and dynamical processes occurring in the atmosphere (e. g., emissions; horizontal as well as vertical transport; chemical transformation; interaction of solar and terrestrial radiation with the earth-atmosphere system; convective processes and associated cloud formations; deposition; etc.) in terms of mathematical equations. The set of mathematical equations such as the continuity equation, momentum equation, equation of state etc. are solved to compute the changes in the meteorological and chemical fields. The atmospheric processes are complex and that a variable can get affected by different processes resulting in a set of coupled non-linear partial differential equations (PDEs), which cannot be solved exactly. The solutions of the equations are therefore obtained numerically employing the techniques such as finite differences (e.g. Jacobson, 2005; Brasseur and Jacob; 2017).

Atmospheric modelling is required for the interpretation of the field measurements and to calculate the contributions from individual processes to the observed magnitude and variations in one or other atmospheric parameter. Atmospheric models are essential for prediction future evolution of the atmosphere and

are commonly used to forecast cyclones, dust episodes, and air quality, etc. Atmospheric models act as an independent dataset of the changes occurring spatially and temporally filling the gaps of observations especially in the regions where observations are sparse. Therefore, atmospheric modelling is a vital tool in the field of atmospheric-chemistry climate interactions and the model provided information is often used in policy making. Prior to the utilisation of a model for either purpose, the performance of the model needs to be evaluated against the observations. Atmospheric models are being continuously developed, evolved and improved to include more processes, which results in increased complexities. Additionally, with the availability of more computational resources, models are shown to be able to resolve most complex terrains of the globe with greater success (e.g. Singh et al., 2016).

Based on the science objectives and spatio-temporal scales under the considered, models could be from 0-dimension (box model), 1-dimension (simple radiative transfer codes accounting for vertical profiles only), or fully coupled 3-dimension models involving the chemistry as well as dynamics. Depending upon the spatial scales, the 3-D models are further categorized into a regional or global atmospheric model. Earth System Models (ESMs) are global models that are the most complex because they also include processes happening in the cryosphere, oceans, and volcanic influences etc. (Jöckel, 2012)

Global models basically consider complete globe as a set of several grid boxes of about 2° x 2°. These models provide the advantage to simulate the processes over the global scale including an explicit treatment of the stratospheric processes. These models therefore need a longer (few years) spin up time (i.e., the time over which models stabilise) before producing useful output. Additionally, they have limited ability to resolve highly urbanized or geographically complex areas adequately due to coarse resolution (e.g. Ojha et al., 2012; Hakim et al., 2018). Few examples of global atmospheric models are: MOZART (Model for OZone and Related chemical Tracers; https://www2.acom.ucar.edu/gcm/mozart-4), ECHAM5/MESSy Atmospheric Chemistry (EMAC) where ECHAM is fusion of EC from ECMWF and HAM for Hamburg, Germany; and MESSy stands for Modular Earth Submodel System), MATCH-MPIC (Model of Atmospheric Transport and Chemistry - Max Planck Institute for Chemistry; http://cwf.iass-potsdam.de/match/match_overview.html), GEOS-Chem (Goddard Earth Observing System coupled with chemistry; http://acmg.seas.harvard.edu/geos/), etc. Global models have provided the information on the global atmospheric composition and the influences of large-scale processes including Asian monsoon and

intercontinental transport. Recent study using the EMAC model (Lelieveld et al., 2018) shows that the south Asian monsoon sustains a remarkable cleansing mechanism but some pollution can get uplifted above clouds influencing the global stratosphere.

Regional models are particularly useful to simulate the influences of urbanisation and to adequately resolve the highly complex terrains as well at finer model resolution (10 km or so). Long-range transport as well as stratospheric composition is not computed explicitly, instead they basically take the global model inputs. Since their boundaries are updated from a global model simulation, a shorter spin up (1 week or so) can suffice in case of regional-scale simulations. Some of the intensively used regional models include the RegCM (Regional Climate Model), WRF-Chem (Weather Research and Forecasting (WRF) model coupled with Chemistry), WRF-CMAQ (WRF and Community Multiscale Air Quality), etc. In this study, the photochemical box model and WRF-Chem are used to simulate the observed chemistry and spatio-temporal features respectively.

1.15 Global scenario in tropospheric Carbon monoxide: Seasonal variation and longterm trends

The early study by Jaffe, 1968 has provided a comprehensive picture on the world wide emission of CO, its possible sources and sinks as well as the major chemical reactions in the atmosphere. Novelli et al., 1992 and 1998 reported the global surface CO distributions and seasonal variability. The seasonal cycle in the southern hemisphere is dominated by emissions from biomass burning, and the high CO levels seen in the NH during winter reflect emissions from industrialization in the northern mid latitudes and burning in the northern tropics (WMO, 2018). The pre-industrial CO level was about 50 ppbv (ice cores measurements) over central Antarctica during the last two millennia and the level increased to 110 ppbv by 1950 in Greenland (Haan and Raynaud, 1998). The surface CO over the globe had increased further during 1950 to 1985 (Khalil and Rasmussen, 1988) at the rate of 0.8 - 1.4% year^{-1}. Later, a decreasing trend in surface CO mixing ratio (-2.6±0.8% per year^{-1}) was seen during 1988-1992, based on the observations at few sites which were representative of background levels over different regions namely polar, middle and tropical latitudes (Khalil and Rasmussen, 1994). Novelli et al., 1994 also had reported the decreasing trend in CO during 1989-1993. In 2016, the global mean surface CO was 90±1 ppbv based on in-situ measurements at the WDCGG network (WMO, 2018). CO also shows considerable interannual variability

(WMO, 2018). The long-term trend over the globe is addressed over time period of 2000–2018 in Chapter - 5.

The zonally averaged surface CO, de-seasonalised CO and growth rate during 1992-2016 based on WMO report (2018) is shown in the figure 1.11. While the higher CO amount is seen in the northern hemisphere, it is significantly lower in the southern hemisphere. This is mainly because of higher anthropogenic activities leading higher CO emissions in the northern hemisphere. The surface CO exhibits seasonal variation. Along with higher level, seasonal amplitude is also high in the Northern hemisphere as compared to that over southern hemisphere. The seasonal cycle has opposite phase in the southern hemisphere.

As seen in the figure 1.11, the growth rate has significant interannual variation. In general, the higher growth rate is corresponding to higher biomass burning which occurs during El Niño years. The growth rates were higher during 1993–1994, 1997–1998 and 2002, and they were low in 1992 and 1998–1999 (WMO, 2018). Very high forest fires events in Indonesia during 1997 and in Siberia during 1998 (Novelli et al., 1998) caused higher growth rates. Interestingly, the low growth rate of CO is attributed to the volcanic eruption (Mt. Pinatubo) in 1991. The pumping of aerosols in the stratosphere caused depletion of stratospheric ozone which allowed more UV radiation in the troposphere which intern generated higher OH radical in the troposphere. Higher OH destroyed the CO leading to low growth rate (Dlugokencky et al., 1996).

CO

CO deseasonalized
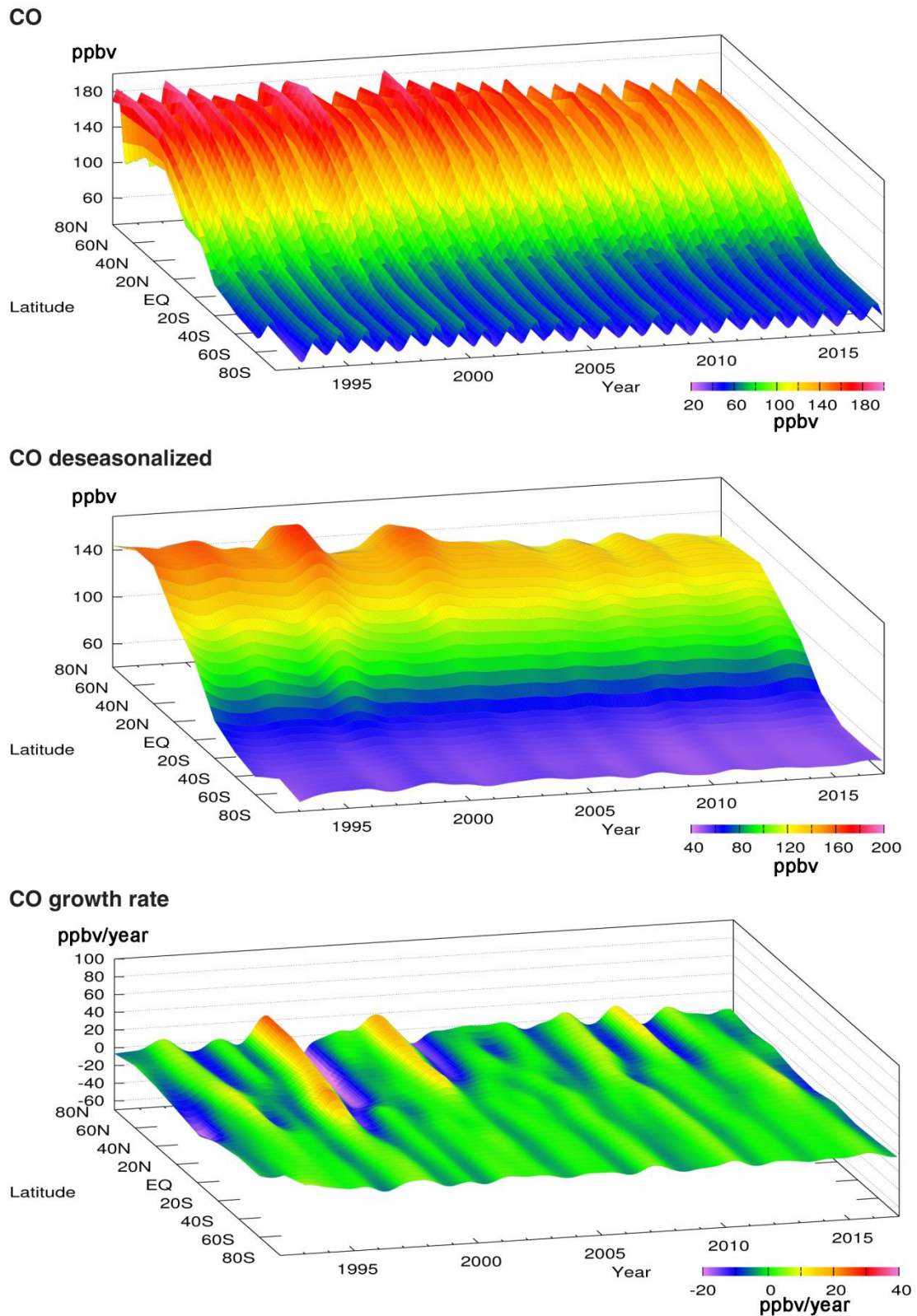
CO growth rate

Figure 1.11: longitudinally averaged latitude variation of surface CO, de-seasonlized CO and CO growth rate during 1992-2016 based on the global network observations (WDCGG/NOAA). The figure is adapted from WMO report, 2018.
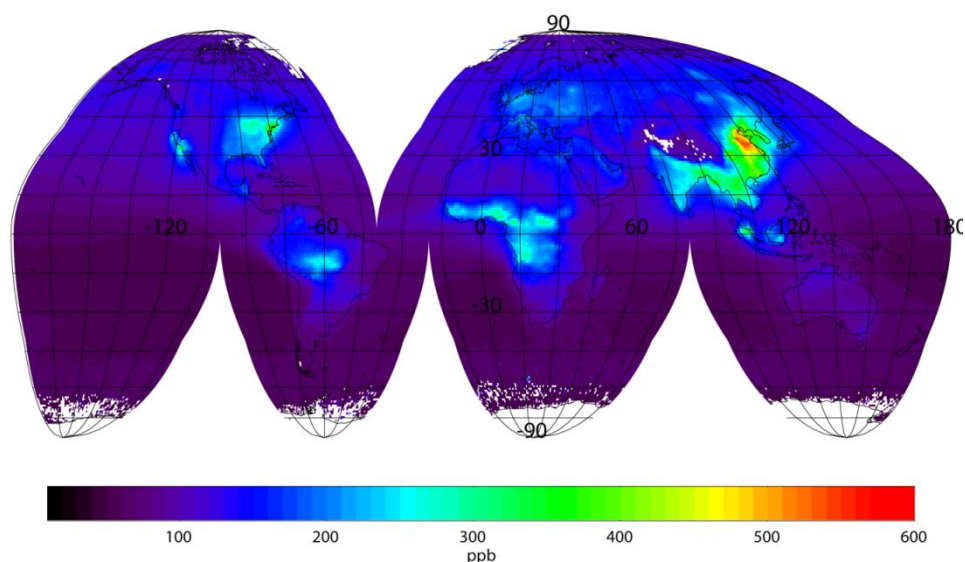
Figure 1.12: The mean distribution of surface CO over the globe: climatology (MOPITT data)

Figure 1.12 shows the global mean spatial distribution of CO over the globe. This is obtained by averaging 18 year of MOPITT retrieval and hence represents the climatology of CO mixing ratios near the surface. Over southern hemisphere, where anthropogenic activity is less, CO mixing ratios are significantly lower as compared to the northern hemisphere. The higher mixing ratios of CO are seen over the Asian region. It should be noted that both the figures 1.12 and 1.13 correspond to 1° x 1° degree resolution and hence features like higher emissions by point source are averaged out.

Figure 1.13 shows the global mean vertical profile of CO mixing ratios in the troposphere. It is obtained by averaging 18 years of MOPITT retrievals over the globe. With altitude mixing ratio decreases and the slope of decrease is sharp above ~300 hPa (~9 km). Important point to note is that the variability near to the surface is highest as compared to that at higher altitude. This is expected due to diverse emission sources and various anthropogenic activities. This is almost identical to the profile being used as a priori information for the algorithm for retrieval of CO profile. The overall variability in the profile would appear smaller and this is due to consideration of large number of profiles over the globe as the standard deviation amplitude reduces with increase in the number of points utilised for its calculation.
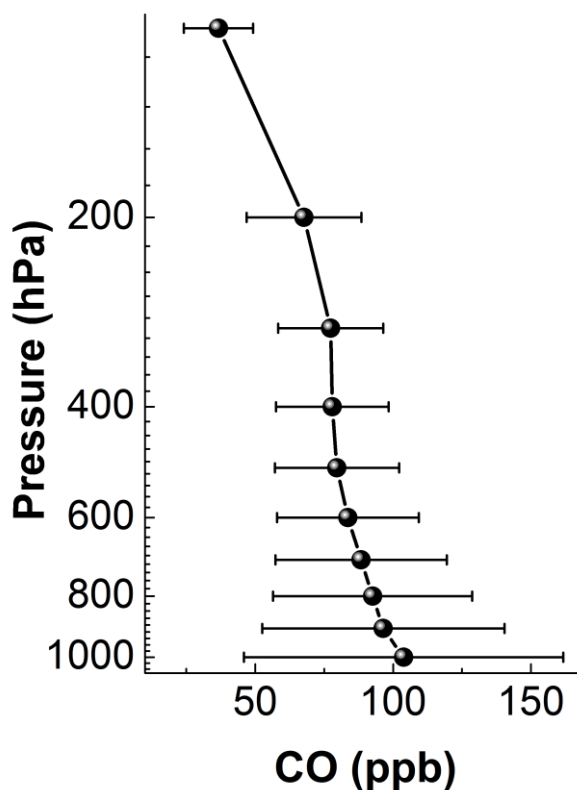
Figure 1.13: Globally averaged CO profile: Climatology (MOPITT data).

1.16 Scenario of Carbon monoxide over India and surrounding marine environment

Over Indian region, in-situ measurements of near-surface CO are available over a few sites like Ahmedabad, Agra, Anantpur, Bhubaneswar, Cape de Rama, Gadanki, Hyderabad, Hissar, Kanpur, Kochi, Mt. Abu, Nainital, New Delhi, Pune and Trivandrum for a limited study periods. These studies mainly discuss the variabilities in surface-CO on diurnal and seasonal scale. Table 1.5 shows the near-surface CO mixing ratios as well as site specific characteristics over various locations over India.

The studies over all the observational sites listed in the table 1.5 showed that the monthly or seasonal variation is near-surface CO is mainly governed by long-range transport or synoptic scale wind patterns. Variations in CO are also due to effects of local emissions, boundary layer processes, chemistry and local wind pattern and synoptic wind pattern (e.g., Lal et al., 2000). Local emissions also affects in the day-to-day variability significantly. The CO concentrations during weekdays were found to be higher than that during weekends at Trivandrum, Kochi and New Delhi (Kumar et al., 2006) showing the effect of traffic/vehicular pollution on the CO. Since biomass burning is also a significant source of CO, its influences have been observed over many sites. Lal

et al., 2012 has reported the contributions from biomass and biofuel burning as well as from fossil fuel combustion during December, 2004 over Hissar and Kanpur. However, over Gadanki the effect of biomass burning, which mainly occurs from January to May, was not reflected in the CO mixing ratio.

Table 1.5: The near-surface CO mixing ratios as well as site specific characteristics over the various locations over India as obtained from literature.

Observation site	Study Period	CO mixing ratio and peculiar observations	Reference
Ahmedabad (23° N, 72.6° E)	1993-1996, 2002	Winter season: ~850 ppbv, Monsoon season: ~100 ppbv. Higher values during morning (07-09 hr) and late evening hours (19–24 hrs), Lower value during daytime (14–17 hrs). 2002 observations shows mixing ratio 385±200 ppbv	Lal et al., 2000, Sahu and Lal, 2006
Agra, (27.1° N, 78° E)	2003-2005; 2012	Winter season: 710 ± 159.4 ppbv Winter average of 1088±202.75 ppbv at polluted site and 332.5 ±116 ppbv at Dayalbagh During summer period from April to June 2012 at a site located in an urban area of Agra near heavy traffic junction, CO exceeded 4.6 ppmv mixing ratios.	Saini et al., 2008; 2014
Anantapur (14.68° N, 77.60° E)	2001-2003	Annual average: 436±64 ppbv	Ahammed et al, 2006
Bhubaneswar (20.5° N, 85.9° E)	2010–2012	Winter season: 604.51±145.91 ppbv, Monsoon season: ~200 ppbv Higher values during morning (~8 hr) and late evening hours (19-24 hrs), Lower values during daytime (12-17 hrs)	Mahapatra et al., 2014
Cape de Rama (15.08°N, 73.83°E)	1993-2002	Winter season: 220-300 ppbv, Monsoon season: 60-80 ppbv	Bhattacharya et al, 2009
Gadanki (13.5° N, 79.2° E)	1993–1996	Annual average: 237 ± 64 ppbv, Seasonal amplitude: 240 ppbv	Naja and Lal, 2002

Hyderabad, Balanagar (17.5° N, 78.5° E)	March-April 2006, January 2004	Levels during Biomass burning event: 50 to 1500 ppbv Day time lower value: ~70 ppbv, Peak values: 700–950 ppbv	Badarinath et al., 2007 Latha and Badarinat, 2004
Hissar (29.14° N, 75.7° E)	December, 2004	Range: 300–1200 ppbv	Lal et al., 2012
Kanpur (26.46°N, 80.33°E, 125 m amsl	December, 2004, 2009-2013	Range: 300–1800 ppbv Annual average: 721±403 ppbv Winter high: 1000 ppbv, monsoon low: ~500 ppbv	Lal et al., 2012 Gaur et al, 2014
Kochi (10.1° N, 76.3° E)	1997 -2005	Seasonal variation: 1000–2000 ppbv	Kumar et al., 2006
Mt. Abu (24.6° N, 72.7° E, 1680m amsl)	1993–1997	Annual average: 131.4±35.8 ppbv Range: 50–350 ppbv (higher during winter season)	Naja et al., 2003
Nainital (29.37°N, 79.45°E, 1958 amsl)	2009-2011 2006-2008	Springtime higher: 215.2±147 ppbv, monsoonal lower CO: 146.6 ± 71 ppbv As per observations during 2006–2008, Annual average: 276±145 ppbv	Sarangi et al., 2014 Kumar et al., 2010
New Delhi (28.61° N, 77.23° E)	2000-2009	Annual average: 2940±1729 ppbv	Chelani 2012
Pune (18.54°N, 73.81°E)	2003 -2004	Seasonal maximum during winter: ~750 ppbv Seasonal minimum during monsoon: ~250 ppbv Diurnal peak during morning hours (8–9 hrs)	Beig et al., 2007
Trivandrum (8.5° N, 76.9° E)	2003, 2004	Diurnal variation: One in the morning (~8 hrs) and another in the late evening (~20 hrs). Seasonal maximum during winter: ~50 ppbv, Seasonal minimum during monsoon: ~550 ppbv. 2004 observations shows winter-time average of 352 ppbv, followed by 108 ppbv during summer and 32 ppbv during monsoon	Kumar et al., 2006

Since CO is a precursor for O_3, a good correlation between O_3 and CO is observed over many sites in India. Correlation (close to zero to 0.35) between CO and O_3 is found to be season and airmass dependent over Bhubaneswar (Mahapatra et al., 2014). The statistical analysis based on prevailing near-surface CO at Bhubaneswar showed that comparatively low CO concentrations at the site do not lead to any health effects even during winter. The slope corresponding O_3 and CO correlation (which gives ozone production efficiency) was 0.13 over Mt Abu (Naja et al., 2003) which is similar to those of other studies over the Asian region. The O_3-CO slope is found to be lower at Nainital as compared to that over other locations. Lower value represents role of long-range transport and aged airmass at the observational site.

In-situ measurements of CO over the Bay of Bengal (BoB) have been conducted in various campaigns: INDOEX during the winter months of 1998 and 1999 (Lelieveld et al., 2001; Mühle et al., 2002); the Integrated Campaign for Aerosols, gases, and Radiation Budget (ICARB) during the March–May (pre-monsoon season) of 2006 (Srivastava et al., 2011; 2012); the Bay of Bengal Experiment (BOBEX)-I during February–March 2001 (Lal et al., 2006); the Bay of Bengal Process Studies (BOBPS) during September–October 2002 (Sahu et al., 2006); BOBEX–II during February 2003 (Lal et al., 2007); and another campaign conducted during October–November 2010 (Mallik et al., 2013). The surface CO mixing ratios ranging from 108 to as high as 292 ppbv were observed over the BoB during aforementioned campaigns. These surface observations revealed transport of CO from different regions under the synoptic wind patterns. There is still a lack of observations of surface CO and tropospheric CO over the BoB during the winter and monsoon season. This is addressed in the present study using the in-situ and satellite based observations. The limited CO observations over the Arabian Sea and Indian Ocean during BOBEX-I, ICARB-2006 and INDOEX-1999 showed large latitudinal gradients (Naja et al, 1999). The ozone-to-CO ratio in air coming from India was lower than that observed over North America indicating higher level of pollutants (Stehr et al 2002). The observations made during INDOEX-1999 showed that airmass from southern hemisphere (50 ppbv) have lower CO levels as compared to the airmass from northern hemisphere (200 ppbv) and the sharp change was seen across the Inter Tropical Convergence Zone during the campaign.

MOPITT retrievals of CO, over India and southern China showed enhancement of CO in the upper troposphere (UT) during Asian summer monsoon, indicating the effect of deep convective transport. MOZART-2 simulations also indicated transport of boundary layer CO to the tropopause during the monsoon season (Fadnavis et al., 2011).

Similarly, zonal mean height latitude cross-sections for the months of September–December, 2002 indicate deep convective transport of CO from biomass burning in the southern tropics. In winter, MOPITT retrievals at 850 hPa detected the strongest source areas over the eastern states of Bihar and West Bengal, thus confirming the so-called "Bihar pollution pool" (Kar et al., 2004; 2008; 2010). The emissions from Southeast Asia have significant impact over the Bay of Bengal and the eastern Indian Ocean, while emissions from the rest of India dominate over the Arabian Sea and the western Indian Ocean (Ghude et al., 2011).

Detailed evaluation of the WRF-Chem model over the South Asian region (Kumar et al., 2012) showed that this model reproduced the temporal as well as spatial distribution of trace gases like O_3, CO and NO_2 over the Indian region successfully. However, total column CO was under estimated during February–July and overestimated during other months when compared with the retrievals from MOPITT, nevertheless, model successfully captured the observed seasonal cycle. Based on model simulations, the anthropogenic sources are major contributor (40-90%) to the boundary layer CO during the winter over India, while in the free troposphere the major contribution (50–90%) is due to transport across the boundaries model domain (i.e., study region; Kumar et al., 2013). Model simulations over Indian region showed maximum decadal increase in CO is about 50–70 ppbv (10–18%) in the boundary layer (Beig and Brassure, 2006).

Model-based studies using WRF-Chem and MOZART reproduced the seasonal variation of CO as observed at sites, Ahmedabad, Mt. Abu and Gadanki (Kumar et al., 2012). WRF-Chem simulations reproduced the general features of and CO distributions over the South Asian region during summer-monsoon as obtained by the in-situ measurements of CO profiles from the CARIBIC flight data. However, the absolute CO concentrations in lower troposphere are typically underestimated (Ojha et al., 2016). The average underestimation (Mean Bias) of CO in the lower-troposphere is found to be 12.6±4.4, 22.8±12.6 and 19.9±7.5 ppbv during June, July and August respectively, as calculated from all the ascend and descend profiles of CARIBIC flights (Ojha et al., 2016). WRF-Chem successfully reproduced the general features of O_3 and CO distributions over the South Asian region during the summer monsoon (Ojha et al., 2016). However, model typically underestimated CO levels throughout the lower troposphere over Chennai. The study highlighted a need to conduct more aircraft-based and ship-based measurements over the Oceanic regions adjoining South Asia and improvement of the emission inputs.

1.17   Objectives of the study

In view of the limited information on the distribution of CO and its variability over the Indian region including the land mass and the surrounding oceans, the present work focuses on a comprehensive study on the three dimensional (3D) distribution (latitude-longitude-altitude) of CO over this region with emphasis on the marine environments of BoB and northern IO. The study is based on the in-situ measurements of surface CO conducted in the campaign mode over the BoB, IO and AS, extensively supported by the satellite based data and modelling. The satellite data have been validated before using it to characterise various observed features.   The specific objectives of this study include: (1) Characterisation of the spatial and seasonal characteristics of the near-surface CO, altitude distribution of tropospheric CO, and the columnar CO over the BoB along with their seasonal variabilities. This study also aims to identify the season-dependent sources and transport pathways of CO over BoB making use of airmass back trajectories, airflow patterns and emission inventories. (2) Spatial variation of near-surface CO and the tropospheric CO over the northern Indian Ocean/southern AS during winter season, when north easterlies are conducive for the advection from continental region. Association of the spatial variation of CO with its residence time over land is also addressed in this work. A comparison of the change in CO over a period of ~20 years is also attempted making use of INDOEX data (3) A comprehensive study on the tropospheric distribution of CO in terms of lower, upper and columnar CO on regional scales, over the Indian landmass making use of satellite-based observations and the limited, available in-situ measurements. The region-dependent seasonal and long-term changes in tropospheric CO are examined addressing the effect of biomass burning, anthropogenic activities and meteorology. The long-term trend in CO over Indian region is addressed and compared with the global trends. (4) Model simulations of the observed spatial variations over the marine environment of the BoB and northern IO to understand the role of chemistry and to delineate the anthropogenic contributions.

<div align="center">***</div>

<div align="right">

Chapter - 2

</div>

<u>Experimental techniques and Data</u>

2.1   Introduction

The main focus of this work is on the spatio-temporal variations of CO over India and the adjoining oceanic environments addressing its near-surface, lower tropospheric and upper tropospheric components along with the columnar CO. In order to study the distribution of near-surface CO and its variability, in-situ measurements were carried out by using the state-of-art online CO analyser. The spatial and temporal features of lower and upper tropospheric CO were investigated based on satellite observations, mainly from Measurements Of Pollution In The Troposphere (MOPITT). Also, lower and upper tropospheric CO as well as columnar CO from various other satellite-borne instruments like, Atmospheric Infrared Sounder (AIRS), Tropospheric Emission Spectrometer (TES), Microwave Limb Sounder (MLS), and Infrared Atmospheric Sounding Interferometer (IASI); and in-situ measurements available from the global network of NOAA have also been utilised to understand the trend over Indian region and the globe. Other in-situ measurements over Indian region, available from previous studies were also made use for comparisons and to evolve a comprehensive picture.

In addition to the in-situ and satellite based CO data, mean air flow pattern as well as vertical wind from ERA-Interim [ECMWF (European Centre for Medium-Range Weather Forecasts) Re-Analysis], and airmass back-trajectories from HYSPLIT (HYbrid Single Particle Lagrangian Integrated Trajectory) model were also made use to understand the meteorological conditions, associated dynamical processes, and the transport pathways. The surface meteorological data of temperature, relative humidity (RH), and pressure recorded by an Automatic Weather Station (AWS) operational at the experimental location are also used in this study. To delineate the chemistry, Photochemical Box model simulations were carried out and to investigate the transport along with chemistry, WRF-Chem (Weather Research and Forecasting model coupled with Chemistry) simulations were used. Apart from these, for source characterisation and WRF-Chem simulations, CO emission inventories like, Intercontinental Chemical Transport Experiment Phase B (INTEX-B) inventory, Regional Emission inventory in

ASia (REAS), Emissions Database for Global Atmospheric Research (EDGAR), Hemispheric Transport of Air Pollution (HTAP), and MACCity inventory [MACC (Monitoring Atmospheric Composition and Climate) and CityZen under ACCMIP (Atmospheric Chemistry and Climate Model Intercomparison Project)] are used.

This chapter gives brief accounts of each of the measurement techniques, instrumentation and the various datasets used in this work. The uncertainties and error estimates of the respective methodologies and data are also included in the respective sections.

2.2   In-situ measurements

2.2.1 Measurement of CO mixing ratio using Gas filter Correlation CO analyser

The in-situ measurements of mixing ratios of near-surface CO were carried out using Gas filter Correlation CO analyser (model CO12 M) of Environnement S.A, France. Figure 2.1 shows the CO analyser (along with other trace gas analysers) and the experimental setup used for the measurements of surface CO. The following section describes the measurement principle, technical specifications, calibration procedure, and measurement uncertainty.

2.2.2 Principle of measurement and technical details of the analyser

Figure 2.2 shows the molecular absorption spectra of CO which is characterised by two absorption peaks centred around 4.67 and 2.34 µm (2141 and 4273 cm^{-1}) corresponding to the vibrational-rotational transitions [ν : 0 → 1 and 0 → 2]. These spectra are generated from the HITRAN (HIgh Resolution TRANsmission) molecular spectroscopic database (Rothman et al., 2013; Gordon et al., 2017) utilising JavaHAWKS (Java Hitran Atmospheric WorKStation) package. The stronger band around 4.67 µm is used for the measurements of mixing ratios of CO. The intensity for the absorption band at 2.34 µm decreases rapidly (by a factor of ~100). It may also be noted that there exists an extremely weak band centred around 1.57 µm [vibrational-rotational transitions ν: 0 → 3] which is not shown in the figure 2.2 and it is utilised in the measurement technique of Vacuum Ultraviolet Resonance Fluorescence. In addition, CO also has absorption around 1.3 mm (230.5 GHz) which is utilised in satellite based measurements of CO especially in the upper-troposphere and stratosphere/mesosphere.
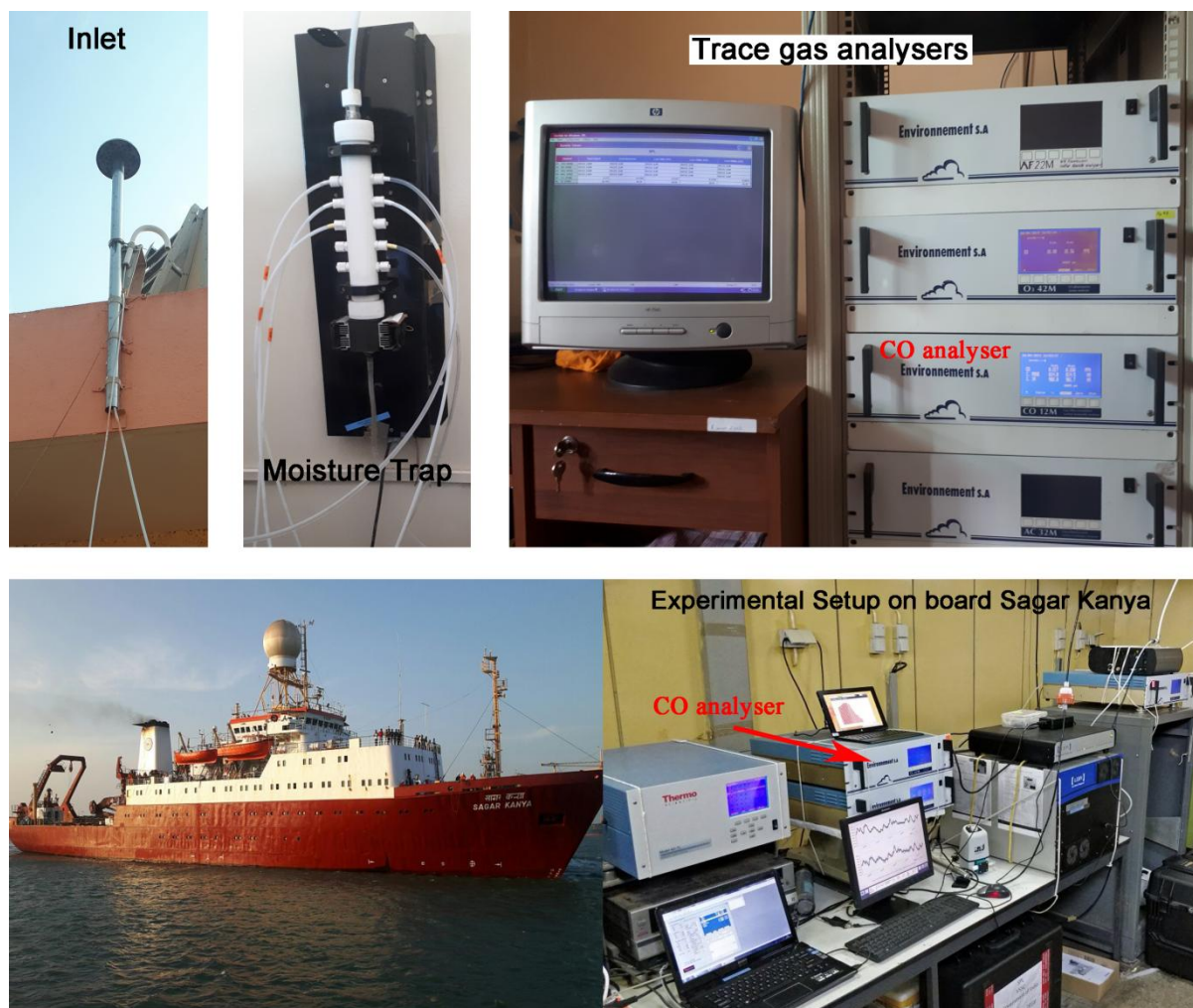
Figure 2.1: The experimental set up (Inlet, moisture trap and CO analyser) in the laboratory at Thumba, Thuruvananthapuram and on board ship, Sagar Kanya.

The CO analyser works on the principle of Non-Dispersive InfraRed (NDIR) absorption around 4.67 μm (~0.27 eV). The measurement principle is presented in the figures 2.3 and 2.4. Air sample is drawn in the measurement chamber from a height of about 6 m above the ground through a standard air inlet system. The air inlet system includes a funnel (to avoid rain as well as bigger dust particles), Teflon tubing and Peltier cooler based moisture removing system. The Teflon tube is connected to the rear end of the analyser where an inlet dust filter made of Teflon is attached. The maximum recommended length of Teflon sampling tube is 6 m. The air sample is sucked up by an internal pump placed at the end of the flow circuit through the measurement chamber. A control flow meter attached to the pump ensures a constant flow of ~1.3 litre min^{-1} with the help of a regulation circuit supplying the pump voltage.
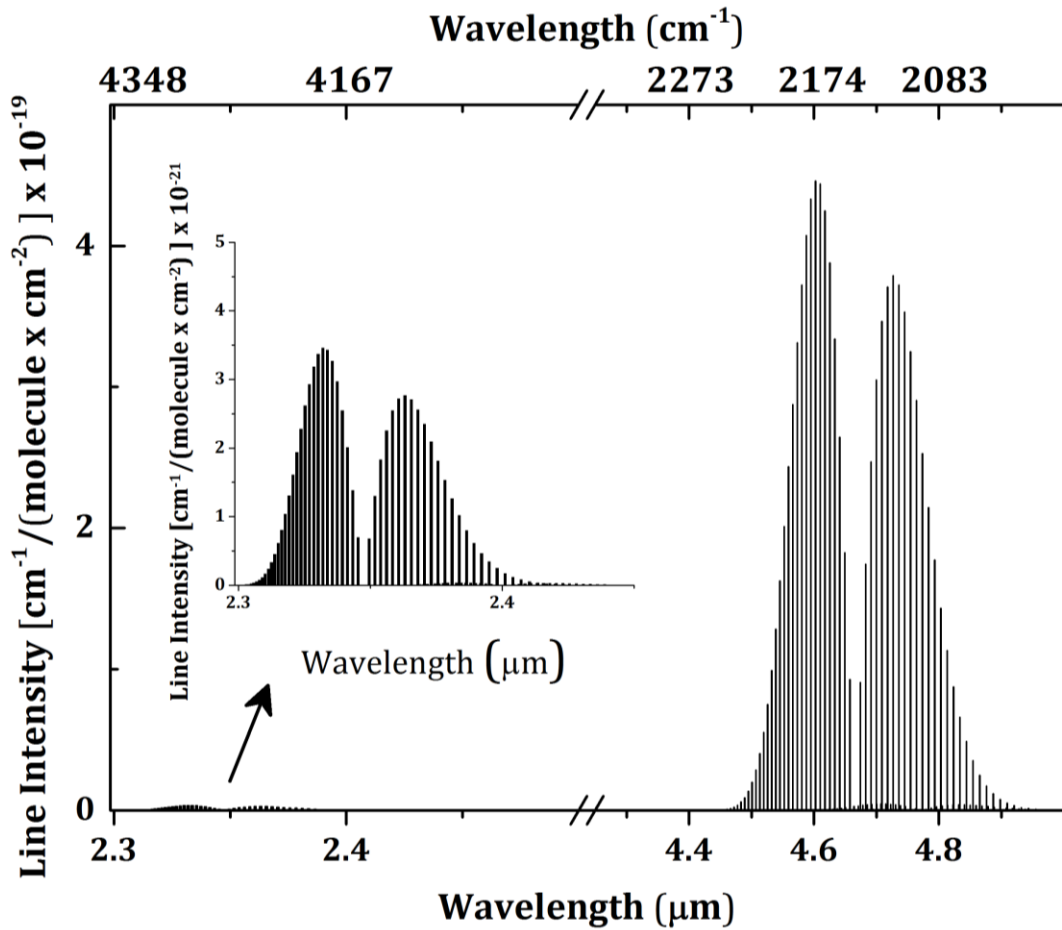
Figure 2.2: Absorption spectrum of CO molecule at 296 K as obtained from HITRAN database showing absorption bands in Infrared regimes.
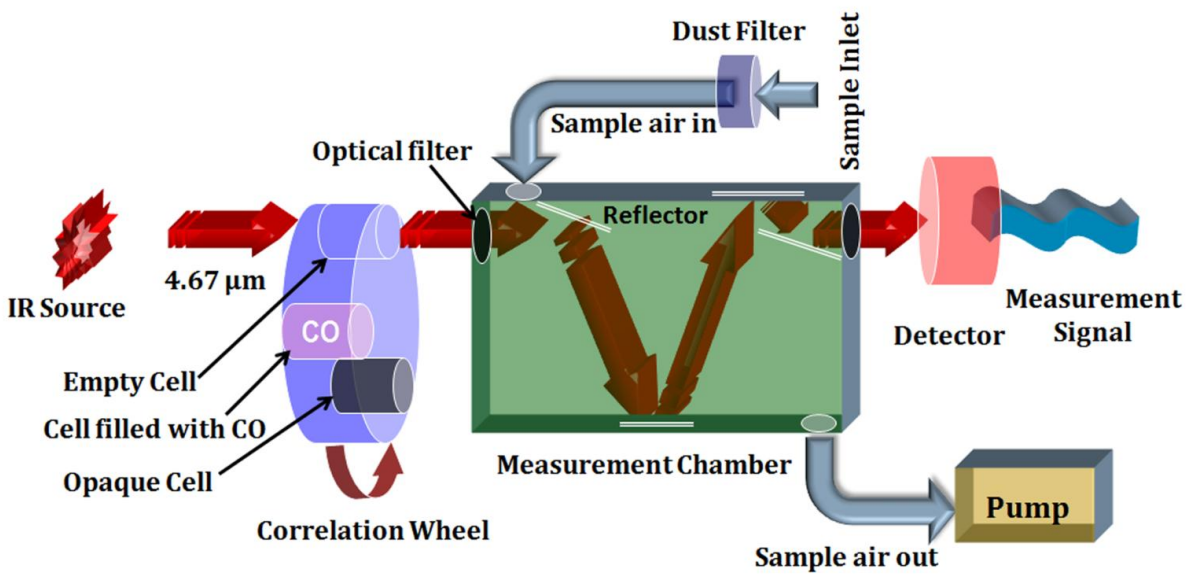
Figure 2.3: Schematic diagram depicting the working principle of CO analyser.
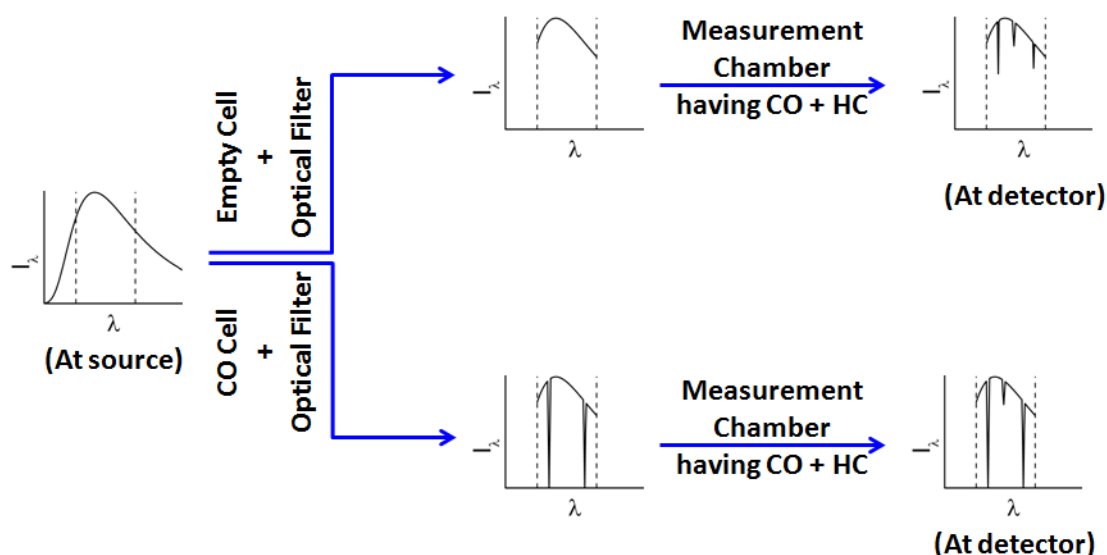
Figure 2.4: Schematic representation of the radiation absorption at different stages of measurement in the CO analyser.

The infrared source is made of a resistive wire winding. When heated to a given temperature, the filament emits IR radiation around ~4.7 μm. The emitted radiation at the source would be similar to the one shown in the sketch in the figure 2.4. The emitted IR radiation passes through the correlation wheel and narrow-band optical filter before entering to the measurement chamber.

The correlation wheel consists of two sets of three cells. Each set comprises of one empty cell, one cell filled with CO, and one opaque cell, as shown in the schematic figure 2.3. The two sets are used to increase the measurement accuracy. The wheel is rotated by a DC motor at a speed of 2206 rpm (rotation per minute). Corresponding to the passage of radiation through these three cells, the radiation is divided in to three parts, which will be converted into three electronic signals by the detector as following. After passing through each of the different cells in the correlation wheel and measurement chamber, the following signals are generated at the detector:

(1) Dark signal D—when the radiation faces the opaque cell. The total suppression of IR radiation incident on the opaque cell makes the condition that IR radiation emitted from source does not reach to the measurement chamber as well as to the detector and hence the signal generated at the detector is the dark signal, which need to be subtracted from subsequent signals corresponding to the empty and CO-filled cells.

(2) Measurement signal M—when the radiation passes through empty cell and through measurement chamber. Thus, the signal generated at the detector is corresponding to the CO concentration present in the air sample inside measurement chamber. The

radiation pattern before and after the measurement chamber would look similar to the one shown in figure 2.4. Since it is non-dispersive measurement technique, a single value is generated at the detector corresponding to a small band of wavelength having the absorption feature of CO. Note that the signal would contain the smaller contribution from interfering hydrocarbons (HCs) in addition to the major contribution from CO absorption. (One of the spikes in the sketch (figure 2.4) could be assumed to be from HC)

(3) Reference signal R—when the radiation passes through CO cell and through measurement chamber. Since the cell is filled with higher concentration of CO, radiation corresponding to the CO absorption lines gets fully removed before passing through the measurement chamber. The radiation while passing through the measurement chamber remains unaffected by CO present in the measurement chamber, rather gets changed by the interfering HCs.

The ratio of measurement signal to reference signal after removal of dark signals is a measure of CO concentration in sample air. However, amplifications of the signals, integration over time (many rotations of the wheel), etc. are performed for the absolute measurement of CO. It is to be noted that the cell filled with CO act as a filter for CO absorption lines thus achieving highly specific absorption measurement using gas of interest as filter in front of measurement chamber/detector. Absorption (or emission) structures of the gas correlate 100% with the "filter". This justifies the name of measurement technique, i.e., "Gas filter Correlation Non-Dispersive IR (GFC NDIR) absorption" or just "Gas filter Correlation".

The IR radiations corresponding to above mentioned three cells are measured with a PbSe (Lead Selenide which has direct band gap of ~0.27 eV) photoconducting detector. The detector is a rapid responding detector and cooled to -30° C by a Peltier element in order to reduce the noise before electronic amplification.

As shown in figure 2.5, over the rotation of wheel (0–180°), three signals corresponding to the three cells are detected by detector. To synchronise the signal for its acquisition by the microprocessor, the correlation wheel is fitted with needles whose position is detected by a photo-interrupter at the beginning of each cell.

Table 2.1 shows the technical specifications of model CO12M, CO analyser of Environnment S.A. The analyser was operated in the laboratory having controlled temperature of 24–26 °C. The measurement range was set to automatic mode for the study period. The response time was also set to automatic for the study period as the software function "automatic response time" enables filtration of measurements

depending upon evolution of CO concentration. Response time is the electronic response time and do not include the physical response of the analyser which is limited by the defined air sample flow.
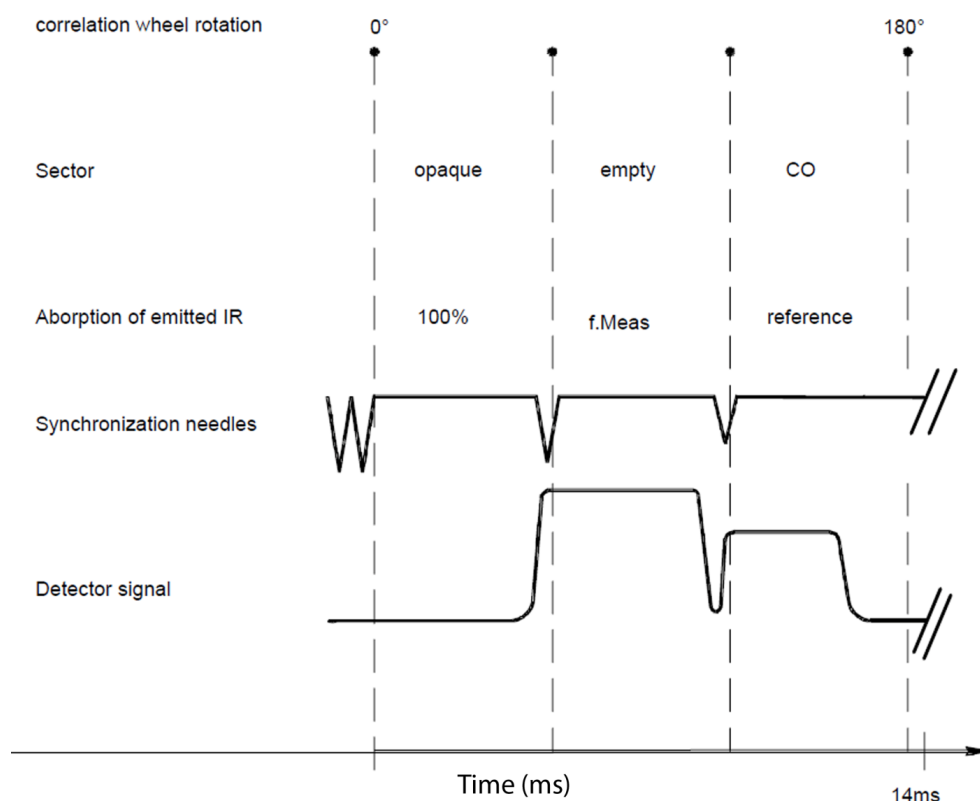
Figure 2.5: Schematic showing the signal synchronisation during the rotation of correlation wheel. (The figure is adopted from the manual of CO analyser)

For each signal —dark, measurement, and reference—, 20 samples are acquired. A complete cycle of dark-measurement-reference takes approximately 27 milliseconds. Integration is performed over 60 rotations of the correlation wheel.

Drk = Σ D, Mes = Σ M, Ref= Σ R (summation over 60 turns which takes ~ 2 s)

Table 2.1: Technical specifications of CO analyser (model CO12M of Environnment S.A)

Parameters	Value/Range/Description
Measurement range	Automatic/Programmable (maximum of 200 ppmv)
Typical noise	25 ppbv (Response time of 30 s)
Lower detection limit	50 ppbv (Response time of 30 s)
Response time	Automatic/Programmable (minimum of 30 s)
Data averaging interval	5 minutes
Zero drift	± 0.2 ppmv per 15 days
Span drift	± 1 % on full scale

Linearity	± 1 %
Sample flow rate	1.3 litre min^{-1}
Pressure influence	Automatic pressure compensation
Operational temperature range	+5 to 40° C
Power consumption	75 Watt Maximum
Dimension and weight	Length: 591 mm, Width: 483 mm, Height: 133 mm, weight: 8 kg
Uncertainty (hourly measurement)	10% (As estimated using calibration standard and also reported by Tanimoto et al., 2007)

The raw data of CO is determined as following.

The instantaneous ratio R_{int} corresponding to the measurement and the reference signal is:

R_{int} = (Mes - Drk) /(Ref - Drk)

Under the automatic response time RT, three signals (i.e. D, M, R) are integrated over a minimum integration time of approximately 12 seconds.

R_{ave}= RT/60 × Σ R_{int}

Based on above R_{ave} and the calibration coefficient defined during calibration procedure (section 2.2.3.1), CO concentration can be defined. However, the correction for zero drift needs to be incorporated.

Internal zero reference cycle

For the zero drift correction, the analyser has the built-in zero filter, which is palladium beads packed in a small cylinder. There is a provision to set zero reference cycle at certain time interval and sampling through the built-in zero filter for the programmed period. During the zero reference cycle, measurement chamber gets filled with the air free from CO. The analyser incorporates the correction electronically if analyser has drifted for zero mixing ratio of CO. In the present study, zero reference cycle was set to 600 s at the interval of 6 hours. The value of R_{ave} is memorised by the end of zero reference cycle, as R_{aveZ}. This value, Abs, is also accounted for determination of absorption by CO, using following formula.

Abs = (R_{aveZ} - R_{ave})/ R_{aveZ}

Based on above value of Abs and the calibration coefficient, concentration of CO (molecules cm^{-3}) is determined. Using the pressure (P) and temperature (T) of the

measurement chamber, CO concentration is converted into CO mixing ratio as, (concentration x k_B x T)/P where k_B = 1.38 x 10^{-23} JK^{-1}. This conversion is done by built-in electronics of the analyzer.

2.2.3 Regular maintenance

As shown in the table 2.2, various operations were performed at specific time interval for the maintenance of the CO analyser.

Table 2.2: Various operations and their frequencies for preventive maintenance of the CO analyser.

Operation	Time interval
Replacement of dust filter (PTFE filter of 47 mm diameter having 5 µm porosity)	1 month (The measurement site/regions being relatively cleaner, interval of a month is acceptable. However, in polluted environment filter need to be replace at 15 days interval)
Cleaning of acrylic filter for protection of internal fans	1 month
Calibration	1 month
Replacement of internal zero filter (i.e., palladium beads)	6 months
Cleaning of measurement chamber, checking of electronic parameters, diaphragm as well as pump valves, and replacement of faulty parts (IR source, detector, electronic board, etc)	Annual

2.2.3.1 Periodic check and Calibration

In addition to above, the analyser is checked periodically (every 15 days) for instrumental drift corresponding to the zero air and span gas. Zero air is the air which has negligible (ideally zero) mixing ratios of CO and other contaminations like hydrocarbons, NOx, SO_2, etc. Span gas is a standard reference gas where CO mixing ratios are known accurately. The multipoint multi-gas calibrator manufactured by SONIMIX (model 6000) has inbuilt zero air generator which generates zero air using a set of internal chemical filters. Also, the zero air generator (model 1160 manufactured by Thermo Fisher Scientific, USA) is used for zero air during check of zero drift. In the zero drift check, zero air is fed to the analyser at ambient pressure. Following to the zero reference cycle (minimum 600 s) from internal zero filter of the analyser; the analyzer is operated for approximately an hour and monitored the instrument drift for zero air.

Similarly, another check is performed for span gas (having a fixed known mixing ratio of CO) and span drift is monitored. These checks help to decide whether calibration is required or to decide the frequency of calibration.

To ensure the accuracy of the measurements, the CO analyser needs to be calibrated. There are two ways of calibration, two-point calibration and multipoint calibration. In the present study, two-point calibration is performed monthly, as per the procedure described below.
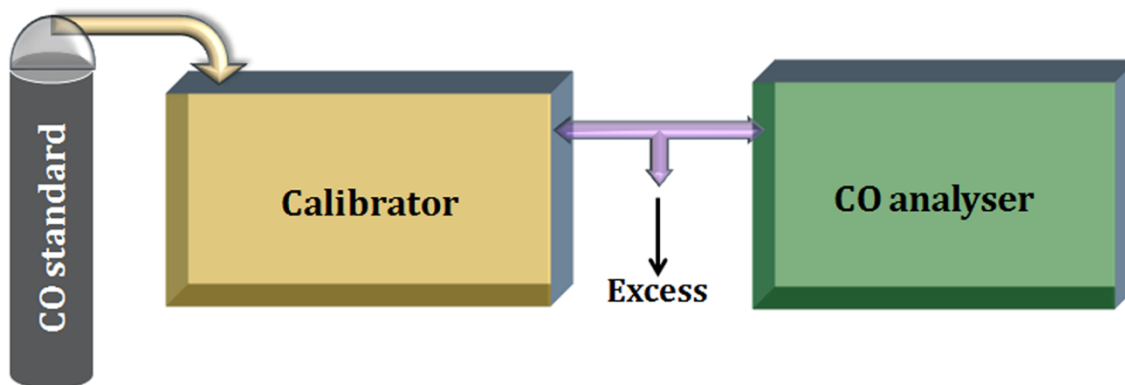
Figure 2.6: Schematic of experimental setup for calibration of CO analyser.

As shown is the figure 2.6, a cylinder of CO is connected to the calibrator. Calibrator is pressurised to 20–30 psi. Calibration standard, traceable to NIST used for the calibration has analytical accuracy of ±5%. Zero air from the in-built zero air generator of calibrator is used for zero correction and dilution of standard gas. Following steps are followed for the calibration. (1) Zero air is fed to the analyser at ambient pressure till the reading get stabilised. When the measured value comes close to zero, the base line is offset for consistent measurements. Adjustment of offset is required because of the measurement noise or drift in the base line. (2) Selecting suitable option in the calibrator, the required mixing ratios of CO is generated. With the help of mass flow controller, calibrator dilutes the standard/span gas utilising the zero air to generate desired mixing ratio of CO. The output of calibrator is fed to the CO analyser. Since the output of calibrator has higher flow than the required for the CO analyser, the excess is vented. CO analyser is allowed to show stable reading. In the present study, 1.1 ppmv and 0.6 ppmv of CO mixing ratios were used for the calibration. Calibration coefficient is calculated using following formula.

K_{new} = K_{old} × (span mixing ratio)/(analyser reading without offset)

K_{old} is calibration factor existing prior to the calibration. K_{new} is calibration factor for the ongoing calibration.

The calibration is accomplished by setting the calibration factor in the instrument under calibration coefficient menu/tab. After the calibration, analyser is operated for a fixed span values for 2–3 hours to ensure the stability of the analyser.

The inter-comparison between four different measurement techniques (i.e., NDIR, VURF, GC- HgO and GC-FID) showed that the agreement among all techniques was better than 2% deviations for hourly averaged data (Zellweger et al., 2009).

2.2.4 Data filtering prior to the analysis

The present study includes ship-based in-situ measurements of CO, and there are chances that ship-exhaust could contaminate the measurements. A contamination of ship-based observation could occur when ship is stationary as well as when winds are calm. Measurements were taken in the upwind are not contaminated when winds are strong carrying the ship-exhaust downwind. The possibility of contamination of data from ship exhaust has been checked by constantly monitoring the wind direction and speed. Along with CO measurements, the continuous NOx measurements also were performed and since NOx amount in the fossil fuel burning is very high, NOx measurements are used as tracers of ship exhaust. Based on these two factors (i.e., wind direction and NOx) all the contaminated data have been discarded. The NOx observations are not included in the present study as it is out of the scope of present study.

2.3 Supporting in-situ measurements

2.3.1 Surface CO mixing ratios from NOAA network

The Carbon Cycle Greenhouse Gases (CCGG) group at the ESRL, NOAA in Boulder, Colorado, USA maintains a co-operative air sampling network of over 100 sites around the world. Air samples are taken weekly in glass flasks from various locations all over the globe and flasks transported back to the CCGG group for the measurement of various trace gases. Different techniques (i.e., gas chromatography; GC, HgO reduction detection, CO fluorescence in the vacuum ultra violet) were used for the measurement of CO mixing ratio. Most of the time, air samples are taken in pairs, weekly for land sites and every three weeks per five degree latitude zone for Pacific Ocean. If the difference between the mixing ratios corresponding to the pair samples is less than 3 ppbv, the samples were accepted; otherwise they are not used in further analysis (Novelli et al., 1998; Novelli et al., 2003). In this study the in-situ measurements of surface CO across the globe from 82 sites (as shown in the figure 2.7) were used for the confirmation of

observed trend in lower-tropospheric CO estimated from MOPITT retrievals. The monthly averaged CO mixing ratios (Petron et al., 2018) available for the period of 2000–2017 were obtained from ftp://aftp.cmdl.noaa.gov/data/trace_gases/co/flask/surface/ and are utilised in the study. Measurements using GC and HgO reduction methods have 1 ppbv of precision as well as experimental uncertainty (Masarie et al., 2001).
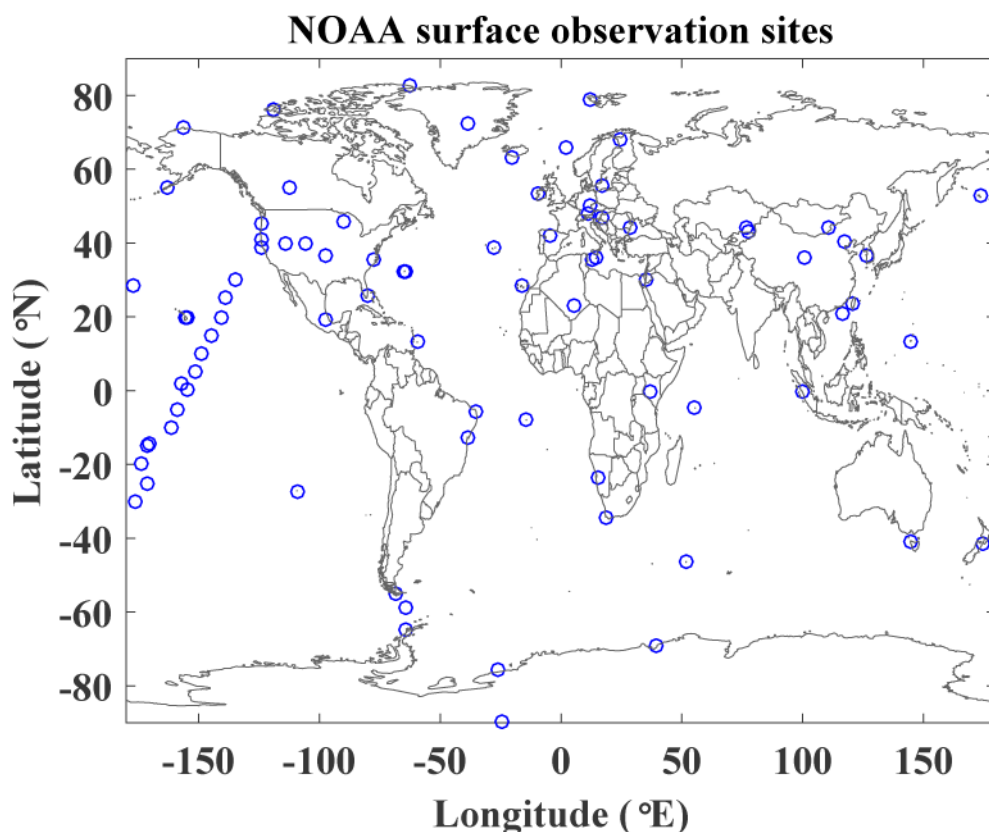
Figure 2.7: Selected surface observation sites of NOAA network where CO observations are available since year 2000.

A site, Cape Rama (15.08° N, 73.83° E; 60m amsl) on the west coast of India is one of the locations from where the air samples are being collected for greenhouse/trace gas measurements including CO as part of CSIRO's (Command wealth Scientific and Industrial Research Organisation) global sampling network. Air samples are collected in the afternoon hours in 500 ml glass flasks at a pressure of 190 kPa (Bhattacharya, et al., 2002) and are analysed at CSIRO Atmospheric Research's GASLAB (Global Atmospheric Sampling LABoratory). Further details of GASLAB operation are given in Francey et al., 1996. Samples were analysed by gas chromatography with a mercuric oxide reduction gas detector. CO reduces HgO to Hg vapour which is detected by UV absorption (http://ds.data.jma.go.jp/gmd/wdcgg/pub/products/cd-

rom/dvd_04/metadata/co/observation/200909020004.html). CO observations are available for the period of 1993 to 2010 with a gap of observations during 2003–2008. Data is obtained from http://ds.data.jma.go.jp/gmd/wdcgg/pub/products/cd-rom/dvd_04/menu/data.html.

2.3.2 Measurement of BC mass concentrations using Aethalometer

Since BC and CO are the co-products of incomplete combustion, the association between BC and CO helps to estimate/validate the BC emission (knowing the CO emission) which is examined in the present study. The measurement of near surface BC mass concentrations was carried out by using an Aethalometer (model: AE31 of Magee Scientific) working on the principle of optical attenuation technique. Aethalometer is widely used for the estimation of aerosol BC mass concentration. The ambient air drawn into the analyser continuously at a flow rate of 5 litre min^{-1} and aerosols get deposited on a quartz fibre filter tape. The change in optical attenuation measured at every 5 min interval was converted to BC mass concentration using the specific mass absorption cross section of 16.6 $m^2\,g^{-1}$ (Hansen, 1996). The high value of absorption cross section used in this technique is to account for the multiple scattering and loading effects within the filter tape (Arnott et al., 2005; Nair et al., 2007). Several studies have shown excellent inter-comparison between optical attenuation techniques with other techniques such as thermal and photo-acoustic. The uncertainties in the measurements using Aethalometer technique arises because of the multiple scattering effects in the filter tape (the so called "C" factor) and the shadowing effects ("R" factor). Accordingly, considering the experimental configuration for Aethalometer and the technique, the uncertainty in BC mass concentration is estimated to be ~10%. The more details of BC measurements using the Aethalometer and the inherent uncertainties in the filter based optical techniques are available in the literature (e.g., Babu et al., 2004; Nair et al., 2007).

2.3.3 Measurement of surface Ozone mixing ratio using Ozone analyser

Since CO is one of the precursors for the tropospheric O_3, the O_3/CO ratio is indicative of ozone production efficiency and this ratio is examined in the present study to characterise the chemical nature of airmasses. Surface O_3 measurements were carried out using an online ultraviolet photometric ozone analyzer (Model: O3 42), manufactured by Environnement S.A, France. The analyser utilises the absorption of UV radiation by O_3 molecules at 253.7 nm and derives O_3 mixing ratios using the Beer–

Lambert law. This UV absorption-based analyser has an uncertainty of about ±5% (Tanimoto, 2007), corresponding to ~1–3 ppbv for the observed range of O_3. The analyser has zero noise, lower detection limit and linearity of 0.5 ppbv, 1 ppbv and ±1% respectively. The analyzer was operated on auto-response mode, where responses could be 10–90 seconds depending upon changes in O_3 mixing ratios. However, data were recorded continuously at 5-minute intervals and hourly averaged values are used for the analysis.

2.3.4 Measurement of meteorological parameters using the Automatic Weather Station

The surface meteorological parameters viz., wind speed, wind direction, temperature, relative humidity, solar radiation, pressure, and rainfall were measured over the oceanic region using an AWS (Campbell Scientific, Canada). AWS was mounted on a ~7 m long boom fixed at the bow of the ship during the ship campaigns. The data was recorded at averaging interval of 1 min and hourly averaged values of temperature, relative humidity, and pressure were utilised for the inter-comparison with WRF-Chem simulated parameters. The table 2.3 shows the sensor type, range of measurements, response time and accuracy for various parameters.

Table 2.3: Technical details of the sensors used in the AWS as per the user manual of the instrument.

Parameter	Sensor Type	Range and Response	Accuracy
Temperature	Platinum resistance temperature detector (Pt100RTD)	-40 to 60 °C (<5 s)	± 0.1 °C
Relative humidity	Capacitive sensor, HygroClip-S3	0–100% (12–15 s)	± 1.5%
Pressure	Electronic Barometer	600–1100 hPa (<2 s)	± 0.5 kPa

2.4   Satellite data

Various scientific instruments (payloads) such as MOPITT and MODIS aboard Terra (Latin word for Earth) satellite; AIRS and MODIS aboard Aqua (Latin word for water) satellite; TES, OMI and MLS aboard Aura (Latin word for air) satellite, IASI aboard MetOp-A satellite, etc. (https://terra.nasa.gov/, https://aqua.nasa.gov/, https://aura.gsfc.nasa.gov/,

https://www.eumetsat.int/website/home/Satellites/CurrentSatellites/Metop/index.ht

ml) provides altitude profile of CO, columnar CO, NO_2, fire events, etc. globally. One of the main datasets used in this study is the CO data retrieved by MOPITT aboard Terra spacecraft. In addition, CO, O_3, NO_2, fire events from TES, AIRS, MLS, IASI, OMI, and MODIS, were also used as supporting data. Terra, Aqua, Aura spacecrafts were launched in 1999, 2002 and 2004 respectively, which orbit at the altitude of ~705 km (orbit period of ~ 99 min) in a near polar sun-synchronous orbit (orbit inclination of ~ 98°). These satellites are part of NASA's Earth Observing System (EOS). These satellites have 16 days repeat cycle, i.e. every 16 days they crosses the same spot on the earth. The equator crossing time for Terra spacecraft is 10:30 h local time (descending node). Aqua and Aura spacecrafts are part of the "A-Train" satellite constellation. Aura spacecraft flies 15 minutes behind the Aqua satellite. The equator crossing time for Aqua and Aura spacecrafts are ~13:30 and ~13:45 h local time respectively in the ascending node. MetOp, a meteorological satellite is a part of EUMETSAT (European Organization for the Exploitation of Meteorological Satellites) Polar System (EPS). MetOp-A (launched in 2006) and MetOp-B (launched in 2012) are in polar sun-synchronous orbit (inclination of ~ 98°), at an altitude of 817 kilometres. The equator crossing time for MetOp-A is 9:30 h local time (descending node).

2.4.1 CO measurements by MOPITT

2.4.1.1 MOPITT Instrument and its working principle

MOPITT aboard Terra spacecraft is a nadir viewing gas correlation radiometer designed to retrieve the CO in different layers of troposphere (Drummond, 1992). It scans across the flight track to ~ ±26° from nadir in 13 s, with a sampling frequency of 0.45 s. The resolution of instrument is 22 km x 22 km, swath is approximately 600 km and thus achieves global coverage in approximately 4 days (65 orbits) (Drummond, 1992; Caldwell et al., 2005). Figure 2.8a shows the schematic of MOPITT instrument indicating various components and figure 2.8b shows the Terra spacecraft showing MOPITT instrument. Figure 2.9 shows the MOPITT scan pattern. A complete description of the MOPITT instrument can be found in the mission description document (Drummond, 1996). In this study the MOPITT retrievals were used extensively as the dataset is available for the longest period, ~ 18 years.
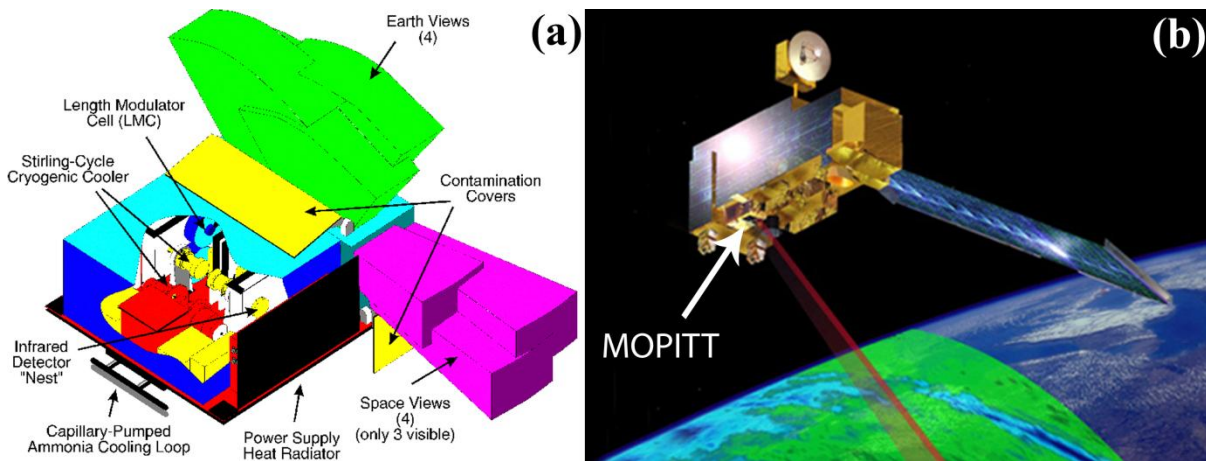
Figure 2.8: (a) Schematic of MOPITT instrument and (b) Terra spacecraft (Courtesy: https://www2.acom.ucar.edu/sites/default/files/mopitt/ and http://www.asc-csa.gc.ca/eng/satellites/mopitt.asp)
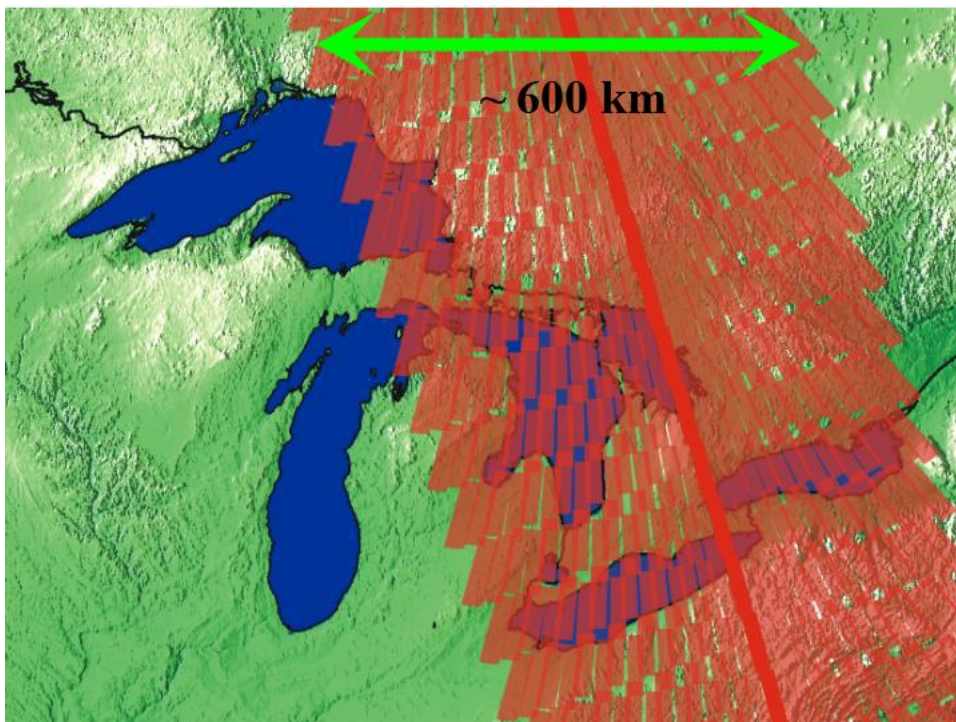
Figure 2.9: MOPITT scan strategy (Courtesy: Adopted from Drummond, 1992; https://www2.acom.ucar.edu/mopitt/concepts).

2.4.2 MOPITT Measurement technique

Figure 2.10 depicts the MOPITT measurement approach and viewing geometry. MOPITT measures the extra terrestrial radiation using gas correlation spectroscopy. The earth and atmosphere emits thermal infrared radiation, which passes through atmosphere and gets partially absorbed. The transmitted component of the radiation is measured. Also it measures near infrared corresponding to the reflected solar radiation

which has passed through the atmosphere, reflected at the earth's surface, and transmitted through the atmosphere. MOPITT measurement in thermal channels (~4.7 μm, where strong CO absorption lies) corresponds to the radiation emitted from the earth's surface and emitted as well as absorbed by the atmosphere. The measurement of near-infrared (2.2 and 2.3 μm channels) includes the reflected radiation which is the dominant signal. Only daytime measurements are possible in the wavelengths 2.3 and 2.2 μm, while thermal channels (4.7 μm) measurements are performed during day as well as night.
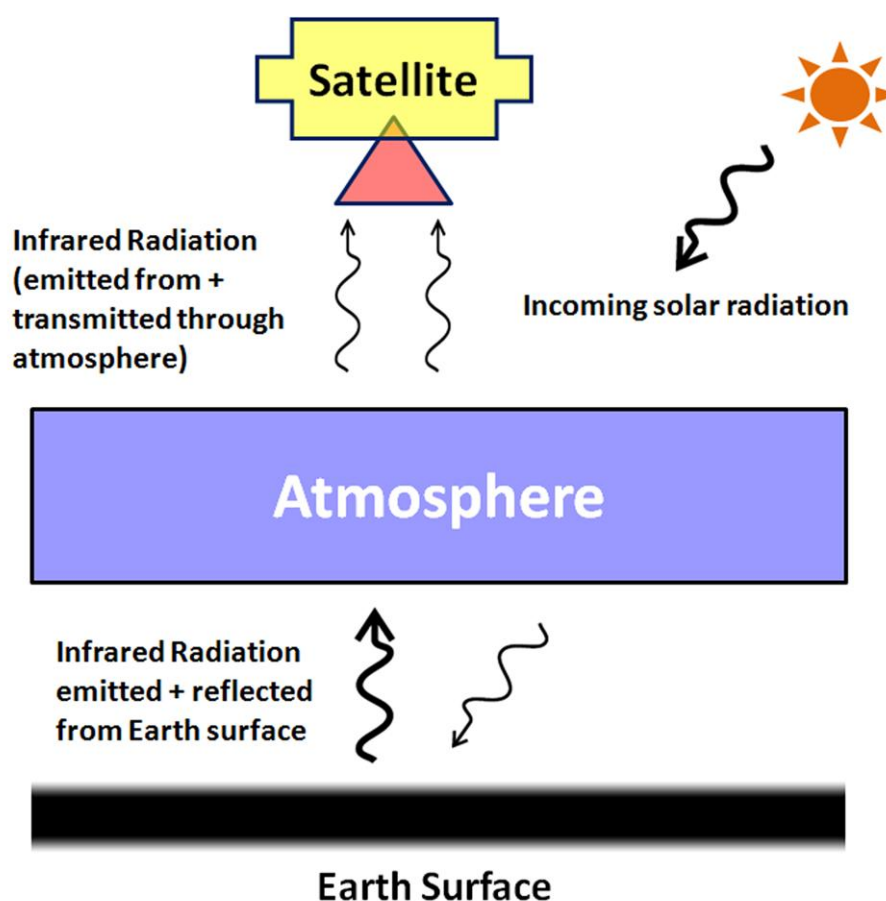
Figure 2.10: Schematic diagram of MOPITT measurement system (adapted from algorithm theoretical basis document, level 2).

The MOPITT instrument uses the principle of correlation spectroscopy, in which a cell of the target gas (i.e., CO) is used as an optical filter. The principle of correlation spectroscopy is that of spectral selection of wavelengths by a sample of target gas as an optical filter (http://www.atmosp.physics.utoronto.ca/MOPITT/mdd_93/m93-31.htm). This allows a simultaneous measurement at all spectral lines of interest as all spectral lines correlate precisely. This leads to improved sensitivity as the signal at the detector is corresponding to many spectral lines. However, summing radiation all spectral lines leads to complex calculations for the retrievals of target species. The amount of gas in

the cell is modulated by varying either the pressure or the length, correspondingly called Pressure Modulator Cell (PMC) and Length Modulator Cell (LMC). The MOPITT instrument has two PMCs and four LMCs to form eight spectral channels, six are designed to be used for CO retrievals and two for CH_4. By using a series of PMRs and LMRs at different cell pressures, MOPITT retrieves the vertical profile of CO by sampling different parts of the wings of absorption lines.
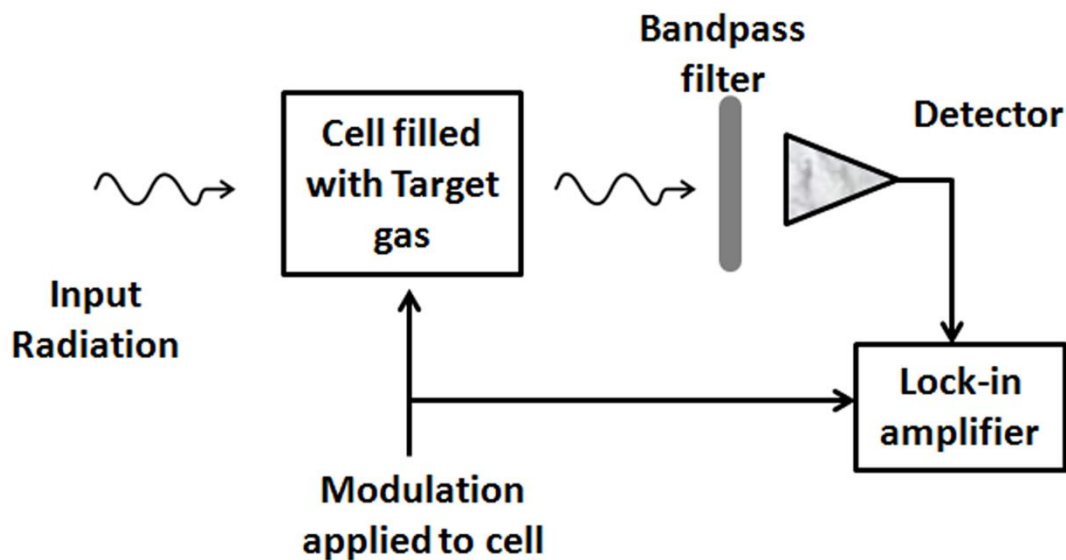
Figure 2.11: Schematic of gas correlation spectroscopy (adapted from algorithm theoretical basis document, level 2)

The technique of correlation spectroscopy is shown in figure 2.11. Assume the radiation enters from the left and is detected by the system on the right, the output as a function of spectral frequency is shown in Figure 2.12 for two different amounts of gas in the absorption cell. The detector views through two different filter just by changing the amount of gas in the cell.

In this technique, pressure inside the cell in the case of the PMC (or the effective gas cell length in the case of the LMC) is modulated. It results in a modulation in the opacity of the cell due to that component of the radiation gets modulated. This produces fluctuations in the signal at the detector only inside the spectral lines of the target species contained in the cell. Two signals are possible: the difference (D) signal and the average (A) signal. The D-signal results from differencing the signals for low and high opacity of the cell. The A signal is obtained by asynchronously chopping the input signal with the modulation. This is to measure the mean radiation transmitted by the cell. The information corresponding to the two signals —difference and average— are complementary to each other. This provides information on the background radiance,

which includes the surface emission and the absorption due to other atmospheric constituents. The D response function is high only at the spectral line positions of the gas in the cell (i.e. CO) and is nearly opaque for other spectral intervals. This signal provides the information of CO in the atmosphere (algorithm theoretical basis document, level 2).
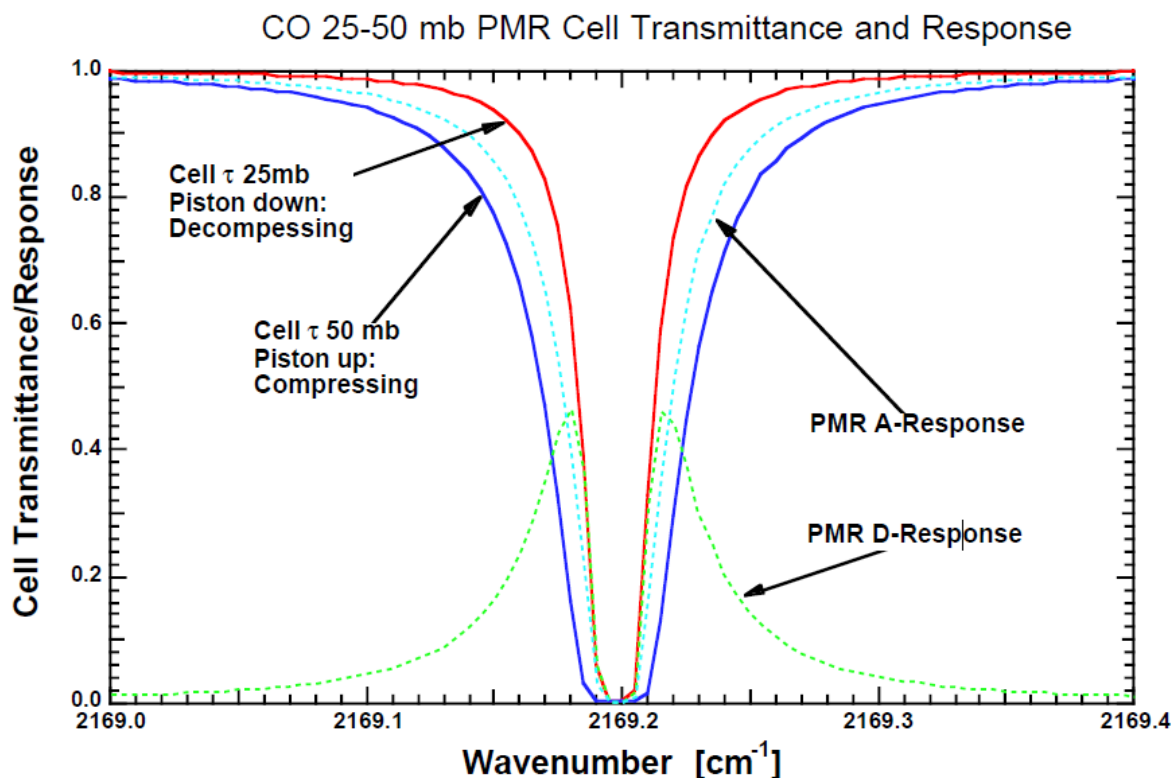
Figure 2.12: A- and D-signal response functions for a single spectral line in a 25–50 mb PMR used in the CO thermal 4.7 µm measurement. The cell transmittances at 25 and 50 mb are shown together with the difference (D) and average (A) responses of the cell. (Courtesy: algorithm theoretical basis document, level 2).

$$S_a^{thm} = \int_v \left\{ I_s(v) + \int_0^\infty \left[B(v, T(z)) - I_s(v) \right] \frac{d\tau(v,z,\infty)}{dz} \right] dz \right\} \tau_f(v) \left[\frac{\tau_c(p_l) + \tau_c(p_h)}{2} \right] dv$$

$$S_d^{thm} = \int_v \left\{ I_s(v) + \int_0^\infty \left[B(v, T(z)) - I_s(v) \right] \frac{d\tau(v,z,\infty)}{dz} \right] dz \right\} \tau_f(v) \left[\tau_c(p_l) - \tau_c(p_h) \right] dv$$

Where, S_a^{thm} stands for CO thermal channel average signal, and S_a^{thm} stands for CO thermal channel differential signal. $I_s(v)$ is the top of the atmosphere radiance. $B(v, T(z))$ is the Planck function. $\tau(v, z, \infty)$ is the atmospheric transmittance from altitude z to top-of-atmosphere. $\tau_f(v)$ is the MOPITT instrument transfer function.

$\tau_c(p_l)$ is the CO cell transmission function at low cell pressure of p_l. $\tau_c(p_h)$ is the CO cell transmission function at low cell pressure of p_h. MOPITT fast radiative transfer model, so-called MOPFAS, calculates these signals which form the MOPITT operational retrieval. Details of MOPFAS can be found at Edwards et al., 1999.

The above signal equations can be generalized as the following equation, which relates the instrument signals to profiles of the target gas (i.e., CO), other interference gases profiles, earth surface parameters, and MOPITT instrument functions.

$$Y = F(X,b) + Ninst$$

where, Y is the measurement vector consisting of 8 MOPITT CO thermal channel signals (4 average signals and 4 difference signals). X is the state vector consisting of CO mixing ratios at a number of selected pressure levels, surface emissivity at CO thermal channels and surface temperature Ts. b is the vector of known parameters such as ancillary data and instrument parameters. The direct solution of equation is not possible because it is typically ill-conditioned. X is found by minimizing the difference between observation Y and calculation F(X,b) by the forward modelling. More details are given in Wang et al., 1999, Deeter et al., 2003 and Pan et al., 1998.

2.4.2.1 MOPITT channels

Figure 2.13 shows the schematic of MOPITT channels and also describes how the satellite reaching radiation passes from scanning mirrors to the detectors. MOPITT comprises of eight channels can be divided into two groups. (1) Channels 1 to 4: These channels do not collect data due to the failure of one of the coolers (Caldwell et al., 2005) and (2) Channels 5 to 8 another group: Though channels 1 to 4 do not work, channels 5 to 8 operate and the instrument continues to function at its capacity (Caldwell et al., 2005). The Indium antimonide (InSb) detectors for each group are cooled at approximately 90 K by two separate Stirling Cycle Cryogenic Coolers. Channels 1 to 4 (or 5 to 8) contain three CO channels and one CH_4 channel. Scan mirror relay the radiation toward chopper which rotates at 1800 rpm. The stray-light is blocked by the chopper. The radiation is then routed to the LMCs, or PMCs which contain the target gas samples for the modulation. The radiation passes through the cells, and other optics finally reaches to the detectors. For the purpose of on board calibration, there are blackbodies near to the scan mirror.
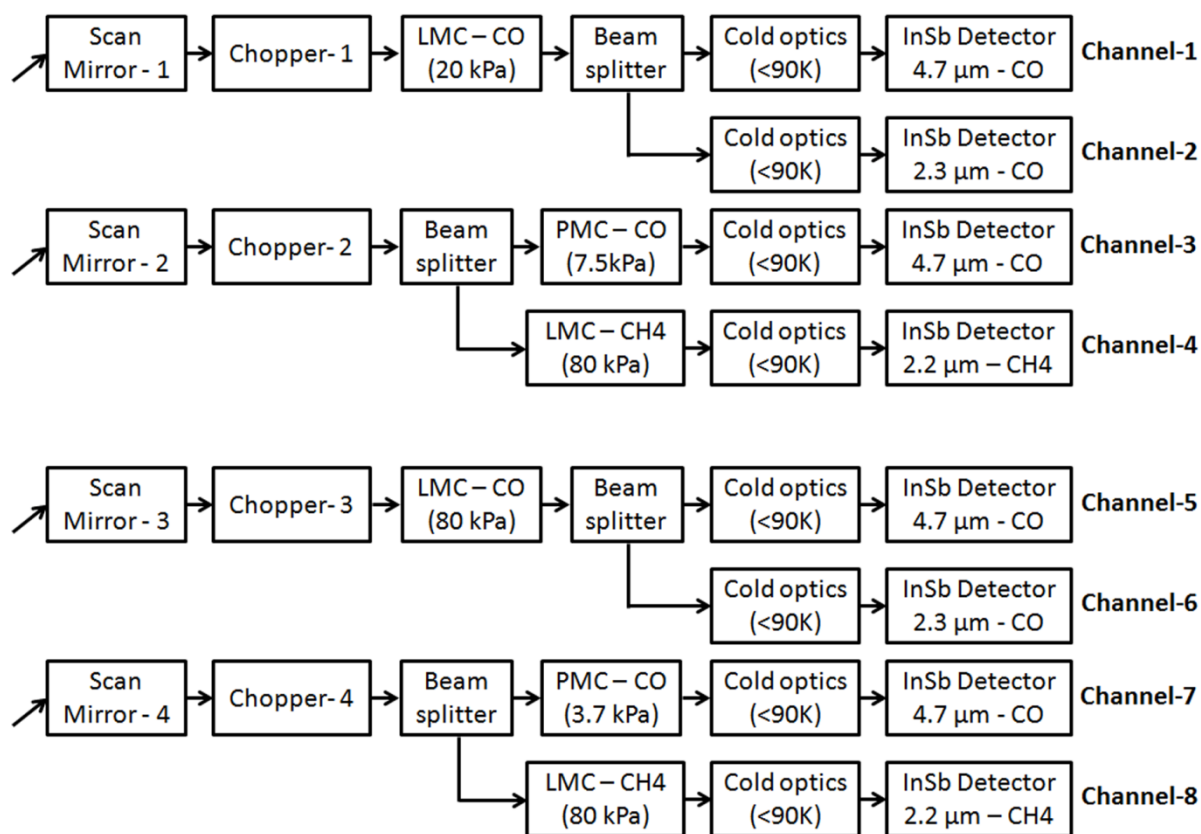
Figure 2.13: Schematic of two groups of measurement channels of MOPITT instrument (adapted from Drummond et al., 2010).

2.4.2.2 Radiometric calibration of the MOPITT thermal channels

Onboard calibration of MOPITT is essential to minimise any offset and gain errors due to instrument thermal variations, condensation and damage to the optics, or detector degradation. There is space-viewing port and blackbody target with the MOPITT. The blackbody is used for the radiometric calibration and gain correction. To find the instrument offset, every two minutes (10 swaths) the instrument scan mirror rotates to look at deep space for 5 stares. After every 10 minutes (every fifth space-view), the scan mirror rotates to view an internal blackbody target for 20 stares. The blackbody targets are kept at 295 K and measurements corresponding to blackbody observation provide a channel gain correction.

2.4.3 Uncertainties in MOPITT retrievals

As described in the algorithm theoretical basis document, level 2, there are many factors which contribute to the uncertainty in the retrieval. The MOPITT instrument has limited vertical resolution. Due to this limitation, the retrieval does not resolve small scale variations in the profile. As a result, for certain types of situations, retrievals will have large "shape error" as discussed by Rodgers (1990). The instrument noise can

increase the uncertainty up to ~ 2%. Tropospheric temperature profiles are important input data for CO retrievals and uncertainty in the temperature profile also causes uncertainty in the retrieval of CO profile. The simulation results indicate that a 2 K random error in a temperature profile will cause about 2% increase in the profile variance. The main interfering species in the profile measurement are H_2O and N_2O. Approximately, 3–5% of uncertainty in the H_2O profile produces ~1% error in the CO profile retrieval. In addition, calibration error, the influence of a priori information, smoothing error, model parameter error, and forward model error adds to the uncertainty. The major error is due to smoothing error (Deeter et al., 2003). The MOPITT validation using ground-based infrared spectroscopy shows that columnar CO estimates are accurate within 10% (Emmons, et al., 2004). The retrieval errors over Indian region are less than 40 ppbv at 850 hPa (Kanawade, 2010). The detailed analysis done by Deeter et al., 2003 shows that the retrieval uncertainties (at 500 hPa) are approximately 20% in the tropics and mid-latitudes, and 30–40 % at high latitudes. The estimation of retrieval uncertainty is provided along with the CO retrievals data. In the analysis, these uncertainties are considered.

2.4.4 MOPITT dataset used in the study

The MOPITT based CO data are available with different algorithms i.e., Version 3(V3), Version 4 (V4), Version 5(V5), Version 6(V6), and Version 7(V7). This V7 algorithm offers three products "Thermal IR" (V6-TIR), "Near IR" (V6-NIR) and "Thermal and Near IR Joint" (V6-TIR/NIR). Whereas the V6-TIR data is available for all scenes (day/night, land/ocean), the V6-NIR data is available for clear-sky daytime scenes over land only. The V7-TIR (or V6-TIR) product is a true optimal estimation retrieval similar to the V4 product and V6-TIR (and V5) product showed reduced retrieval bias-drift associated with long-term instrumental changes (less than 1% year[-1] at all levels) which is negligible in total columnar CO (Deeter et al., 2013; 2014). Due to these reasons, V7-TIR data were selected for the present study as obtained from the ftp server, ftp://l5ftl01.larc.nasa.gov/MOPITT/.

The present study uses level 3 V7 gridded (1° × 1°) daily and monthly averaged altitude profiles of CO as well as columnar CO as retrieved from MOPITT. The detailed description, validation and the improvements in V7 are given by Deeter et al., 2017 and "Version 7 Product User's Guide", 2016. Level 3 data, compared to Level 2 are less affected by random retrieval errors. The CO mixing ratio profiles are available at 10 pressure levels (surface, 900, 800, 700, 600, 500, 400, 300, 200 and 100 hPa). CO mixing

ratio at a pressure levels represents CO mixing ratio for the layer (100 hPa thick) above the pressure level (Version 7 Product User's Guide, 2016 and Version 5 Product User's Guide, 2011). The retrieval at 100 hPa represents the uniform mixing ratio in the layer extending from 100 to 50 hPa.

In V7 data, the updated radiative transfer model is used for CO retrieval algorithm which accounts for the steady growth of atmospheric N_2O concentrations (Version 7 Product User's Guide, 2016). In this recent version of MOPITT retrieval algorithm, temporal change in MOPITT averaging kernels or retrieval bias-drift associated with long-term instrumental changes is negligible (Deeter et al., 2013; 2014; 2017). Thus, artefact in the estimation of trend due to change in instrumental parameters is expected to be negligible. The retrieval algorithm requires temperature and water vapour profiles as well as a priori surface temperature values. For V7, meteorological profiles from the recently released MERRA-2 product ('Modern-Era Retrospective Analysis For Research And Applications') are used. Only clear sky observations are processed for CO retrievals. The clear/cloudy determination is based both on MOPITT's thermal-channel radiances and the MODIS cloud mask. In V7, MODIS Collection 6 cloud mask files are used. The radiance-bias correction for TIR radiances is done by applying scaling factors, determined by minimizing observed retrieval biases at 400 and 800 hPa estimated from in-situ CO profiles. There exists a retrieval anomaly in a small number of nighttime/land scenes, known as a striping pattern in retrieved surface level CO. The retrieval anomalies due to this effect are typically small (< 10 ppbv). The level 3 V7-TIR gridded daytime retrievals (Surface CO and profile of CO) having degree of freedom (DOF) > 1 and retrieval uncertainty<30% (<10% in case of column CO) are only used in the analysis.

2.5   Supporting datasets

Lower and upper tropospheric CO as well as columnar CO from AIRS, TES, MLS, and IASI are used in the study for estimation of long-term trends in CO. In addition, fire count data from MODIS for investigations on biomass burning influence, and tropospheric NO_2 column to identify the anthropogenic activity over the region are also used.

2.5.1 AIRS

AIRS is a cross-track scanning instrument aboard Aqua spacecraft (Aumann et al., 2003; https://airs.jpl.nasa.gov/mission_and_instrument/instrument). AIRS is a thermal

infrared grating spectrometer covering 3.7 to 16 μm spectral range with 2378 channels (Version 6 Data Release User Guide dated 27 November 2017 and https://airs.jpl.nasa.gov/resources/guides). It has a scan-mirror which rotates (49° either side of the nadir) around the line of flight which redirects the IR radiation coming from the earth to the instrument. The spatial footprint of the infrared channels is 1.1° in diameter corresponding to about 15 x 15 km at the ground in the nadir view. The spectrometer has resolutions, $\lambda/\Delta\lambda$, ranging from 1086 to 1570, in three bands: 3.74–4.61 μm, 6.20–8.22 μm, and 8.8–15.4 μm. CO is retrieved from the 2183–2200 cm^{-1} (4.58–4.50 μm) region of the spectrum on the edge of the 1–0 vibration-rotation band of CO (McMillan et al., 2005). The AIRS CO retrieval sensitivity is broad and centred in the mid-troposphere between approximately 300 and 600 hPa (Warner et al., 2007). The comparison of AIRS retrieved CO profiles with in-situ measured profiles in the northern mid-latitudes showed that AIRS V5 CO retrievals have bias of 6–10% between 900 and 300 hPa with a root-mean-square error of 8–12% (McMillan et al., 2011).

Monthly averaged upper-tropospheric CO mixing ratios and columnar CO gridded at 1° × 1° (level-3, version-6) retrievals for the period of 2002 to 2018 (~16 years) were utilised in the study for calculation of trend. Following the user guide of AIRS retrievals (Version 6 Data Release User Guide dated 27 November 2017), various precautions were taken as followings. Prior to the analysis, the data were screened where Quality Assurance (QA) was best or good (QA = 0 for "best", QA = 1 for "good" and QA = 2 for "do not use"). The data were selected for daytime (ascending orbits) in this study. The degree of freedom (computed by summing the diagonal elements of the 9 x 9 CO averaging kernel) provides a measure of the amount of information in the CO retrieval. The CO retrievals having degree of freedom higher than 0.5, are used in the study. In addition, retrievals for which error value is negative or greater than 50% of CO mixing ratio were excised.

2.5.2 TES

The TES is an infrared high spectral resolution Fourier Transform Spectrometer (FTS) aboard Aura satellite (Beer, 2006). TES measures the infrared radiance emitted by thermal emission of the earth's surface and gases in the atmosphere as well as reflected sunlight, providing day-night coverage over the globe. TES has significantly higher spectral resolution than that of the AIRS (https://aura.gsfc.nasa.gov/tes.html). TES operates in a global survey mode (Nadir observations, 16 orbits) approximately every two days. It operates for special observations every alternate day. The TES spectral

range is from 650 to 3250 cm^{-1} (3.3–15.4 μm). The spectral resolution (smoothed) 0.10 cm^{-1} (however, spectra recorded at 0.06 cm^{-1}) during nadir viewing, which is used for global survey mode observations. However, the resolution of 0.025 cm^{-1} (limb viewing) is also available for special observations (Level 2 Data User's Guide V6, 2013). The horizontal resolution is 5 km x 8 km, separated by ∼ 180 km for global survey mode. CO is retrieved from the measurements in the spectral window between 1890–2260 cm^{-1} which includes 4.7 μm CO absorption band (Worden et al., 2004). The validation studies show that the difference between TES based CO profiles and in-situ aircraft-based measurements and the MOPITT retrievals are within TES retrieval errors and equivalent to CO spatial/temporal variability (Luo et al., 2007a, b). On average, the TES CO volume mixing ratio profile is 0–10% lower than the adjusted DACOM CO profile (Differential Absorption CO Measurement) from the lower to middle troposphere (Luo et al., 2007b). The direct comparisons of the CO mixing ratio at 681 and 215 hPa between TES and MOPITT show that TES CO is slightly higher than that of MOPITT by <5% in global averages. CO profiles typically have a retrieval uncertainty of 10–20% and the mean bias or difference with reference to aircraft based measurements was 4% (Lopez et al., 2008). In the TES sensitive pressure range, 700–200 hPa, the in-situ profiles and TES profiles shows good agreement within 5–10% (Loperz et al., 2008).

The latest release of Level 2 retrievals, Version 7 data (V007) are used in the study. Comparisons of profiles of CO between TES and MOPITT show better (compared to Version 6 data) agreement when a priori information is accounted for correctly. V006 of TES data had a lower bias, which is no longer the case for CO mixing ratios from TES V007. The CO VMRs are slightly higher than V006 in the upper troposphere (Aura-TES L2 Products: Version 7, Data Quality Description). TES CO agrees to within the estimated uncertainty of the aircraft instruments, including both errors and the variability of CO itself. The data with quality flag = 1 (i.e., good) were considered for the analysis.

2.5.3 MLS

MLS aboard Aura spacecraft is a small radio radiometer (Waters, 2006) measuring microwave emission of the earth's atmosphere to retrieve CO mixing ratio profiles (https://mls.jpl.nasa.gov/). Each scan across the limb provides radiance measurements at 120 tangent altitudes. These are separated by ∼ 300 m in the troposphere. We have used CO retrievals at 215 hPa (the upper troposphere). CO measurements are made by the 240 GHz radiometer. This has band 9 (25 channels, ranging from 6–96 MHz) and band 25 (129 channels with a width of 97.6 kHz) centred

on the 230.538 GHz (~1.3 mm) spectral line of CO. The optimal estimation algorithm (Livesey et al., 2006; Pumphrey et al., 2007) is used for the retrieval of CO profile. The vertical resolution is in the range 3.5–5 km from the upper troposphere to the lower mesosphere. The standard retrievals for CO are between 215 – 0.46 hPa with a vertical resolution of ~3 km in the upper troposphere and the stratosphere are useful for scientific studies. The along-track resolution of the CO measurements is ~200 km between 215 and 10 hPa. As per version 2.2 algorithm, CO accuracy is estimated at 30 ppbv +30% for pressures levels of 147 hPa and less (Livesey et al., 2008). Level 2 version-4 data having quality index higher than 1.5, convergence lower than 1.03, status field equals even number, and precision equals positive number, etc. were considered for the analysis [Level 2 (Version 4.2x) data quality and description document, 2018]. Artefacts of thick clouds associated with deep convection on the upper-tropospheric CO are removed by aforementioned quality and convergence filter criteria (Level 2, Version 4.2x, data quality and description document, 2018). The resolution, precision, and accuracy corresponding to the CO retrieved at 147 hPa are 5.1 km × 570 km (vertical x horizontal), 16ppbv, and ±26 ppbv (±30%), respectively.

2.5.4 IASI

IASI is a TIR Fourier Transform Spectrometer (FTS) aboard MetOp-A measures infrared radiation at a horizontal resolution of ~12 km over a swath of ~ 2200 km (https://www.eumetsat.int/website/home/Satellites/CurrentSatellites/Metop/MetopD esign/IASI/index.html). The spectral range of IASI is from 645 to 2760 cm^{-1} with resolution of 0.5 cm^{-1} and using IASI measurements the profile and column of several different trace gases are retrieved (Clerbaux et al., 2009). CO profiles are retrieved based on an optimal estimation approach using the radiance in the spectral range of 2128–2206 cm^{-1} (4.53–4.69 μm), implemented in the Fast Optimal Retrievals on Layers for IASI (FORLI) software (Hurtmans et al., 2012). The IASI CO retrievals were validated against ground based observations (Kerzenmacher et al., 2012), aircraft data (Pommier et al., 2010, De Wachter et al., 2012) and satellite measurements (George et al., 2009). The CO profiles processed with the recent retrieval code, v20100815 is used in the study. The data was filtered as described by Hurtmans et al., 2012 as following. The data for which bias values lower than -0.15 × 10^{-9} W/(cm^2 cm^{-1} sr) and higher than 0.25 × 10^{-9} W/(cm^2 cm^{-1} sr) were removed. In addition, the data for which RMS greater than 2.7 x 10^{-9} W/(cm^2 cm^{-1} sr) were removed. The data was obtained from http://ether.ipsl.jussieu.fr. However, this link has become obsolete and data is available

from   alternate   link,
https://navigator.eumetsat.int/product/EO:EUM:DAT:METOP:IASIL2COX.

2.5.5 Fire counts from MODIS

Biomass burning is a significant source of CO in the atmosphere and to trace the open biomass burning, fire events detected by MODIS is used in the study. It is retrieved from both 4 μm brightness temperature and the difference between 4 and 11 μm brightness temperatures (Giglio et al., 2003). The MODIS fire channels are sensitive to the temperatures reaching about 450 and 400 K respectively. A detection confidence estimate, which ranges between 0 to 100%, is used to assign one of the three fire classes, low-confidence (0 to 30) fire, nominal-confidence fire (30 to 80), or high-confidence fire (80 to 100) to all fire pixels. The fire locations having detection confidence greater than 80% (confidence class defined as "high") are only considered in the analysis. These fire locations data was used to generate total counts in 1° x 1° grids. The fire event locations and counts from the MODIS instrument aboard Terra and Aqua spacecrafts (Giglio, 2015, MODIS Collection 6 Active Fire Product User's Guide) were obtained from ftp://fuoco.geog.umd.edu/modis/C6/mcd14ml/   or https://firms.modaps.eosdis.nasa.gov/download/. Version 6 data includes fire detection for offshore gas flaring over oceans and other large water bodies. Also, it has reduced incidence of false alarms caused by small forest clearings (Giglio, 2015, MODIS Collection 6 Active Fire Product User's Guide).

2.5.6 Tropospheric NO_2 from OMI

CO is emitted from anthropogenic activity like fossil fuel burning, during which significant emission of NO occurs which gets converted to NO_2. Tropospheric NO_2 is often used as a tracer for the anthropogenic activity. OMI aboard Aura satellite makes measurements of NO_2 along with O_3, at a ground resolution of 13km × 26km (near nadir) in a swath of 2600 km. Total NO_2 column is estimated from the satellite-retrieved radiance in the spectral range 402–465 nm using the Differential Optical Absorption Spectroscopy (DOAS) algorithm (Krotkov et al., 2017; Platt, 1994). Daily gridded (0.25° x 0.25°) tropospheric NO_2 data (Level-3 Version-3), filtered for good quality (i.e., sky conditions where cloud fraction is < 30%) retrievals are used in the study (https://disc.gsfc.nasa.gov/datasets/OMNO2d_003/summary).   The   data   can   be obtained   from https://acdisc.gesdisc.eosdis.nasa.gov/data/Aura_OMI_Level3/OMNO2d.003/   or https://search.earthdata.nasa.gov/search/. The tropospheric vertical column has the

precision of 35–60% over regions with a large contribution of the troposphere to the total column (Boersma et al., 2004).

2.5.7 CO emission data

In addition to fire count, CO emission from open biomass burning, CO emission flux from the monthly gridded (0.25° x 0.25°) CO fire emissions (van der Werf et al., 2017) were used in the study as obtained from Global Fire Emissions Database, version 4 (GFED4) from their website, https://www.globalfiredata.org/data.html. This emission includes emissions from all kinds of biomass burning, namely, (1) agricultural waste burning, (2) boreal forest fire (3) tropical forest fire (3) peat fires (4) temperate forest fire and (5) savanna, grassland, and shrubland fire. Based on the burned area and the emission factor (which depend on type of biomass), CO emission is estimated. Further details can be found in the van der Werf et al., 2017 and reference therein.

In addition, The MACCity data (Granier et al., 2011) of anthropogenic CO emission were utilised in the study. MACCity emission inventory is an extension of ACCMIP (Atmospheric Chemistry and Climate Model Intercomparison Project) under the projects of European Union, namely, MACC (Monitoring Atmospheric Composition and Climate) and CityZen. The gridded (0.5° x 0.5°) anthropogenic emissions of CO were obtained from ECCAD (Emissions of atmospheric Compounds and Compilation of Ancillary Data) website, http://eccad.aeris-data.fr/#DataPlace: OR https://eccad3.sedoo.fr/. The anthropogenic data of emission is divided in to 9 sectors, namely, (1) agricultural (animal, rice, soil) (2) agricultural waste burning (3) residential and commercial (4) energy (i.e., power plants, energy conversion, and extraction) (5) Industry (i.e., combustion and processing) (6) International shipping (7) Solvent (8) surface transportation (i.e., vehicular emission) (9) waste (i.e. emission from landfills, waste water and incineration). Total anthropogenic emission is the sum of all sectors.

2.5.8 Synoptic wind

In order to understand the role of horizontal as well vertical transport, synoptic scale wind (zonal wind—u, meridional wind—v, and vertical wind—w) from ERA-Interim reanalysis (ECMWF Re-Analysis; where ECMWF is the European Centre for Medium-Range Weather Forecasts) is utilised (Dee et al., 2011). The reanalysis products are based on many available data sources (satellite, radiosondes, aircraft, buoy data, stations, etc) and global assimilation provides a comprehensive picture of the atmospheric dynamics. ERA-Interim uses a fixed version of a numerical weather

prediction (NWP) system (IFS-Cy31r2) to produce reanalysed data (https://confluence.ecmwf.int/display/CKB/What+is+ERA-Interim). The system includes a 4-dimensional variational analysis (4D-Var) with a 12-hour analysis window. The assimilation fields are sampled twice during each window, to produce fields at 00, 06, 12 and 18 UT each day. The basic spatial resolution of ERA-Interim data is 0.75 degree (Dee et al., 2011). However, different resolution data used in the study is obtained by simple interpolation techniques. More details are available in Dee et al., (2011). The data is available at 37 vertical pressure levels (1000 to 1 hPa). Since the present study focuses on variations of surface and tropospheric CO, winds (u, v, and w) over pressure levels 1000–100 hPa obtained from ECMWF website, http://apps.ecmwf.int/datasets/data/interim-full-daily/levtype=sfc/ were utilised in the study.

2.5.9 Airmass back trajectories

The airmass back trajectory is the most probable trajectory or path of an air parcel would have travelled back in time in three dimensional space. In order to understand role of transport and to identify the regions from which airmass is getting transported, airmass back trajectories were obtained from HYSPLIT model. The HYSPLIT model is a system for computing simple air parcel trajectories, as well as complex atmospheric transport and dispersion simulations (https://www.arl.noaa.gov/hysplit/hysplit/). The HYSPLIT model has evolved initial version (Draxler and Taylor, 1982) to the recent HYSPLIT Version 4 (Rolph et al., 2017; Stein et al., 2015; Draxler and Hess, "description of the HYSPLIT_4 modeling system", 2018). In the Lagrangian model, the dispersion is computed following the particle, however, here the HYSPLIT model is used for simple trajectory calculation which is in fact advection of airmass in the atmosphere. The advection of a particle is computed independently using the meteorological data (u, v, w; three components of vector wind velocity), interpolated to the internal model grid. The advection of a particle is calculated from the mean three-dimensional velocity vectors for the initial-position r(t) and the first-guess position r'(t+Δt). The velocity vectors are linearly interpolated in both space and time. V is three dimensional wind velocity vector and Δt is the time step.

The first guess position is,

r'(t+Δt) = r(t) + V(r,t) Δt

and the final position is

r(t+Δt) = r(t) + 0.5 [V(r,t) + V(r',t+Δt)] Δt

The vector integration method (e.g. Kreyszig, 1968) is used for position calculation.

The error in the simulation of trajectories is primarily due to the errors in input meteorological data and from the numerical methods used in the calculation. In order to reduce uncertainties, an ensemble of trajectories is used in the present work.

The model can be run through the website (https://www.ready.noaa.gov/hypub-bin/trajtype.pl?runtype=archive) or computer based software. In this study, computer based HYSPLIT software having graphical user interface was downloaded from https://ready.arl.noaa.gov/HYSPLIT_hytrial.php and trajectories were simulated for various regions and study periods. It requires gridded four-dimensional (x, y, z, t) meteorological fields (reanalysis or forecast fields) from the weather prediction models. The Global Data Assimilation System (GDAS) is a Global Forecast System (GFS), the system of National Center for Environmental Prediction (NCEP) to assimilate the observations (surface observations, balloon data, wind profiler data, aircraft reports, buoy observations, radar observations, and satellite observations) into a gridded model space. The GDAS assimilated data of meteorological parameters at grid resolution of 1° × 1° was obtained from ftp://arlftp.arlhq.noaa.gov/pub/archives/gdas1. Note that since GDAS data at grid resolution 0.5° x 0.5° does not contain vertical velocity field and vertical velocity is critical for calculating backward trajectories (Su et al., 2015), GDAS data at grid resolution 1° x 1° containing vertical velocity field is used in the analysis. Also, topography data gridded at 0.5° x 0.5° was used for the trajectory simulation. A week or two weeks longer back trajectories, owing to the shorter and longer lifetime of CO in the lower and upper troposphere, are used in the analysis.

2.5.10 MACC reanalysis and CAMS forecast data

For comparison with the in-situ observations conducted as part of this study, and as supportive evidence for the explanation of the observed results, retrospective analysis (reanalysis) data on CO were used in the study. Monitoring Atmospheric Composition and Climate (MACC) reanalysis data is generated by assimilating satellite data into a global model and data assimilation system. This reanalysis provides fields of CO, O_3, NO_2, CHOCHO, aerosols, and GHGs globally for both the troposphere and the stratosphere at a horizontal resolution of about 80 km (Inness et al., 2013). Tropospheric CO values from the MACC reanalysis are on average 10–20% lower than routine observations through the troposphere, and have larger negative biases in the boundary layer at urban sites having by air pollution (Inness et al., 2013).

A global reanalysis model dataset, MACC reanalysis data were obtained at a horizontal resolution of 0.25° × 0.25° and time step of 3 hrs. MACC model consists of ECMWFs' (European Center for Medium range Weather Forecasting) Integrated Forecast System (IFS) coupled with the MOZART (Model for OZone and Related chemical Tracers)-3 chemistry transport model (115 species). More details of the MACC reanalysis can be found through its website (https://www.gmes-atmosphere.eu/oper info/macc reanalysis/) or from previous studies (e.g., Inness et al., 2015 and references therein). MOPITT V4 CO retrievals (day and night) were assimilated in the MACC reanalysis from 2003 to 2010. IASI CO retrievals were assimilated from April 2008 onwards.

The global CAMS system (http://www.copernicus.eu/main/atmosphere-monitoring) is built on the heritage of the EU-funded GEMS project (Hollingsworth et al., 2008) and a series of MACC projects at the ECMWF. Indeed, CAMS is an extension of MACC. Near Real Time (NRT) forecasts from CAMS provides a global reanalysis dataset of atmospheric composition since 2012. The data assimilation (Inness et al., 2013; Wagner et al., 2015) of satellite retrieval is able to successfully reduce the biases of the simulated CO fields (Gaudel et al., 2015). Near Real Time (NRT) forecasts from the CAMS available at a horizontal resolution of 0.25° × 0.25° at various pressure level has been used. The validation report of CAMS forecast can be found elsewhere, https://atmosphere.copernicus.eu/global-production-eqa-archive or https://atmosphere.copernicus.eu/user-support/validation/verification-global-services.

MACC data during the period of December 2008–January 2009 and CAMS data during the period, January–February 2018 were used.

2.6   Model description

In this study two models are used. A photochemical box model, namely NCAR's Master Mechanism (NCAR-MM) is utilised to understand the role of chemistry. The model simulates chemical evolution of an air parcel taking into account gas phase chemistry among ~2000 gases involving ~5000 reactions. No dynamical features (horizontal/vertical transport) are included in the model. A three dimensional regional chemistry transport model, namely, WRF-Chem is used to simulate the observations, inter-comparison with in-situ measurements and to delineate the role of anthropogenic emissions. The detail descriptions of both the models are given in Chapter - 6 along with the results obtained through modelling.

Chapter - 3

Seasonal distribution of CO over the Bay of Bengal

3.1   Introduction

As CO is primarily of anthropogenic origin, its distribution over the oceanic region is indicative of extent of the continental and human influence over the marine regions. In addition, CO being a precursor for tropospheric ozone through generation of hydroperoxyl radical, HO_2, its elevated mixing ratios under the continental influence would alter the chemistry of the region (Seinfeld and Pandis, 2006). Depending on the strength of continental emission sources and prevailing synoptic meteorological conditions, distribution and concentration levels varies. The experiments conducted over the marine environments adjacent to the Indian region have revealed considerable spatial heterogeneity in the distribution of trace gases and aerosols (Dickerson et al., 2002; Lal et al., 2006; Sahu and Lal, 2006; Sahu et al., 2006; Girach and Nair 2010). Lawrence and Lelieveld (2010) provided a detailed review of the outflow of trace gases and aerosols from South Asia to the surrounding marine regions. Transport of airmasses between the Indian subcontinent and the adjacent marine regions has strong seasonal dependence associated with the monsoonal circulation.

The marine environment of the Bay of Bengal (BoB), the largest bay in the world, is surrounded by landmasses on three sides, making it highly suitable to observe enhanced concentrations of trace species of continental origin. Further, seasonal changes in synoptic winds make this a unique region to study variations in trace species due to transport and en route photochemistry. Considering the aforementioned special characteristics of the BoB, as well as the considerable heterogeneity in the distribution of trace gases, in-situ measurements covering large areas are essential for investigating the distribution of pollutants and the controlling atmospheric processes.

Extensive in-situ measurements of surface CO over the BoB have been conducted in the various field campaigns, e.g., the winter phase of Integrated Campaign for Aerosols, gases, and Radiation Budget (W_ICARB) during 2009 and Continental Tropical Convergence Zone (CTCZ) experiment during monsoon season of 2009. In this chapter, the spatial and temporal variations of CO over the BoB during two contrasting seasons

(winter and summer monsoon) is analysed in detail and the effects of transport is discussed. This study utilised the ship-based in-situ measurements of CO mixing ratios carried out as part of two field campaigns, W_ICARB and CTCZ, supplemented by MOPITT observations and MACC reanalysis data. To complete the seasonal picture of CO distribution during pre-monsoon and post-monsoon seasons, the satellite-based MOPITT observations data have been utilised, supported by the in-situ measured CO mixing ratios from Srivastava et al., 2012 and Mallik et al., 2013, respectively. Transport pathways and source regions were identified for the observed variation of surface CO. MOPITT retrieved surface CO and MACC reanalysis is compared with in-situ measured surface CO. The distributions of upper tropospheric CO is analysed using the MOPITT retrievals. The satellite data were filtered, prior to its use, as discussed in section 2.4.4. MOPITT CO retrievals (level-3 V7-TIR daytime retrievals) were filtered for the degree of freedom>1 and uncertainty <30 % (10% in case of columnar CO). MODIS fire events were filtered for the fire detection confidence >80%. OMI retrieved NO_2 were filtered cloud fraction <30%. Transport pathways were identified based on the back trajectory simulation using HYSPLIT model. Considering the lifetime of CO in the lower troposphere, it is reasonable to use seven-day back-trajectory. However, in this study, temporal extend is limited to five-days because under the prevailing wind conditions back-trajectories crossed/reached the source region (i.e., region having elevated CO levels) within five days.

The CO mixing ratios show large spatial variations over the BoB which are season-dependent. Oceanic sources of CO contribute only about 5% of that produced through burning of fossil fuel (Stubbins et al., 2006). Thus, the significant CO levels and their variations are mainly due to transport from nearby continental regions where stronger sources of CO exist. Different patterns of synoptic winds prevail during various seasons, bringing airmasses of different origins, leading to distinct spatial distributions of CO.

3.2 Wintertime CO distribution over the Bay of Bengal

3.2.1 The Cruise tracks and background conditions

The W_ICARB experiment was carried out during winter season (December 27, 2008 to January 30, 2009) under the Geosphere Biosphere Programme of the Indian Space Research Organization (ISRO-GBP) to study the outflow characteristics from the Indo-Gangetic Plains (IGP) and the East Asia. As a part of W_ICARB, measurements of CO mixing ratio were carried out over the BoB aboard the Oceanic Research Vessel (ORV)

Sagar Kanya along the cruise track (cruise number SK 254) shown in figure 3.1. The ship started sailing from Chennai (80.3° E, 13.1° N) on December 27, 2008 and returned to Cochin (76.3° E, 10.1° N) on 30 January, 2009 after completing 34 days of successful expedition. It is to be noted that for the first time in-situ measurement of trace gases were carried out over eastern part of the BoB. The arrows in figure 3.1 show the mean synoptic wind flow pattern at 925 hPa as obtained from ERA-interim reanalysis (See section 2.5.8 for details on ERA-Interim). In general, calm northerlies prevailed over the northern BoB (north of ~16°N) and strong north-easterlies prevailed over the southern BoB.
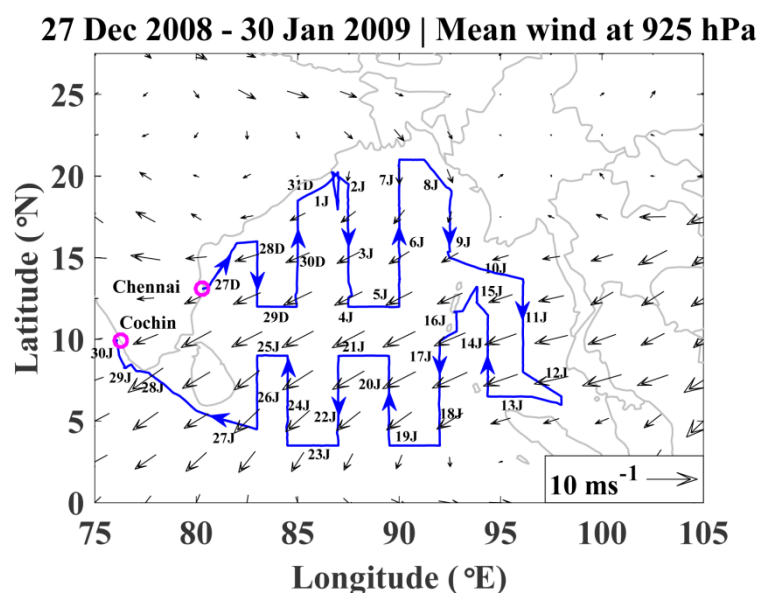
Figure 3.1: Cruise track (continuous blue line) of the Research Vessel Sagar Kanya along with synoptic winds at 925 hPa (black arrows) during W_ICARB campaign (winter season). The arrows marked on the track show the direction of the ship. The dates corresponding to approximate ship positions are marked along the track. The start and end positions of the cruise are shown by the magenta circles. In date labels, D represents December month and J represents January month.

The measurements of surface CO mixing ratios were made using an online CO analyzer (Model CO12 Module, Environnement S.A, France) (See section 2 for details on principle of operation, calibration, etc). Air was drawn from a height of approximately 15 metre above the sea surface through a Teflon tube. The analyser was calibrated periodically on-board ship using a custom-made calibrator.

Surface CO mixing ratio measured over the cruise track during W_ICARB campaign is presented by coloured circles in the figure 3.2 along with the colour scale shown by the side. The CO mixing ratio varied in the ranges of 80–480 ppbv (average of 240±90ppbv) during winter season (figure 3.2) showing the spatial heterogeneity in the distribution of CO. A few data points which were below the detection limit of the

instrument are discarded from the analysis. The higher surface CO mixing ratios of ~302±68 ppbv (range: 140–450 ppbv) was observed northern BoB (81–91° E; 16–21.5° N) which was under the influence of northerlies and hence the outflow from the IGP region. The highest CO values ~340±89 (range: 93–480 ppbv) were observed over the eastern BoB (94–98° E; 6–15° N) with the maximum value being 480 ppbv. The lowest mixing ratios ~168±37 ppbv (range: 60–298 ppbv) were observed over southern BoB (82–89° E; 3–11° N).
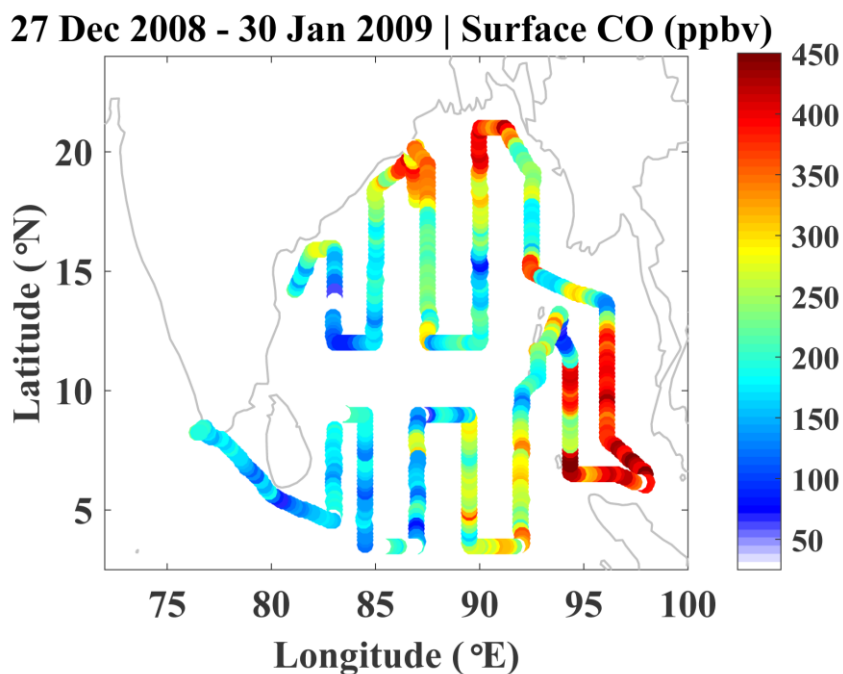
Figure 3.2: Spatial variation of surface CO mixing ratios along the cruise track during winter corresponding to the W_ICARB campaign (December 2008–January 2009).

In order to find the source regions and causative mechanisms for the observed spatio-temporal variability, back-trajectory analysis is carried out in conjunction with MOPITT retrieved CO and MODIS derived fire event locations. Prior to the use of MOPITT retrieved CO, it is necessary to carry out the comparison with in-situ measurements.

3.2.2 Comparison of in-situ measurements and MPOITT retrievals

As described in the Chapter-2, the sensitivity of MOPITT is smaller for the lower-tropospheric CO as compared to the mid and upper tropospheric CO. Deeter et al., 2007 showed that the normalized averaging kernels give sensitivity to CO in the lower troposphere also and Kar et al., 2008 has shown that the sensitivity of MOPITT in the lower troposphere is sufficient to detect the surface sources during winter. In the present study, the in-situ measured surface CO over BoB were compared with the Level-

3 (1° x 1° gridded) surface retrievals (algorithm version V7-TIR) of MOPITT. The co-located (in terms of time and space) MOPITT surface CO mixing ratios were obtained on daily basis corresponding to the time and location of in-situ measurements. For the comparison, the in-situ surface data were gridded to MOPITT grid size and the data points co-located in terms of time (day or night) and space were compared.

Figure 3.3a shows the comparison of MOPITT retrieved surface CO with the surface CO measured during W_ICARB (winter season). The linear regression analysis shows correlation coefficient of 0.7 (level of significance $p < 0.0001$) and slope of 0.5. Two points (so-called points of discrepancy) shown by hollow circles remained away from the linearity in the regression analysis. This comparison is extended utilising the available in-situ measurements over the BoB carried out during various campaigns as shown in figure 3.3b. The in-situ measured surface CO corresponding to the ICARB-2006, BOBPS-2002, BOBEX-I-2001, BOBEX-II-2003, and a campaign during 2010 were adopted from Srivastava et al., 2012; Sahu et al., 2006; Lal et al., 2006; 2007; and Mallik et al., 2013, respectively. Different colours represent the data points corresponding to the different campaigns. It is to be noted that the number of data points and the spatial coverage are significantly high during W_ICARB. While considering more observations for the comparison, the correlation coefficient and slope remains more or less same or increases slightly. However, one to one match between MOPITT surface CO and in-situ CO is not expected due to following reasons. (1) MOPITT retrievals have limited sensitivity for boundary layer/surface CO. (2) In-situ measurements are the point measurements which are being compared with 1° x 1° gridded satellite retrievals. In nutshell, the fairly good correlation between MOPITT surface CO and in-situ surface CO shows the potential of MOPITT surface retrievals and it can be used to identify large scale variation and source regions of CO.

In order to examine the possible causes of the deviation of those two/few points of discrepancy (hollow circles in figure 3.3), an analysis of surface-level averaging kernels of V7 was carried out. The averaging kernels corresponding to these points were found to be lower compared to those of other points (~0.6). But, it was also noted that for a few other observations which compared well with the MOPITT retrievals, the corresponding averaging kernels remained on the lower side. Thus, the deviation of the MOPITT retrieved values from the in-situ measurements may not be fully attributed to differences in the averaging kernels. As mention before, for the surface level CO retrievals, MOPITT has lower sensitivity as compared to mid and upper troposphere and hence, the surface level retrievals could have significant dependency on the a priori

information, used for the retrievals. Thus, the discrepancy in MOPITT retrieved values could be partly due to the inadequacy of a priori information.
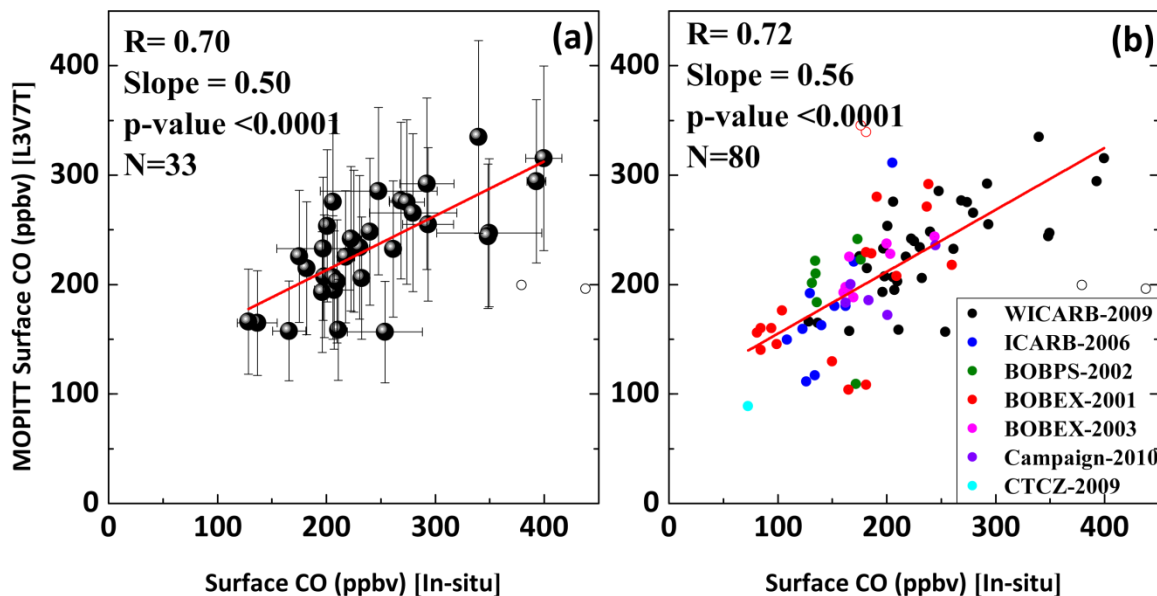
Figure 3.3: (a) scatter plot between MOPITT retrieved surface CO and in-situ surface CO during W_ICARB campaign (winter) over the BoB. The y-error bar shows the MOPITT retrieval uncertainty and x-error bar shows the standard deviation in the in-situ surface CO. (b) is same as (a) but including the data points corresponding to the various campaigns. The red line represents the linear regression fit considering the weighing by MOPITT retrieval uncertainty. The points shown by the hollow circles are not included in the fit.

3.2.3 Impact of long-range transport: Airmass back-trajectory analysis

HYSPLIT model was used to simulate five-days airmass back trajectories arriving at 500 m (a height that falls within the marine atmospheric boundary layer) above the measurement locations. As shown in the figure 3.4, trajectories are colour-coded to show the altitude variations of the air parcels along their path. The discussion of trajectory analysis is carried out in conjunction with MOPITT retrieved surface CO data and the fire events, indicative of the open biomass burning. Figure 3.5a shows the monthly mean surface CO distribution as obtained from MOPITT during January representing the winter season. The magenta dots in figure 3.5b represent the location of monthly fire events as obtained from MODIS (Aqua and Terra) during the study period.

Figure 3.4 shows three groups of airmass back trajectories corresponding to three kinds of airmasses, (1) IGP, (2) southeast Asian, and (3) marine airmasses observed during W_ICARB campaign. Figure 3.4a represents the back-trajectories reaching the cruise track over northern BoB. These trajectories originate from the

eastern IGP (Bangladesh/West Bengal/Bihaar) region. As seen in satellite map (figure 3.5a), the surface CO is high over these regions, being around 300–400 ppbv. In addition to fossil fuel burning, the biomass burning over eastern IGP contribute significantly for the enhanced CO levels. The higher concentration (1.9±0.6 ugm^{-3}) of Potassium—a trace for biomass burning (Andreae, 1983)— over the northern BoB during the same cruise (Aryasree et al., 2015) provides evidence for the presence of biomass burning activity over the eastern IGP region. The biomass burning activity is mainly for the heating purpose during winter season and as it is not open-burning, it is not seen over the eastern IGP region in MODIS detected fire events. Transport of CO from this region causes the higher level of surface CO over northern BoB. The surface CO mixing ratios over northern BoB are slightly lower than those seen over the eastern IGP due to dilution and mixing with cleaner marine airmass.
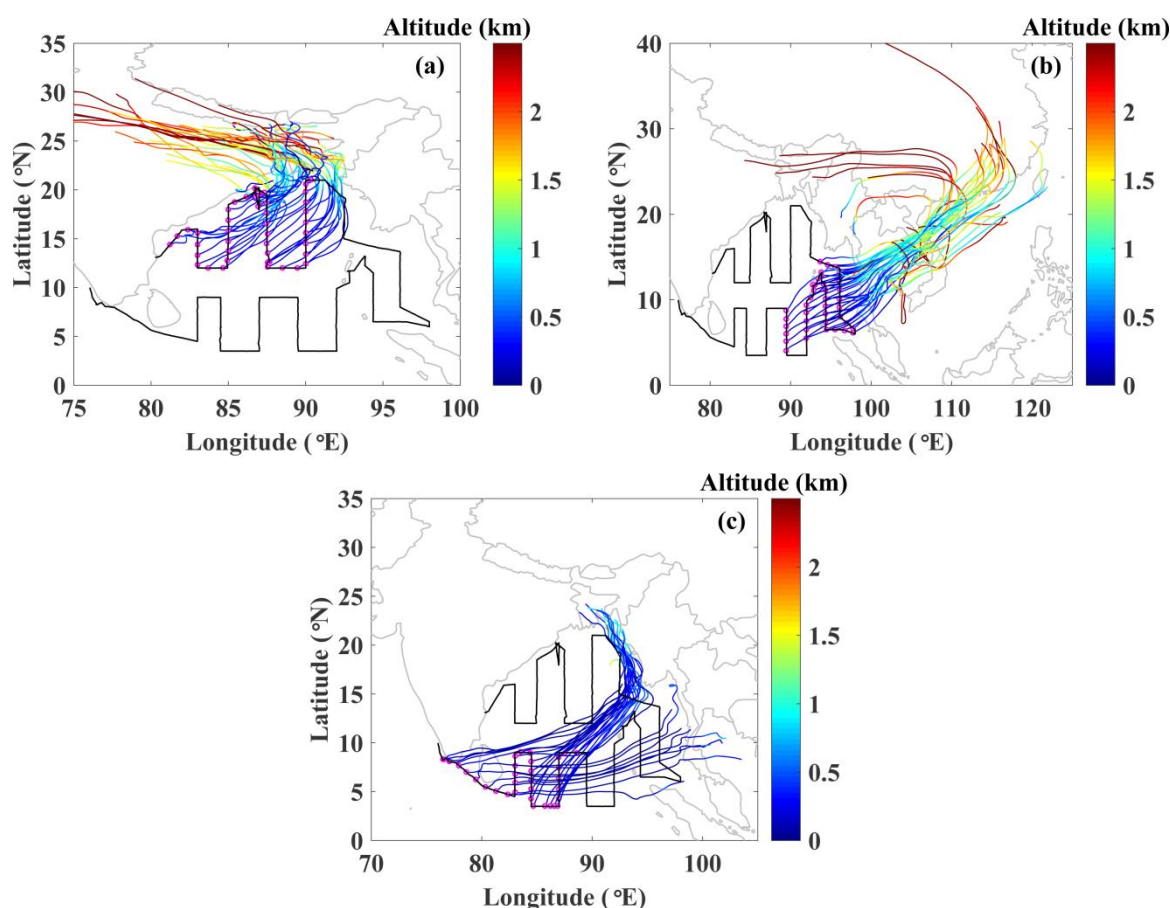
Figure 3.4: Five-day airmass back-trajectories ending at the measurement locations (small magenta circles) grouped for corresponding airmasses from (a) IGP (b) southeast Asia, and (c) marine region of BoB during winter. The colour scale shows the height (in km, agl) of the air parcel along the trajectory.

Figure 3.4b represents the back-trajectories corresponding to the measurements over eastern BoB, where surface CO is higher than that over northern BoB. It is to be

noted that, due to higher wind speed over southeast region, the airmass traversed more than ~15 degrees in longitude during the period of five-days as indicated by the back-trajectories. Trajectories are from Southeast Asian regions (i.e., China, Thailand, and Cambodia) where surface (as well as columnar) CO values are extremely high (500–700 ppbv) as can be seen from figure 3.5a. The open-biomass burning over Southeast Asia is very high as shown in the figure 3.5b. The CO emitted from biomass burning and anthropogenic activities over Southeast Asia gets transported over to the eastern BoB causing higher levels over the region.
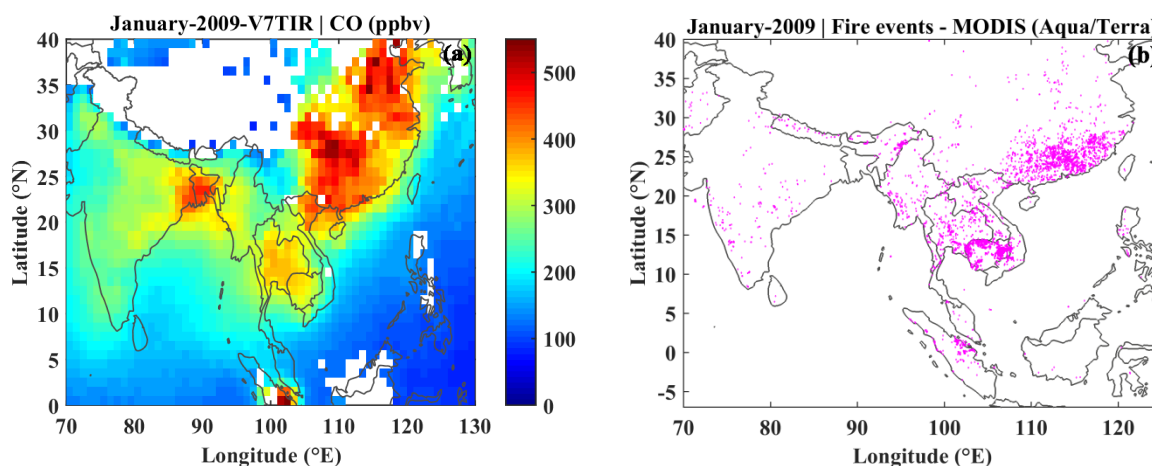
Figure 3.5: (a) Distribution of MOPITT retrieved monthly mean surface CO during January 2009 representing the winter seasons. (b) Fire events (magenta dots) as detected by MODIS (Terra and Aqua) during January 2009.

Figure 3.4c represents the back-trajectories corresponding to the measurements over southern BoB along the cruise track. Originating over northern/eastern part of BoB, these trajectories spent most of the time over the marine region of the BoB. As seen in the figure 3.4c, the airmass has travelled long marine path, where there is no strong source of CO, and subsequent dispersion/removal would cause relatively lower mixing ratios over southern BoB.

The observed variations of surface CO are investigated by calculating the fractional residence time of airmasses over the marine region of BoB, using simulated five-day back trajectories shown in figure 3.4. Figure 3.6a shows the variations of CO along with percentage residence time of airmass over the oceanic region of BoB during the W_ICARB experiment. The percentage residence time of airmasses over the BoB is estimated as the ratio of residence time over the BoB to the total time spent by the trajectory in five days. As seen in figure 3.6b, the anti-correlation between the estimated residence times and surface CO is R = -0.49 (p<0.0001) which shows that the longer the airmass resides over oceanic region, CO mixing ratios reduces or vice-versa. This could

be due to following reasons. (1) When airmass resides longer over marine region, it would undergo mixing (e.g., vertical mixing in the marine boundary layer) processes leading to the dilution in mixing ratios. (2) Over marine region where stronger source of CO does not exist, the destruction of CO through OH radical is dominating chemical process. Under the longer residence time, chemical destruction could reduce CO mixing ratios.
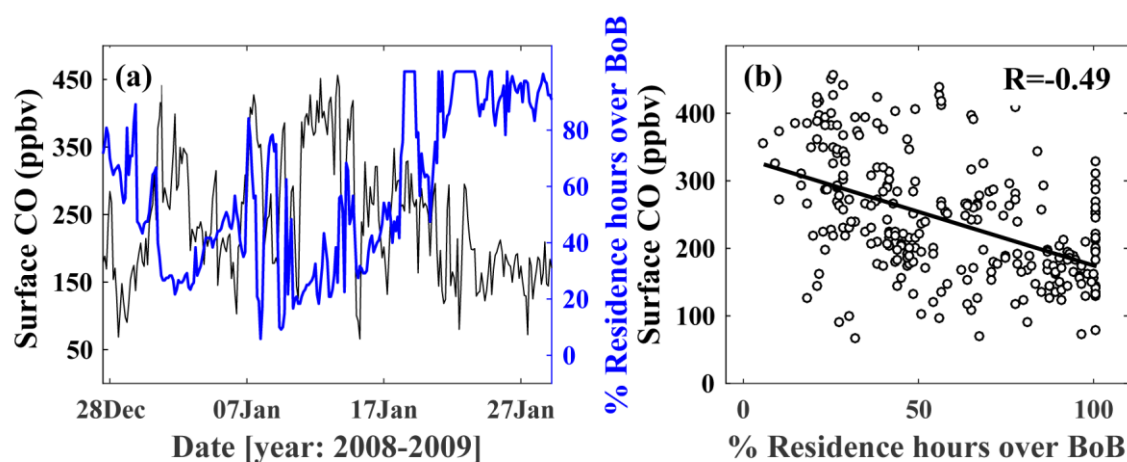
Figure 3.6: (a) Spatio-temporal variations of surface CO (black line) and percentage residence time airmass over BoB (blue line) along the cruise track during the W_ICARB campaign. (b) Scatter plot between surface CO and percentage residence time over BoB corresponding to (a). The black line represents the linear regression fit.

To analyse the role of transport further, MACC reanalysis data is utilised in conjunction with HYSPLIT airmass back-trajectories. Prior to the analysis with MACC data, it is validated for the study region by carrying out the inter-comparison with in-situ observations.

A comparison is made between MACC simulated CO at 1000 hPa with the in-situ measured surface CO over the BoB. Figure 3.7a shows variations of in-situ measurements of surface CO along with MACC reanalysis CO. The MACC model captures the spatio-temporal variations in CO reasonably well (correlation coefficient = 0.6; figure 3.7b), although the model slightly overestimates the absolute CO levels by ∼ 10 ppbv (mean bias = mean MACC simulated CO minus mean in-situ measured CO). This comparison shows that MACC reanalysis captures the surface CO variability fairly well and it can be further utilised for broader inferences. MACC reanalysis data is further utilised in conjunction with airmass back trajectories to locate the source regions of CO contributing to the observed variations over the BoB. An interpolation of MACC gridded data is carried out in space (latitude, longitude and altitude) and time along the airmass back trajectories and trajectories (figure 3.8) are color coded showing CO mixing ratio.
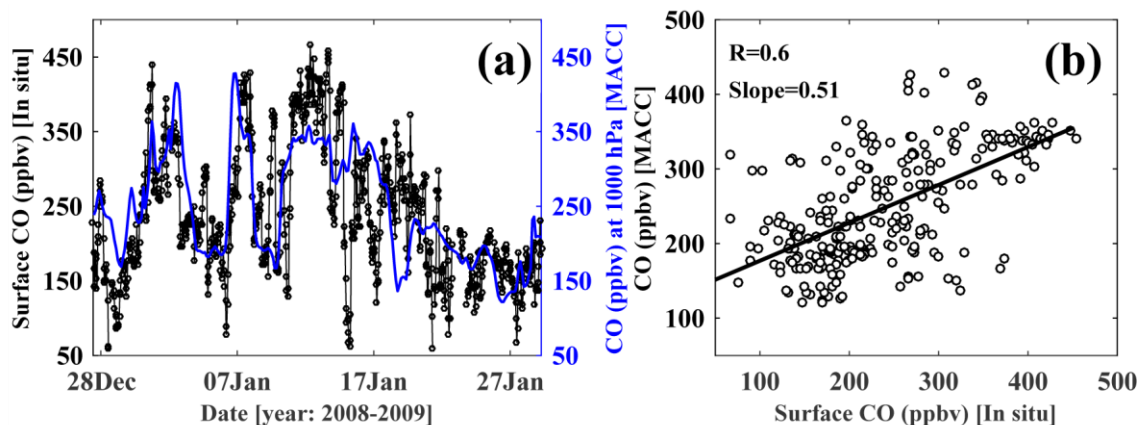
Figure 3.7: (a) A comparison of surface CO variations along the cruise track from MACC reanalysis and in-situ observations. (b) Scatter-plot between collocated observations and MACC CO over the BoB corresponding to (a). A linear regression fit is shown as a black line.
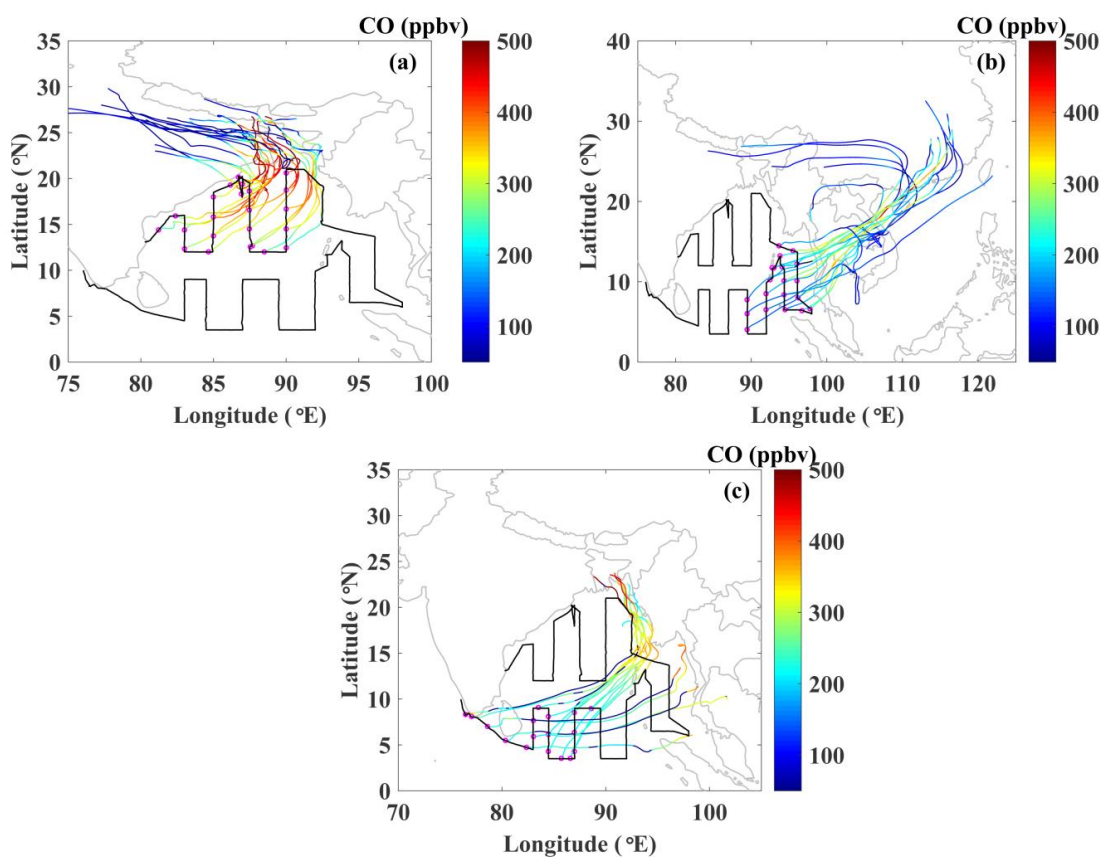
Figure 3.8: Same as figure 3.4 (back-trajectories) but color shows the CO mixing ratio along trajectory as obtained from MACC.

The higher CO mixing ratios in IGP airmasses over northern BoB is mainly contributed from the Bangladesh/coastal parts of eastern-IGP regions as airmasses got enriched in terms of CO over this region. As seen in figure 3.8b, CO mixing ratios along trajectories enhanced mainly over the region of Thailand, and Cambodia (also, contributions from coastal region of China) before reaching eastern BoB. Biomass

burning over these regions would have contributed significantly to the higher surface CO mixing ratios over eastern BoB. Figure 3.8c shows that airmass got enriched in CO near to Myanmar region but due to long residence time over BoB and subsequent mixing process, dilution occurs which is clearly seen along the trajectories reaching the southern BoB.

3.2.4 Hot spot of surface CO over northeast-BoB during winter: impact of fires and anthropogenic activities

This is a case study which reveals that a small channel/transport pathway which opens up during winter enables transport of gases and aerosols from the valley region of Myanmar to the marine environment of BoB. One striking feature seen in the distribution of CO over the cruise track is that, over the north eastern leg, small patch of significantly high mixing ratios (300–400 ppbv, in orange colour) sandwiched between the low values (100–250 ppbv, in violet and green) is observed as zoomed in the figure 3.9a. In this context, the airmass back-trajectories reaching this region at 200 m above ground level obtained using HYSPLIT model were examined. Figure 3.9a shows the back trajectories over northeast region of BoB corresponding to relatively lower CO values, as shown along the cruise track. Figure 3.9b is same as 3.9a but for the relatively higher CO. From figure 3.9a, it is clear that some trajectories were confined to near-by region (because of hilly region of Myanmar as shown in the digital elevation map in figure 3.9c as obtained from National Geophysical Data Center, NOAA) where as some originate from northwest region. Both these regions are unpolluted regions and hence resulted in relatively low CO mixing ratios. But the group of trajectories ending at the high CO region (figure 3.9b) originated from the valley region of Myanmar (figure 3.9c) where anthropogenic activities as well as biomass burning prevailed which produce large amounts of CO, NO_2, and other trace gases (Streets et al., 2003). From daily fire events detected by MODIS (Aqua), fire counts were obtained by summing up over 0.25° × 0.25° grid size spanning over 5 days corresponding to the period of back-trajectories and plotted in figure 3.9b. This shows that CO emitted from biomass burning over valley region of Myanmar got transported to BoB as seen by back-trajectories causing high CO mixing ratios over the region. The anthropogenic activity like traffic and industrial emission also contribute significantly to the tropospheric NO_2, and hence tropospheric NO_2 is used as a tracer for anthropogenic activity.
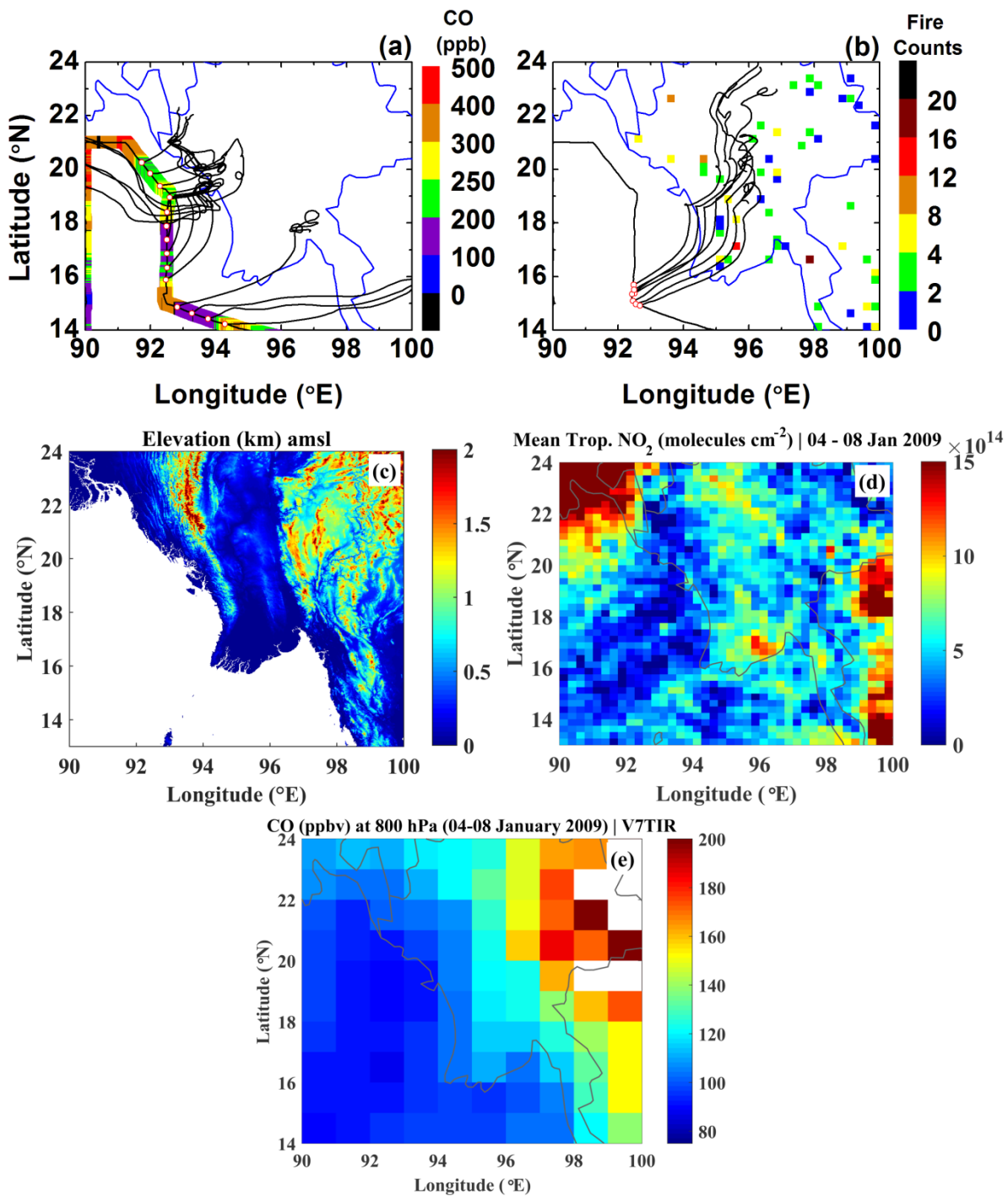
Figure 3.9: (a) Five-days aimass back trajectories arriving at 200m above surface for the regions where relatively low CO mixing ratios were observed along with distribution of CO along the cruise track, (b) same for regions where high CO mixing ratios were observed along with the MODIS (Aqua) retrieved fire counts summed over 0.25 degree, (c) Digital elevation map (in meters above mean sea level) of Myanmar region, (d) Monthly averaged (January 2009) tropospheric NO_2 as obtained from OMI. (e) Spatial distribution of CO mixing ratio at 800 hPa as obtained from MOPITT retrievals.

Figure 3.9d shows the monthly mean tropospheric NO₂ over Myanmar region. It is clearly seen that over valley region of Myanmar, tropospheric NO₂ was high which indicate the higher anthropogenic activity and hence emission of CO also. Figure 3.9e shows the CO at 800 hPa averaged over 04 to 08 January 2009 which confirms the higher concentration over Myanmar region (east of 95° E). Thus, in addition to biomass burning as indicated by fire counts, emission of CO due to anthropogenic activity over Myanmar region caused a localized hot spot in near-surface CO over NE-BoB.

This case study is an example of sharp changes in the trace gas concentrations with the changes in airmass. A strong biomass burning event or some anthropogenic activity over Myanmar region occurring during winter can significantly change the concentration of trace gases over BoB affecting the regional chemistry. The airmass getting transported over BoB would have different trace gases with different levels than those prevailed over BoB. This airmass, getting mixed with prevailed airmass of BoB, could lead to different chemical reactions as well as could bring the scatter/deviations in the observation of other trace gases.

3.2.5 Latitudinal variations

The winds over the northern BoB are mostly northerly/north-westerly during winter season. The back-trajectories show that CO gets transported mainly from the eastern parts of IGP. The north to south gradient provides information on the combined effects of chemical transformation and dispersion of these gases over this region. Surface CO measurements corresponding to the latitudinal legs (longitude sector 87.5° E and 90.0° E) were binned to 1° latitude; and the latitudinal variation estimated. Using the mean values weighed with standard deviation latitudinal gradient is estimated to be 41 ppbv degree^{-1} over northern BoB (latitude: 15–22° N) as shown in the figure 3.10. CO gradients obtained in this study are compared with previously reported values over the BoB during different study periods as shown in the table 3.1.

The latitudinal gradient in CO (~41 ppbv degree^{-1}) observed in the present study is significantly higher as compared with previous observations. This could be attributed to the spatial and temporal heterogeneity in CO concentrations over the BoB which is under the influence of IGP airmass during winter season. It is also to be noted that the estimated gradients corresponds to the available measurements over the BoB and not over the northern part of BoB alone and not for the same season as evident from the table 3.1.
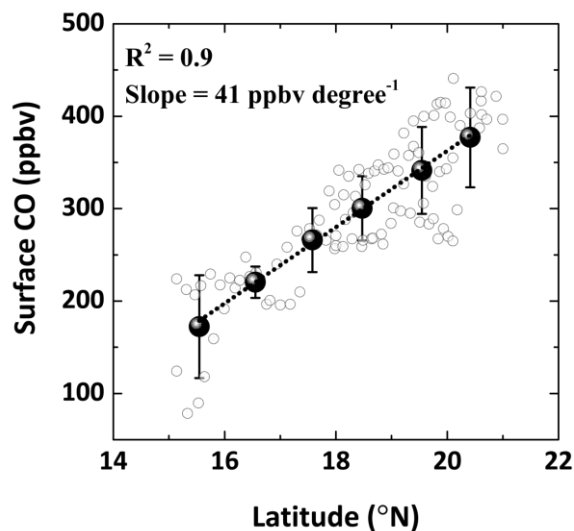
Figure 3.10: Latitudinal variation of mean surface CO over northern BoB (latitude>15N) considering the measurements over two latitudinal legs along 87.5° E and 90.0° E during winter (W_ICARB campaign).

Table 3.1: Latitudinal gradients in surface CO over the BoB during different seasons.

Study period	Campaign	Region over the BoB	CO Latitudinal gradient (ppbv degree^{-1})	Reference
14 September–12 October, 2002	BOBPS-2002	6–21° N, 80–89 E	4.2	Sahu et al., 2006
March 17–May 11 2006	ICARB-2006	12–22° N, 82–95° E	9.9	Srivastava et al., 2012
19–28 February 2003	BOBEX-II, 2003	6–20° N; 80–87° E	10	Lal et al., 2007
14–23 March, 2001	BOBEX-I, 2001	10–22° N, 80–90° E	15	Lal et al., 2006
28 October–17 November 2010	–	7–18° N, 82–91° E	16.5	Mallik et al., 2013
16 July–17 August 2009	CTCZ-2009	12–22° N, 80–91° E	No significant gradient	Present study
27 December 2008–30 January 2009	W_ICARB-2009	15–21° N; 86–91° E	41	Present study

3.2.6 Columnar CO over the BoB
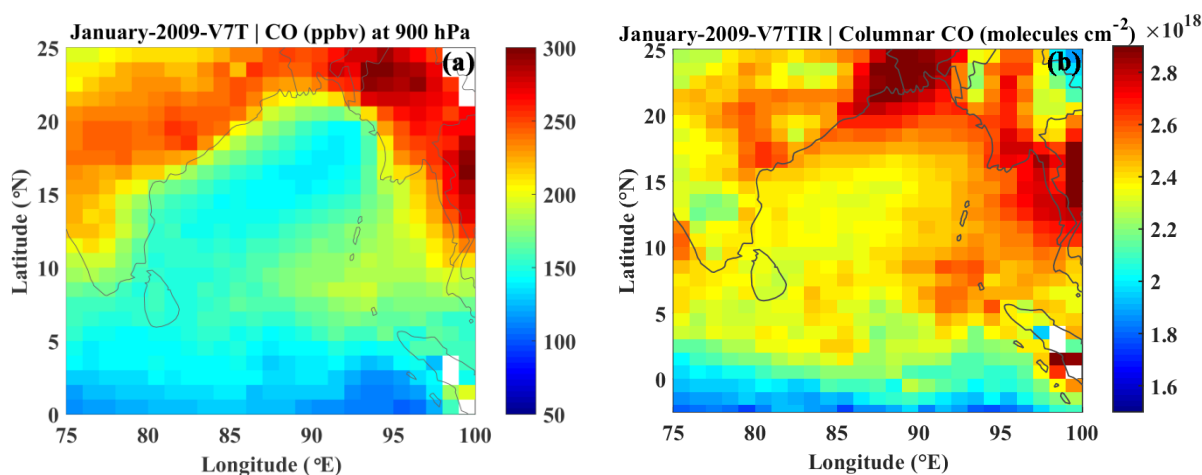
Figure 3.11: CO at 900 hPa (a) and columnar CO (b) during January 2009 over the BoB.

Figure 3.11a and b show the monthly mean spatial distribution of CO at 900 hPa (DOF>1, Uncertainty<30%) and column CO (DOF>1, Uncertainty<10%) over BoB during January 2009 as obtained from MOPITT retrievals. The retrieval product at 900 hPa corresponds to the mean volume mixing ratio in the layer between the 900 and 800 hPa (MOPITT Product User's Guide by Merritt N. Deeter). Examination of above figures shows that the spatial distributions of surface and columnar CO are similar over northern and eastern BoB. However, significant amount of columnar CO is seen over the southern BoB which is comparable or slightly lower (~15%) as compared to that over eastern BoB. The comparable columnar CO along with the low surface CO over southern BoB is an indication of the presence of higher mixing ratios over high altitude region. In other words, the altitudinal distribution of CO was not similar over the entire BoB. In this context, the vertical profiles of CO were examined and discussed in the following section.

While MOPITT surface retrievals of CO is validated against the in-situ measurements, in the absence of in-situ measured vertical profile of CO, the vertical profile of CO from MOPITT is compared with that of TES retrievals. This is to ensure that broad features obtained by MOPITT are consistent.

Over the three different regions of the BoB, where in-situ measurements are available, the altitude profiles of CO during January 2009 (W_ICARB) from MOPITT and TES were also examined. Exactly co-located profiles were not available and hence profiles were chosen for nearest locations over northern BoB (figure 3.12a), eastern-BoB (figure 3.12b) and southern BoB (figure 3.12c) where closeby measurements are available. There is good agreement among CO profiles from MOPITT and TES. However,

a detailed inter-comparison between MOPITT and TES profiles is not attempted in this study since the measurements are not exactly co-located and the equator crossing times of the two satellites are not coinciding.
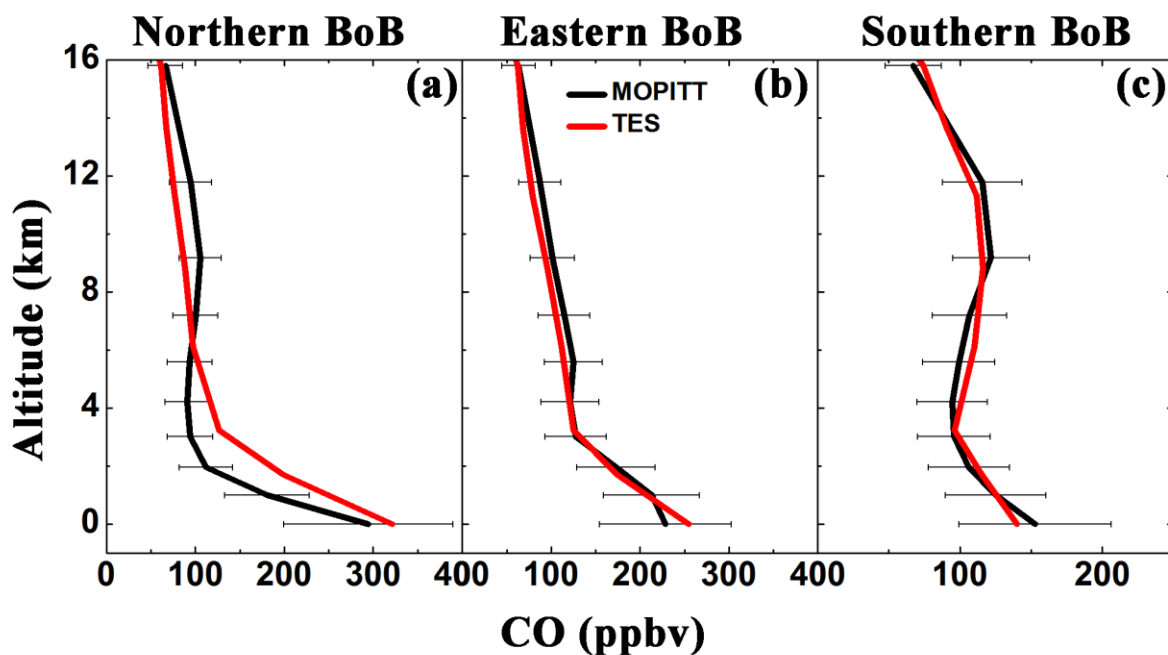
Figure 3.12: Comparison of CO profiles from MOPITT and TES during January 2009 over northern BoB (a), eastern BoB (b) and southern BoB (c). The x-error bar shows the uncertainty in the respective profile.

All the profiles showed sharp decrease of CO mixing ratio with altitude up to ~3 km (~700 hPa). Over the southern BoB, in the altitude range 400–200 hPa (~ 5 to 12 km), CO mixing ratios of about 125 ppbv (figure 3.12c) were observed which are comparable to those at/near the surface. On the other hand, over other two regions (northern and eastern BoB), the near-surface values were ~2–3 times higher than that around ~ 300 hPa. This could be one of the reasons for comparable column CO over southern region, while surface CO remaining low as seen in the figures 3.2 and 3.5a.

After gaining the confidence of reasonableness of MOPITT retrieved vertical profiles of CO, three dimensional distribution of CO over the BoB is addressed in the following sections.

3.2.7 Longitude-latitude-altitude distribution of CO over BoB

In order to investigate the vertical distribution of CO over the entire BoB, the distribution of monthly mean CO as obtained from MOPITT for January 2009 is shown in figure 3.13. The altitude-latitude-longitude variations in the CO mixing ratio can be seen more clearly in the latitude slices (at 83° and 90° E longitude representing western and

eastern BoB) and longitude slices (at 5° and 18° N latitude representing northern and southern BoB) the presented in figure 3.13a and b respectively. Along with this, the spatial distribution of CO specifically at the 900 and 300 hPa pressure levels (representing lower and upper troposphere) are also presented (figure 3.13c). To have better insight, the upper-tropospheric distribution of CO (at 300 hPa) is shown in figure 3.13d on the enlarged scale, however, it is the same as CO layer shown in 3.13c.
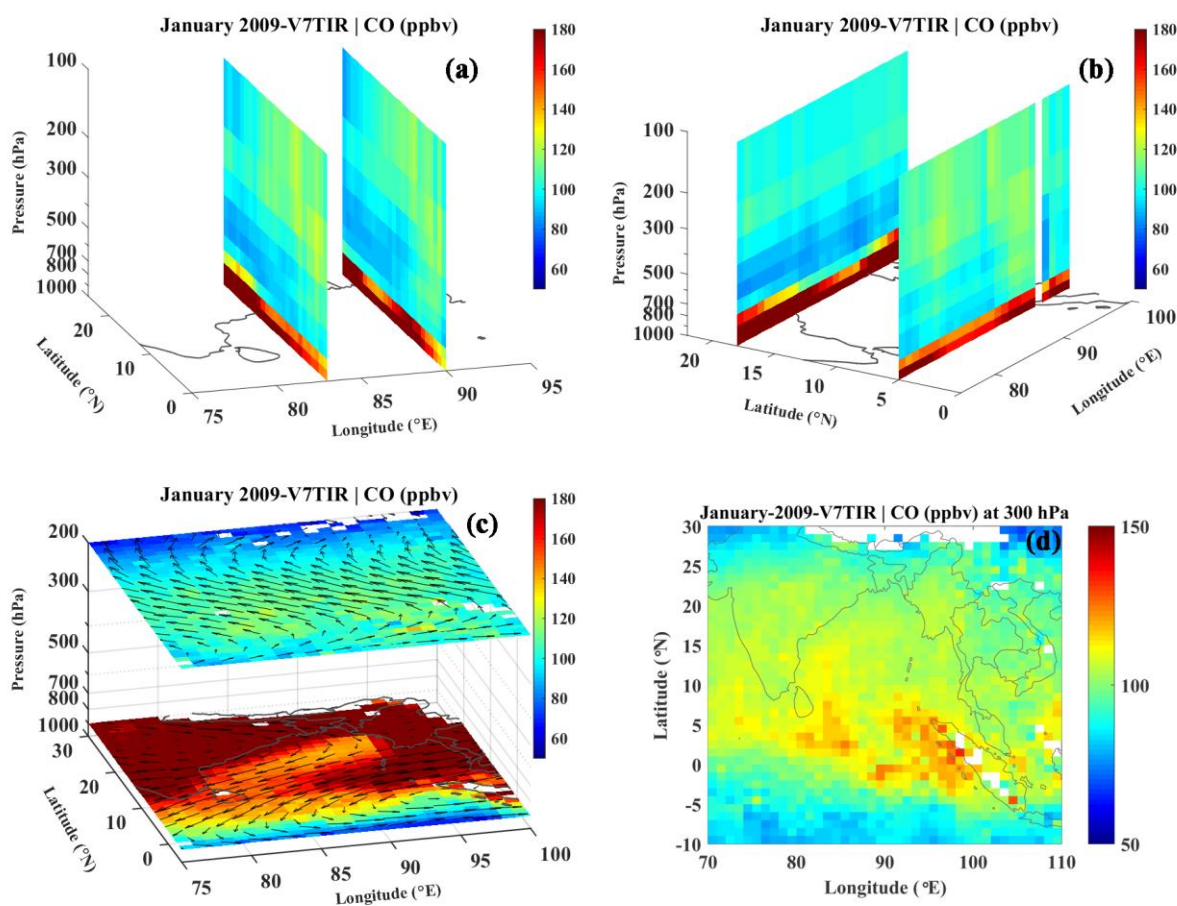
Figure 3.13: (a-b) latitude slices (at 83° and 90° E longitude representing western and eastern BoB), longitude slices (at 5° and 18° N latitude representing northern and southern BoB), and (c) layers (at 900 and 300 hPa representing lower and upper troposphere) of mean CO over the BoB during winter season (January 2009). The mean synoptic wind is superimposed on the layers of CO (900 and 300 hPa). Figure (d) is same as shown CO layer at 300 hPa in (c) but on the enlarged scale.

The most prominent features as observed in the above figures are the following. (1) The northward increase in CO mixing ratio at surface level and lower altitudes (< 3km) is seen over the entire BoB (a positive latitudinal gradient towards north), irrespective of longitude (figure 3.13a, b and c). (2) Over northern BoB (latitude >15° N), where surface as well as column CO showed high mixing ratios, the altitude profiles showed significantly high CO levels close to surface compared to that at higher altitudes

(figure 3.12a and 3.13b). (3) The upper tropospheric CO mixing ratio (at 300–200 hPa) showed a southward increase/negative latitudinal gradient unlike at the lower altitudes (figure 3.13a and d), where the gradient was positive. (4) The higher mixing ratios centred around 9–12 km (300–200 hPa, figure 3.12c and 3.13a) is more prominent in the southern latitudes (< 10° N). Over southern-BoB/equatorial Indian Ocean, the upper tropospheric CO was as high as 125–140 ppbv which is comparable to those measured near to the surface over southern-BoB as seen in figure 3.13d.
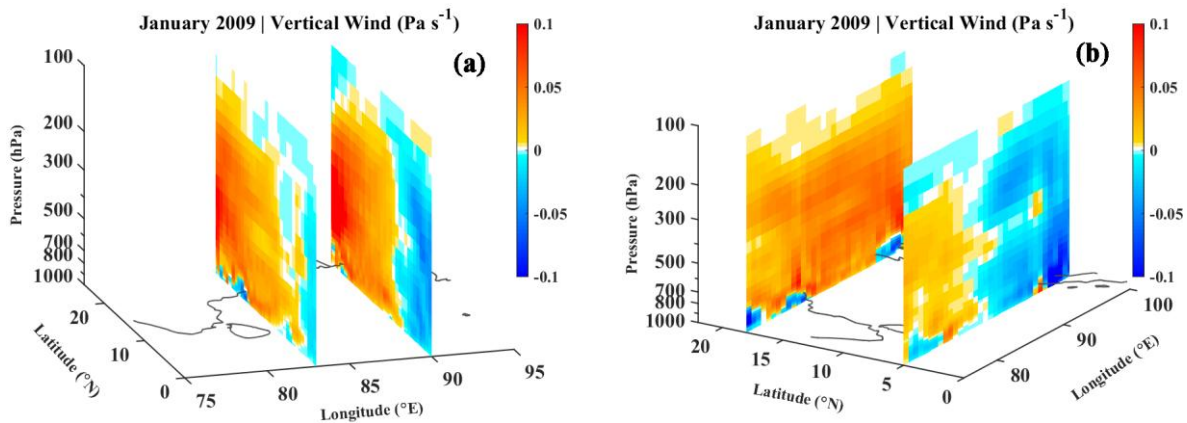
Figure 3.14: (a-b) latitude slices (at 83° and 90° E longitude representing western and eastern BoB) and longitude slices (at 5° and 18° N latitude representing northern and southern BoB) of mean vertical wind over the BoB during winter season (January 2009).

The dominant sources of CO being situated at ground, one of the causative mechanisms for the high altitude CO layer could be vertical updrafts and consequent lifting of airmass to higher altitudes. In this context, the presence of vertical transport was examined in terms of the vertical winds during this period. Figure 3.14 show the latitude/longitude slices of monthly averaged vertical wind velocity (hPa/s) for January 2009 for the same latitude/longitude slices as in the case of CO in figure 3.13a and b, as obtained from ERA-Interim. The positive values in vertical wind denote downdraft and the negative values updraft. It was seen that updraft persisted for latitude <10° N over the entire BoB. This vertical motion often extended up to tropopause (~100 hPa). The updrafts during the study period (January-2009) ranged from –0.02 to ~ –0.1 Pa s^{-1}. The vertical updraft over southern BoB would have lifted the lower tropospheric (or boundary layer) CO to higher altitudes causing a high concentration (comparable to surface values) in the upper troposphere over southern region of the BoB. Note that fire events are seen over Indonesia (figure 3.5) over which convective updraft is seen (blue colour in figure 3.14). Under the convection, CO emitted from biomass burning over Indonesia region would get uplifted to upper troposphere.
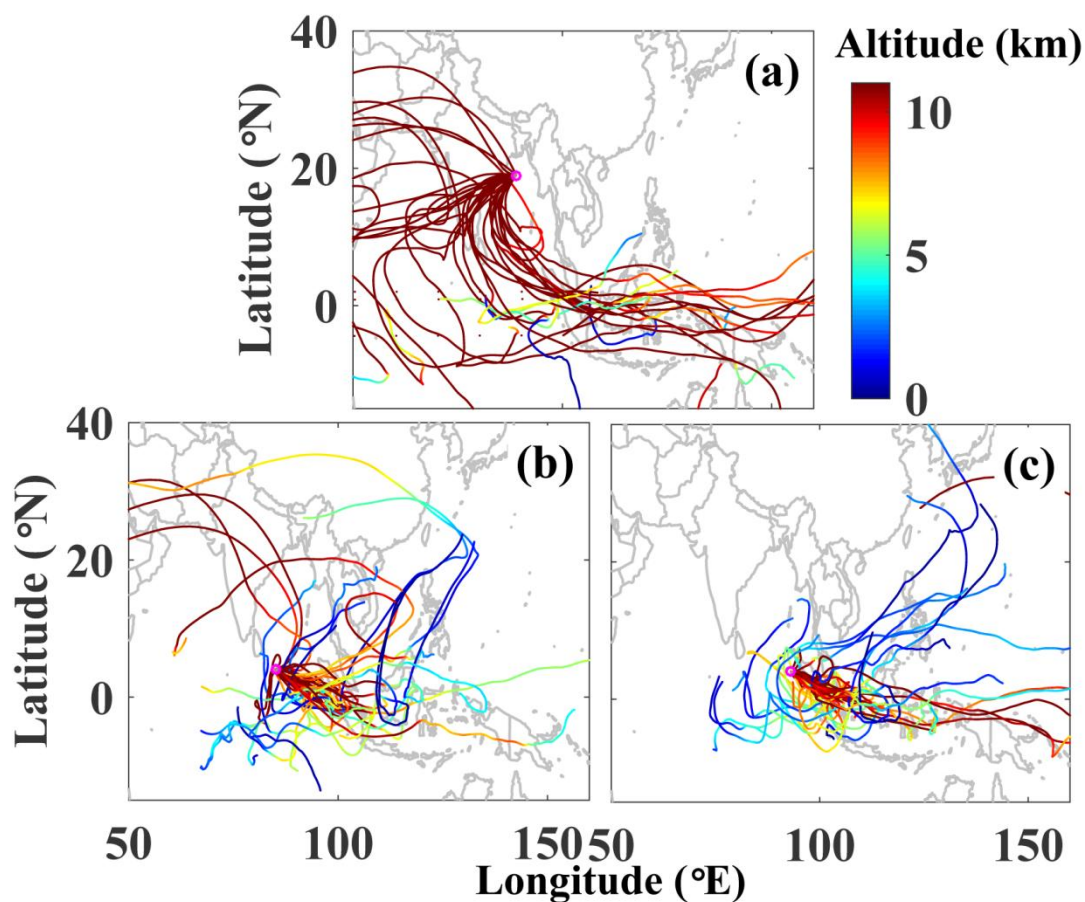
Figure 3.15: Twelve-day back-trajectories ending at the altitude of ~ 11 km for January 2009 at regions of relatively lower CO mixing ratios over northern BoB (a) and relatively higher CO mixing ratios over southern BoB (b and c). Colour bar shows the height of the air parcel. The end-points of the trajectories are shown by magenta circles.

In addition to vertical updraft, associated long range transport is another factor responsible for the spatial heterogeneity in the upper troposphere. In order to examine the role of long range transport in contributing to the upper tropospheric CO which is more prominent over southern BoB, 12-days airmass back-trajectories (in view of longer residence time of CO in the upper-troposphere) reaching at 11 km obtained using HYSPLIT model were examined. Since CO at 300 hPa is representative of 300–200 hPa layer (i.e., 9–12 km), 11 km of altitude was chosen as a representative of this layer. The back-trajectories were computed for three locations (marked by the magenta circles) representing northern (19° N, 89° E) and southern (4° N, 85° E; 4° N, 93° E;) part of BoB on daily basis for January 2009 resulting in 31 trajectories. Figure 3.15 shows the back-trajectories reaching upper troposphere over northern (figure 3.15a) and southern regions of BoB (figure 3.15b and c). The colour codes denote the altitudes of the air-parcel along its path. Over southern BoB, several trajectories originated from lower altitudes/boundary layer (<2–3km, as seen by more blue coloured trajectories) indicating the possibility of transport from those regions where more pollutants were

present, thus supporting the occurrence of high CO mixing ratios in the upper troposphere over southern BoB. On the other hand, over northern-BoB, most of the trajectories were from higher altitude (above boundary layer, >4 km) where possibility of higher CO concentration was less and hence mixing ratios of CO at these altitudes were low over northern BoB. Thus, convection around Indonesian region uplift the lower tropospheric CO to higher altitude and outflows over to the southern BoB (and equatorial IO), causing the enhancement in the upper tropospheric CO over the southern BoB. CO emitted over Southeast Asia due to biomass burning and other anthropogenic activities get transported over upper-troposphere of southern BoB as well as the equatorial IO.

3.3   Monsoonal distribution of CO over the Bay of Bengal
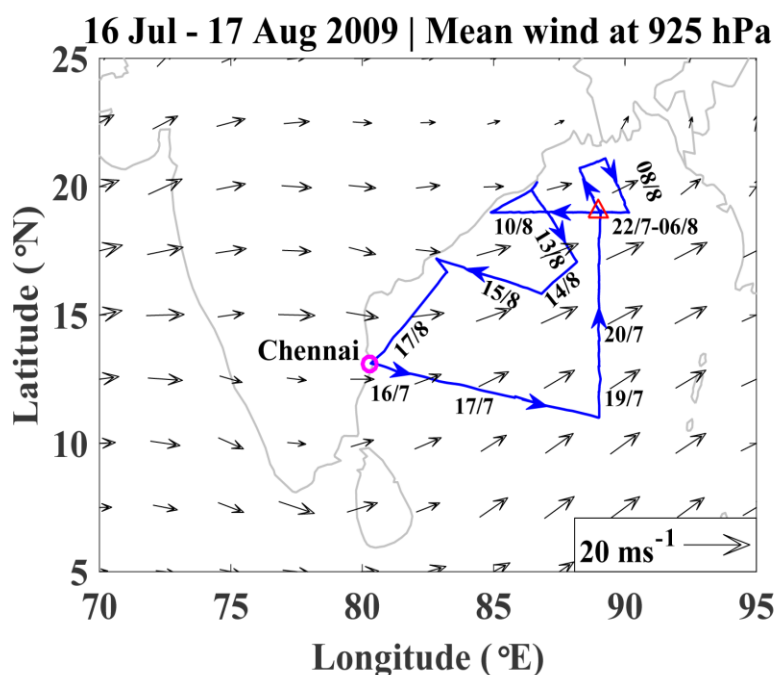
Figure 3.16: (a) Cruise track (continuous blue line) of the Research Vessel Sagar Kanya along with synoptic winds at 925 hPa (black arrows) during CTCZ campaign (summer monsoon season). The arrows marked on the track show the direction of the ship. The dates corresponding to approximate ship positions are marked along the track. The start and end positions of the cruise are shown by the magenta circles. The stationary position of the ship during 22 July to 06 August 2009 is shown by a triangle.

The CTCZ experiment (http://www.incois.gov.in/portal/datainfo/pdctcz.jsp) was carried out during 16 July to 17 August 2009 under the Indian Climate Research Programme (ICRP). Figure 3.16 shows the cruise track of the ORV Sagar Kanya during the CTCZ campaign (cruise number SK 261). The arrows marked on the track show the direction of the ship, which sailed from Chennai (80.3° E, 13.1° N; marked by a circle) on

16 July 2009. The cruise offered greater coverage in the northern BoB than the southern or central BoB areas. To take time series measurements, the ship was kept stationary for 15 days (22 July to 6 August 2009) at 89° E, 19° N as marked by a red triangle in the figure 3.16. After several tracks, covering latitude sector 11.0 to 21.1° N and longitude sector 80.3° to 90.1° E, the cruise ended on 17 August 2009 at Chennai, completing its 32 days of voyage. The average wind pattern at 925 hPa obtained from ERA-interim during the cruise period is also shown in figure 3.16. The prevailing westerly and south-westerly winds transport the trace gases from the Indian landmass to the BoB during the study period.

The in-situ measured CO mixing ratio along the cruise track is plotted in figure 3.17 as coloured circles on hourly mean basis along with the colour scale aside. The CO mixing ratio varied in the ranges from 50–200 ppbv (with an average of 96±25 ppbv) during this campaign (16 July –17 August 2009). These monsoon values are significantly lower as compared to that observed during winter (see figure 3.2). During the stationary period of 15 days (22 July to 6 August 2009), the CO mixing ratio varied from 58 to 144 ppbv with temporally averaged value of 91±19 ppbv. The CO mixing ratios below the detection limit of the instrument are discarded from the analysis.
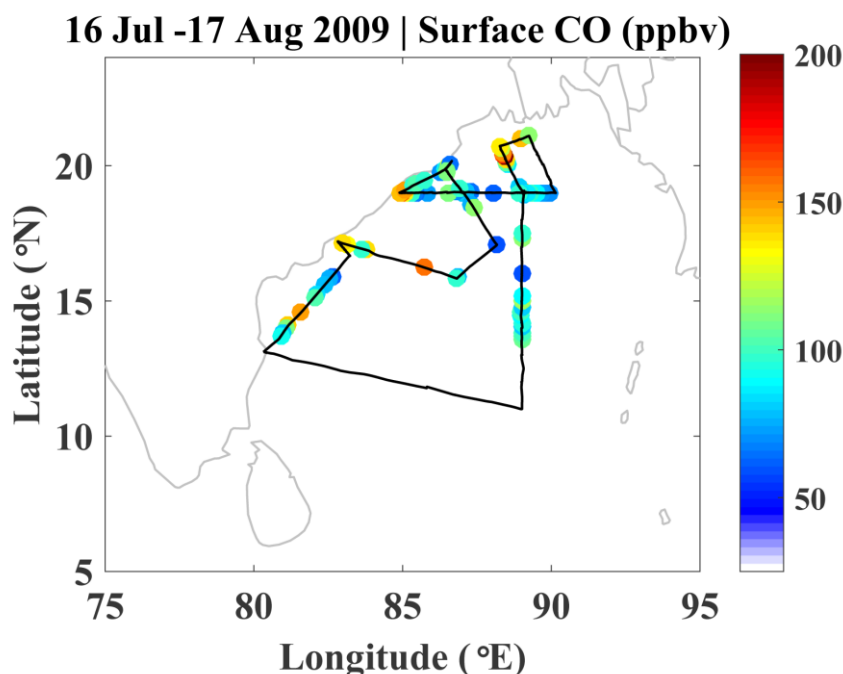
Figure 3.17: Spatial variation of surface CO mixing ratios along the cruise track during summer monsoon corresponding to the CTCZ campaign (July–August 2009). Black line shows the cruise track.
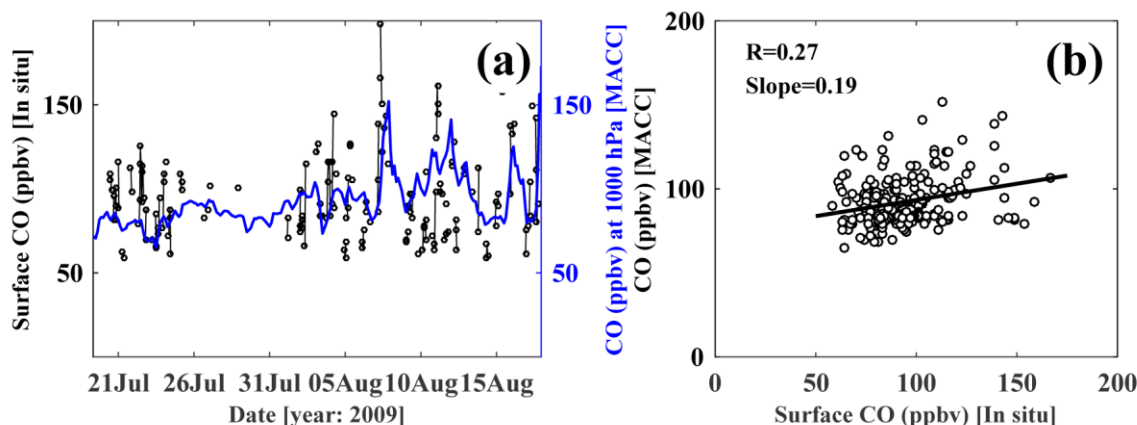
Figure 3.18: (a) A comparison of surface CO variations along the cruise track from MACC reanalysis and in-situ observations during CTCZ experiment. (b) Scatter-plot between collocated observations and MACC CO over the BoB corresponding to (a). A linear regression fit is shown as a black line.

As done for the winter season (figure 3.7), a comparison is shown in figure 3.18 between MACC simulated CO at 1000 hPa and the in-situ measured surface CO over the BoB for monsoon (CTCZ campaign). While the MACC model captured the spatio-temporal variations in CO well during winter season (see figure 3.7), during monsoon they are poorly correlated with the correlation coefficient being ~0.3. However, the model has captured several transient enhancements observed over northern BoB.

3.3.1 Long-range transport over the BoB during monsoon

As in the case of winter, the airmass back trajectories reaching the cruise track (figure 3.19) during this period were also examined. The discussion of trajectory analysis is carried out in conjunction with MOPITT retrieved surface monthly mean CO mixing ratios (figure 3.20a) and the MODIS retrieved locations of fire events, caused by the open biomass burning (figure 3.20b) during the monsoon month of July 2009.

During the monsoon season, the BoB is under the influences of two different airmasses as observed during the CTCZ experiment (figure 3.19). Over the central BoB, the airmass back trajectories cross southern India (i.e. <13° N). In contrast to winter (figure 3.4), most of the air trajectories over northern BoB come across the central Indian region (figure 3.19), where anthropogenic emissions are relatively less as compared to that over IGP. The CO mixing ratios (CO: 95±25 ppbv) over northern BoB (where the corresponding airmasses originated/passed through central/northern India) are comparable to that over central BoB (101±27 ppbv; where the airmasses originated/passed through from southern India). However, in the airmasses from central/northern India, surface CO showed transient enhancements as mentioned in

section 3.3.2 (marked by red arrows in figure 3.21). Due to rainy conditions during monsoon, fire event are not expected and negligible events are detected over the Indian region during July–August 2009 (figure 3.20b). Thus, CO over the BoB has negligible or minimal contribution from open biomass burning during monsoon as compared to that during winter. The MOPITT retrieved surface CO shows lower levels over Indian region except over IGP region (figure 3.20a). However, no airmass from IGP was observed over BoB during the monsoon season.
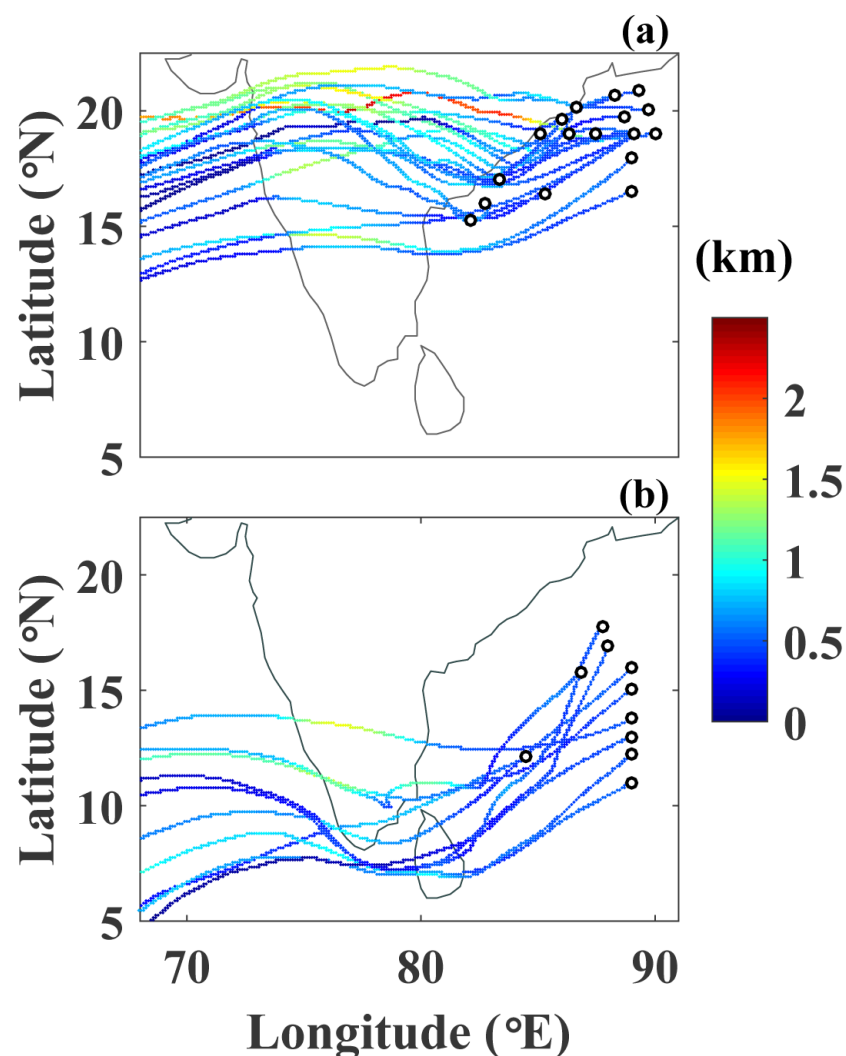
Figure 3.19: Five-day airmass back trajectories during the CTCZ campaign ending at the altitude of 500 m over the measurement locations (small black circles) grouped for corresponding airmasses from (a) central/northern India and (b) southern India. The colour scale shows the height (in km) of the trajectories.
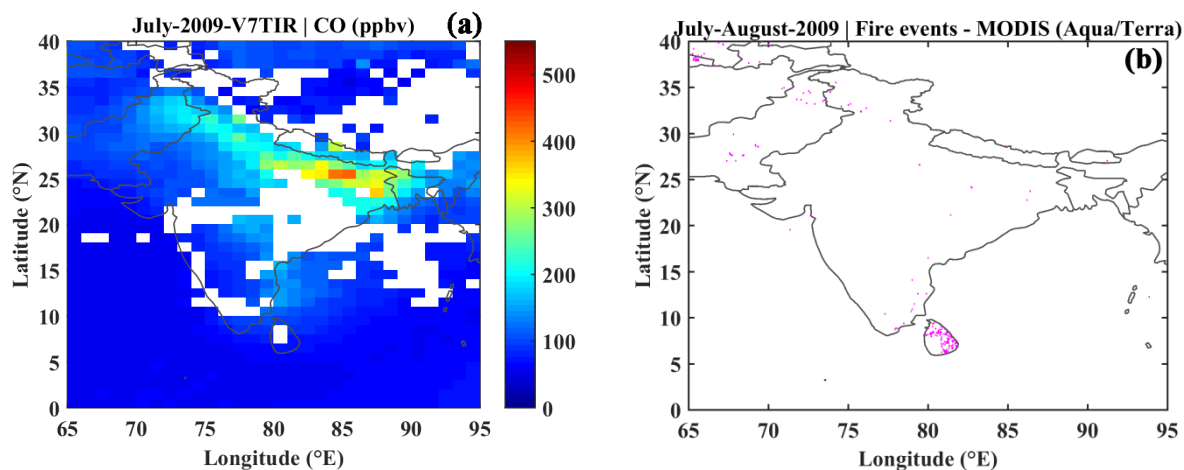
Figure 3.20: (a) Distribution of MOPITT retrieved monthly mean surface CO during July 2009 and (b) Fire events (magenta dots) as detected by MODIS (Terra and Aqua) during July–August 2009 representing the monsoon seasons.

3.3.2 Fractional residence time of airmasses over land and CO

Figure 3.21a shows the temporal variations of CO on hourly basis (black circles) during the CTCZ experiment along the cruise track. The corresponding variation in latitude and longitude are shown in 3.21b. The observed spatio-temporal variations of CO over BoB are further examined by calculating the fractional residence time of airmasses over land, based on the HYSPLIT simulated five-day back trajectories. The percentage time spent by the airmasses over the Indian landmass is estimated by taking the ratio of residence time (hours) over land to the total trajectory time for five days and shown in figure 3.21a (blue line). Those residence times have only been included in the analysis in which the trajectory lies within 1.5 km, as the surface emissions might not have direct influence on the airmasses aloft. CO shows positively correlated variability with the estimated residence times over the land (correlation coefficient of R = 0.4, p-value <0.0001). This correlation indicates the influences of transport from the landmass on the observed spatio-temporal variations over the BoB. The occasions on which one-to-one correspondence is not observed can be attributed to varying source strengths, vertical mixing or dilution, and en-route photochemical processes. However, photochemical processes would have smaller contributions under rainy/cloudy conditions prevailing during monsoon.
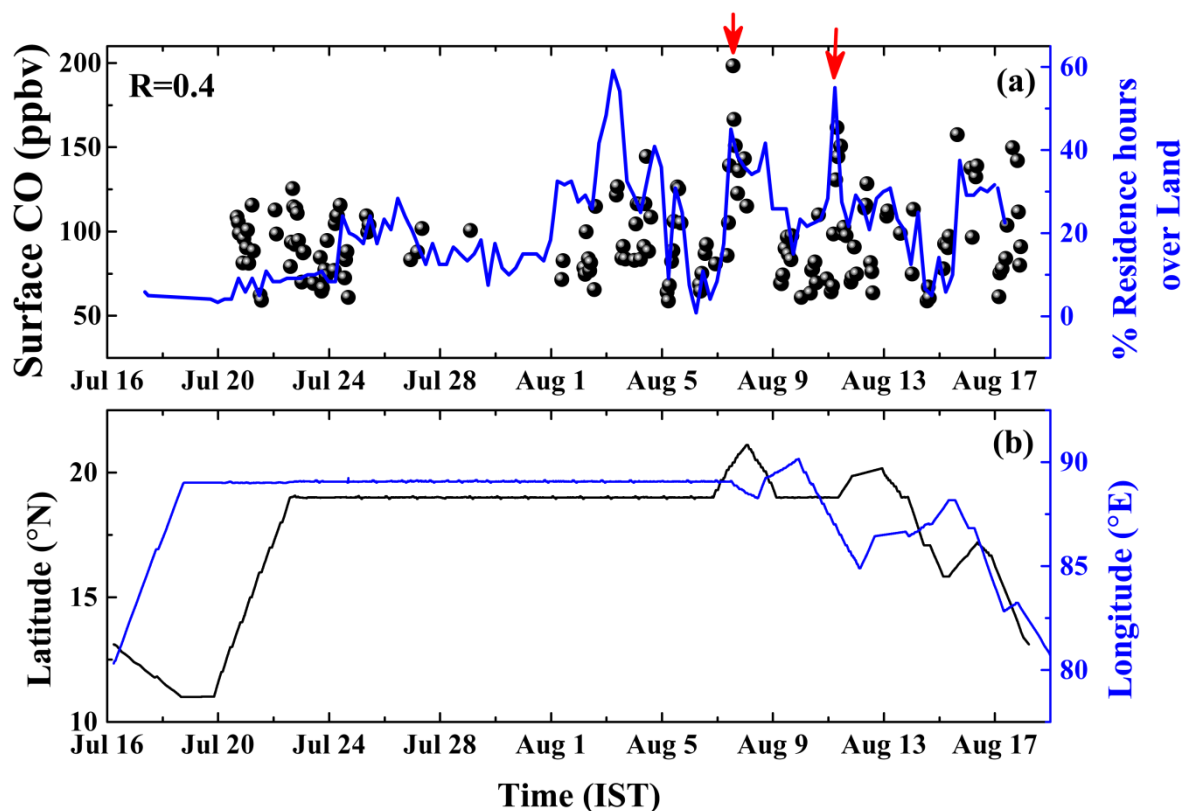
Figure 3.21: (a) Variations in surface CO (black dots) and percentage residence time of airmass over land (blue line) during the CTCZ campaign. Sharp enhancement in CO during is marked with red arrows. (b) Variations in measurement locations (latitude and longitude).

3.3.3 Hot spot of surface CO over northern-BoB during monsoon: impact of anthropogenic emission

In figure 3.21a, the CO mixing ratio shows a sharp enhancement (denoted with red arrows in the figure) on August 7 and 11, 2009, coinciding with a longer residence time over the Indian region. These enhancements are captured by MACC as seen in figure 3.18. Figure 3.22 shows airmass back trajectories above these measurement locations, along with the distribution of anthropogenic CO emissions from the INTEX-B inventory. The airmass trajectories reaching the BoB on these days obviously pass through the emission hotspots (corresponding emission of 250–350 mol km^{-2} hr^{-1}, red and yellow region). The airmasses took about half a day to be transported from the emission hotspot to the observation location and hence did not get much time to get diluted/mixed with cleaner marine airmasses. CO mixing ratios measured at Bhubaneswar (20.30° N; 85.83° E), a station within the hotspot region, was ~251±58 ppbv during the monsoon season (June–August 2011–2012; Mahapatra et al., 2014), with the elevated CO emissions in the Bhubaneswar region being attributed to industrial activities. The higher CO mixing ratios ~200 ppbv is in line with the monsoonal values

observed at Bhubaneswar. The CO mixing ratios around 150 ppbv were sampled on August 11, 2009 near the coastal source regions.
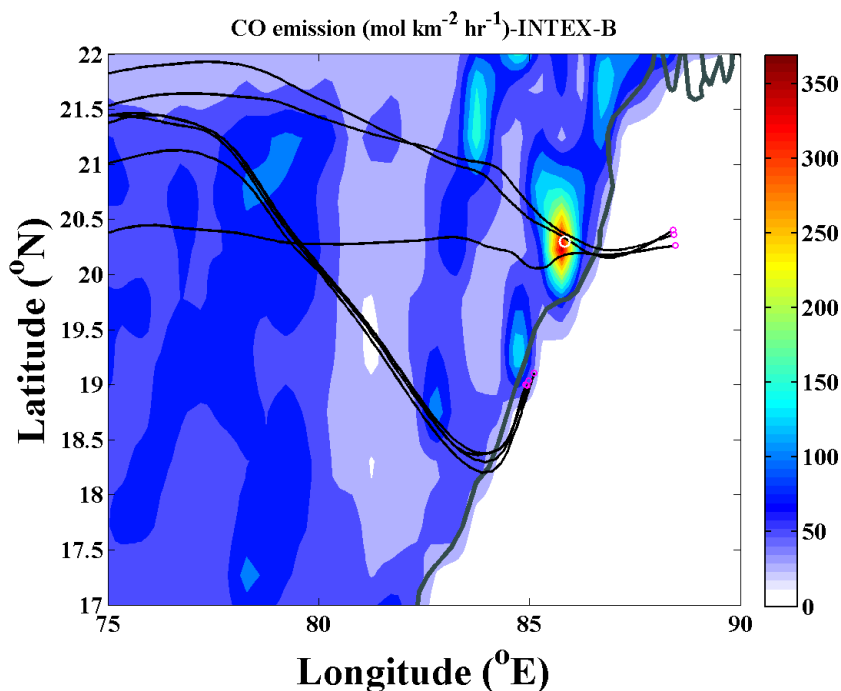
Figure 3.22: Airmass back-trajectories (black curves) 500 m above the location of higher CO observations as marked by red arrows in figure 3.21 during August 7 and 11, 2009. The background colour map shows the spatial distribution of anthropogenic CO emissions over the Indian region for the year 2006 from INTEX-B inventory. The small circles in magenta represent the points where observations were made, as well as the end-point of trajectories. The white circle over the hot-spot region denotes an observational site, Bhubaneswar.

3.3.4 Longitude-latitude-altitude distribution of CO over the BoB during monsoon

The longitude-latitude-altitude distribution of CO during monsoon season is shown as the latitude slices (figure 3.23b; at 84° and 90° E longitude representing western and eastern BoB), the longitude slices (figure 3.23a; at 8° and 17° N latitude representing northern and southern BoB), and the layers of CO at the 900 and 200 hPa pressure levels (figure 3.23c; representing lower and upper troposphere). Since the MOPITT data during monsoon season of 2009 (i.e. period of CTCZ campaign) are for limited days of July (10 days), the typical monsoon data as obtained for the year 2010 is shown in figure 3.23. The figure 2.23d and e show altitude versus longitude and latitude slices of vertical wind as obtained from ERA-Interim for the same period, similar to figure 3.23a and b.

The longitude and latitude slices (figure 3.23a and b) along with the spatial distribution of CO at 900 and 200 hPa (figure 3.23c) over the BoB reveals following monsoonal features in CO distribution.

(1) As seen in figure 3.23a, over the northern-BoB (>12° N), the upper-tropospheric CO (200–100 hPa) is relatively higher as compared to the lower-tropospheric CO (900–500 hPa). Over the southern-BoB (<12° N), the upper-tropospheric CO (300–100 hPa) is comparable to that in lower troposphere (900–500 hPa).

(2) As seen in figure 3.23b and c, longitudinal variability in the lower troposphere shows that CO mixing ratio exhibits eastward negative gradient (decreases from west to east) over northern BoB. This is mainly due to westerlies/south-westerlies transporting the CO from Indian landmass to the BoB (figure 3.23c). There exists insignificant longitudinal variability in the lower tropospheric CO over southern BoB (figure 3.23b and c).

(3) The north-south gradient in the upper tropospheric CO is stronger around 200 hPa as compared to that at 300 hPa (figure 3.23a and b). The CO mixing ratio at 200 hPa (~12 km) is higher than that at 300 hPa (~9km) showing that the upper-tropospheric enhancement is shifted to higher altitude during monsoon season. This could be due to stronger updrafts (as seen in figure 3.23d and e) persisting under deep-convective conditions of monsoon season.

(4) As seen in figure 3.23d and e, entire South Asia is convective showing the updraft over Indian landmass and the BoB as being the monsoon season. The relatively higher concentration over Indian landmass (especially over northern Indian region of IGP, figure 3.20) gets uplifted to higher altitude and prevailing westerly in the upper troposphere transport the CO over to the BoB. The westerlies prevailing in the upper troposphere transport the convectively uplifted CO over to the BoB in the upper troposphere. This causes higher mixing ratios of CO in the upper troposphere.
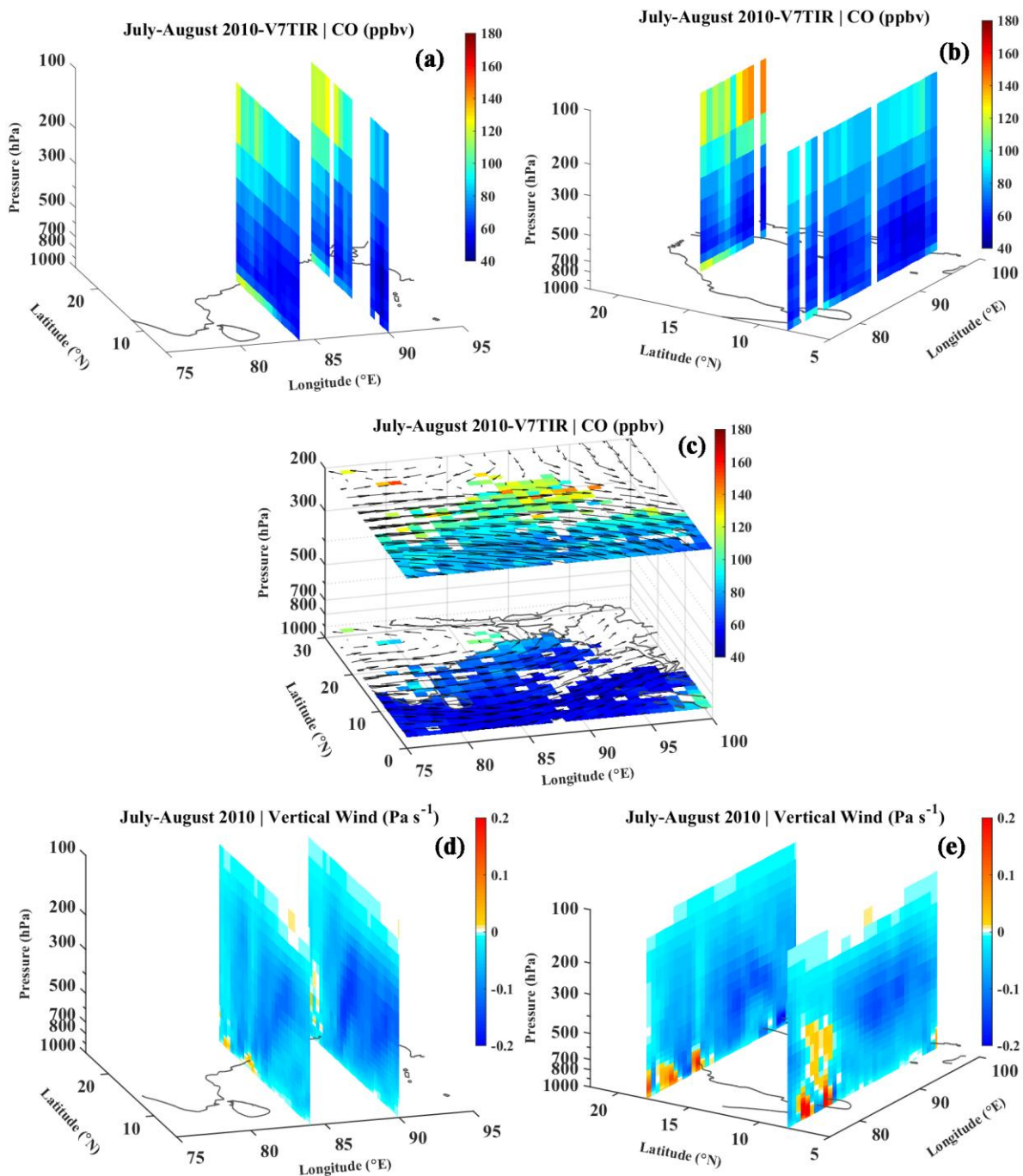
Figure 3.23: (a-b) latitude slices (at 84° and 90° E longitude representing western and eastern BoB), longitude slices (at 8° and 17° N latitude representing northern and southern BoB), and (c) layers (at 900 and 200 hPa representing lower and upper troposphere) of mean CO over the BoB during monsoon season (15 July–15 August 2010). (d-e) are same as (a-b) but for vertical wind. The mean synoptic wind is superimposed on the layers of CO (900 and 200 hPa).

3.4 CO distribution during pre-monsoon and post-monsoon

Since no in-situ measurements of surface CO have been carried out over BoB during pre-monsoon and post-monsoon as part of this study, for the completeness of the seasonal picture, the satellite retrieved CO distributions were utilised to understand the pre-monsoonal and post-monsoonal features. However, the results from the few cruise-based measurements reported by Srivastava et al., 2012 (ICARB campaign during 18 March–12 April 2006) and Mallik et al., 2013 (a campaign during 28 October–17 November 2010) during these seasons also have been examined.

Figure 3.24 shows the spatial distribution of surface CO over the BoB during pre-monsoon and post-monsoon seasons as adopted from Srivastava et al., 2012 and Mallik et al., 2013, respectively. While pre-monsoon time CO measurements were done as part of ICARB-2006 campaign during 18 March–12 April 2006, post-monsoon measurements were made during a campaign conducted during 28 October–17 November 2010. In the figure 3.24, the cruise track is labelled with the dates which are corresponding to the daily mean approximate position of the ship. The synoptic wind (ERA-Interim) was averaged over respective measurement periods and superimposed over the CO distribution as shown in the figure 3.24.
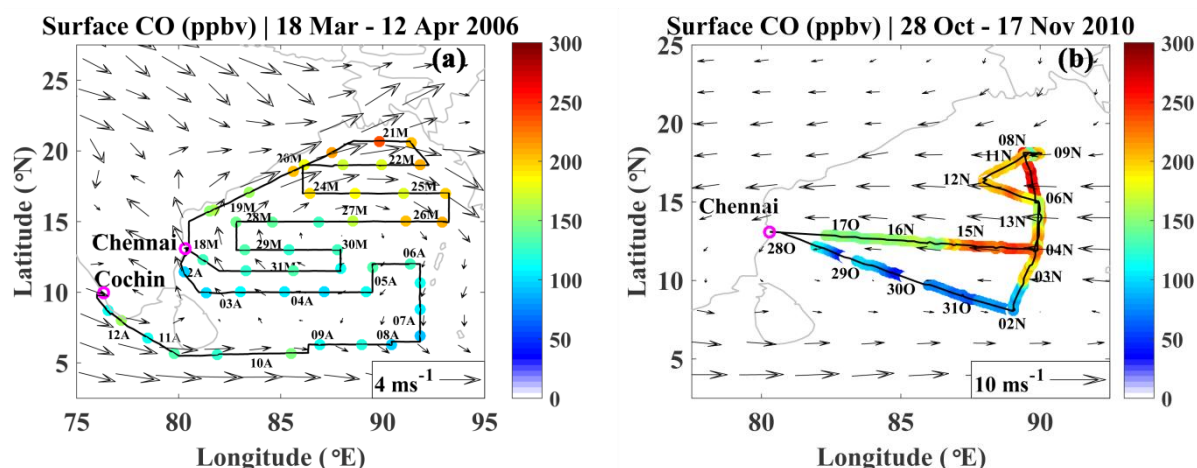
Figure 3.24: Cruise track (continuous black line) of the Research Vessel Sagar Kanya along with synoptic winds at 925 hPa (black thin arrows) during pre-monsoon (a) and post-monsoon (b) seasons. The start and end positions of the cruise are shown by the magenta circle. The color shows the surface CO mixing ratio during the ICARB campaign (18 March – 12 April 2006; Srivastava et al., 2012) and a campaign during 28 October – 17 November 2010 (Mallik et al., 2013). The dates corresponding to approximate ship positions are marked along the track. In date labels, M represents March month, A represents April month, O represents October month, and N represents November month.

Surface CO mixing ratio varied from ~88 to 235 ppbv (average of ~146±38 ppbv) over the BoB during pre-monsoon season being higher over northern BoB and

lower over central and southern BoB. The surface CO measurements were made during the ICARB 2006 campaign by Aneesh et al., 2008 and Srivastava et al., 2012. For this study, the data from Srivastava et al., 2012 was examined. As discussed by Srivastava et al., 2012 and seen in the synoptic wind pattern (figure 3.24a), the higher levels of CO over northern BoB is primarily due to transport from IGP region. The minimum CO mixing ratios were observed over central part of BoB where the airmass is of marine origin and due to the mixing of polluted air with pristine marine air CO is comparatively lower in these airmasses. The CO mixing ratios over the southern BoB are influenced mainly by the airmasses arriving from the Indian Ocean. The slightly higher surface CO (~30 ppbv) is seen over southern BoB (along the longitude track at 6 N) as compared to central BoB. Figure 3.25 shows tropospheric NO_2 averaged over the period of 18 March–12 April 2006. A clear channel of enhanced NO_2 is seen along the ~ 6N over the BoB. This region is the international ship route over the BoB. Since ship emits significant amount of NOx, it is clearly detected by satellite in tropospheric column NO_2. The concentration of CO emitted from ships is smaller and not detected in satellite retrieved CO. Thus, CO emitted by the ships over this ship route would be responsible for higher surface CO over southern BoB as compared to that over central BoB.
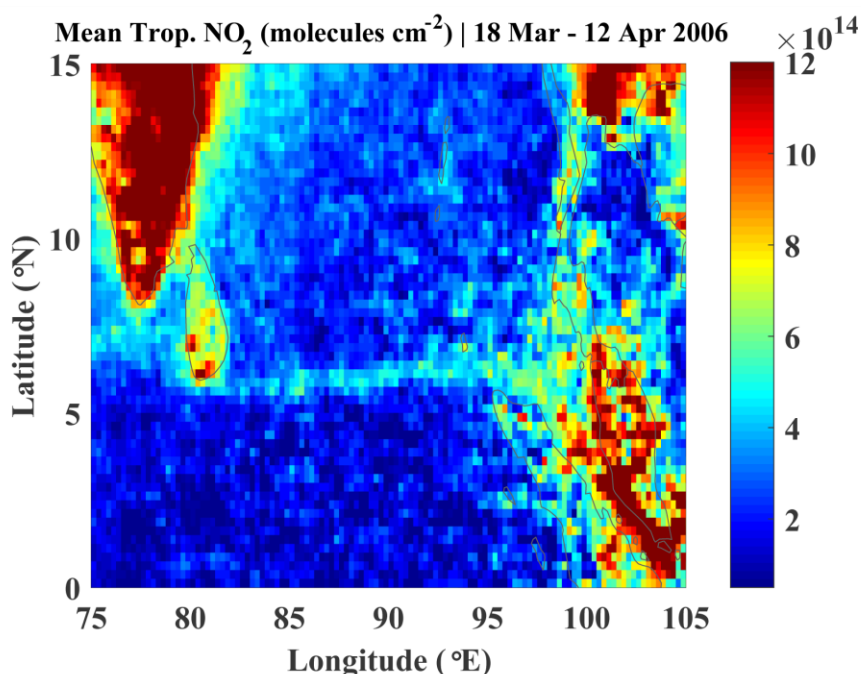
Figure 3.25: Tropospheric NO₂ averaged over the period of ICARB-2006 campaign as obtained from OMI retrievals (filtered for sky conditions where cloud fraction is < 30%).

During post-monsoon season, it varied from ~40 to 280 ppbv (average of 177 ± 63 ppbv) being higher over central/northern BoB and lower over southern BoB. The higher surface CO over central BoB is due to transport form Southeast Asian countries

(Myanmar, Thailand, and Vietnam) as seen from the synoptic wind pattern as well as reported by Mallik et al., 2013. Similar to other season, the higher mixing rations over northern region was due to transport from Myanmar, Bangladesh, and northeast India. The fire events over Myanmar and Thailand as contributed to high levels of CO over certain days over central BoB (Mallik et al., 2013). The surface CO over southern BoB was lower as this region was under influence of pristine airmass from Indian Ocean.

3.4.1 Longitude-latitude-altitude distribution of CO during pre-monsoon and post-monsoon over the Bay of Bengal

As shown for winter and monsoon seasons (figure 3.13 and 3.23), the longitude and latitude slices of the altitude distribution of CO mixing ratios over the BoB during pre-monsoon is shown in figure 3.26a and b. The spatial distributions of CO at 900 and 200 hPa (figure 3.26c) as well as at 700hPa (separately in figure 3.26d) along with the synoptic wind are also shown in the figure. Along with CO, the longitude and latitude slices of vertical winds corresponding to the figure 3.26a and b are shown in 3.26e and f. This reveals the following features in CO distribution.

(1) Lower tropospheric CO shows higher CO over northern BoB as compared to those over southern BoB (figure 3.26a and b). The synoptic wind pattern shows that the higher CO over northern BoB could be due to transport from east-coastal as well as IGP region, where higher CO emission/concentration exist as seen in figure 3.27c.

(2) As seen in figure 3.26a and b, the surface influence (significant higher values of CO) is observed up to 600 hPa (~4 km) over northern and western part of BoB during pre-monsoon season, in contrast to that observed during winter season (See figure 3.13, the higher values are restricted to lower altitude of ~ 700 hPa (~2.5 km)). The higher vertical extend of surface influence during pre-monsoon season is prominent over the northern BoB (figure 3.26a and b). This could be combined effect of convective updrafts over Indian landmass (figure 3.26e) and horizontal winds in the lower troposphere around 700 hPa (figure 3.26d). As seen in the figure 3.26e and f, the vertical updraft persists over northern Indian landmass upto ~600 hPa which uplifts the boundary layer CO to the higher altitudes (~3–4 km). And the synoptic wind (westerlies) transport the CO over to the northern as well as western BoB as seen in the synoptic wind pattern at 700 hPa (figure 3.26d).

(3) As seen in figure 3.26e and f, similar to the winter season, there is updraft over southern BoB extending upto ~8° N during pre-monsoon seasons. The synoptic winds in

the upper troposphere bring the airmass from equatorial region (figure 3.26c). There exist no significant latitudinal gradient (north-south) or the spatial heterogeneity is minimal in the upper troposphere (300–200 hPa) during pre-monsoon season.
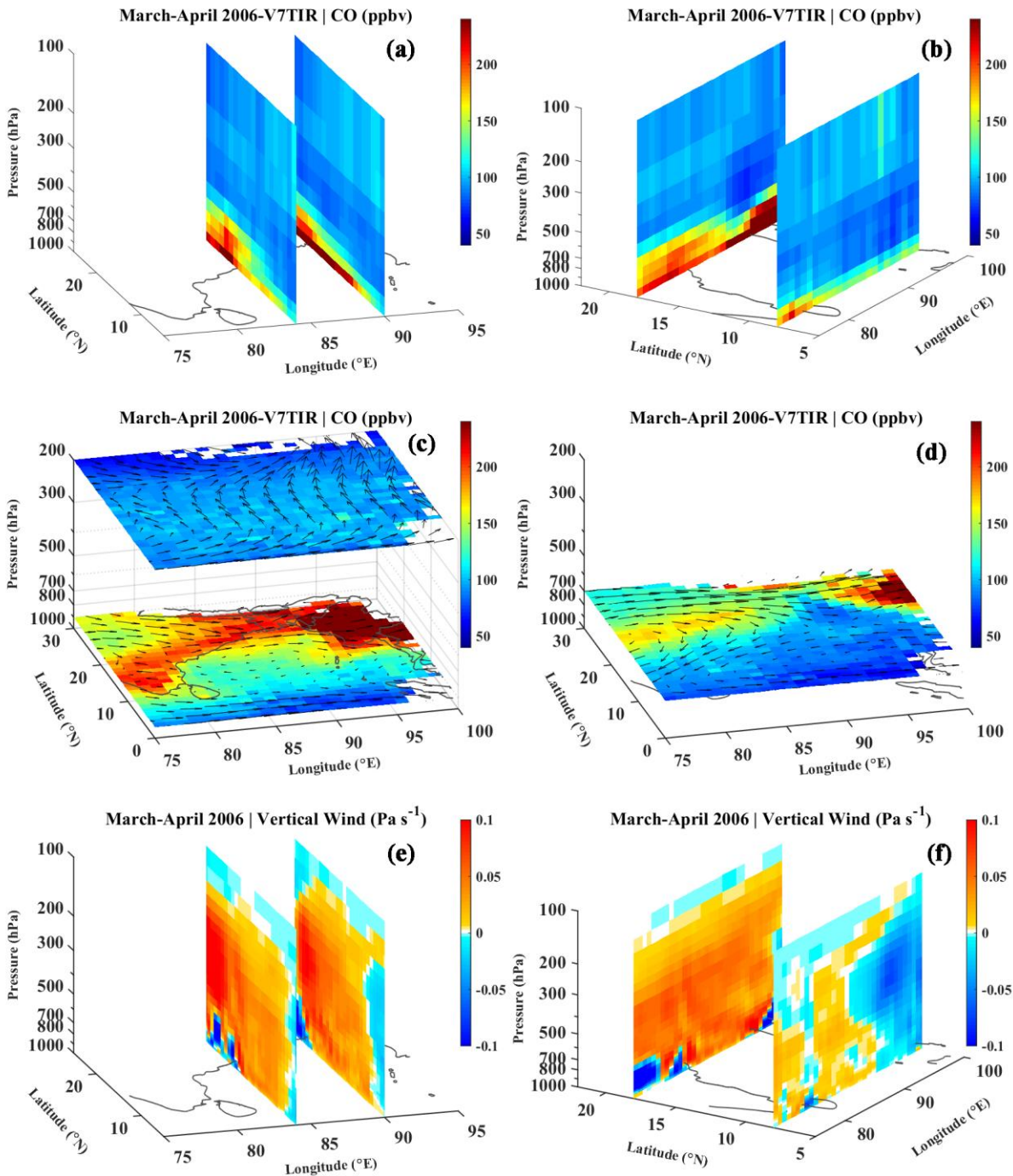
Figure 3.26: (a-b) longitude slices (at 8° and 17° N latitude representing northern and southern BoB), latitude slices (at 84° and 90° E longitude representing western and eastern BoB) and (c) layers (at 900 and 200 hPa representing lower and upper troposphere) of mean CO over the BoB during pre-monsoon season (18 March–12 April 2006). (d) represents the CO layer at 700 hPa. (e-f) are same as (a-b) but for vertical wind. The mean synoptic wind is superimposed on the layers of CO (900, 200 and 700 hPa).
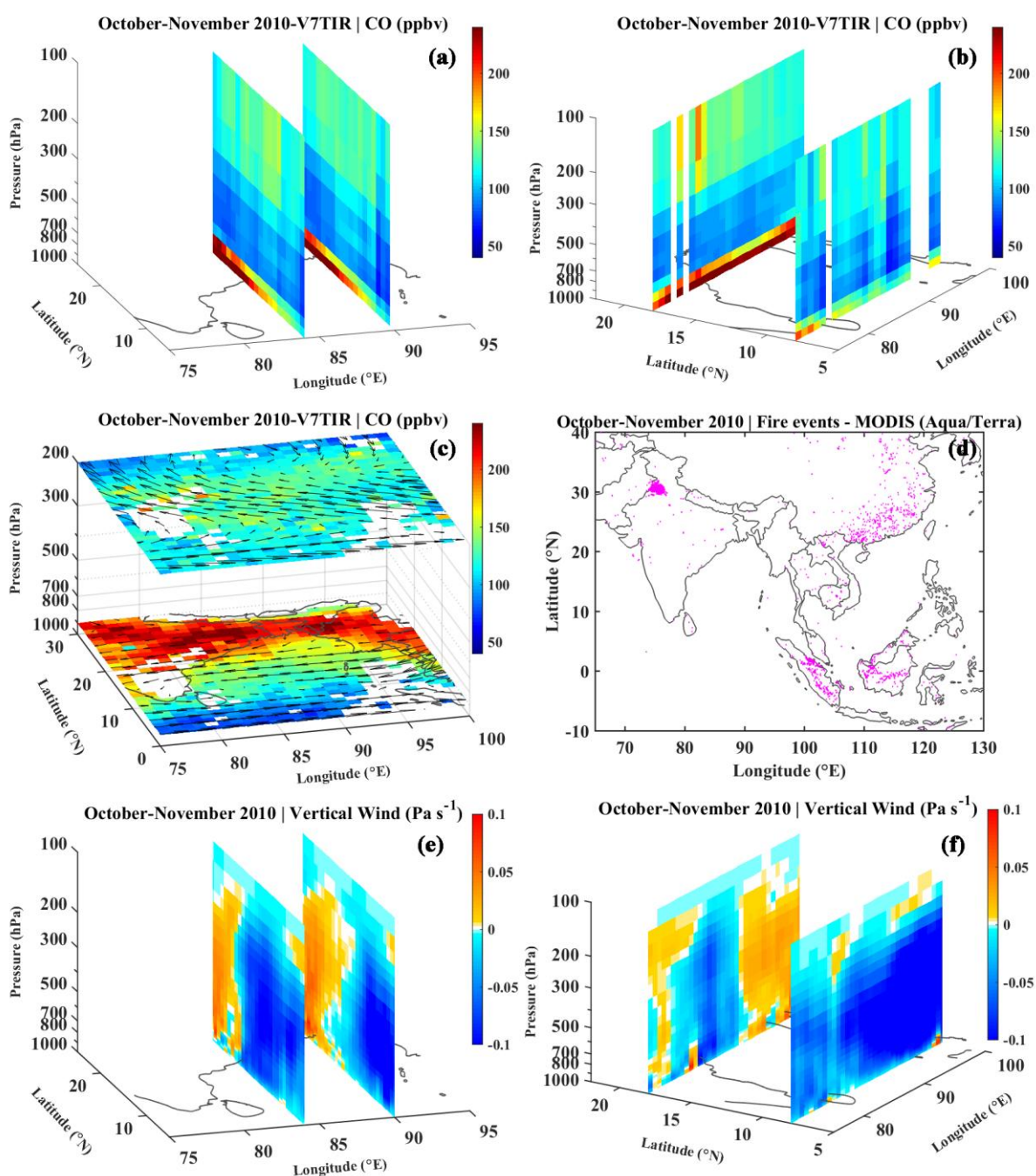
Figure 3.27: (a-b) longitude slices (at 8° and 17° N latitude representing northern and southern BoB), latitude slices (at 84° and 90° E longitude representing western and eastern BoB) and (c) layers (at 900 and 200 hPa representing lower and upper troposphere) of mean CO over the BoB during post-monsoon season (28 October–17 November 2010). (d) shows the fire events (magenta dots) as detected by MODIS (Terra and Aqua) during post-monsoon season (October–November 2010). (e-f) are same as (a-b) but for vertical wind. The mean synoptic wind is superimposed on the layers of CO (900 and 200 hPa).

As discussed for other seasons (figures 3.13, 3.23 and 3.26), the three-dimensional distribution (longitude-latitude-altitude) of mean CO along with vertical and horizontal winds during post-monsoon seasons are shown in figure 3.27. The

altitude versus longitude and latitude slices as well as spatial distribution of CO in the lower and upper troposphere over the BoB shown in figure 3.27a and c reveal following post-monsoon features in CO distribution.

(1) As can be seen in figure 3.27a and b, the surface influence (significant higher values of CO) is observed up to 800 hPa during post-monsoon seasons, almost similar to that observed during winter season. The higher values in the lower troposphere over northern BoB are due to transport from Southeast Asia (mainly from Myanmar region) as seen in the synoptic winds at 900 hPa (figure 3.27c).

(2) CO mixing ratios in the upper troposphere (300–100 hPa) is higher during post-monsoon as compared to other seasons (figure 3.27a, b and c). There exists convective updraft over southern BoB as seen in the vertical winds (figure 3.27e and f). The CO emitted from biomass burning (fire events as seen in the figure 3.27d) over Indonesia region during post-monsoon season gets uplifted to higher altitude and the south easterly synoptic wind in the upper troposphere transport it over to the BoB. Thus, biomass burning over Indonesian region contributes to higher levels in the upper troposphere during post monsoon season. The biomass burning over Indonesia influences the upper tropospheric CO over the BoB as well as equatorial Indian ocean as observed in other studies also (Srivastava and Sheel, 2013).

Putting all (in-situ and satellite observations) together, seasonal and spatial variation in mean surface and profile of CO can be summarised in the following section.

3.5   Seasonal variations of surface CO over different parts of the Bay of Bengal

The winter and monsoon time measurements of CO taken in the present study are combined with data from satellite measurements and previous campaigns to bring out the overall seasonal variations in CO over the BoB (figure 3.28). CO mixing ratios are averaged over northern (87–93° E, 17–21° N), central (83–91° E, 11–15° N), southern (83–91° E, 4–9° N), and eastern (94–98° E, 6–15° N) BoB regions. These regions are marked by blue boxes in figure 3.28a. Figure 3.28b shows the seasonal variations in surface CO for the regions marked in figure 3.28a. The figure 3.28b also provides the regional differences in CO levels for different seasons. CO mixing ratios were higher over northern BoB followed by central and southern BoB during all seasons. The seasonal amplitude in CO mixing ratios is estimated to be ~210 over northern BoB and ~100 ppbv over central BoB. The monsoonal CO mixing ratio (~94 ppbv) is about one-third of

that during the winter season (~304 ppbv) over northern BoB. The mean CO mixing ratio is the lowest over southern region during post-monsoon season. Post-monsoon CO over central BoB is comparable or slightly lower than that during winter season. Here it is to be noted that only smaller parts of northern BoB was covered during post-monsoon measurements. Due to unavailability of in-situ observations over eastern BoB, seasonal variation could not be accounted fully. The pronounced seasonality (of ~210 ppbv) observed over northern BoB emphasises the strong seasonal influence from continental region.
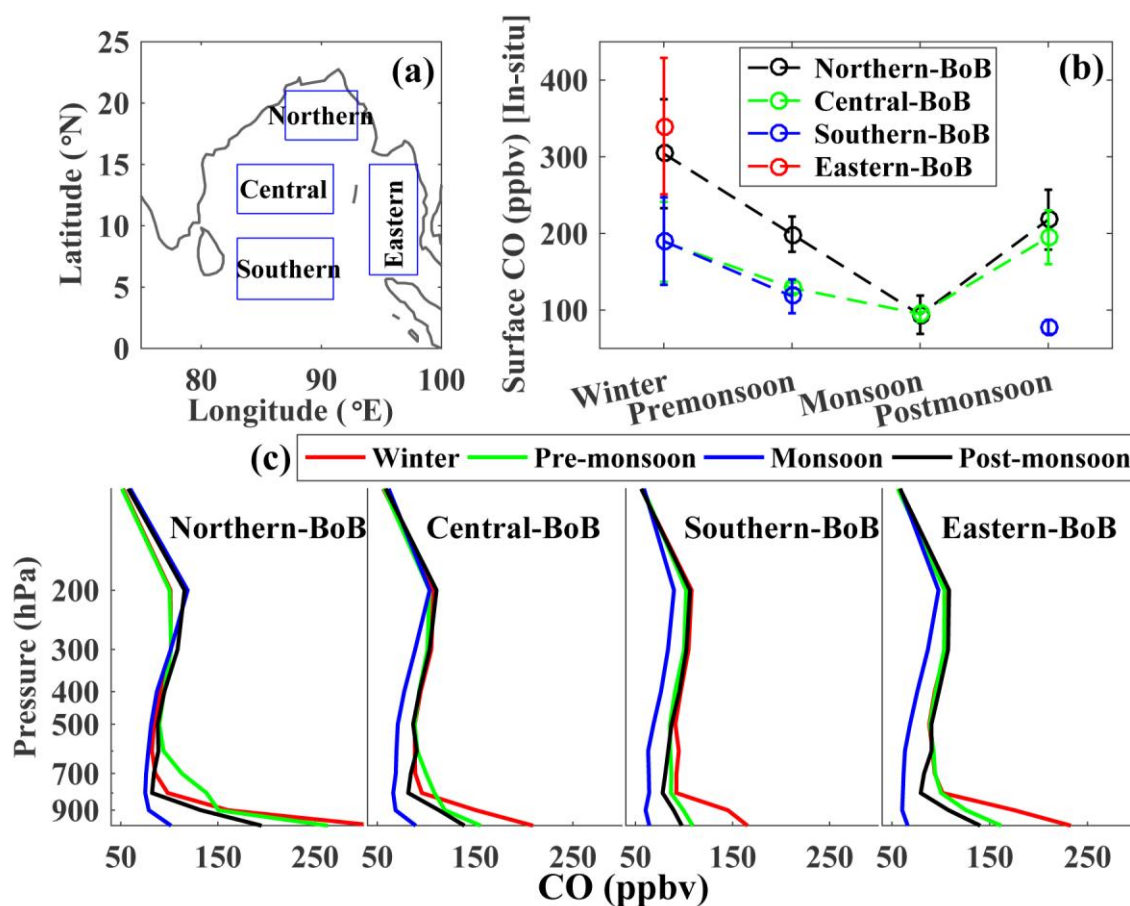
Figure 3.28: (a) different regions of the BoB as marked by blue boxes. (b) Seasonal variation of mean CO mixing ratios over different regions of the BoB as shown in (a). Except for winter and monsoon (i.e., present study periods), other values are obtained from the literature (Srivastava et al., 2012; and Mallik et al., 2013). Error bars show standard deviations for respective study periods. (c) Vertical profiles of CO for the four seasons averaged over different regions of the BoB as shown in (a) considering MOPITT retrievals of ~18 years (2000–2018). Winter, pre-monsoon, monsoon, and post-monsoon correspond to December-January-February, March-April-May, June-July-August, and September-October-November, respectively.

The mean altitudinal distributions of CO during different seasons and over different parts of BoB, were obtained by averaging ~18 years (2000–2018) of MOPITT data and presented in figure 3.28c. This can be referred as the three-dimensional CO

climatology over the BoB. The main climatological features as observed from this figure are summarised below.

- In general, two types profiles are seen, "L-shaped" over the non-convective region (i.e., northern BoB during winter) and "C-shaped" profile over the convective region or the region under influence of outflow of the convection (i.e., pre-monsoon and monsoon).

- Larger seasonal variation in the lower tropospheric CO, below 700 hPa (<2.5 km) being highest over northern followed by eastern, central and southern BoB, as compared to the upper troposphere (600–100 hPa; >4 km).

- Pre-monsoon time, CO enhancement in the lower-troposphere (900–600 hPa; 1–4 km; higher vertical extent) over northern BoB is a distinct feature as not seen over other regions/seasons.

- There is negligible seasonal variation seen in CO at 100 hPa (representation of 100-50 hPa thick layer). The seasonal variation is very small at 200 hPa over central and eastern BoB. However, there is significant seasonal change over northern and southern BoB at high altitudes.

- Monsoon-time CO profile show lower mixing ratios as compared to other seasons except over northern BoB. It is interesting to note that CO mixing ratios at 200 hPa is higher or comparable to that in the lower troposphere during monsoon season.

- CO at 200 hPa over southern BoB is higher during winter season as compared to that over northern BoB (negative north-south gradient), which is opposite in nature to that seen during monsoon, being higher over northern BoB compared to southern BoB.

3.6 Association of CO with Black carbon aerosol: co-emitted by-product of incomplete combustion

BC and CO are the by-products of incomplete combustion. But, their emission ratio varies significantly with type of sources (Street et al., 2003). Generally, BC/CO ratios were used to differentiate the source characteristics and to estimate the BC emission following a top-to-bottom approach (Dickerson et al., 2002; Spackman et al., 2008). The measurements of BC/CO ratios are also used for validating the emission inventories. The relationship between BC and CO has been studied earlier by several investigators over distinctly different environments such as coastal, free troposphere and urban centres (Dickerson et al., 2002; Badarinath et al., 2007; Spackman et al.,

2008). Even though the spatial and temporal distribution of BC (Babu et al., 2004; Nair et al., 2007; 2008) and CO (Lal et al., 2006; Sahu et al., 2006; Srivastava et al., 2012; Girach and Nair, 2010) over the Indian region and the surrounding oceanic regions were studied independently by several investigators, the studies on BC/CO ratios are scarce (Dickerson et al., 2002; Badharinath et al., 2007). In this section, the relationship between the BC and CO over the BoB is discussed for different airmass types corresponding to winter, pre monsoon and monsoon seasons (during post monsoon no BC measurements are available) utilising the ship borne measurements.
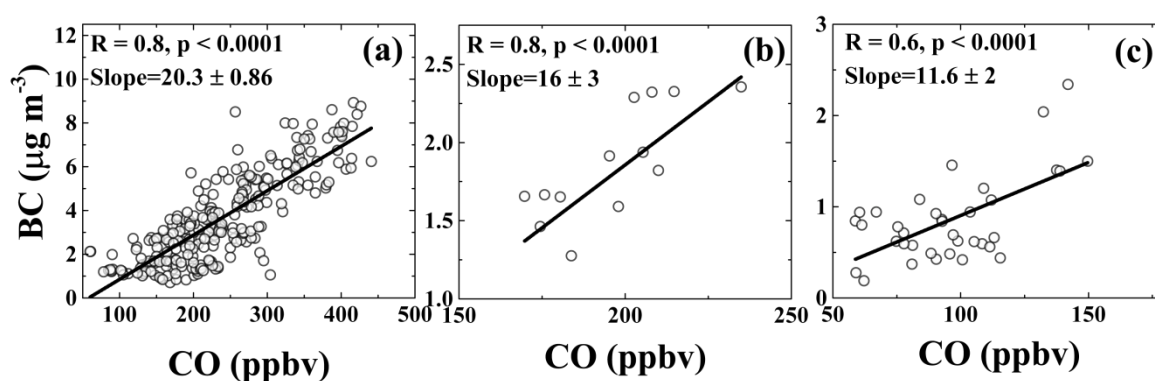
Figure 3.29: Scatter plot between surface BC concentration and CO mixing ratios corresponding to the measurements over northern BoB (airmass from IGP/northern Indian region) during winter (a), pre-monsoon (b), and summer-monsoon (c). The figure (c) is corresponding to the measurements during non-rainy days (13–17 August 2009).

Figure 3.29 shows the scatter plot between BC mass concentration and CO mixing ratio over northern BoB during winter (27 December 2008 to 08 January 2009), pre-monsoon (19 March 2006 to 27 March 2006) and summer monsoon respectively (non-rainy days, 13–17 August 2009). The variations of BC and CO over northern BoB were very similar during both, winter and pre-monsoon exhibiting strong positive correlation as high as 0.8 (figure 3.29a and b). During these seasons, airmass of IGP origin prevails over northern BoB. During summer monsoon, unlike CO, BC aerosols (which are particulates) get removed by washout/rainout along the transport pathways and hence insignificant correlation was found during this season. However, considering non-rainy days over northern BoB (airmass from central/north Indian region), the correlation was found to be 0.6 during summer monsoon season (figure 3.29c). The BC/CO ratio estimated as 20.3±0.9, 16±3.2 and 11.6±2.6 ng m^{-3} ppbv^{-1} (as given by the slope of the linear fit to the data) with the significance level p <0.0001 during winter, pre-monsoon and summer monsoon season respectively.

On the contrary, no positive correlation was observed between BC and CO over eastern BoB during winter season when Southeast Asian airmass prevailed, probably

due to the significant dilution and mixing en-route. Similarly, over southern BoB also, significant positive correlation was not observed during winter season, probably due rainy conditions existed there during the campaign period, over this region.

The BC/CO ratios over USA, Europe, southeast and east Asia and south Asia reported by several investigators ranged from 0.29 to 29.83 ng m^{-3} ppbv^{-1} (Matsui et al., 2011; Cristofanelli et al., 2012). The measurements over Indian Ocean, and Arabian Sea during INDOEX (February–April 1999) showed the high BC/CO ratio of 14.3 ng m^{-3} ppbv^{-1} (Dickerson et al., 2002). In addition, the measurements over the island of Kaashidhoo in the Maldives showed higher BC/CO ratio reaching 17.2 ng m^{-3} ppbv^{-1} (Dickerson et al., 2002). In India, BC/CO ratio of ~32 ng m^{-3} ppbv^{-1} (35.689 mgCO mgBC^{-1}) was observed over Hyderabad during a forest fire event (Badarinath et al., 2007). In contrast, Latha and Badarinath (2004) have reported BC/CO ratio of ~7 ng m^{-3} ppbv^{-1} (6.4 ngBC mgCO^{-1}) over Hyderabad (urban centre) during normal conditions. These studies show that, BC/CO values vary significantly with the type of sources. The literature survey reveals that BC/CO ratios over Indian region are relatively higher than that over other part of the globe.

Table 3.2: BC emission estimates from Indian region depending on BC/CO ratio and available CO emission inventories.

Emission inventory	CO emission (Tg year^{-1})	BC emission (Tg year^{-1}) as estimated using BC/CO ratio 20.3 ng m^{-3} ppbv^{-1} (winter)	BC emission (Tg year^{-1}) as estimated using BC/CO ratio 16 ng m^{-3} ppbv^{-1} (pre-monsoon)	BC emission (Tg year^{-1}) as estimated using BC/CO ratio 11.6 ng m^{-3} ppbv^{-1} (monsoon)
EDGAR (version-4.2)	58.32	1.0	0.8	0.6
Streets et al., 2003	63.34	1.1	0.9	0.6
Dickerson et al., 2002	66.7	1.2	0.9	0.7
Dalvi et al., 2006	69.37	1.2	1.0	0.7
REASv2.1 Kurokawa et al., 2013	61.80	1.1	0.8	0.6

The measurements of BC/CO ratios were used for validating/estimating the emission inventories of BC using top-down approach (e.g., Dickerson et al., 2002). The BC/CO ratios over the northern BoB, lying in the downwind of IGP and East Asia, are considered as the representative for the Indian region. BC emission is estimated by multiplication of CO emission into BC/CO ratio incorporating the unit conversion from ppbv to gm^{-3} at surface pressure of 1013 hPa and temperature of 300 K. Following table 3.2 shows the estimated BC emission from Indian region using three different measured BC/CO ratios. The assumption in the estimation is that the observed BC/CO ratio is same as that of BC-CO emission ratio.

Considering the uncertainty in the CO emission inventories and the limitation of the representativeness of BC/CO ratio for entire region, an approximate range of BC emission from India can be inferred. Based on the emission flux of CO and the observed BC/CO ratios during winter, pre-monsoon, and summer monsoon, the BC emission for India is estimated to be in the range of 0.6–1.2 Tg $year^{-1}$, as shown in the table 3.2. This estimate is comparable to the estimation by REAS i.e. 0.62 Tg $year^{-1}$ and Sahu et al., 2008 (1.34 Tg $year^{-1}$).

3.7   Summary

The in-situ measurement of surface CO carried out over the BoB during two contrasting seasons winter and monsoon, the observations available during other seasons, and MOPITT retrieved vertical profiles as well as columnar CO were analysed in detail in the light of synoptic winds, airmass back trajectories, biomass burning activities, and MACC reanalysis data to bring out the seasonal changes in the three dimensional distributions of CO over the BoB. The results of the analysis can be summarised as followings.

- The surface CO over the BoB shows significant spatial heterogeneity and seasonal variation. Surface CO mixing ratios ranges from 80–480 ppbv being higher over northern (302±68 ppbv; east-IGP airmass) as well as eastern BoB (340±89 ppbv; Southeast Asian airmass) and lower over southern BoB (168±37 ppbv; marine airmass) during winter season. The lower mixing ratios are observed during monsoon season being 95±25 and 101±27 ppbv over northern (airmass from central/northern India) and central BoB (airmass from southern India) respectively. Combining the observations during other seasons, the seasonal amplitude is ~ 210 and 100 ppbv over northern and central BoB. The CO mixing

ratios are higher over northern BoB as compared to the southern BoB, irrespective of the season.

- CO from the biomass burning and anthropogenic activities over landmass surrounding landmasses gets transported to the BoB depending upon the prevailing synoptic wind patterns. While the transport from eastern IGP during winter and pre-monsoon causes higher levels of surface CO over northern BoB, it is due to transport from central/northern India during monsoon season and from Myanmar, Bangladesh and northeast India during post-monsoon season. The central BoB experiences direct influence from eastern IGP, southern India, and Southeast Asian courtiers during winter, monsoon and post-monsoon seasons. The highest surface CO observed over eastern BoB during winter season is due to biomass burning over Thailand, Cambodia and eastern China, in addition to anthropogenic activities over these regions.

- The MOPITT retrieved surface CO was validated utilising in-situ measurements as available over the BoB during different campaigns and seasons. The correlation coefficient between MOPITT retrieved surface CO and in-situ measured surface CO is found to be around 0.7 which shows the potential of MOPITT surface retrievals to study the regional and seasonal changes in CO. The MOPITT retrieved vertical profiles of CO over the BoB show consistent feature with that from TES retrieved profiles.

- While MACC reanalysis shows good agreement with in-situ observations of surface CO (correlation coefficient of 0.6) during winter season, it shows the limitation in reproducing the variations during monsoon season over the BoB.

- Analysis of vertical profiles over the BoB shows the CO mixing ratios are higher in the lower troposphere (below 700 hPa; ~2.5 km) as compared to that in the mid and upper troposphere during most of the seasons, except during monsoon (higher or comparable CO mixing ratios in the upper-troposphere). In addition, lower-tropospheric CO exhibits larger seasonal amplitudes as compared to upper troposphere.

- The vertical extent of CO is higher, upto 600 hPa ($\sim$ 4 km) during pre-monsoon season over the northern BoB. This is due to convective updraft over IGP and eastern India uplifts the CO to higher altitude and horizontal winds around 700–600 hPa transport it over to the northern BoB.

- The region under the influence of convection tends to show "C-shaped" profile. In other words, there exists enhancement in the upper-tropospheric CO around

300–200 hPa. The strong convective activity over the Indian region during summer monsoons seasons uplifts the lower tropospheric CO to higher altitude (upto 200–100 hPa) and synoptic winds (westerlies around 9–12 km) transport the CO over to the BoB. The influence of biomass burning and anthropogenic activities prevailing over the Southeast Asian region causes the enhancements in the upper-tropospheric CO over southern and central BoB due to convective uplifting and associated outflows over Indonesian region during post-monsoon and winter seasons.

- Utilising the CO observations along with its companion species, Black carbon (BC), the BC emission from India is estimated to be in the range of 0.6–1.2 Tg year^{-1}.

<div align="center">***</div>

<div align="right">

Chapter - 4

</div>

Winter-time distribution of CO over the northern Indian Ocean: Continental influence

4.1   Introduction

Understanding on the concentration levels and photochemistry of CO over the northern Indian Ocean (IO), which includes the Arabian Sea and the equatorial IO, is very important as the continental polluted air mixes with the pristine air over IO through Inter-Tropical Convergence Zone (ITCZ). The continental airmass from south Asia and southeast Asia outflows over to northern IO and hence higher concentrations of trace gases and aerosols are observed over north of ITCZ as compared to south of ITCZ. One of the main aims of the field experiment INDOEX (Indian Ocean Experiment) conducted in 1998 and 1999 was to characterize the atmospheric chemical composition of the outflow from South and Southeast Asia to these marine environments during the dry winter season when the prevailing synoptic air flow is northerly/north-easterly. Lelieveld et al., 2001 has shown that the agricultural burning and in particular, the use of bio fuel over South and Southeast Asia enhanced the CO concentrations over entire northern IO (toward the ITCZ which was situated around 6° S). As discussed the spatial heterogeneity in distribution of CO over the Bay of Bengal (Chapter-3), a significant spatial heterogeneity has been observed in CO over the northern IO during INDOEX campaigns (Lal et al., 1998; Naja et al., 2004; Chand et al., 2001; De Gouw et al., 2001; Burkert et al., 2003; Mandal et al., 2006, Aneesh et al., 2008).

The Arabian Sea (AS) being a part of northern Indian Ocean is surrounded by distinctly different landmasses on three sides. Different patterns of synoptic winds during different seasons bring the continental pollutants over to this marine region from different landmasses. Further, this region has been an important marine trade route and emissions by ships also would contribute to the trace gases and aerosols over this marine environment. The observations of CO during pre-monsoon seasons (March 2001 and April – May 2006) as part of BOBEX-2001 and ICARB-2006 campaigns (Lal et al., 2006; Aneesh et al., 2008 and Srivastava et al., 2012) also showed heterogeneity in its distributions over the AS.

Extensive measurements of various trace gases over northern IO were conducted during winter season and transition (winter to pre-monsoon) periods during different phases of INDOEX (1996–1999). These measurements were done approximately 2 decades ago. Over the time, the anthropogenic emissions of trace gases and aerosols would have changed due to growth in the population, energy requirement, industrial activities, etc. However, since the INDOEX-1999, no winter-time in-situ CO observations have been carried out over equatorial IO and AS.

After a period of about 19 years, extensive in-situ measurements of surface CO were conducted over the northern Indian Ocean as part of the ICARB field campaign during the winter season of 2018. In this chapter, the spatial and temporal variations of CO over the AS and equatorial IO during winter is analysed in detail with emphasis on the transport processes. The present study utilised the ship-based in-situ measurements of CO mixing ratios, supplemented by MOPITT observations and CAMS (Copernicus Atmosphere Monitoring Service) reanalysis data. The earlier in-situ observations available over the AS and IO reported by Lal et al., 2006 and Srivastava et al., 2012 are also utilised for comparison. Utilising the satellite and model data, transport pathways and source regions were identified for the observed variation of surface CO. MOPITT retrieved surface CO and CAMS reanalysis are compared with the in-situ measured surface CO. The distributions of upper tropospheric CO is analysed using the MOPITT retrievals. The chemical nature of airmass in terms of O_3 production efficiency in the airmass is also discussed based on co-located surface O_3 and CO measurements. As mentioned in chapter-2 and 3, satellite data (MOPITT and MODIS) were filtered prior to its use in the analysis (see section 2.2.4).

4.2   Distribution of surface CO over the northern Indian Ocean

4.2.1 The cruise tracks and background conditions

The ICARB-2018 experiment was carried out over southeast AS and the equatorial IO during winter season (16 January to 14 February, 2018) under the Geosphere Biosphere Programme of the Indian Space Research Organization (ISRO-GBP) to study the outflow characteristics from South/Southeast Asia. As shown in figure 4.1, surface CO was measured as a part of ICARB-2018 along the cruise track (cruise number SK 345) covering latitude from 15° N to 3° S and longitude from 65° to 88° E. The ship started sailing from Goa (73.8° E, 15.4° N) on January 16, 2018 and returned to Tuticorin (78.2° E, 8.7° N) on 14 February, 2018 after completing 30 days of successful expedition. The voyage covered a distance of 3802 nautical miles with an average speed

of 5.8 knots. The ship was kept stationary for a day during 12–13 February 2018 as marked by a triangle. In order to avoid contamination from ship-exhaust when ship was stationary, ship was reoriented such that sampling inlet is in the upwind.
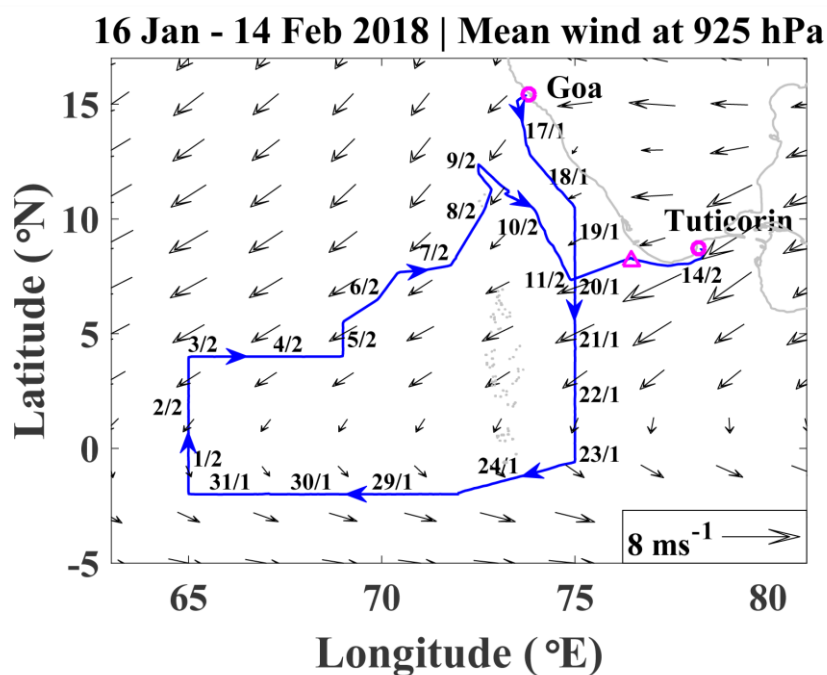
Figure 4.1: (a) Cruise track (continuous blue line) of the Research Vessel Sagar Kanya along with synoptic winds at 925 hPa (black arrows) during ICARB-2018 campaign (winter season). The arrows marked on the track show the direction of the ship. The dates corresponding to approximate ship positions are marked along the track. The start and end positions of the cruise are shown by the magenta circles. The stationary position of the ship during 12–13 February 2018 is shown by a triangle.

The arrows in figure 4.1 show the mean synoptic wind flow pattern at 925 hPa as obtained from ERA-interim reanalysis for the cruise period (See section 2.5.8 for details on ERA-Interim). During winter season, the north-easterly winds are persistent, and convection over the source regions (northern latitudes/continental landmass) is suppressed. In general, north-easterly winds prevailed over the southeast AS and north westerly winds prevailed over the equatorial IO during the observation period.

4.2.2 Experimental details and data

The measurements of surface CO were carried out using an online gas filter correlation CO analyser (Model CO12 Environnement S.A, France). The CO-analyser works on the principle of Non Dispersive Infrared (NDIR) absorption of CO at 4.67 μm. More technical details of the analyser are given in section 2.2.2. Air was drawn from a height of approximately 20 meter above the sea surface through a Teflon tube. Before and after the cruise, the analyzer was calibrated using a custom-made calibrator, and

calibration factors remained same. The measurements affected by ship exhaust were filtered prior to the analysis. The data filtering was carried out based on the wind direction data available on board ship and the concurrent measurements of NOx on board. NOx measurements are highly sensitive to ship-exhaust. In the presence of ship-exhaust NOx value rises above 100 ppbv, which is used to be otherwise <2 ppbv. See for the more details on data filtering is available in section 2.2.4.

4.2.3 Surface CO distribution during ICARB-2018
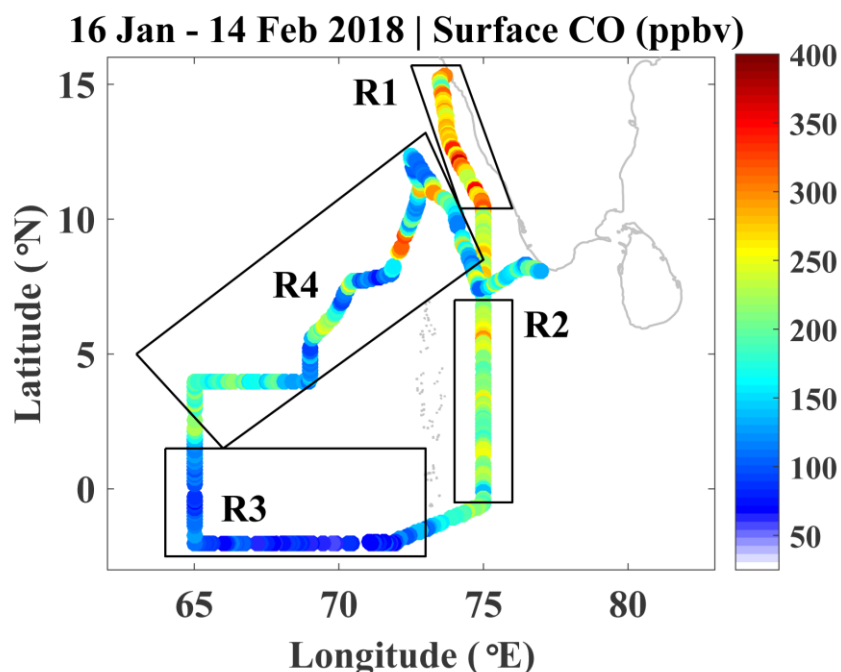
Figure 4.2: Spatial variation of surface CO over southeast AS and the equatorial IO along the cruise track of ICARB-2018 during winter season (16 January – 14 February 2018). The boxes marked with R1, R2, R3, and R4 shows four regions corresponding to which trajectories are discussed in figures 4.4 and 4.8.

The mixing ratio of surface CO along the cruise track during ICARB-2018 campaign is presented by coloured circles in the figure 4.2. A large spatial heterogeneity was observed in surface CO over southeast AS and the equatorial IO during this period (winter). As shown in figure 4.2, surface CO varied from <50 to 365 ppbv (mean=179 ppbv; standard deviation=67 ppbv) over this marine region. The maximum value of 365 ppbv was observed over southeast AS (near to the southwest coast of India) during 18 January 2018. As seen from the synoptic wind pattern (figure 4.1), transport from South Asia causes higher level of CO (and other trace gases) over the AS and IO. The minimum CO value was observed over the latitudinal leg along 2°S. In this track, ~2% of total data points (CO mixing ratio) have fallen below the detection limit of the instrument, i.e. 50 ppbv and these are discarded from the analysis.

Prior to further analysis, in-situ observation of surface CO is compared with MOPITT retrieved surface CO as well as CAMS simulated surface CO. In order to find the source regions and causative mechanisms for the observed spatio-temporal variability, back-trajectory analysis is carried out in conjunction with CAMS simulated CO, MOPITT retrieved CO and MODIS derived fire events.

4.2.4 Comparison of MPOITT retrievals
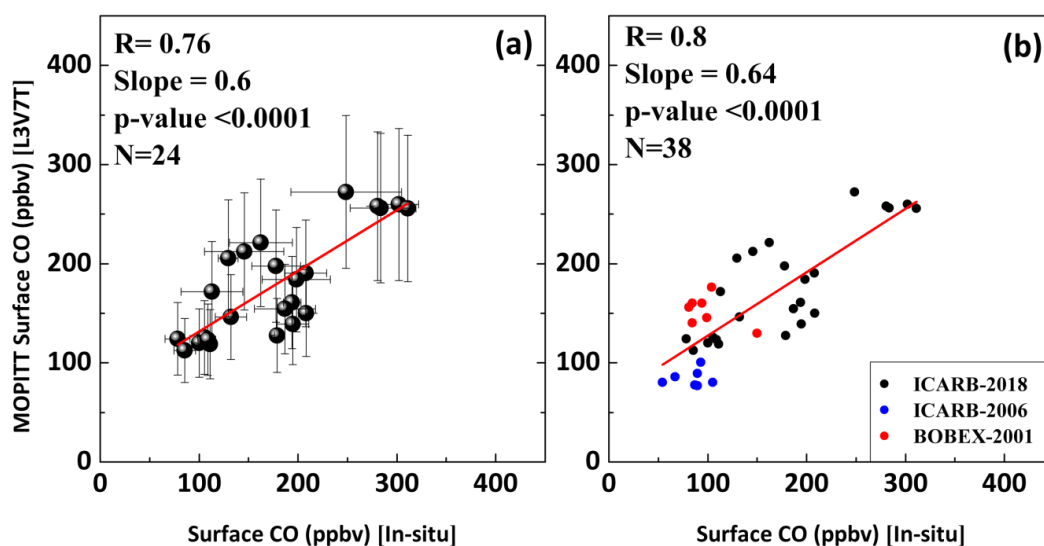
Figure 4.3: (a) scatter plot between MOPITT retrieved surface CO and in-situ surface CO during ICARB-2018 campaign (winter) over the northern IO. The y-error bar shows the MOPITT retrieval uncertainty and x-error bar shows the standard deviation in the in-situ surface CO. (b) is same as (a) but including the data points corresponding to the various campaigns conducted over the northern IO. The red line represents the linear regression fit considering the weighing by MOPITT retrieval uncertainty.

As discussed in the chapter-3, the in-situ measured surface CO values over the AS were compared with the Level-3 (1° x 1° gridded) surface retrievals (algorithm version V7-TIR) of MOPITT values. The co-located (in terms of time and space) MOPITT surface CO were obtained daily basis corresponding to the time and location of in-situ measurements. For the comparison, the in-situ surface data were gridded to MOPITT grid size and points co-located in terms of time (day or night) and space were compared. Figure 4.3a shows the comparison of MOPITT retrieved surface CO with the in-situ measured surface CO measured during ICARB-2018. The linear regression analysis shows correlation coefficient of 0.76 (level of significance p < 0.0001) and slope of 0.6. In addition, comparison is extended further utilising the available in-situ measurements over the AS and the IO carried out during various campaigns as shown in figure 4.3b. The in-situ measured surface CO corresponding to the ICARB-2006, and BOBEX-I-2001 were adopted from Srivastava et al., 2012; Lal et al., 2006; respectively. Different colours

represent the data points corresponding to the different campaigns. When more observations are included for the comparison, the correlation coefficient and slope increases slightly (R=0.8 and Slope=0.64) as evident in figure 4.3b. However, one to one match between MOPITT surface CO and in-situ CO is not expected for the reasons discussed in section 3.2.2. Even though surface CO measurements are available prior to year 2000 (i.e., during INDOEX), no satellite data are available for the comparison.

4.2.5 Continental influences: Role of transport

Utilising the HYSPLIT model, seven-days airmass back trajectories arriving at 100 m were simulated for the measurement locations along the cruise track at every 6 hour interval. Trajectories are colour-coded to show the altitude (agl) variations of the air parcels along their path. The airmasses remained in the lower troposphere or boundary layer (below 2 km) during entire study period. The discussion of trajectory analysis is carried out in conjunction with MOPITT retrieved surface CO data and the fire events (figure 4.5), indicative of the open biomass burning. Figure 4.5 shows the surface CO distribution averaged over the study period as obtained from MOPITT. The magenta dots in this figure represent the location of fire events as obtained from MODIS (Aqua and Terra) during the study period. The trajectories were grouped for the airmasses from southern/central India (a/d), IGP (b), and AS (c) corresponding to the four regions, R1 (a), R2 (b), R3 (c), and R4 (d) as marked in figure 4.2. Figure 4.4a represents the back-trajectories reaching the cruise track over coastal AS (R1). These trajectories originate/pass through central/southern India. As seen in satellite map (figure 4.5), the surface CO (representing 1000–900 hPa thick layer) is around 250–300 ppbv over these regions. In addition to fossil fuel burning, some biomass burning events (magenta dots) are also seen over this region. The Potassium (K) content in atmospheric aerosols is considered as a potential tracer for biomass burning (Andreae, 1983). The chemical composition measurements conducted during this campaign revealed significantly higher concentration of K (0.98±0.17 ugm^{-3}; range: 0.74-1.3 ugm^{-3}, data received from aerosol chemistry group at Space Physics Laboratory, Vikram Sarabhai Space Centre, Thiruvananthapuram, India) over the R1 region giving evidence for the presence of biomass burning contribution in the airmass. Note that this Potassium concentration is lower than that observed northern BoB (1.9±0.6 ugm^{-3}) in the IGP airmass as seen in winter ICARB-2009 (Aryasree et al., 2015; also discussed in Chapter 3). This indicates lower contribution of biomass burning in the airmass from central/southern India as compared to that from IGP. The R1 region being close to the source region (i.e.

continent), surface CO mixing ratios were relatively higher as compared to those measured over other regions.
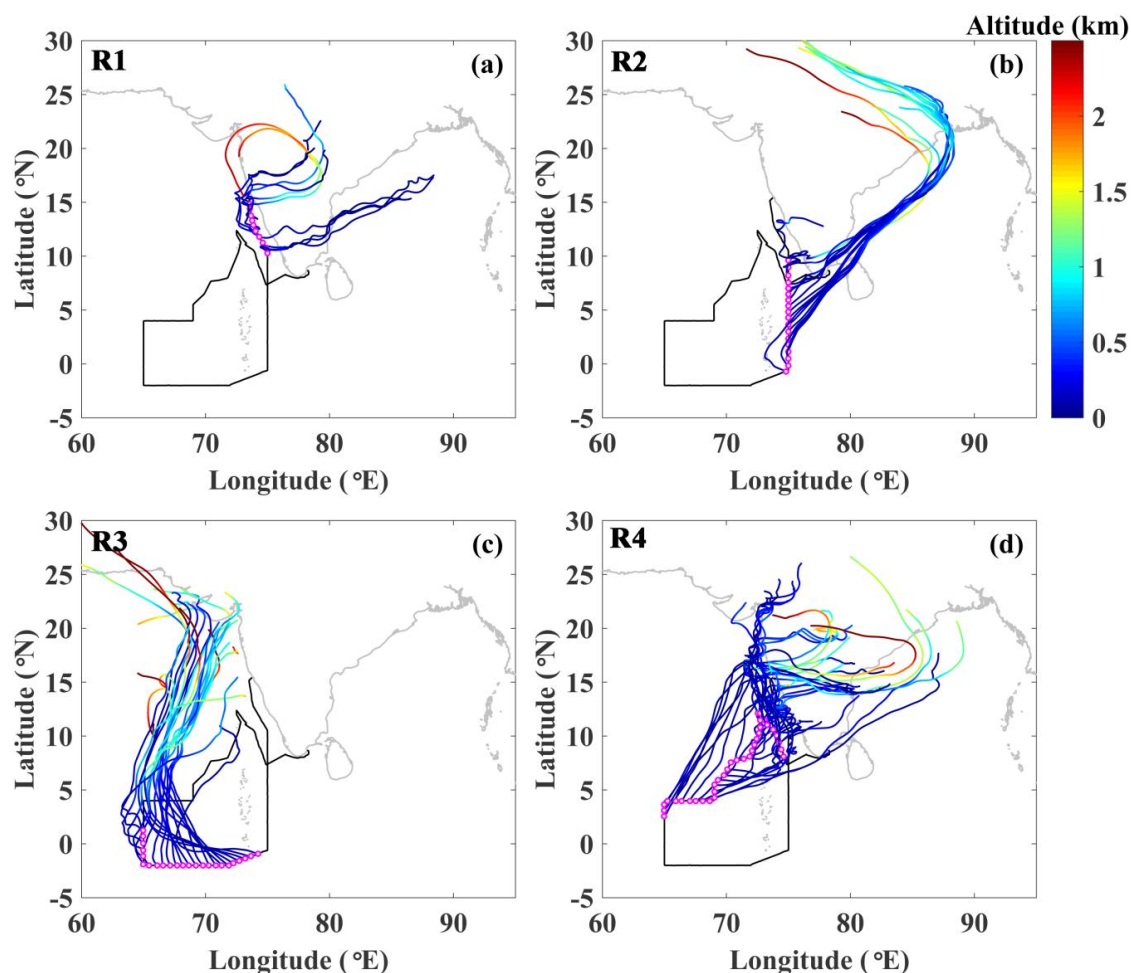
Figure 4.4: Seven-day airmass back trajectories during the ICARB-2018 experiment ending at the altitude of 100 m over the measurement locations (small magenta circles) grouped for the four regions, R1 (a), R2 (b), R3 (c), and R4 (d) marked in figure 4.2 corresponding to the airmasses from southern/central India (a/d), (b) IGP, and (c) AS. The colour scale shows the height (in km agl) of the trajectories.

Figure 4.4b represents the back-trajectories corresponding to the measurements over R2 region. Trajectories are from eastern part of IGP regions where surface (as well as columnar) CO values are extremely high (500–600 ppbv) as can be seen from figure 4.5. The CO emitted from biomass burning and anthropogenic activities over eastern part of IGP gets transported over to the R2 region though the oceanic region of BoB. Since airmasses have spent significant time over marine environment allowing more mixing with pristine airmass, the observed mixing ratio over R2 region is smaller than that over R1 region. This aspect is elaborated in section 4.2.6. Figure 4.4c represents the back-trajectories corresponding to the measurements over R3 region (equatorial IO). Originating over northern part of AS, the airmasses spent most of the time over the

marine region of the AS (so-called marine airmass). The airmass has travelled long marine path, where there is no strong source of CO, and subsequent dispersion/removal would cause relatively lower mixing ratios over R3 region. Figure 4.4d represents the back-trajectories corresponding to the measurements over R4 region. Similar to R1, the airmasses over R4 region is from central/southern India. However, airmasses corresponding to the R4 region have spent higher time over marine region as compared to airmasses corresponding to the R1 region.
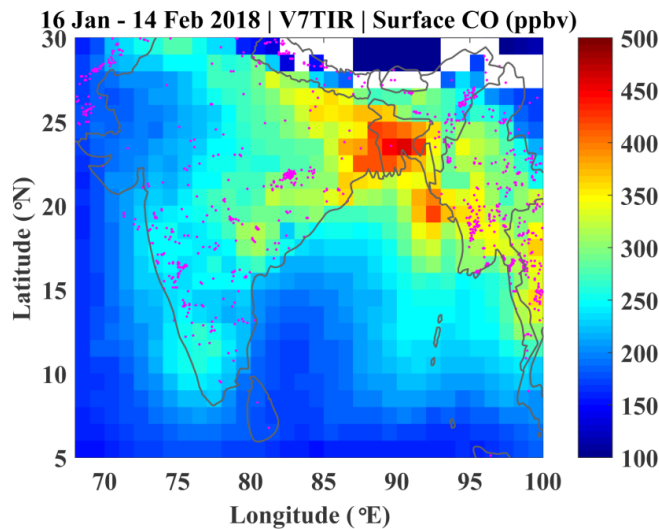
Figure 4.5: Mean MOPITT retrieved surface CO along with fire events (magenta dots) as detected by MODIS (Terra and Aqua) during the cruise period of ICARB-2018.
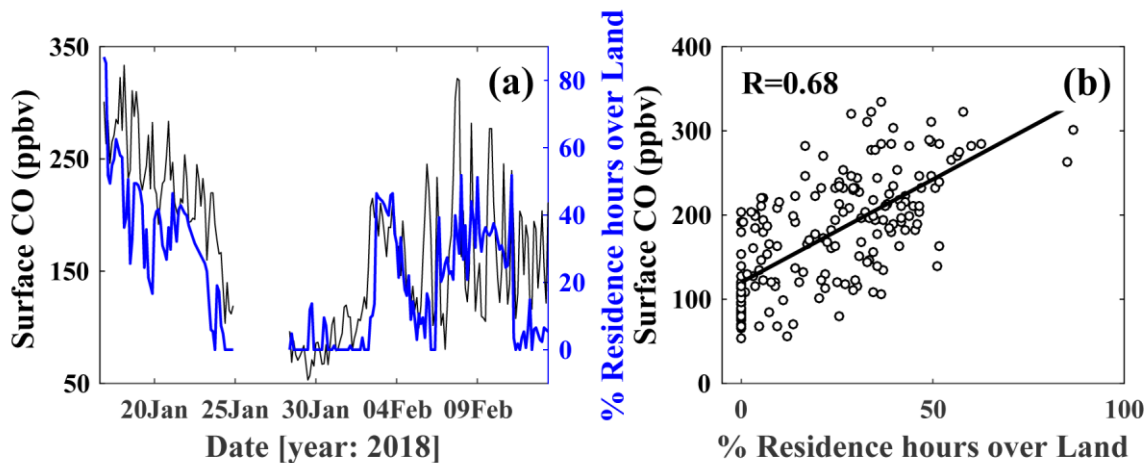
Figure 4.6: (a) Spatio-temporal variations of surface CO (black line) and percentage residence time of airmass over land (blue line) during the ICARB-2018 campaign. (b) Scatter plot between surface CO and percentage residence time over land corresponding to (a). The black line represents the linear regression fit.

128

4.2.6 Spatio-temporal variations of CO and airmass residence time over the land

The observed spatio-temporal variations of CO are further investigated by estimating the fractional residence time of airmasses over land, using HYSPLIT simulated seven-day back trajectories. Figure 4.6a shows the variations of CO and residence time of airmasses over land along the cruise track during the ICARB-2018 experiment. The percentage of residence time of airmasses over the landmass is estimated by the ratio of residence time over land to the total trajectory time of seven days. The hours of residence have only been included in the analysis if the altitude along trajectory is less than 2 km (agl), as the surface emissions might not been directly influence the airmasses aloft. CO being a primary pollutant species (unlike ozone which is a secondary pollutant) shows good correlation (R = 0.68, p<0.0001) with the estimated residence times over the land. The longer the airmass resides over land, higher is the mixing ratio. The reverse is also true as discussed in section 3.2.3, i.e., longer the airmass resides over the marine region, lower is the mixing ratio. This analysis indicates the influences of transport from the landmass on the observed spatio-temporal variations. Due to obvious reasons (like spatial heterogeneity in the strength of CO emission, vertical mixing or dilution, and en-route photochemical processes), perfect correlation is not expected.

4.2.7 Comparison with CAMS reanalysis and identification of source regions
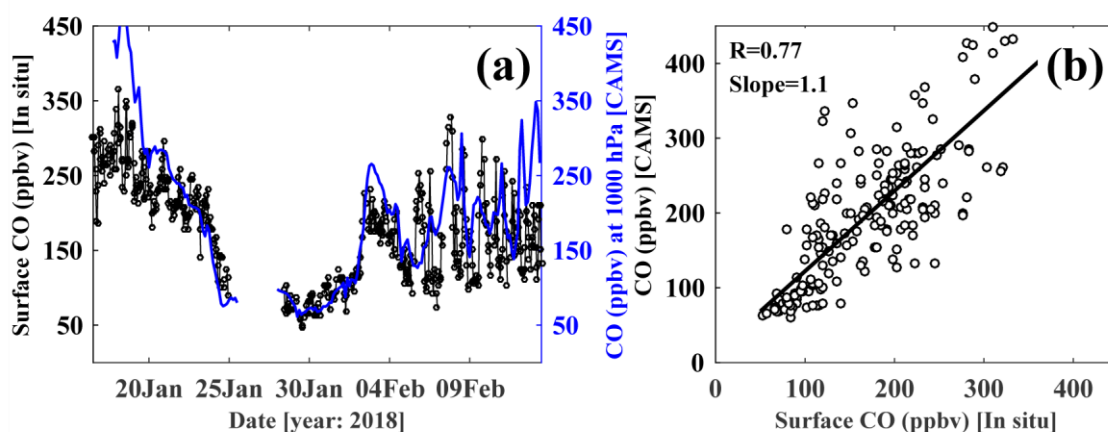
Figure 4.7: (a) A comparison of surface CO variations from in-situ observations (black line) and collocated CAMS model CO (blue line) along the cruise track during ICARB-2018. (b) Scatter plot between collocated observations and CAMS CO (at 1000 hPa) corresponding to the variations shown in (a). The black line represents the linear regression fit.
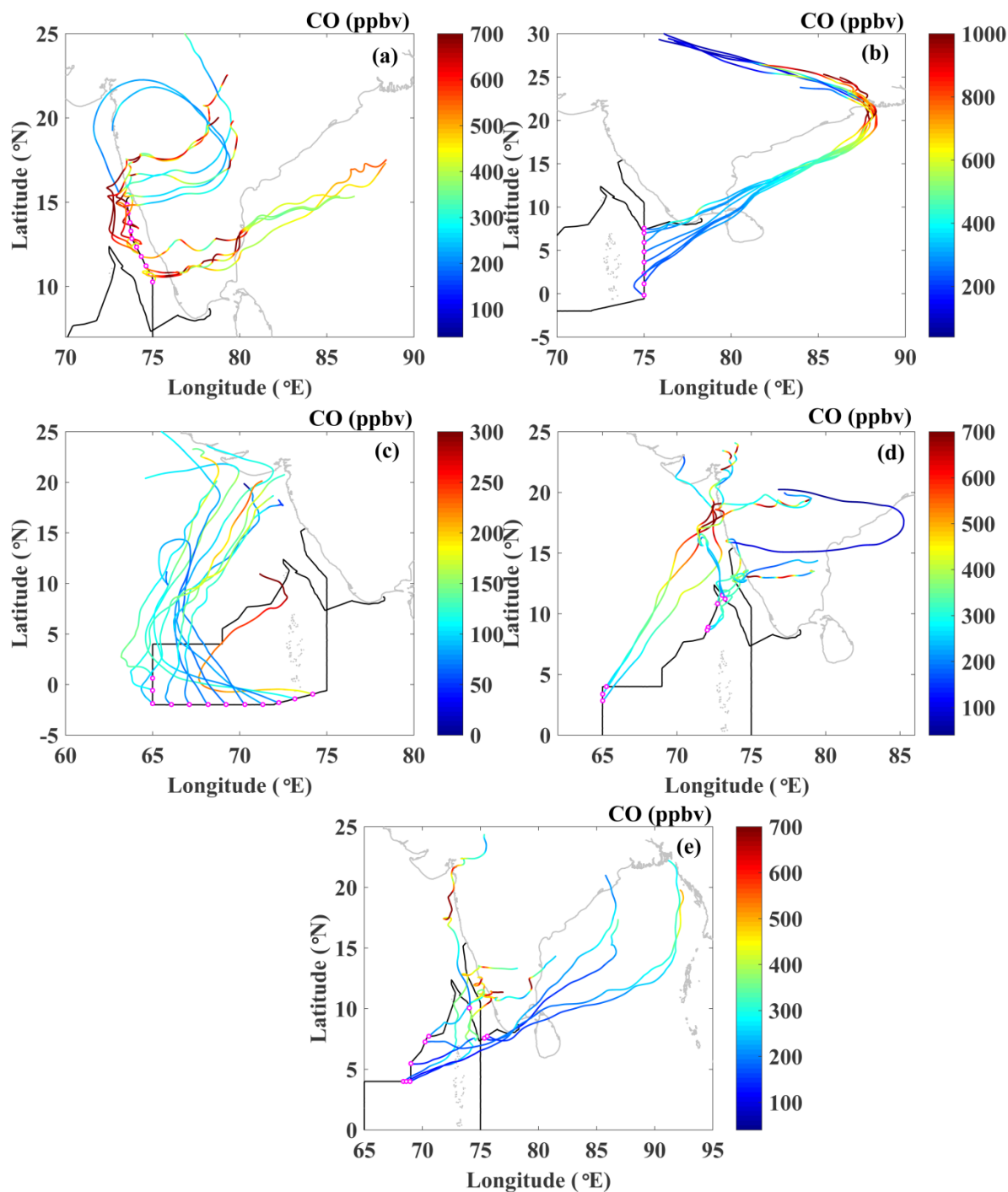
Figure 4.8: CO mixing ratios along the seven-day airmass back trajectories during the ICARB-2018 experiment ending at the altitude of 100 m over the measurement locations (small magenta circles) grouped for the four regions, R1 (a), R2 (b), R3 (c), and R4 (d-e) as marked in figure 4.2. The colour scale shows CO mixing ratio as obtained from CAMS model data. While Figure (d) is corresponding to relatively higher CO over R4, figure (e) is corresponding to relatively lower CO over R4.

The figure 4.7a shows the variations of surface CO during ICARB-2018 along with co-located CAMS model generated CO (at 1000 hPa representing surface/boundary layer

CO) over the AS and IO and figure 4.7b shows scatter pots between them. The one-to-one comparison between CAMS simulated CO and the in-situ measured surface CO shows that the CAMS model reproduced the observed spatio-temporal variations in CO with correlation coefficient of +0.77. However, the model slightly overestimates the absolute CO levels by about 15 ppbv (mean bias = mean CAMS simulated CO minus mean in-situ measured CO). This comparison shows that CAMS captures the surface CO variability fairly good and it can be further utilised to make broader inferences. Further, CAMS model data is utilised to investigate how CO mixing ratio varies along the airmass trajectories. Figure 4.8 is similar to figure 4.4, the difference is that the color along the trajectories shows CO mixing ratio as obtained from CAMS model data, instead of altitude of the trajectories. An interpolation of CAMS gridded data is carried out in space (latitude, longitude and altitude) and time along the airmass back trajectories. The variation of CO along the trajectories is discussed in conjunction with source regions. Figure 4.9 shows the anthropogenic emission of CO averaged for January and February months as obtained from HTAP (Hemispheric Transport of Air Pollution) emission inventory. The higher emission over IGP is clearly seen in the figure 4.9. The grid cell of $1° × 1°$ around megacities like Kolkata, Mumbai and Delhi shows very high CO emissions ($≥ 1.5 \times 10^{-9}$ kg m^{-2} s^{-1}) as marked by arrows in the figure 4.9.

The trajectories corresponding to R1 region (figure 4.8a) shows that the airmasses over central/southern India have higher mixing ratios that those measured over this region. Trajectories corresponding to R2 region are from IGP region (figure 4.8b), and the airmasses gets enriched with CO over the west Bengal region of IGP, over which higher CO mixing ratios (~1000 ppbv) as well as higher emissions exist (especially over Kolkata city; figure 4.9: HTAP emission). All the trajectories crossing the megacity, Kolkata where wintertime CO mixing ratios observed to be ~1210 ± 270 ppbv (Mallik et al., 2014). This is in line with the higher mixing ratios seen in CAMS data (figure 4.8b). As trajectories passes through oceanic region of the BoB, reduction in mixing ratios occurs due to mixing with relatively pristine marine airmass and removal by OH as can be seen clearly along the trajectories. Figure 4.8c shows some of the trajectories with higher CO mixing ratios over the AS, but while reaching over to the R3 region, reduction in CO mixing ratios are seen. Surface CO over R4 regions shows both higher and lower mixing ratios, and figure 4.8d–e shows the trajectories for the location of observed higher and lower mixing ratios over R4. As seen from figure 4.8d, some of the trajectories corresponding to the relatively higher CO over R4 region are from the region around Mumbai (previously known as Bombay) where emissions are very high

(figure 4.9). However, a corresponding enhancement is not seen in satellite observations (figure 4.5). The studies conducted during INDOEX campaigns has described the transport of polluted airmass from Western/North-western India over the AS as the "Bombay Plume" (Lobert and Harris, 2002; Lelieveld et. al., 2001). The "Bombay Plume" and transport from central/southern India partly contributed to the higher CO mixing ratios over R4 region. As shown by the trajectories in figure 4.8e, the higher CO mixing ratios are seen over the locations from where they originate but the airmasses spent longer time over marine region and due to dilution or removal of OH would have lead to relatively lower mixing ratios over R4 region. The reduction in mixing ratio along the trajectories is clearly seen.
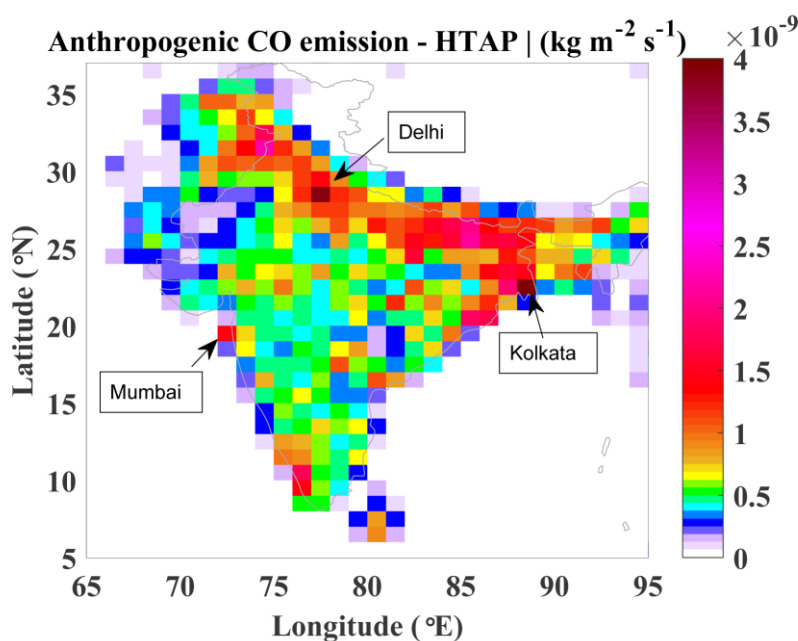
Figure 4.9: Anthropogenic emission of CO averaged over January and February months as obtained from HTAP emission inventory. This emission excludes biomass burning emission.

4.2.8 CO in association with surface O_3: A tracer for chemical nature of airmasses

The tropospheric O_3 is of photochemical origin produced from precursors like CO, NMHCs, NOx, etc. through chemical reactions in the presence of sunlight (Seinfeld and Pandis, 2006). However, the O_3 production rate is nonlinear with the concentrations of precursors. The O_3/CO ratio is one of the important parameters to understand the chemical nature of airmasses. O_3/CO ratio also can be referred as the ozone production efficiency in the given type of airmass (Parrish et al., 1998). The O_3/CO ratio is estimated from the slope of linear regression fit between the concentrations of O_3 and CO. There exist three situations, i.e., negative slope, slope close to zero and positive slope (Parrish

et al., 1998). The negative slope indicates removal/destruction of ozone due to titration of O_3 under higher anthropogenic emissions. This would happen for the polluted airmass which generally have higher levels of NO or VOC/NOx (Parrish et al., 1998, Stehr et al., 2002). The near-zero slope is indicative of approximate balance between ozone production and destruction. Generally, this balance accounts for disappearance of correlation between O_3 and CO. The positive slope is indicative of photochemical production O_3 or production is dominating over the destruction.
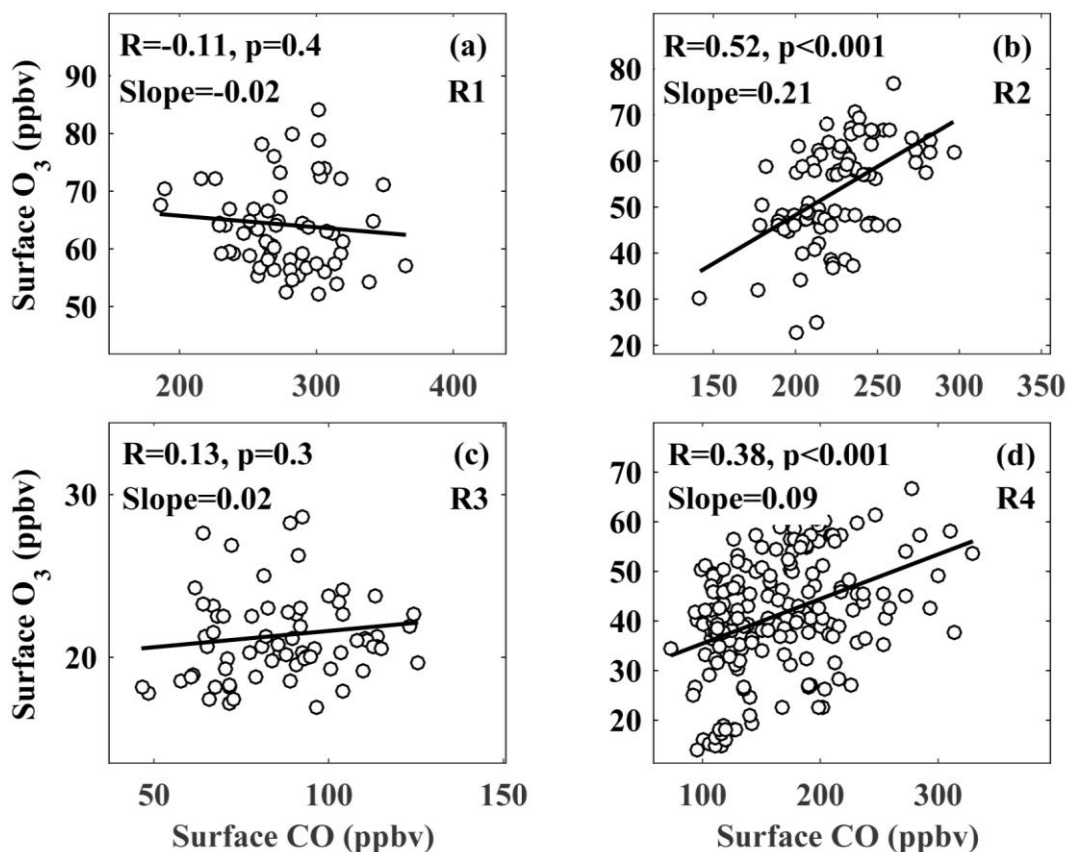
Figure 4.10: Scatter plot between in-situ measured hourly averaged O_3 and CO for the four regions as marked in figure 4.2. The black line represents the linear regression fit.

Figure 4.10 shows the O_3-CO correlation along with O_3/CO slope. The near-zero slope with statistically insignificant correlation (slope=-0.02) between O_3-CO over R1 (coastal) region shows the polluted airmass where production of O_3 would get balanced by destruction, approximately. This region is close to the source region and airmass is relatively fresh (i.e., less photochemically processed). The positive slope of 0.21 over R2 region represents the moderately aged airmass where O_3 production is dominating. This slope is slightly higher than that observed during INDOEX-1999. Stehr et al., 2002 have reported O_3-CO slope of 0.14 in the polluted airmasses from India during the INDOEX, indicating lower ozone production efficiency as compared to those in the mid-latitudes

(slope of 0.3–0.4). While at an urban site, Ahmedabad in India, the ratio was lower (0.16; Lal et al., 2008), the higher ratios (0.24–0.33) have been observed in some of the rural region of India (Lal et al., 2008). The R3 region is under influence of marine airmass and shows the near-zero slope, a situation similar to what is seen for R1. However, absence of significant positive/negative correlation could be due following reasons. Since the airmass is of marine origin and have very low amount of NOx (<0.2 ppbv; figure not shown here) and destruction of O_3 (photolysis of O_3 under sunlight and higher water vapour) would have prevailed over R3 region. The smaller value of 0.09 with statistically significant correlation is seen over R4. The airmass corresponding to the observations over R4 is from central/southern India similar to that over R1, but airmass has spent significant time over marine region and undergone photochemical processing. Also it represents mixed type of airmass. In a nutshell, the positive correlation with O_3/CO ratio of 0.21 over R2 region for the moderately aged IGP airmass shows the relatively higher ozone production efficiency as compared to other regions over the AS and IO.

4.2.9 Comparison of CO levels with previous observations

For the purpose of comparison and assessing trends, the in-situ measurements made in previous campaigns are utilised. Here, the observations of INDOEX-1999, BOBEX-2001 and ICARB-2006 were adopted from INDOEX website (https://data.eol.ucar.edu/dataset), Lal et al., 2006, and Srivastava et al., 2012, respectively. The observations made during BOBEX-2001 and ICARB-2006 campaigns represents the pre-monsoon seasons.

Figure 4.11 shows the spatial distribution of CO over the AS and IO during pre-monsoon season measured during BOBEX-2001 (10–23 March 2001) and ICARB-2006 (18 April–10 May 2006) campaigns. The details of the campaigns are available in Lal et al., 2006 and Srivastava et al., 2012. As seen in figure 4.11a and b, while CO mixing ratio over the equatorial IO was in the range of 120–220 ppbv (BOBEX-2001), it was between 55–125 ppbv over the AS (BOBEX-2001 and ICARB-2006) during pre-monsoon. The higher mixing ratios over the equatorial IO as compared to that over AS is mainly because of the strong synoptic winds which bring continental airmass over to the equatorial IO. The winter-time value was slightly higher (around 250 ppbv, as measured during ICARB-2018, figure 4.2) as compared to that during pre-monsoon over the equatorial IO. An anticyclonic flow centred around 13° N, 62° E (Srivastava et al., 2012; Nair et al., 2013) circulates the marine airmass over the AS and hence due to mixing and chemical removal through OH, surface CO over the AS (figure 4.11b) is lower during pre-

monsoon season (Srivastava et al., 2012). The surface CO mixing ratio was around 100 ppbv near to coastal (southeast AS) region which is much lower than that observed during winter season (250–400 ppbv) as revealed by the present study. The higher values during winter near to the coastal region are due to continental outflow (north-easterly) bringing the polluted airmass.
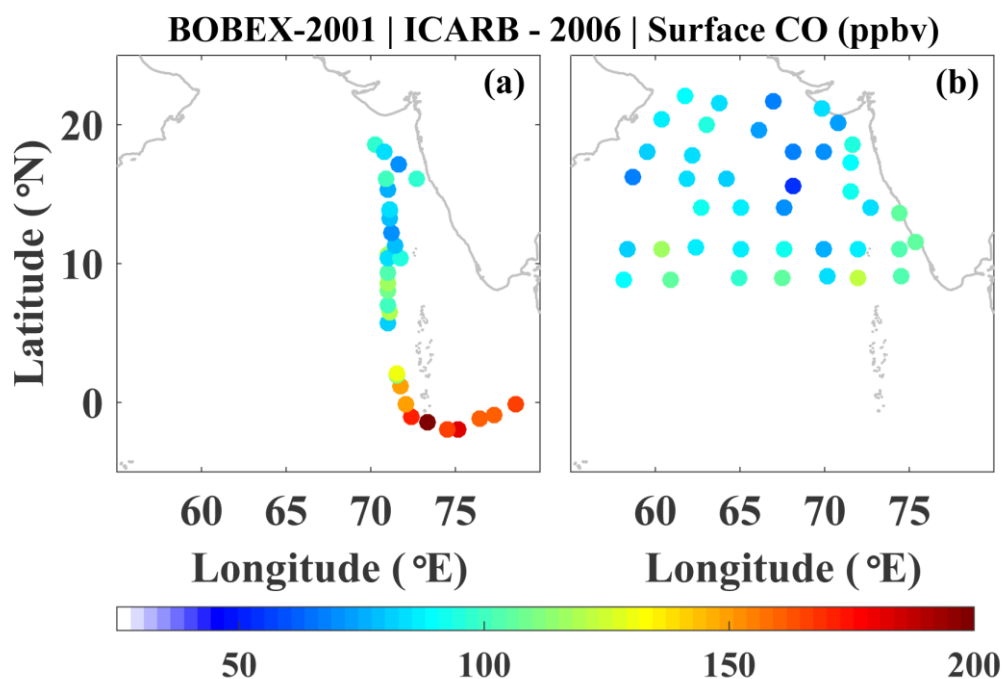
Figure 4.11: (a) Spatial distribution of surface CO over the AS and IO during pre-monsoon season as measured during BOBEX-2001 (10–23 March 2001) and ICARB-2006 (18 April – 10 May 2006) campaigns. The data is adopted from Lal et al., 2006 and Srivastava et al., 2012.

Figure 4.12 shows the spatio-temporal variation of surface CO over northern IO during ICARB-2018 (16 January–14 February 2018) and INDOEX-1999 (22 February–30 March 1999) campaigns. The CO mixing ratios measured during INDOEX-1999 were obtained from the website https://data.eol.ucar.edu/dataset/22.022 (Dickerson, 2007) and the variabilities observed during INDOEX-1999 are discussed in detail by de Laat et al., 2001 and Burkert et al., 2003. Under the INDOEX project, the surface CO measurements were carried out by the University of Maryland during the three legs of the ship Ron Brown's voyage (Leg 1: 22 February–1 March, Leg 2: 4–23 March, Leg 3: 26–30 March). A TECO 48 CO instrument was used for the measurements. The data have been averaged into 30 minute time bins. The identical measurements of CO were carried out by Wagner, V. and Fischer, H., Max Plank Institute (https://data.eol.ucar.edu/dataset/22.156). However, due to some data gaps, the observations made by Dickerson and co-workers (University of Maryland) are utilised in the study.
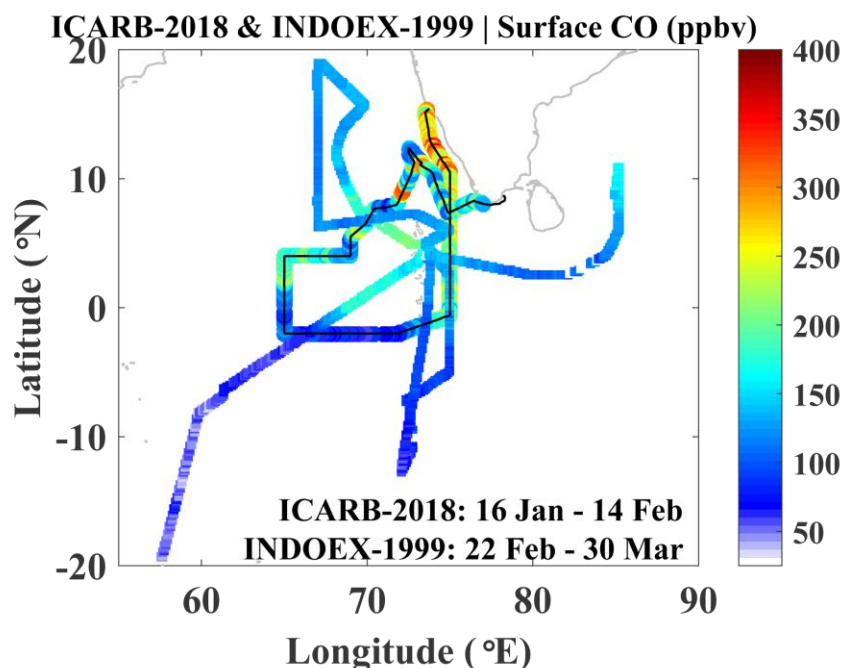
Figure 4.12: Spatial distribution of surface CO mixing ratios over northern IO during ICARB-2018 (16 January–14 February 2018) and INDOEX-1999 (22 February–30 March 1999) campaigns. The observations of CO during INDOEX-1999 were obtained from https://data.eol.ucar.edu/dataset/22.022 (Dickerson, 2007). The continuous black curve distinguishes observations corresponding to the ICARB-2018.

Note that the time period of the measurement corresponds to winter to spring transition. The surface CO mixing ratios around Maldives over the equatorial IO was higher, around 200 ppbv (range: 150–250 ppbv). The measurement covered the southern BoB, where mixing ratios were around 170 ppbv. Over the AS, it was in the range of 100–150 ppbv. The lower CO mixing ratios (50–100 ppbv) over south of the equator was observed. The position of ITCZ during INDOEX-1999 was 3° N–8° S (Naja et al., 2004). South of the ITCZ, CO values were below 50 ppbv as seen in the figure 4.12. As seen from the figure, the regional differences in CO mixing ratios over the northern IO observed during ICARB-2018 are comparable to that during INDOEX-1999. However, the measurements made aboard the ship Ron Brown did not cover south-eastern AS or the coastal AS, where CO mixing ratios were found to be much higher as seen during ICARB-2018. The CO measurements made aboard Sagar Kanya as part of INDOEX, covered the coastal AS also, as compared in the following section.

Figure 4.13 shows the regional changes in surface CO over the IO as observed during various campaigns conducted as part of INDOEX program. INDOEX-1996 (05 January–03 February) and INDOEX-1997 (27 December 1996–31 January 1997) were pre-INDOEX campaigns with only Indian participation. While, INDOEX-1998 (18 February–30 March) was the First Field Phase (FFP) of INDOEX, INDOEX-1999 (20

January–12 March) was Intense Field Phase (IFP) of INDOEX. The variations in regional surface CO levels are shown for the four regions, namely, the coastal AS, AS, IO and southern IO. These regions are defined as 2 degree from the coastline of India, north of 5° N, 5° N–5° S and south of 5° S, respectively. The data, for INDOEX campaigns, were adopted from Naja et al., 2004. Though there exist differences in magnitude over a given region, the regional change in CO mixing ratios are clearly evident. The higher levels of surface CO over coastal AS region, followed by, AS, IO and southern IO is observed during all the campaigns including ICARB-2018, except during INDOEX-1998. Obviously, the higher mixing ratios over the coastal AS is due to proximity to the source region (i.e. continental sources/anthropogenic emission) and minimum mixing ratios over the southern part of IO is due to the fact that it is away from the source region. The mixing with pristine marine air, in addition to removal by OH would also cause reduction in surface CO over the far oceanic region. The higher values of CO over during 1997 is due to the fact that year 1997 is a strong El Niño year. Multivariate ENSO (El Niño Southern Oscillation) Index (MEI) was ~+2.2 (https://www.esrl.noaa.gov/psd/enso/mei/) which represents strong El Niño condition. Dry conditions during El Niño year is conducive for forest fires as well as weak photochemical removal leading to the enhanced level of CO (Sahu et al., 2016).
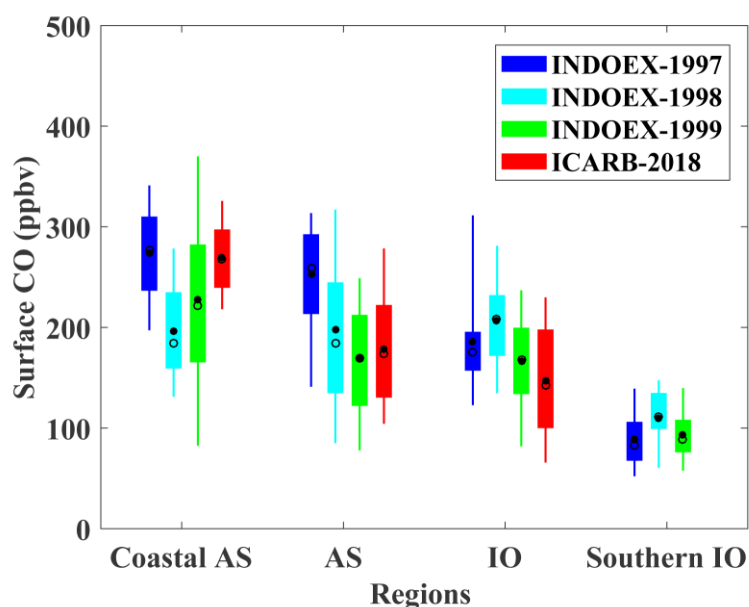
Figure 4.13: Surface CO mixing ratios over different regions of northern IO as measured during various campaigns. In the box plot, while box boundaries represent 25th and 75th percentiles, the whiskers represent 5th and 95th percentiles. The black dots and circles represent the means and medians respectively. The data, except for ICARB-2018, were adopted from Naja et al., 2004.

The changes over a given region during different campaigns reflect the inter-annual variability due to changes in sources, transport or other meteorological

conditions. However the variations can also be attributed to following factors. (1) The defined regions are broader and the measurement locations over the ship-track were not exactly the same during different campaigns. (2) Number of data points over a given regions varied for different campaigns. (3) Measurement period during different campaigns is not identical (INDOEX-1997, 1998, and 1999 were conducted during 27 December 1996–31 January 1997, 18 February–30 March 1998 and 20 January–12 March 1999, respectively).
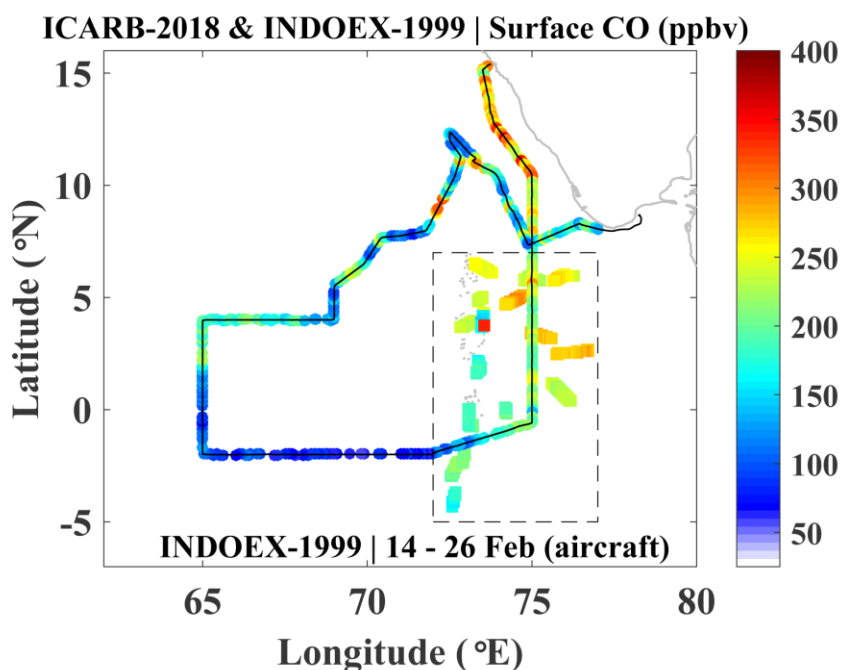
Figure 4.14: Spatial distribution of surface CO mixing ratios over northern IO during ICARB-2018 (16 January – 14 February 2018) and INDOEX-1999 (14–26 February 1999) campaigns. The INDOEX-1999 observations shown in the figure are corresponding to the measurements (within boundary layer, close to the surface, >950 hPa) made aboard the Citation aircraft by Wong and Fischer (and co-workers). The continuous black curve distinguishes observations corresponding to the ICARB-2018.

Figure 4.14 shows the changes in CO over R2 region from 1999 to 2018. The CO mixing ratios was around 250–300 ppbv over R2 region during INDOEX-1999 (14–26 February). Note that though aircraft measurements were made during 14 February–21 March, it is shown for limited period of 14–26 February in order to restrict for winter season. The aircraft measurements shown here are those which were taken below 950 hPa (~550 m) during INDOEX-1999 and hence well within the marine boundary layer. However, our recent measurements over the same region show the CO mixing ratios around 200 ppbv. The averaged CO over the box shown in figure 4.14 during INDOEX-1999 campaign was 229±40 ppbv, which was 200±43 ppbv during ICARB-2018. Reduction of ~30 ppbv over ~19 years corresponds to rate of decrease 0.7% year[-1] with

respect to the level observed during 1999. The long-term trend discussed in next chapter is in line with this observation of reduced CO levels.

4.3   Vertical distribution of CO over the northern Indian Ocean

4.3.1 CO profiles during INDOEX-1999
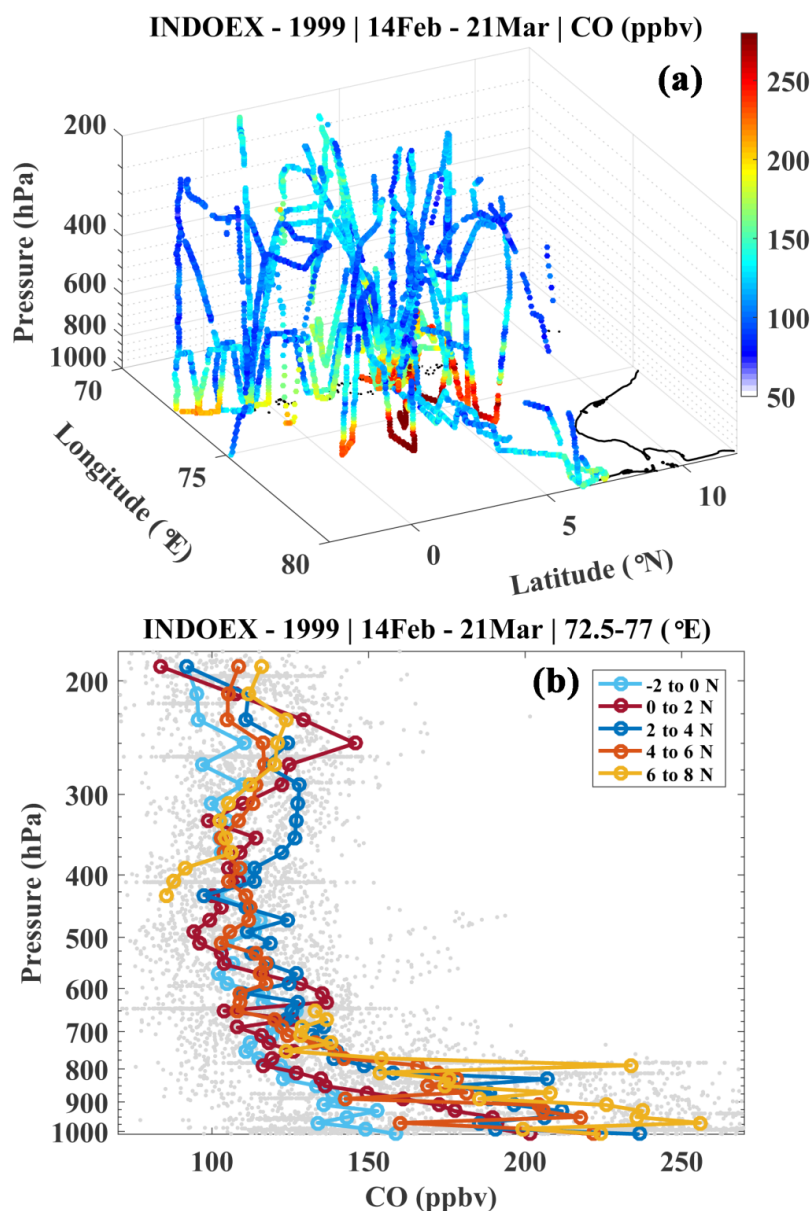
Figure 4.15: Vertical profile of CO mixing ratio over the northern IO during INDOEX-1999 campaign (14 February–21 March). (b) Mean vertical profile of CO mixing ratio averaged over different latitude sectors corresponding to the profiles shown in figure a. The data were obtained from https://data.eol.ucar.edu/dataset/22.159 (Wong and Fischer, 2013). Gray dots show the data points used for averaging.

Figure 4.15a shows the three-dimensional distribution of CO measured during various flights as part of INDOEX-1999 campaign (14 February–21 March). These

observations were made aboard the Citation aircraft by Wong and Fischer (and co-workers) from the Max Planck Institute for Chemistry in Mainz, Germany. A tunable diode laser absorption spectrometer (see Wienhold et al., 1998 for technical details) was used onboard the Citation to determine ambient CO mixing ratios (de Gouw et al., 2001). The altitudinal variations are discussed in detail by de Gouw et al., 2001. As seen in figure 4.15a, the CO mixing ratio is significantly high in the marine boundary layer and decreases with altitude. The data corresponding to the profiles shown in figure 4.15a were separated for different latitude sectors, -2° to 8° N at interval of 2 degree and averaged over respective sectors to show the latitudinal changes in the profiles. Figure 4.15b shows the mean tropospheric profile of CO for different latitude sectors over the IO (longitude sectors: 72.5–77° E). Large spatial variability (125–260 ppbv) is seen in the lower troposphere (below ~800 hPa). Over the southern region (2° S–0° N), CO mixing ratios are significantly lower as compared to that over northern region (0–8° N). Minimum variability and less spatial heterogeneity are seen in the mid-troposphere (700–400 hPa), with the mixing ratio being around 75–125 ppbv. The slight enhancement around 300–200 hPa (around ~9–11 km) is seen in most of the profiles. This upper-tropospheric enhancement was prominent for over 0–2° N region and not seen for the southern region 2° S–0° N).

The above analysis revealed the upper tropospheric enhancement over equatorial IO was observed during INDOEX-1999. Due to the lack of in-situ measurements of CO profiles during ICARB-2018, the variations in upper-tropospheric CO is analysed using satellite-borne MOPITT data and discussed in following sections.

4.3.2 Upper tropospheric CO during ICARB-2018

Figure 4.16 shows the distribution of upper tropospheric CO (at 300 hPa) along with the synoptic winds there during January and February 2018 as obtained from monthly mean data of MOPITT and ERA respectively. Relatively high CO mixing ratios of ~ 100–120 ppbv were observed over southeast AS and equatorial IO (> 67 E) during January 2018 where the wind was easterly or south-easterly which is the typical condition of this month. The higher values in the upper troposphere is similar to that observed during INDOEX-1999 (figure 4.15) However, a significant enhancement (130–150 ppbv) is seen in CO mixing ratio in February 2018 over the equatorial IO (figure 4.16b). Interestingly, a reversal of wind to westerly or south-westerly is observed during February 2018 coinciding with this enhancement. The magenta rectangle depicts the region of maximum increase in CO mixing ratios during February as compared to that

during January (figure 4.16a and b). The region shown by magenta rectangle almost coincides with the region R3 (i.e., equatorial IO; figure 4.2). The enhancement seen over this region during February 2018 is compared with the mean CO mixing ratio for 10 years of February month.
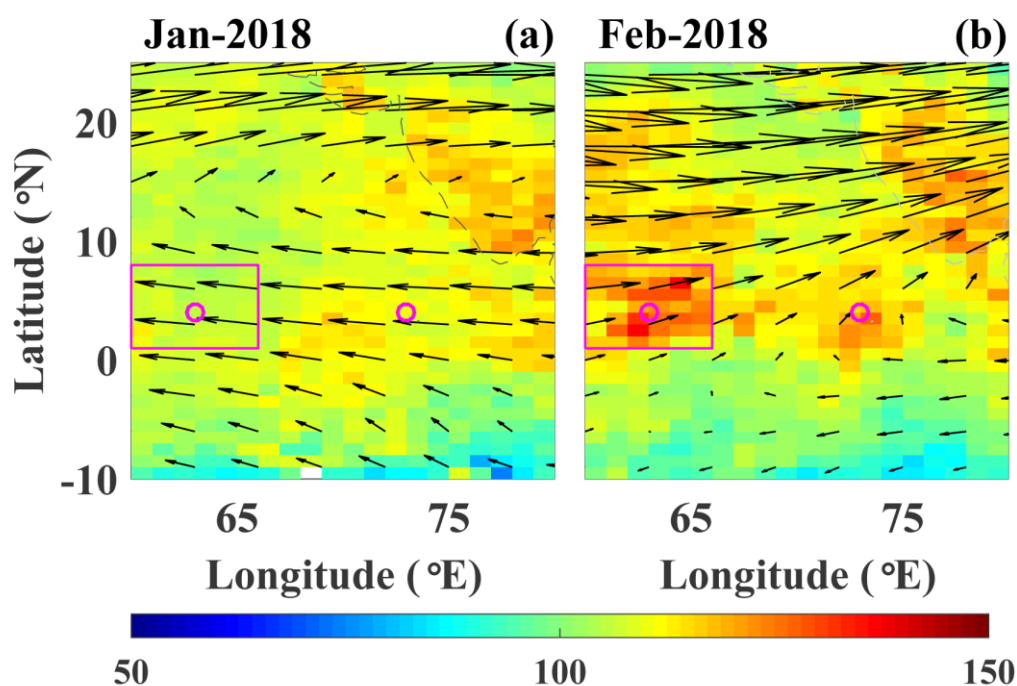
Figure 4.16: Spatial distribution of monthly mean CO at 300 hPa as obtained from MOPITT over northern IO during January and February 2018. Magenta box marks the region where CO enhancement and wind reversal is seen during February 2018 as compared to January 2018. The black arrows super imposed on CO distribution shows the mean synoptic wind at 300 hPa. Magenta circles show the locations over which trajectories are shown in figure 4.18.

Figure 4.17 shows the distribution of percent change/enhancement in upper tropospheric CO (at 300 hPa) February 2018 as compared to mean data of February months of 2007–2017 (10 years). As seen from the figure 4.17 the enhancement is up to 40% over the region as marked by rectangle in figure 4.16. However, there exists enhancement of ~ 10–20% all over the region, which could be due to increase in background level or due to enhanced emission during 2018. Note that CO corresponding to the February 2016 is not included in this mean due to unusual enhancement in this year under the influence of peat fire over Indonesia (Field et al., 2016). Though the extreme fire events were over September–October 2015, its effect was seen till February 2016 (figure not shown here). It is important to note that normally easterly or south-easterly prevails over this region during winter season, but the observed westerly or south-westerly during February 2018 is abnormal.
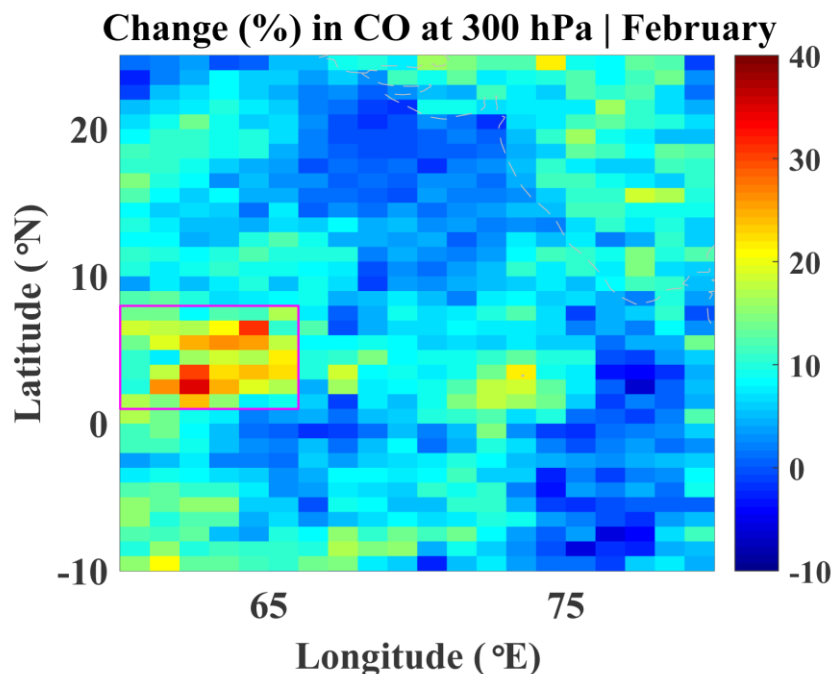
Figure 4.17: Spatial distribution of percentage change/enhancement in CO at 300 hPa during February 2018 as compared to mean of February 2007–2017 (10 years) as obtained from MOPITT over northern IO. Magenta box marks the region where CO enhancement is prominent.

The long range transport is analysed to understand this abnormal enhancement in the upper-tropospheric CO during February. Owing to the longer lifetime of CO in the upper troposphere, 15-days airmass back-trajectories reaching at ~9 km (i.e., ~300 hPa) were obtained using HYSPLIT model. The back-trajectories were simulated for two locations over the equatorial IO as marked by magenta circles in the figure 4.16. Figure 4.18a and b shows the trajectories on daily basis ending over the equatorial IO at ~9km the January 2018 (resulting in 31 trajectories). Figure 4.18c and d are same as figure 4.18a and b but for the month of February 2018. The colour codes denote the altitudes (agl) of the air-parcel along its path. Figure 4.19 shows MODIS detected fire counts during January and February 2018. During the month of January 2018, upper-tropospheric winds over equatorial IO were easterly and corresponding trajectories also from east direction and several trajectories passed/originated from the lower troposphere over Southeast Asia, indicating the possibility of transport from those regions where more pollutants were present (see fire counts over Thailand, and Cambodia in figure 4.19), thus supporting the occurrence of high CO mixing ratios in the upper troposphere over the equatorial IO. However, as mentioned before, synoptic wind is reversed during February 2018 (which is unusual) in the upper troposphere as seen in figure 4.16. Consequently, the trajectories during February 2018 are from western side and several trajectories passed or originated from the lower troposphere over

Africa. As seen in the map of fire counts (figure 4.19) during January and February 2018 as detected by MODIS, biomass burning events are significantly higher over African region where fire counts (sum of fire events over 1° x 1° degree grid) of 0 to 400 reaching 600 were detected (figure 4.19). Thus, transport from the region of high biomass burning over African region would have caused the enhancement in upper-tropospheric CO over the equatorial IO during February 2018.
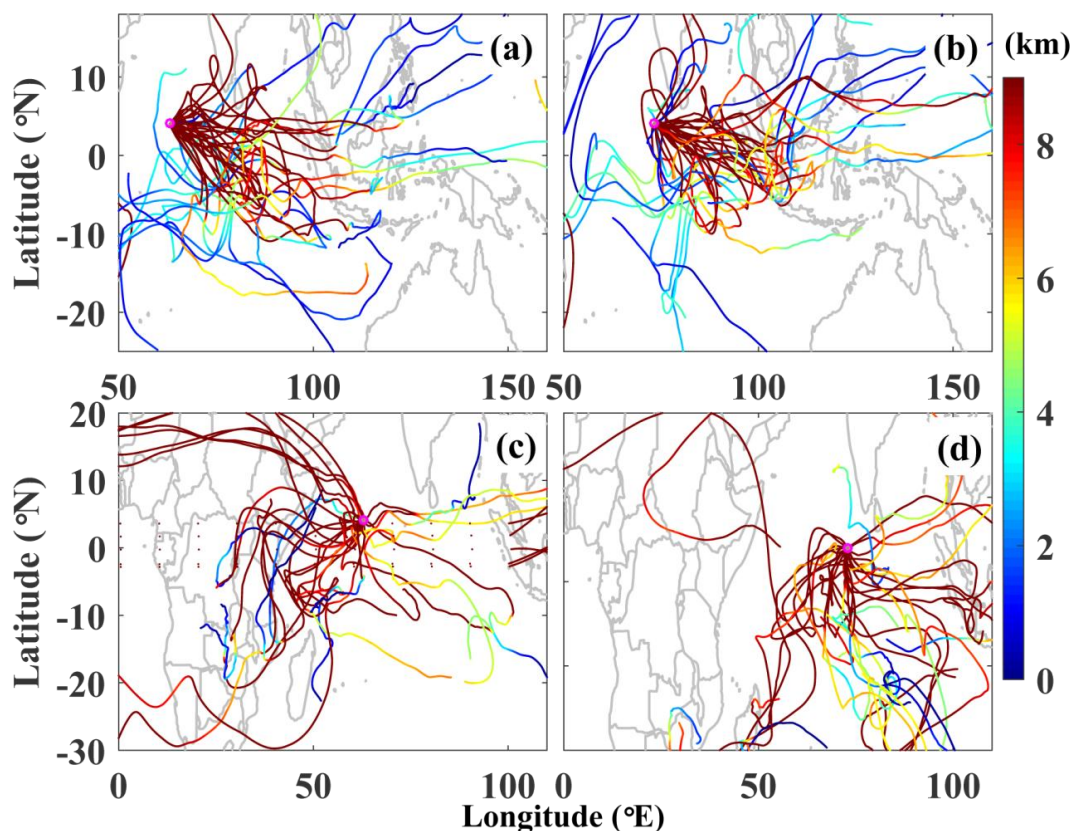
Figure 4.18: Fifteen-day back-trajectories ending at the altitude of ~9 km for January (a-b) and February (c-d) 2009 over equatorial IO at the points marked in figure 4.16. Colour bar shows the height (agl) of the air parcel. The end-points of the trajectories are shown by magenta circles.

In this study, it is also attempted to analyse the upper-tropospheric enhancement in CO during February 2018 on a larger scale, utilising the synoptic vertical and horizontal winds focusing on the walker circulation cell as well as maundering of subtropical jet. Walker circulation is the atmospheric east-west (longitudinal) circulation over the equatorial region (Asnani, 2005; Lau and Yang, 2015). This comprises of different circulation cells spanning over different longitudinal sectors around the equator. One of the major rising branches of the Walker circulation is over the Southeast Asia region including, Indonesia, Philippines and Papua New Guinea. It is located between the Indian and Pacific Oceans, maximising the updraft around the Indonesian (115–120° E) region. The outflow of this rising branch results in easterlies in

the upper-troposphere (300–200 hPa) and the subsidence over the IO, completing the cell (so called "Indonesia-IO cell"). Also, there exists another, comparatively weaker rising branch over Africa region and subsiding over the IO (so called "Africa-IO cell"). This feature prevails throughout the year; however, strength of updrafts/downdrafts varies on seasonal basis (Asnani, 2005; Lau and Yang, 2015).
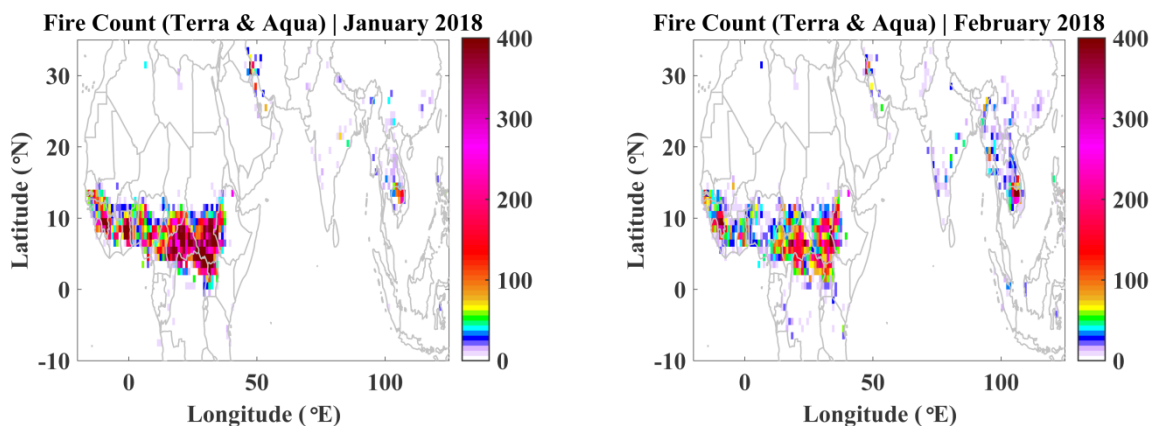
Figure 4.19: Fire counts over 1° × 1° degree grids (detection confidence >80%) as detected by MODIS (Terra and Aqua) during January and February 2018.

Figure 4.20a and b show the longitude slice of mean vertical wind at 2° N latitude (representing equatorial IO) during January 2018 and February 2018. Figure 4.20c and d show cross section of zonal-vertical wind with red arrows depicting updraft/downdraft and outflows. Two of the rising branches (vertical updrafts) of walker circulation cells over African and Indonesian region and descending branch (downdrafts) of the cell over the IO (i.e. IO being a broad region of subsidence) are clearly evident during January 2018, as seen in figure 4.20a and c. The outflow of the convection over Indonesian region results in easterlies (around 300–200 hPa) over the equatorial IO (see the winds in figure 4.20c and e). Note that the high lower tropospheric CO prevails over Southeast Asian region over which fire counts are also seen (figure 4.20a). The updrafts over Indonesian regions brings lower tropospheric CO emitted from anthropogenic activity as well as biomass burning over Southeast Asian region to the upper troposphere (300–200 hPa) over the equatorial IO. This causes enhancement in the upper-tropospheric CO over the region. Interestingly, this walker circulation cell (Indonesia-IO cell) is disturbed during February 2018. Note that the easterly winds in the upper troposphere have changed to westerly during February 2018 (figure 4.20f). The descending branch of walker circulation cell has disappeared over the major part of the IO and instead updraft is seen over the IO as shown in figure 4.20b and d. Extensive forest fire events over African region (fire counts 10–400 as shown in figure 4.19a and

b) enhanced the lower tropospheric CO. The rising branch of Africa-IO cell uplifts the CO to the upper troposphere over African region causing enhancement in the upper-tropospheric CO over the region.
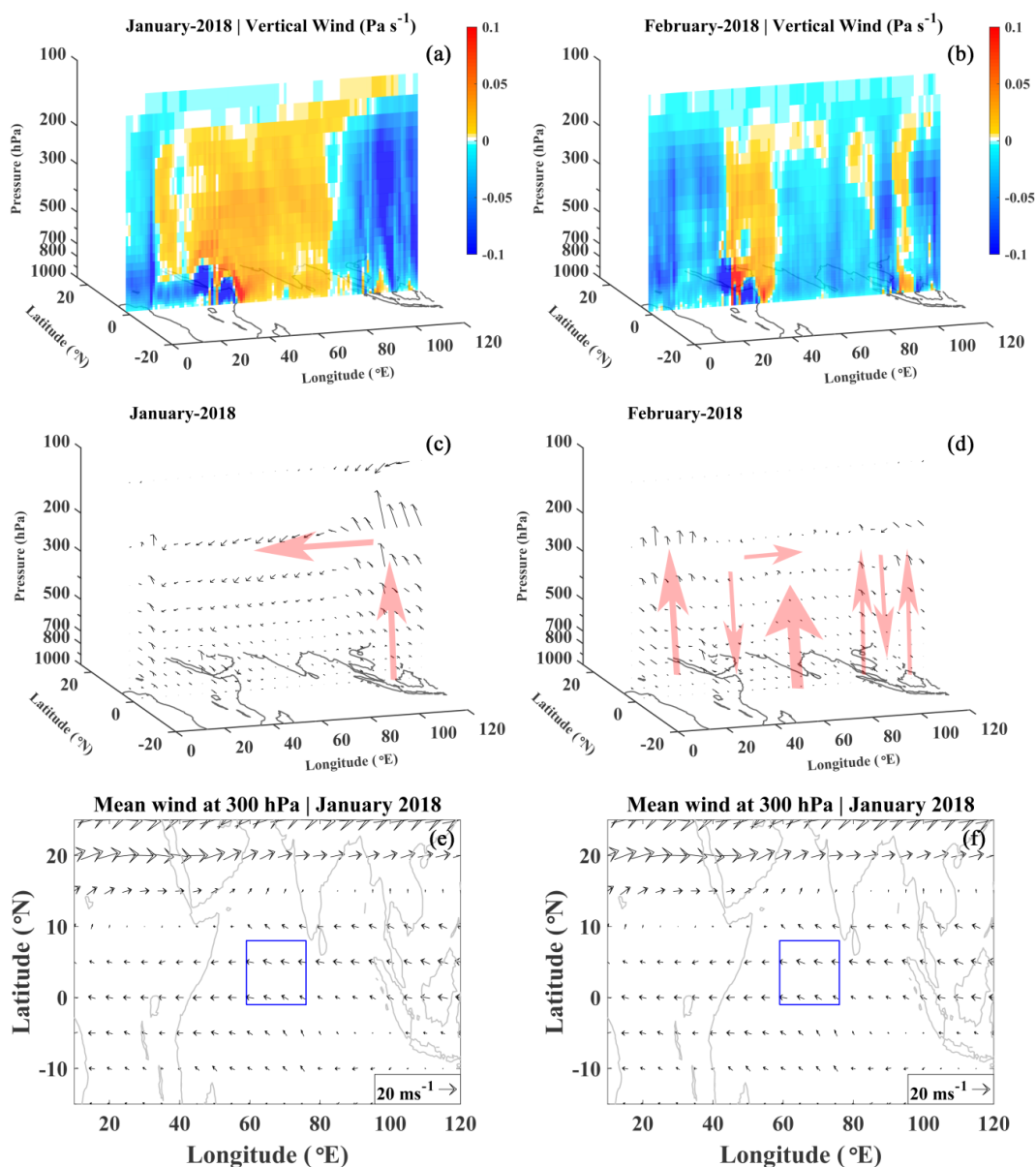
Figure 4.20: The longitude slice (at 2° N latitude representing equatorial IO) of mean vertical winds (a-b), combined zonal and vertical winds (c-d) and spatial distribution of mean synoptic wind at 300 hPa (e-f) during January and February 2018. The red arrows in figure (c-d) mark updraft/downdraft and outflows. The blue rectangle highlights the region of higher CO and wind reversal.

The stronger westerlies around 30° N represent the sub-tropical jet with wavy nature (so-called maundering) along with it. The maundering is the deviations from westerly to south-westerly or north-westerly. This sub-tropical jet with its maundering would penetrate approximately 8–10° N (Asnani, 2005). In January 2018 it penetrated up to ~15° N (figure 4.20e). However, as seen in figure 4.20f, during February 2018, it

has penetrated upto the equator and westerlies/south-westerlies are seen over the equatorial IO. This brings the convectively uplifted CO from African region to the equatorial IO causing upper-tropospheric enhancement in CO as seen during February 2018. Thus, the influence of forest fire occurred over African region caused the higher CO in the upper troposphere during February 2018.

Thus, in short, the combined effect of unusual convection (updrafts) over the equatorial IO and deeper penetration of sub-tropical jet brought the influence of African forest fire burning causing the enhancement of 20–40% in the upper-tropospheric CO over the equatorial IO during February 2018.

In order to investigate whether such changes (i.e., presence of westerlies) are frequent, 10 years of upper-tropospheric CO over the equatorial IO is analysed along with the zonal wind.
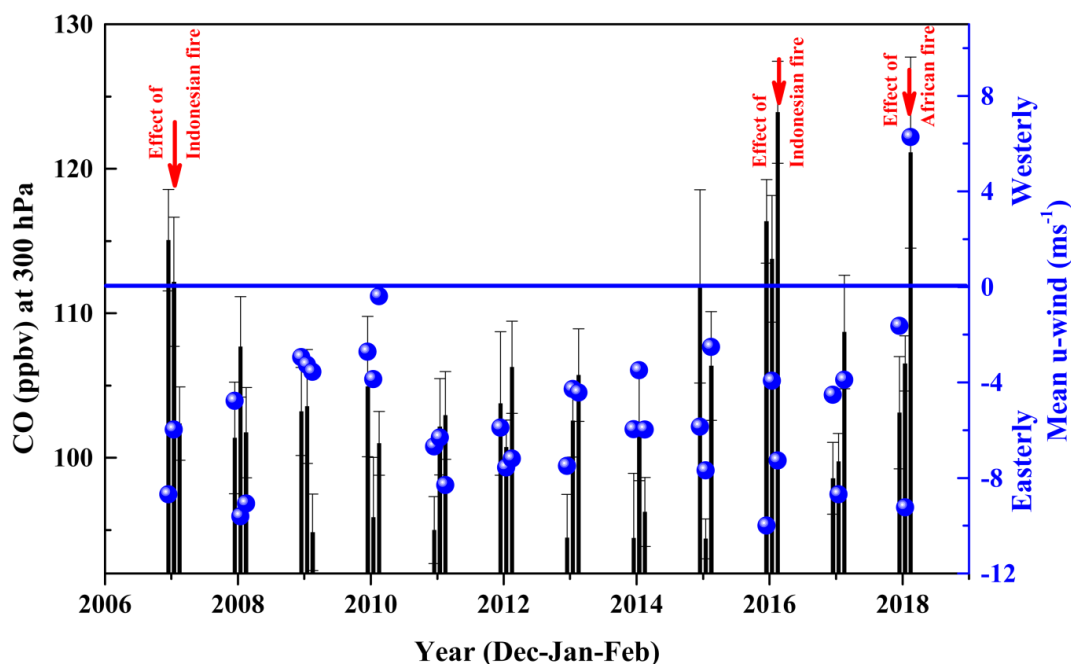
Figure 4.21: The inter-annual variations in winter-time upper tropospheric CO and zonal wind (at 300 hPa) averaged over the box shown in figure 4.17. CO is obtained from MOPITT and u-wind is obtained from ERA-Interim. Error bar represents the standard deviation over the box.

Figure 4.21 shows the winter-time monthly CO and zonal wind at 300 hPa averaged over the region shown by a blue rectangle (60–66° E, 1–8° N) in the figure 4.17 during last 10 years, from 2007–2018. It is clearly seen that over the equatorial IO, easterlies prevails in the upper troposphere during winter. However, it is not the case for February 2018 as wind was westerly over this month alone. Except for the year 2007 and 2016, CO mixing ratios at 300 hPa were in the range of 95–105 ppbv (mean

~100 ppbv). It was around 121 ppbv (~20% higher) during February 2018. The enhancement in the upper-tropospheric CO seen during December-January-February of 2007 and 2016 is corresponding to the extensive peat fire episodes during September-October-November months of 2006 and 2015, as reported by Huijnen et al., 2016 and Field et al., 2016. Owing to the longer lifetime of CO in the upper-troposphere, the remnant effect is seen during of December-January-February of 2007 and 2016. The episode of peat fires 2015 was more prominent than that of 2006 (Huijnen et al., 2016; Field et al., 2016). This is in line with the fact that 2015 was stronger El Niño year (MEI=+2.0) as compared to the El Niño year 2006 (MEI=+0.7; https://www.esrl.noaa.gov/psd/enso/mei/). Thus, while the enhanced CO values during 2007 and 2016 were due to enhancement in the source (i.e., fires over Indonesia), the enhanced mixing ratio during February 2018 is attributed to unusually observed westerly over equatorial IO which would have brought the influence of African fire. Also, this reveals that the observed changes in the upper troposphere during February 2018 was unusual as such changes were not observed over a decade.

The difference between the mean of February 2018 (121 ppbv) as compared to winter months of other years (101 ppbv, excluding year 2016), is approximately 20 ppbv. Note that the mean values presented here are mean over 42 grid points. Considering the retrieval uncertainty in each grid point and following the error propagation formula, the error in this representation of regional mean values is ~5 ppbv. Thus, the enhancement of ~20 ppbv is beyond the error in the mean value and hence this difference is statistically significant. Also note that standard error corresponding to mean values ranges from 0.2 to 2 ppbv.

4.4 Summary

The shipborne in-situ measurements of surface CO conducted over the northern IO during ICARB-2018 (winter season) complemented with satellite based upper-tropospheric CO (from MOPITT) are analysed in the light of synoptic winds, airmass back-trajectories, CAMS reanalysis data and fire counts. The in-situ observations of surface O_3 and CO observations available in the literature are also utilised in the analysis. The major findings of this analysis are summarised as followings.

- The surface CO varied from <50 to 365 ppbv (mean=179 ppbv; standard deviation=67 ppbv) over the southeast AS and the equatorial IO during winter season. The study region encountered three different types of airmasses, from

central/southern India, eastern IGP and marine region of AS. The higher mixing ratios over southeast AS close to the coastal region showed higher CO mixing ratios as high as 365 ppbv which is due to proximity to the source region.

- The comparison of MOPITT retrieved surface CO with the in-situ observations (including previous studies) shows good agreement with correlation coefficient of 0.76–0.8 indicating the potential of surface retrievals of MOPITT for its utilisation to make broader inferences on the variations of CO.

- The residence of airmass over the land was estimated based on HYSPLIT back trajectories which showed positive correlation of R=0.68 with CO variability indicating the continental influences. This shows that the larger the airmass resides over the land (where CO sources exist) as compared to oceanic region, the higher the CO mixing ratios in the airmass.

- The comparison of surface CO observations with CAMS reanalysis data shows good agreement with correlation coefficient of 0.77. The analysis of CO from CAMS in conjunction with airmass back-trajectories and emission inventory shows that how CO mixing ratios gets reduced along the transport pathways due to dilution by mixing with oceanic airmass and removal by OH from its prominent source regions (e.g., Kolkota and Mumbai).

- The mean surface CO level during ICARB-2018 over the IO was lower by ~30 ppbv as compared to the level 19 years before observed during INDOEX-1999. This indicates the possibility of decreasing trend in surface CO (with probable rate of 0.7% year^{-1}).

- The MOPITT retrieved upper-tropospheric CO (at 300 hPa; ~9–12 km) shows enhancement which is in line with that observed during INDOEX-1999 in the in-situ measured profile of CO. Relatively higher CO mixing ratios (100–120 ppbv) was observed over southeast AS and the equatorial IO in the upper-troposphere during January 2018. This is attributed to long-range transport from the lower-troposphere of Southeast Asian region under the prevailing convective updrafts which outflow (easterlies) over the equatorial IO, which is the "Indonesia-IO" walker circulation cell. The biomass burning and other anthropogenic emissions over Southeast Asian region contribute to this.

- Interestingly, upper-tropospheric CO was higher up to 40% (130–150 ppbv) over the equatorial IO during February 2018 as compared to the corresponding February values of previous 10 years. This enhancement coincides with unusually observed westerlies over the equatorial IO. The analysis of veridical as

well as horizontal winds, along with fire counts reveals that usual "Indonesia-IO" walker circulation cell is disturbed during February 2018 and the combined effect of unusual convection (updrafts) over the equatorial IO and deeper penetration (up to the equator) of sub-tropical jet brought the influence of forest fire burning occurring over the African region. The analysis of winter time upper-tropospheric zonal wind along with CO over the equatorial IO shows that easterlies prevail over this region and brings the influence from Southeast Asia including Indonesian forest fires, however, westerlies were not observed over a last decade, except during February 2018 which brought the influence of African forest fires.

<div align="right">

Chapter - 5

</div>

<u>Seasonal and long-term trends in tropospheric CO over Indian landmass on regional basis</u>

5.1   Introduction

The in-situ measurements of surface CO are available for limited study periods over a few sites like Mumbai (Marathe and Murthy, 2015), Delhi (Peshin et al., 2017; Chelani 2012), Kanpur (Gaur et al., 2014), Ahmedabad (Lal et al., 2000; Sahu and Lal, 2006; Chandra et al., 2016), Udaipur (Yadav et al., 2014), Bhubaneswar (Mahapatra et al., 2014), Anantapur (Reddy et al., 2008), Pune (Beig et al., 2007), Agra (Verma et al., 2017; Saini et al., 2009; 2014), Cape Rama (https://gaw.kishou.go.jp/search/graph/co_cri_surface-flask_16_9999-9999_monthly.txt; Bhattacharya et al., 2009), Nainital (Sarangi et al., 2014), Gadanki (Naja and Lal, 2002), Mt. Abu (Naja et al., 2003), Hissar (Lal et al., 2012), Kolakata (Mallik et al., 2014), Hyderabad (Latha and Badarinath, 2004; Badarinath et al., 2007) and Trivandrum (Kumar et al., 2006; 2008 and present study) over the Indian region. These studies mainly discuss the variabilities in surface-CO on diurnal and seasonal scales, with limited duration datasets. However, measurements over the some of the sites (like Hissar, Hyderabad, etc) are during a particular season. Since these observations are limited in terms of time and space, a comprehensive picture of CO over Indian region cannot be brought out. In this context, utilisation of satellite observations becomes helpful in deriving the comprehensive temporal and spatial features.

As discussed in Chapter - 2, various satellites like MOPITT, AIRS, TES, IASI, MLS, and SCIAMACHY (operational till the mission ended in 2012) are in the orbits provide the tropospheric CO with near daily coverage over the globe. However, TES global coverage is available during global survey mode only. The comparison studies have shown that retrievals from these instruments are more or less in agreement among themselves (Luo et al., 2007a; Warner et al., 2007). However, in the present study, MOPITT retrievals were utilised extensively as this dataset is available for the longest period of ~ 18 years (2000–2018). The inter comparison of MOPITT retrievals with in-situ measurements are carried out over the oceanic regions of BoB, AS and IO, as

discussed in section 3.2.2 and 4.2.4. However, due to different (as compared to ocean) thermal emissivity and heterogeneity in it, it is reasonable to validate/compare the MOPITT retrievals with in-situ measurements over the land region.

This chapter presents a comprehensive study on the temporal and spatial variation of tropospheric CO using latest retrievals, V7-TIR, of MOPITT over Indian land mass and its association with biomass burning activities (assessed in terms of fire count), anthropogenic activity and meteorology (synoptic winds and convective activity) based on ~18 years of data from March 2000–February 2018. Prior to this analysis, a comparison of MOPITT data and in-situ measurements is also carried out. In addition, the detailed analysis of long term trend in CO (lower-tropospheric, upper-tropospheric and columnar) is carried out. The trend in lower-tropospheric CO observed by MOPITT on the global scale is verified/validated utilising the in-situ observations of surface CO from the NOAA network. In addition, the trend analysis of upper tropospheric and columnar CO is extended globally utilising the data from multiple satellites.

5.2 Surface CO mixing ratios over India and its seasonal variation: In-situ versus MOPITT
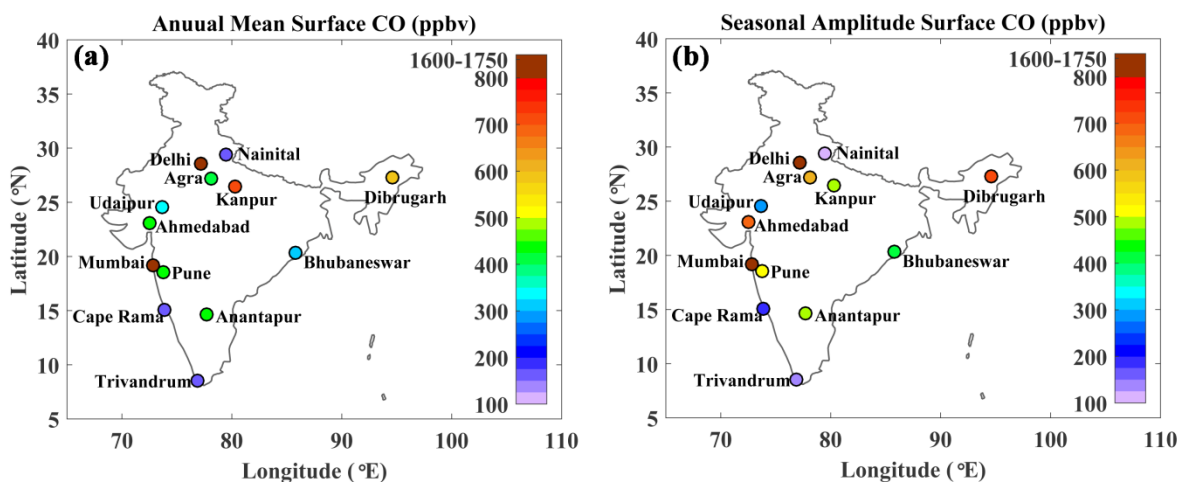
Figure 5.1: Annual mean (a) surface CO mixing ratios (in-situ observations) and (b) Seasonal amplitudes of CO over different sites. Except for Trivandum, monthly mean were obtained from literature as listed in the table 5.1. The names of sites are labelled in the figures.

In order to know the spatial heterogeneity, mean levels of surface CO, and seasonal amplitude, the sites are selected such that in-situ measurements of surface CO with a complete seasonal cycle are available at these locations. Annual mean surface CO was obtained from monthly mean values, which were obtained for different sites from the literature (except for Trivandrum) as shown in table 5.1. The annual average and

the seasonal amplitude are shown in figure 5.1. The highest CO mixing ratios are seen over Delhi (1616 ppbv) and Mumbai (1748 ppbv) with almost same magnitude of seasonal amplitude (1682 ppbv for Delhi and 1627 ppbv for Delhi). These extremely high values correspond to the measurements at the air quality monitoring stations which are situated close to the emission sources (e.g., heavy vehicular traffic area). In case of Mumbai, site is located at Bandra and close to a major roadway which leads to higher levels of pollution from vehicular sources (Marathe and Murthy, 2015). At Delhi, surface CO levels correspond to the eight air quality monitoring stations which are located over vehicular traffic region (Peshin et al., 2017). The studies by Peshin et al., 2014, Tiwari et al., 2015, Tyagi et al., 2016 and Sharma et al., 2016 reported mean mixing ratios of CO as 1620 ± 690, 1970, 2300 ± 600 and 1820 ± 520 ppbv over Delhi during 2011–2013, 2010–2012, 2014 and 2012–2014 respectively.

Table 5.1: The details of sites over which surface CO observations are available as shown in figure 5.1.

Site (longitude, latitude)	Description	Study Period	Reference
Mumbai (72.88° E, 19.2° N)	Polluted	2008–2009	Marathe and Murthy, 2015
Delhi (77.23° E, 28.61° N)	Polluted	2011–2012	Peshin et al., 2017
Agra (78.08° E, 27.17° N)	Urban	2015	Verma et al., 2017
Kanpur (80.33° E, 26.46° N)	Urban	2011–2013	Gaur et al., 2004
Ahmedabad (72.55° E, 23.03° N)	semi-arid, urban	2015	Chandra et al., 2016
Udaipur (73.68° E, 24.58° N)	Urban	2010	Yadav et al., 2014
Bhubaneswar (85.83° E, 20.3° N)	Urban	2011–2012	Mahapatra et al., 2014
Anantapur (77.65° E, 14.62° N)	semi-arid	2001–2003	Reddy et al., 2008
Pune (73.81° E, 18.54° N)	semi urban	2004	Beig et al., 2007
Cape Rama (73.83° E, 15.08° N)	Coastal	2009–2012	https://gaw.kishou.go.jp

Nainital (79.45° E, 29.37° N)	High altitude site (1958 m amsl)	2009–2011	Sarangi et al., 2014
Trivandrum (76.9° E, 8.5° N)	Coastal	2009–2010	Present work
Dibrugarh (94.6° E, 27.3° N)	Urban	2012–2013	Bhuyan et al., 2014

In contrary, Cape Rama, Goa and Trivandrum are on the west coast of India and under the influence of relatively cleaner marine airmasses (specifically during monsoon, in addition to sea breeze during daytime almost over entire year). The site, Cape Rama, is devoid of any vegetation over a scale of 50 m on all sides and is at least a few hundred metres away from sparse habitation. The sampling location is on flat rocky terrain, about 60 m above sea level and overlooks the sea (Bhattacharya et al., 2009). Similarly, the measurements at Trivandrum are corresponding to the site, Thumba, which is situated just 500 m away from the Arabian Sea coast, with sandy terrain and a less populated area. The experimental set-up for trace gas measurements at Thumba observatory is shown in figure 2.1. At this site, the strong sea-breeze (SB)/land breeze (LB) activity prevails during daytime, throughout the year (Narayanan, 1967; David and Nair, 2011). Nainital is a high altitude site (1958 m amsl) located at the Manora Peak in the central Himalayas. Thick vegetation cover surrounds the measurement site and there is no industry in Nainital and total population is about 0.5 million. Observations at Nainital represent free-troposphere, above the boundary layer. The annually averaged surface CO mixing ratios and the seasonal amplitudes are comparable over Cape Rama (175 ppbv) and Trivandrum (140 ppbv). The seasonal amplitude is lowest over Nainital (115 ppbv). The other locations, Ahmedabad, Udaipur, Pune, Anantapur, Kanpur, Agra and Dibrugarh are mainly urban areas, however, unlike Delhi and Mumbai sites, measurement stations are away from the direct influence from polluted/source regions. Over these regions, while annually mean ranges 315–715 ppbv being higher over Kanpur followed by Dibrugarh, the seasonal amplitude ranges 280–700 ppbv.
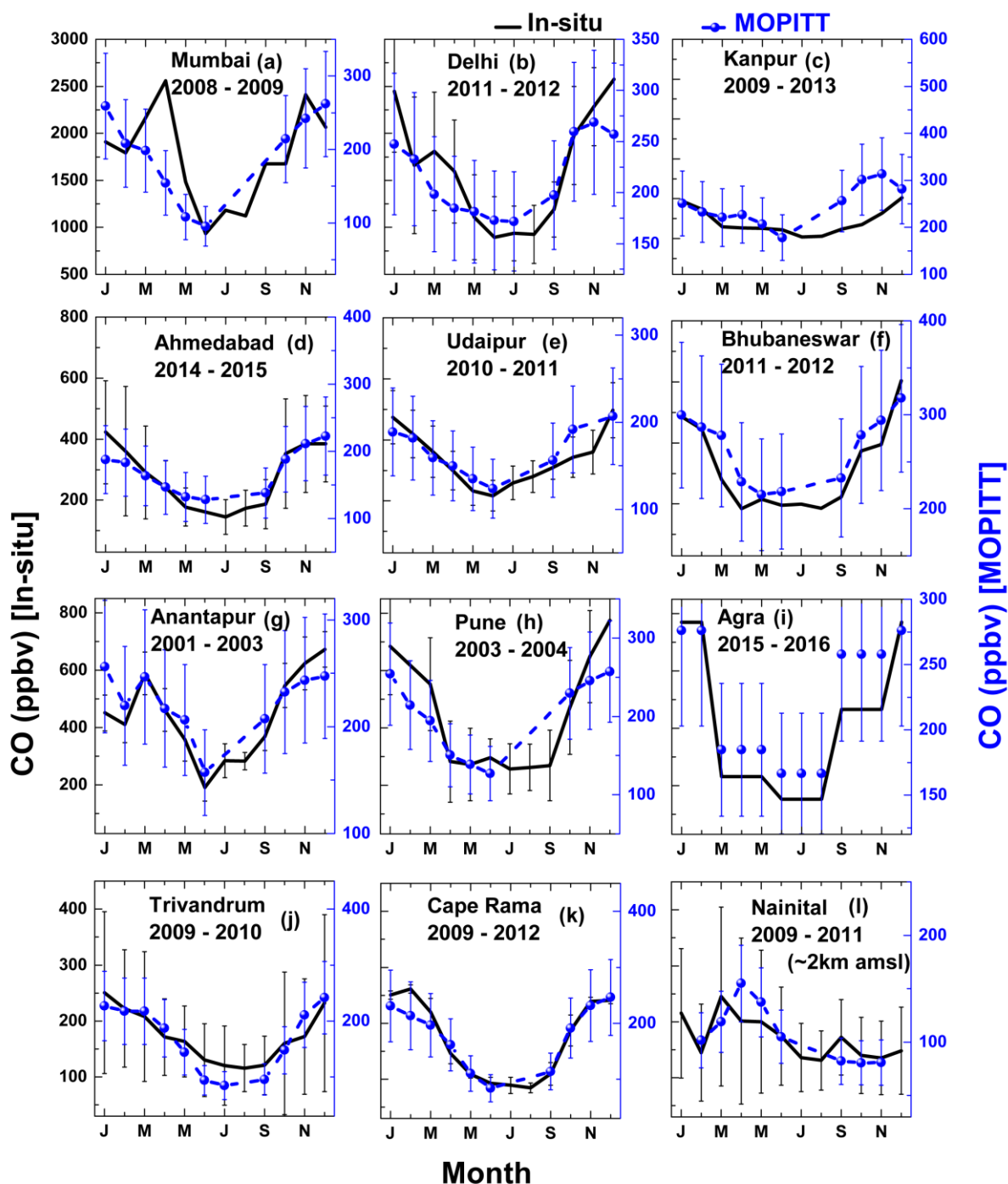
Figure 5.2: Seasonal variation of surface CO from in-situ measurements (black curve) and from MOPITT surface retrievals (blue curve) over different site in India. In-situ measured seasonal variations (except for Trivandrum) are adopted from the literature. The site location and time period of seasonal variation are labelled in the respective plots. The site, Nainital is a high altitude site (~2km amsl). Note that the scale of right Y-axis is different from that of left Y-axis, except for Trivandrum and Cape Rama. For the site, Ahmedabad, the daytime monthly mean values are shown here.

The in-situ measurements over the chosen sites (figure 5.1) are available since 2001 so that inter-comparison of MOPITT retrieved seasonal variation of CO can be done. The inter-comparison between the MOPITT retrievals over 1° × 1° degree grids

and the in-situ measurements were carried out on seasonal basis. In fact, the direct comparison (without considering the averaging kernels and a priori information) evaluates the actual performance of MOPITT retrieval algorithms for surface-level CO (Deeter et al., 2012). Figure 5.2 shows the seasonal variations based on in-situ observations and co-located (within ~110 x 110 km^2) MOPITT retrieved gridded (1° x 1° latitude/longitude) surface CO. Note that the scale for right Y-axis is different from that for left Y-axis (except for Trivandrum and Cape Rama). For coastal locations, Trivandrum and Cape Rama, MOPITT retrievals capture the seasonal pattern as well as the CO levels. However, all other locations, even though MOPITT surface retrievals could capture the seasonal trend, the absolute CO mixing ratios as well as seasonal amplitude is underestimated. This underestimation is very high over Mumbai and Delhi locations. Indeed, it is expected that MOPITT retrieved surface CO will have lower values than in-situ point measurements due to following reasons: (1) In-situ measurements are point measurements and sites like Mumbai and Delhi, measurements are close to source regions (vehicular emission) and measurements are directly influenced by point or line sources. MOPITT retrieved data utilised here are level-3 gridded data with grid size of ~ 100 x 100 km^2 area. Due to averaging over larger area, MOPITT values could be lower. (2) MOPITT has lower sensitivity in the lower troposphere in particular for the surface retrievals. This also could be partially responsible for estimation of lower values of surface CO. In fact, the seasonal trend in surface CO is well captured by MOPITT which shows its potential for the study addressing broader features/changes occurring in the lower-tropospheric CO (3) in the case of in-situ measurements, the monthly averaged values include day as well as night time measurements. During nighttimes boundary layer height is low which limits the mixing of CO to the lower-altitude leading to enhanced mixing ratios during nighttime. Inclusion of these nighttime measurements in the monthly average, raise the monthly mean values. In contrast to this, MOPITT observations utilised in this study are corresponding to daytime (around 10:30 am local time). This also causes underestimation of monthly mean CO (4) Moreover, the surface retrievals of MOPITT represent CO over ~100 hPa thick layer (1000 to 900 hPa). The mixing ratio corresponding to ~100 hPa thick layer would be slightly lower than that at the surface, as source of CO is at the surface.

Apart from the comparison, the seasonal variation over most of the locations show that surface CO peaks during winter and minimises during monsoon seasons. However, the seasonal behaviour is different for the high altitude station, Nainital, where CO peaks during pre-monsoon (summer/spring) months of April-May. This is

due to convective updraft during pre-monsoon seasons and biomass burning activities over northwest (Hariyana-Punjab region) India (Sarangi et al., 2014). The causes for seasonal variations are discussed in section 5.6.

This analysis shows that MOPITT could capture the seasonal changes in surface CO reasonably well and this data can be used to understand the temporal changes on monthly/seasonal scale over broad regions. With this understanding, in this study, the Indian land mass was divided to 8 different regions to study the large scale changes in CO, the details of which are given below.

5.3   Study regions over India
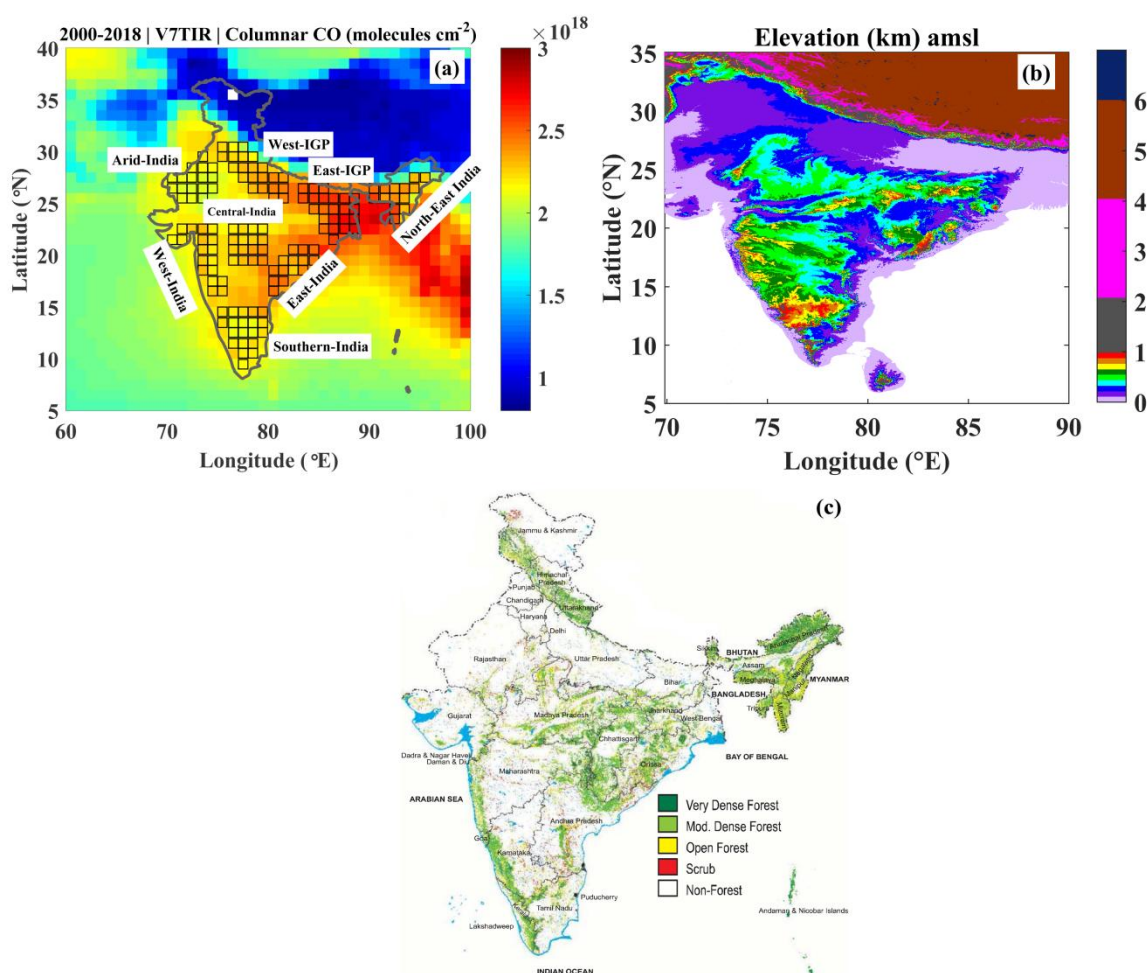
Figure 5.3: (a) Map of India showing the selected 8 study regions. Colour map in the background shows columnar CO averaged over ~18 years (March 2000–February 2018) as obtained from MOPITT (level-3, V7-TIR). (b) Elevation map of India showing the terrain features. (c) Forest cover map of India showing the different forest cover over India as per 2011 report of Forest Survey of India, Ministry of Environment & Forest, Government of India.

The colour map shown in the background of figure 5.3a represents the columnar CO averaged over ~18 years, as obtained from monthly mean level-3 MOPITT retrievals

(V7-TIR, degree of freedom > 1). Based on the spatial patterns in the columnar CO as viewed through satellite based maps (figure 5.3a), and the regional variations in CO emission based on inventories like INTEX-B, REAS, HTAP, etc. (not shown here) eight distinct regions over the Indian landmass were selected for this study. The selected study regions are Arid-India (A-I), West-IGP (W-IGP), East-IGP (E-IGP), NorthEast India (NE-I), West-India (W-I), Central India (Central-I), East-India (E-I), southern India (S-I). Note that each region consists of 14–23 grids of size 1° x 1° latitude/longitude. Figure 5.3b shows the terrain features over the study regions. Since forest fires are also the source of CO, it is important to keep view of forest cover over the study region which is depicted in figure 5.3c as per 2011 report of Forest Survey of India, Ministry of Environment & Forest, Government of India (http://www.fsi.org.in/). Note that NE-I, E-I and Central-I regions covers significant area of forest. The total forest over India is distributed over a geographical area of 3,287,263 km^2. In this work, the monthly mean columnar CO along with the lower and, upper atmospheric CO data averaged on region basis have been utilised.

Table 5.2 summarises the major characteristics/peculiarities of the different study regions along with the annual mean columnar CO as retrieved by MOPITT. Note that CO columnar concentration level over A-I (desert region) is lower as compared to the other land regions where as it is higher over E-IGP as observed by MOPITT. Over W-IGP region, an agricultural zone, agricultural waste burning is prominent as compared to any other region. The regions NE-I, E-I, Central-I and W-I are different geographically, cover the forest area and significant biomass burning activity persist over the regions. The southern part of India, S-I has humid climate and remains under the influence of winds from ocean (AS, BoB) for a significant period of time. The significant columnar CO over oceanic regions, where strong source of CO does not exist, is due to transport from nearby land regions. However, the oceanic regions are not included in this analysis, a detailed account of which is included in chapter 3 and 4. It is important to note here that regional difference in averaged column CO is $\sim$ 3 x 10^{17} molecules cm^{-2} (2.1 to 2.37 x 10^{18} molecules cm^{-2}).

Table 5.2: Characteristic of different study regions over India as shown in figure 5.3a.

Region	Altitude range (m)	Mean column CO x 10^{18} (molecules cm^{-2})	Population Density (persons km^{-2})	Features
Arid-India (A-I)	~0–500	2.12±0.17	100–250	Desert region

West-IGP (W–IGP)	~0–200	2.27±0.18	500–1000	Well-known for agricultural activity of Kharif and Rabi
East-IGP (E-IGP)	~0–600	2.53±0.21	500–1000 or higher	Highly polluted region, mostly flat terrain confined by hilly terrains in north and south
North-East India (NE-I)	~0–2000	2.35±0.31	100–500	Covered by dense forest having hilly terrain
West-India (W-I)	~0–700	2.20±0.21	250–500	Some part of the regions covers industries
Central-India (Central-I)	~0–1000	2.24±0.23	100–500	Covered by forest partially
East-India (E-I)	~0–1000	2.37±0.26	100–500	Covered by forest
Southern India (S-I)	~0–1000	2.10±0.31	250–1000	Western part of the region covered by forest having hilly terrain and humid climate

Before using the satellite retrieved data, the averaging kernels used in MOPITT retrievals were examined to quantify the sensitivity of the retrieved profile to the true profile. Mathematically, the averaging kernel is a matrix and it is a measure of how and where the retrieval is sensitive to the changes in the "true" state (in present case, changes in CO levels). In other words, the averaging kernel is a linear representation of the weighting of information content of retrieval parameters, i.e., CO. The averaging kernel for a given pressure level shows the sensitivity of the retrieval towards the changes in CO at all pressure levels. Thus, the vertical resolution of profiles is reflected in the averaging kernels. Generally, the averaging kernels are affected by the variability of the surface pressure, temperature, atmospheric profile of temperature, and the actual CO profile (Deeter et al. 2004 and reference therein).
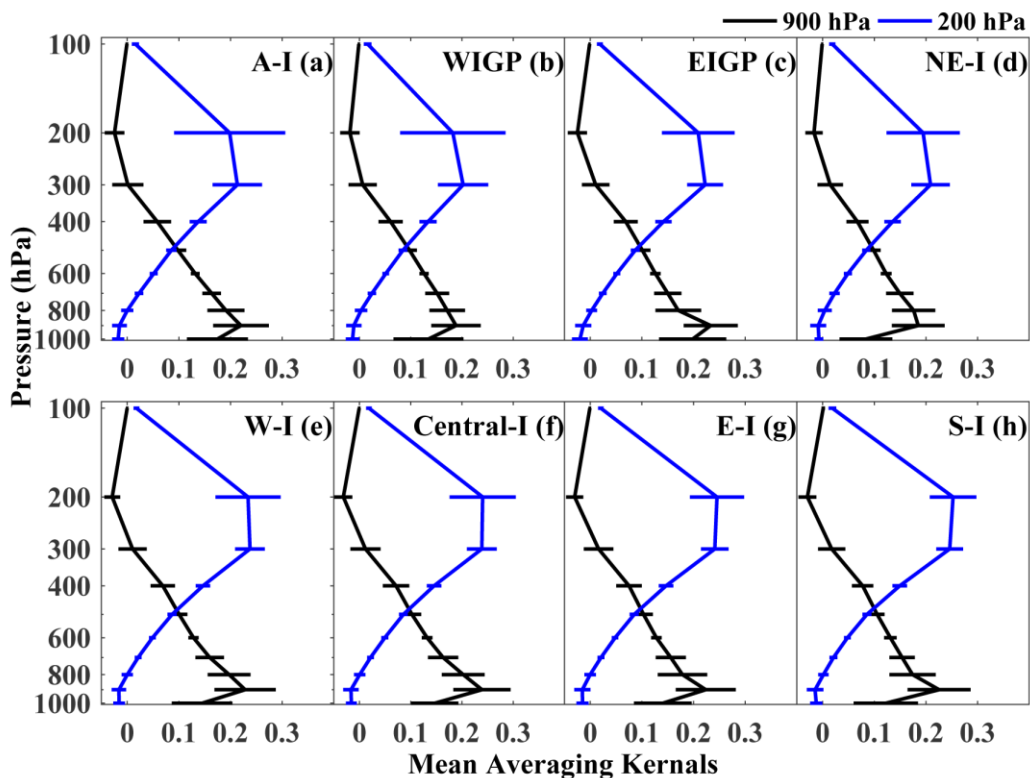
Figure 5.4: Averaging kernels of MOPITT level-3 V7-TIR retrievals (averaged over ~18 years, March 2000–February 2018) at 900 (black) and 200 (blue) hPa over different regions of India as labelled in top-right corner of each box. The error bars represent the standard deviations.

Figure 5.4 shows the mean averaging kernels for 900 and 200 hPa retrievals averaged over the study period for each of the study regions. Over all the study regions, the averaging kernel for 900hPa shows the peak at 900 hPa with magnitude ~0.18–0.23. The averaging kernel for 200hPa shows the broader peak around 200–300 hPa with magnitude ~0.2–0.25. This shows that peak magnitude of averaging kernels for 900 and 200 hPa is comparable or slightly lower for lower troposphere. This indicates that MOPITT retrieval sensitivity to the lower tropospheric CO is significant to capture the broad features of lower-tropospheric CO. Thus, this also shows that the broad features presented in the study are realistic. The main inference from the figure 5.4 is that the averaging kernels for lower and upper troposphere show significant magnitude which ensures the sensitivity to capture the changes in CO on regional scale.

5.4 Mean seasonal variation of CO

Figure 5.5 shows the mean seasonal variations of CO at 900 hPa (representing lower troposphere) and 200 hPa (representing upper troposphere) along with columnar CO as obtained by averaging the MOPITT data over period of March 2000–February 2018 for different regions. The dotted lines correspond to limited data points available for averaging (<25%, and mainly due to cloud cover, particularly in monsoon months).

This figure reveals the heterogeneity in the mean seasonal variations of CO as pointed out below.
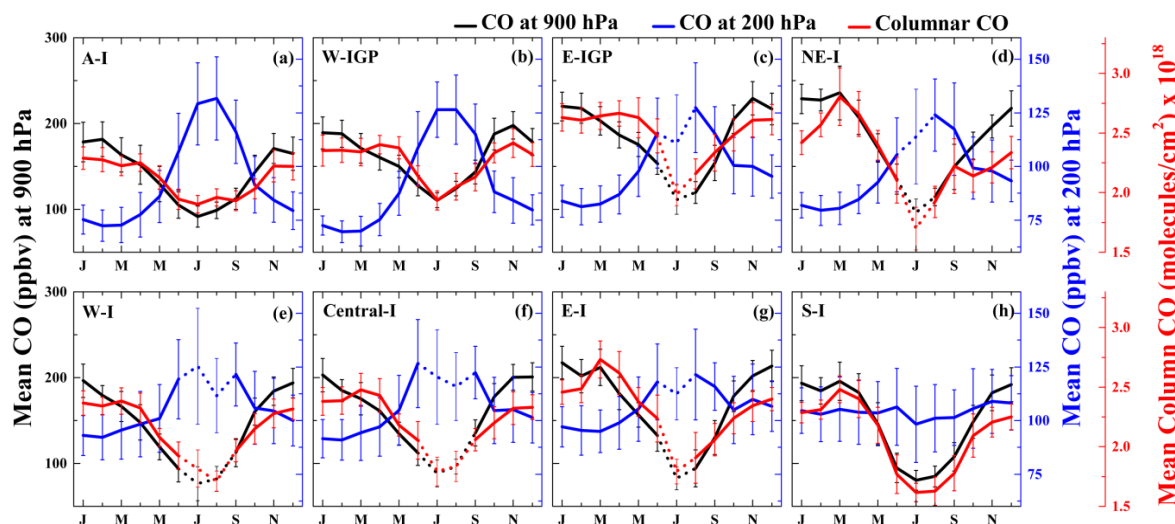
Figure 5.5: Mean seasonal variation of CO at 900 (black), 200 (blue) hPa and columnar CO (red) over different regions of India as labelled in top-left corner of each box. The error bars represent the standard deviations. The dotted lines corresponding to <25% of the data points available for averaging.

1. CO at 900 hPa (lower-tropospheric CO): Over most of the regions, lower-tropospheric CO shows peak in the winter months of December/January/February and dip in the summer-monsoon months of Jun/July/August. The winter and pre-monsoon CO values are comparable over NE-I, S-I and E-I. Seasonal minimum is lower (~75 ppbv) over W-I, and higher (~288 ppbv) over E-IGP. Seasonal maximum is lower (185 ppbv) over Arid-I and higher (235 ppbv) over NE-I. The seasonal amplitude is lowest over W-IGP (~89 ppbv) whereas it is highest over E-I (~137 ppbv).

2. CO at 200 hPa (upper-tropospheric CO): The seasonal variation in high-altitude CO shows opposite behaviour to that of lower tropospheric CO over most of the regions exhibiting higher mixing ratios during the summer-monsoon months of June/July/August. The anti-correlation between the seasonal variations of lower-tropospheric and upper-tropospheric CO is stronger (negative correlation coefficient is in the range of 0.65–0.86) over the northern regions (Arid-I, WIGP, EIGP, NE-I) and moderate negative correlation (0.52–0.61) over the W-I, C-I, and E-I regions. Weak and statistically insignificant correlation is seen over S-I.

Seasonal minimum is lower (~69 ppbv) over WIGP, and higher (~92 ppbv) over E-I. Seasonal maximum is lower (127 ppbv) over S-I and higher (139 ppbv) over NE-I and Arid-I. The seasonal amplitude is lowest over S-I (~37 ppbv) whereas it is highest over Arid-I (~67 ppbv).

3. Columnar CO: The seasonal variation of columnar CO follows almost same pattern as that of lower-tropospheric CO over all the regions (correlation coefficient ranges 0.76–0.91). However, columnar CO peaks during pre-monsoon month of March over NE-I, E-I, and S-I. The winter and pre-monsoon columnar concentrations are comparable over other regions except for Arid-I. The pre-monsoon time columnar CO is slightly higher or comparable to that during winter over E-IGP, which is further discussed in section 5.5.

Table 5.3: seasonal minimum, maximum and amplitude in lower-tropospheric, upper-tropospheric and columnar CO over different region. The minimum, maximum and amplitude were calculated for each year and mean values corresponding 18 years are shown here along with standard deviation.

Regions/Parameter description	Seasonal Minimum CO Mean ± Standard deviation (range within a region)	Seasonal Maximum CO Mean ± Standard deviation (range within a region)	Seasonal amplitude CO Mean ± Standard deviation (range within a region)
Lower tropospheric CO in ppbv (900 hPa)			
Arid-India	89±7 (78–104)	185±16 (162–214)	96±12 (76–120, 87–129%)
West-IGP	109±7 (92–119)	198±14 (171–217)	89±14 (62–115, 57–122%)
East-IGP	114±16 (87–147)	228±14 (209–249)	113±16 (83–136, 56–153%)
North-East India	107±7 (96–119)	235±13 (211–249)	128±19 (98–151, 87–157%)
West-India	75±15 (61–91)	199±13 (184–212)	124±7 (115–131, 126–212%)
Central-India	88±11 (74–111)	211±12 (191–222)	123±14 (104–146, 100–197%)
East-India	87±18 (70–120)	224±11 (207–240)	137±17 (116–167, 97–227%)
Southern India	76±8 (61–93)	200±13 (184–226)	124±9 (112–143, 143–220%)
Upper tropospheric CO in ppbv (200 hPa)			
Arid-India	72±6 (60–87)	139±13 (115–156)	67±10 (47–84, 68–116%)
West-IGP	69±4 (59–78)	135±12 (118–170)	66±12 (52–102, 73–150%)
East-IGP	80±4 (72–86)	131±20 (109–	51±18 (31–103, 38–

		181)	131%)
North-East India	81±6 (75–93)	139±15 (115–162)	58±16 (40–85, 43–109%)
West-India	88±8 (78–95)	137±18 (118–156)	49±11 (40–60, 46–63%)
Central-India	90±7 (78–100)	137±14 (114–156)	48±11 (37–67, 39–75%)
East-India	92±7 (80–103)	133±13 (114–153)	41±11 (25–57, 27–65%)
Southern India	90±8 (77–103)	127±15 (109–161)	37±14 (17–71, 18–79%)
Columnar CO (molecules cm^{-2})			
Arid-India	$1.85\pm0.04 \times 10^{18}$ $(1.79–1.93 \times 10^{18})$	$2.37\pm0.09 \times 10^{18}$ $(2.21–2.59 \times 10^{18})$	$5.17\pm1.04 \times 10^{17}$ $(2.88–7.94 \times 10^{17}, 15–44\%)$
West-IGP	$1.92\pm0.07 \times 10^{18}$ $(1.76–2.06 \times 10^{18})$	$2.50\pm0.10 \times 10^{18}$ $(2.38–2.74 \times 10^{18})$	$5.75\pm1.48 \times 10^{17}$ $(3.33–8.91 \times 10^{17}, 16–48\%)$
East-IGP	$2.07\pm0.13 \times 10^{18}$ $(1.88–2.26 \times 10^{18})$	$2.77\pm0.10 \times 10^{18}$ $(2.65–3.03 \times 10^{18})$	$7.04\pm1.48 \times 10^{17}$ $(4.60–9.34 \times 10^{17}, 21–47\%)$
North-East India	$1.83\pm0.09 \times 10^{18}$ $(1.70–1.94 \times 10^{18})$	$2.84\pm0.19 \times 10^{18}$ $(2.63–3.18 \times 10^{18})$	$10.10\pm1.83 \times 10^{17}$ $(7.45–12.6 \times 10^{17}, 38–65\%)$
West-India	$1.70\pm0.09 \times 10^{18}$ $(1.61–1.82 \times 10^{18})$	$2.48\pm0.10 \times 10^{18}$ $(2.39–2.62 \times 10^{18})$	$7.79\pm1.41 \times 10^{17}$ $(6.51–9.57 \times 10^{17}, 36–58\%)$
Central-India	$1.77\pm0.12 \times 10^{18}$ $(1.58–1.93 \times 10^{18})$	$2.61\pm0.11 \times 10^{18}$ $(2.46–2.79 \times 10^{18})$	$8.40\pm1.06 \times 10^{17}$ $(7.09–9.59 \times 10^{17}, 37–58\%)$
East-India	$1.81\pm0.11 \times 10^{18}$ $(1.65–2.00 \times 10^{18})$	$2.79\pm0.13 \times 10^{18}$ $(2.60–2.98 \times 10^{18})$	$9.71\pm1.77 \times 10^{17}$ $(6.64–12.6 \times 10^{17}, 34–73\%)$
Southern India	$1.58\pm0.06 \times 10^{18}$ $(1.46–1.67 \times 10^{18})$	$2.54\pm0.07 \times 10^{18}$ $(2.43–2.66 \times 10^{18})$	$9.59\pm0.96 \times 10^{17}$ $(8.15–11.2 \times 10^{17}, 51–77\%)$

Seasonal minimum is lower ($\sim1.58 \times 10^{18}$ molecules cm^{-2}) over S-I, and higher ($\sim2.07 \times 10^{18}$ molecules cm^{-2}) over EIGP. Seasonal maximum is lower (2.37×10^{18}

molecules cm^{-2}) over Arid-I and higher (2.84 x 10^{18} molecules cm^{-2}) over NE-I. The seasonal amplitude is lowest over Arid-I (~5.17 x 10^{17} molecules cm^{-2}) whereas it is highest over NE-I (~10.1 x 10^{17} molecules cm^{-2}).

The above discussed seasonal features are also listed in Table 5.3. As shown in the table, the changes or variability in seasonal minimum, maximum and amplitude is significantly smaller for upper-tropospheric CO than that compared to lower-tropospheric CO.

5.5   Association with biomass burning/fire counts
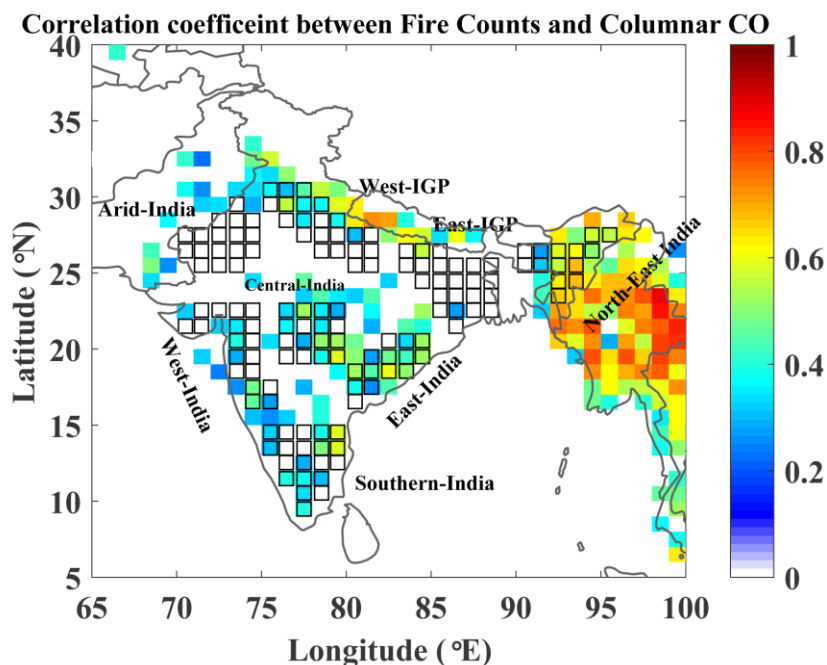
Figure 5.6: Spatial distribution of correlation coefficient (level of significant >95%) between MODIS (Aqua and Terra) retrieved fire counts (fire detection confidence >80%) and MOPITT retrieved columnar CO considering the monthly dataset over the period of ~18 years (2000–2018). Different regions are marked similar to the figure 5.3a.

Biomass burning is considered as a dominant source of atmospheric CO over the regions covering forests or agricultural practices. Biomass burning, includes, forest fires (boreal fire, tropical forest fire, etc), agricultural waste burning, peat fires, as well as savanna, grassland, and shrubland fire. The number of fire events/ counts is a good indicator of presence of biomass burning activity. MODIS detected fire events are utilised in the analysis. However, estimation of CO emission from such fire events is based on database likes GFED4 (which is from combination of satellite observations of fire events and model based estimation of emissions), which is utilised in this study and discussed later in this section.

Figure 5.6 shows the results of the correlation analysis carried out between monthly total fire counts (MODIS on board Aqua and Terra) and columnar CO (MOPITT, V7-TIR) over the period of 2000–2018 and for the entire study regions. The analysis is done on grid-by-grid basis and the figure shows only those correlation coefficients for which statistically significance level is >95%. The strong association of fire counts with CO points to the significant influence of biomass burning in the production of CO and its concentration level in the troposphere. Figure 5.6 reveals the following features.

The pattern of distribution of correlation coefficient between MODIS retrieved fire counts and MOPITT retrieved columnar CO over India (figure 5.6) more or less resembles that of the forest cover (figure 5.3c). This is due to open biomass burning (i.e., forest fires as well as slash or crop residue burning) over forested and agricultural regions which contribute to the tropospheric CO. The small scale biomass burning occurring for heating purposes during winter season over northern India does not get detected by MODIS and hence CO contribution from such closed biomass burning is not accounted in this analysis.

In addition to the contributions from anthropogenic emissions (like fossil fuel burning), contributions from biomass burning activity could raise the CO level to higher magnitude. And the contribution of CO from biomass burning is region dependent. The stronger positive correlation (0.4–0.7) over NE-I, followed by E-I (0.3–0.6) between columnar CO and fire counts indicate that biomass burning is a dominant controlling factor of CO over these regions. The fire counts were highest over NE-I as compared to other parts of India. There was no significant correlation found over Arid-India, obviously due to absence of biomass burning activity. Weak, but statistically significant correlation were found over WIGP, W-I, and S-I regions. This indicates that, over these regions, biomass burning is not the dominating contributor to CO and seasonal patterns are not only controlled by the biomass burning but, other processes like fossil fuel burning and/or photochemical oxidation of hydrocarbons (e.g., methane) also are contributing factors for the variations of columnar CO.
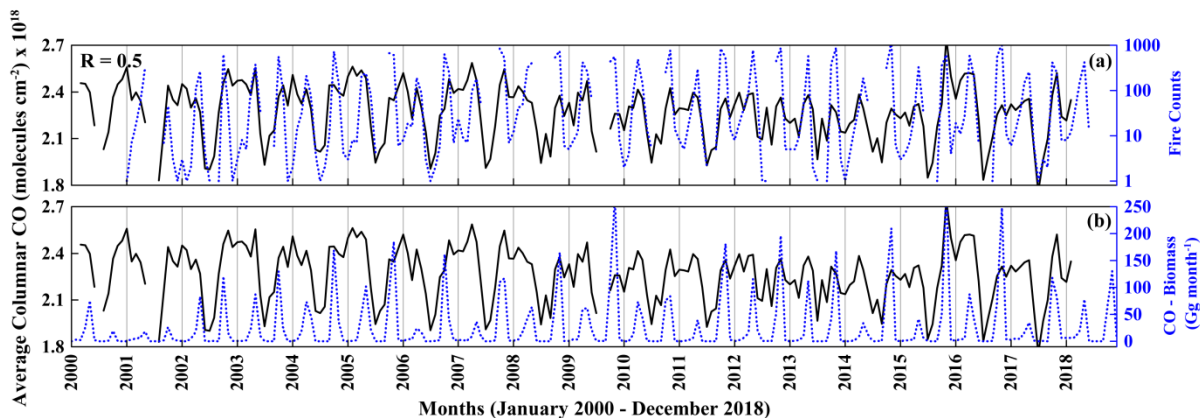
Figure 5.7: Monthly variation of columnar CO along with (a) fire counts from MODIS and (b) CO emission from biomass burning obtained from GFED4 for the period of 2000–2018 over W-IGP region. Note that right-Y axis for the fire counts is in logarithmic scale.

Figure 5.7 shows the mean columnar CO and fire counts (from MODIS) along with the CO emission from biomass burning over W-IGP (obtained from GFED4) in two separate panels. The fire counts and corresponding biomass burning CO emission showed prominent double-peak structure in the seasonal pattern over this region. These two peaks during May (pre-monsoon) and October (post-monsoon) correspond to the two major harvest seasons, Kharif and Rabi respectively. The columnar CO starts increasing in the month of September along with the increase in biomass burning events which maximises in October. The biomass burning events over Haryana/Punjab region corresponding to the crop residue burning (Venkataraman et al., 2006; Kumar et al., 2011) contribute significantly to the high CO emissions over W-IGP. While the emission/fire count shows a dip during January (winter), CO remains high, showing a broad peak centred around the month of January (winter) extending till March. The biomass burning events during pre-monsoon (April–May) further enhances the CO levels. It is important to note that CO emission due to biomass burning has increased during recent years (2005–2016). Similar double peak pattern is observed over E-IGP, E-I and Central-I, but the peak observed during October is less prominent.

Figure 5.8 shows mean columnar CO along with (a) anthropogenic CO emission, (b) fire counts, and (c) biomass burning CO emission the period of 2000–2018 over E-IGP region. The anthropogenic CO emission is obtained from MACCity gridded data (0.5° x 0.5° latitude/longitude) in which the emissions from all sectors (see section 2.5.7) are summed up to obtain total emission. Here, though agricultural waste burning is of anthropogenic nature, it is excluded in the summation for total anthropogenic CO emission. The total emission is further added over the grids covering E-IGP, representing the regional sum. The fire counts (having detection confidence > 80%)

166

obtained from MODIS (Terra and Aqua) are summed over the region. Similarly, the CO emission (0.25° x 0.25° latitude/longitude) from biomass burning obtained from GFED4 (see section 2.5.7) are summed over the E-IGP.
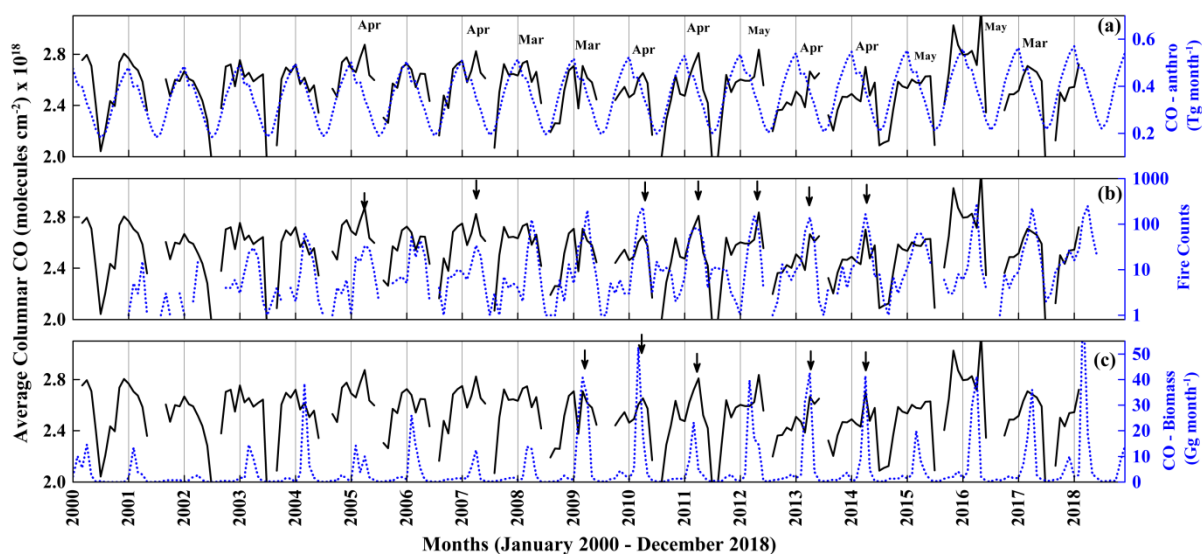
Figure 5.8: Monthly variation of columnar CO (black) and (a) anthropogenic CO emission from MACCity, (b) fire counts from MODIS, (c) CO emission from biomass burning obtained from GFED4 for the period of 2000–2018 over E-IGP region. Note that right-Y axis for (b) is in logarithmic scales. The month over which pre-monsoon peak in columnar CO is comparable or higher than winter peak is labelled by respective month of peak in (a). The arrows in (b-c) shows that over those months peak in columnar CO and fire count/biomass burning emission/fire CO emission coincides exactly.

The seasonal variation of columnar CO almost follows the seasonal pattern of anthropogenic CO emission which is higher during winter and lower during summer monsoon months. In general, the fire count peaks during pre-monsoon months of March/April/May. A closer look over the columnar CO variations reveals the prominence in the pre-monsoon peak of columnar CO during recent years. For the years, 2000–2004 and 2006, pre-monsoon peaks are of smaller magnitude as compared to winter peaks. The month over which pre-monsoon peak is comparable or higher than the winter-peak is labelled by respective month of peak (figure 5.8a). For the recent years 2009–2018, the magnitude of pre-monsoon peak in the columnar CO has increased and it is comparable or even higher than the winter-peak.

In order to find possible cause for prominence in pre-monsoon peak in columnar CO over E-IGP, monthly variation of fire counts and biomass burning emission are shown in figure 5.8b and c respectively. During 2009–2014 year, pre-monsoon peak coincides with the peak in fire count or biomass burning emissions (shown by arrows in figure 5.8b and c). The enhancement in the fire counts (or biomass burning emission) during pre-monsoon is clearly seen over E-IGP (figure 5.8b) over the recent years, 2009–

2018. However, peaks in columnar CO and biomass burning emission do not coincide always. Thus, this indicates that apart from biomass burning over E-IGP, transport from W-IGP or oxidation of hydrocarbon also would be contributing factor for the enhancement in the magnitude of pre-monsoon peak over E-IGP.

5.6　Causes for seasonal variations

The concentration of CO over any region depends upon the sources and sinks over the region and transport from other regions. Meteorology and the associated change of airmass play an important role for the transport of CO depending on seasons. The photochemical oxidation of CO precursors like CH_4 and other hydrocarbons (Seinfeld and Pandis, 2006) also could affect the seasonal pattern of CO. The lower tropospheric CO as well as the columnar CO shows seasonal maxima during winter, over most of the study regions. These higher CO values during winter could be due to following reasons. (1) Higher anthropogenic emission over the regions [over all land regions, anthropogenic CO emission is higher during winter as seen from MACCity data (not shown here). For example, as shown in figure 5.8, higher anthropogenic CO emission seen during winter over E-IGP, could be due to higher energy requirement for heating purposes, (2) weak photochemical removal, (3) meteorologically stagnant condition is partly responsible for higher lower-tropospheric CO during winter.
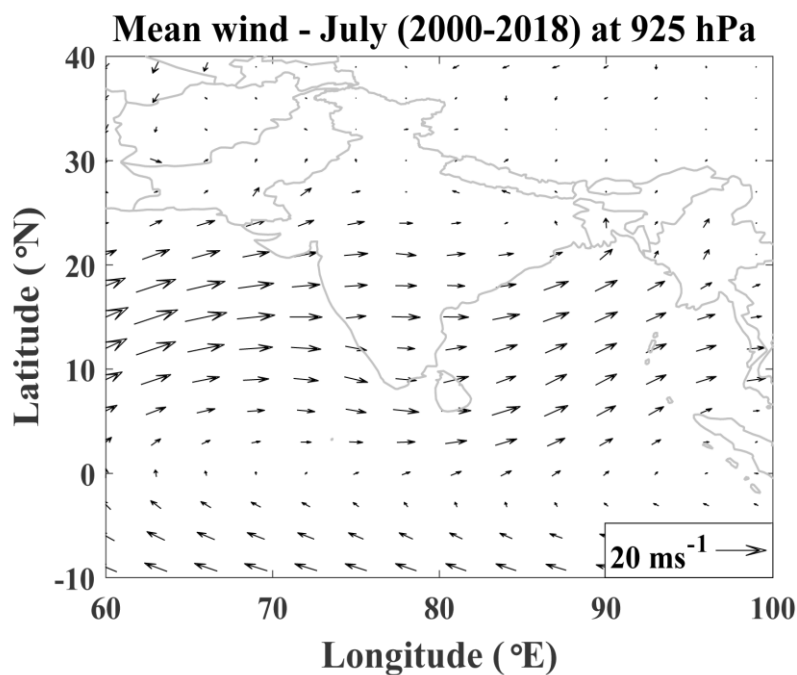
Figure 5.9: Synoptic wind pattern at 925 hPa averaged over July months of 2000–2018 as obtained from ERA-Interim.

The higher mixing ratios in the upper-tropospheric CO in pre-monsoon and summer monsoon season (figure 5.5.) could be due to increased convective activity which can lift CO to higher altitude reducing their concentration level in the lower troposphere (this feature is discussed in the section 5.7).

Seasonal minima in the lower-tropospheric and columnar CO are seen during summer-monsoon over all the study regions. The possible reasons for this seasonal minima include (1) reduction in anthropogenic CO emission [for example, lower anthropogenic CO emission over E-IGP, figure 5.8a]. The minimal biomass burning and the consequent reduction in precursor gases during summer-monsoon season lead to lower mixing ratios. (2) Effect of the monsoonal circulation. Figure 5.9 shows the synoptic wind pattern of July (representing the monsoon season) at 925 hPa averaged over 19 months (July months of years 2000–2018). As seen in the figure 5.9, all the regions receive relatively clean marine air during summer monsoon causing lower concentration in CO. The moisture laden marine airmass over the regions cause enhancement in the tropospheric water content coinciding with minima of tropospheric columnar CO (water vapour variation is not shown here). Note that the contribution of water vapour in reduction of CO would be minimal because of less availability of solar radiation due to cloudy condition and lower ozone concentration during monsoon (since cleaner marine airmass prevails). During monsoonal convection, NOx produced through lightening contributes to recycling of OH which removes CO (as well as other pollutants) in the convective processes (Lelieveld et al., 2018).

5.7   Signature of convective activity

The deep convection associated with Asian monsoon can uplift the ground-level CO to high altitudes and increase of upper tropospheric CO (Kar et al., 2004, 2010; Ghude et al., 2011; Fadnavis et al., 2011). Figure 5.10 shows few examples of the strong signature of convective activity during month of April-2011/2017 and August-2000. The altitude (in terms of pressure) - latitude cross-section of CO mixing ratios as obtained from MOPITT data and that of vertical wind as obtained from ERA-Interim data are shown side by side in the figure 5.10 for two longitude sectors (76° and 85° E). The positive values (orange and red colours in figure 5.10d-e-f) in vertical wind denote the downdrafts and negative values (cyan and blue colours in figure 5.10d-e-f) represent the updrafts.
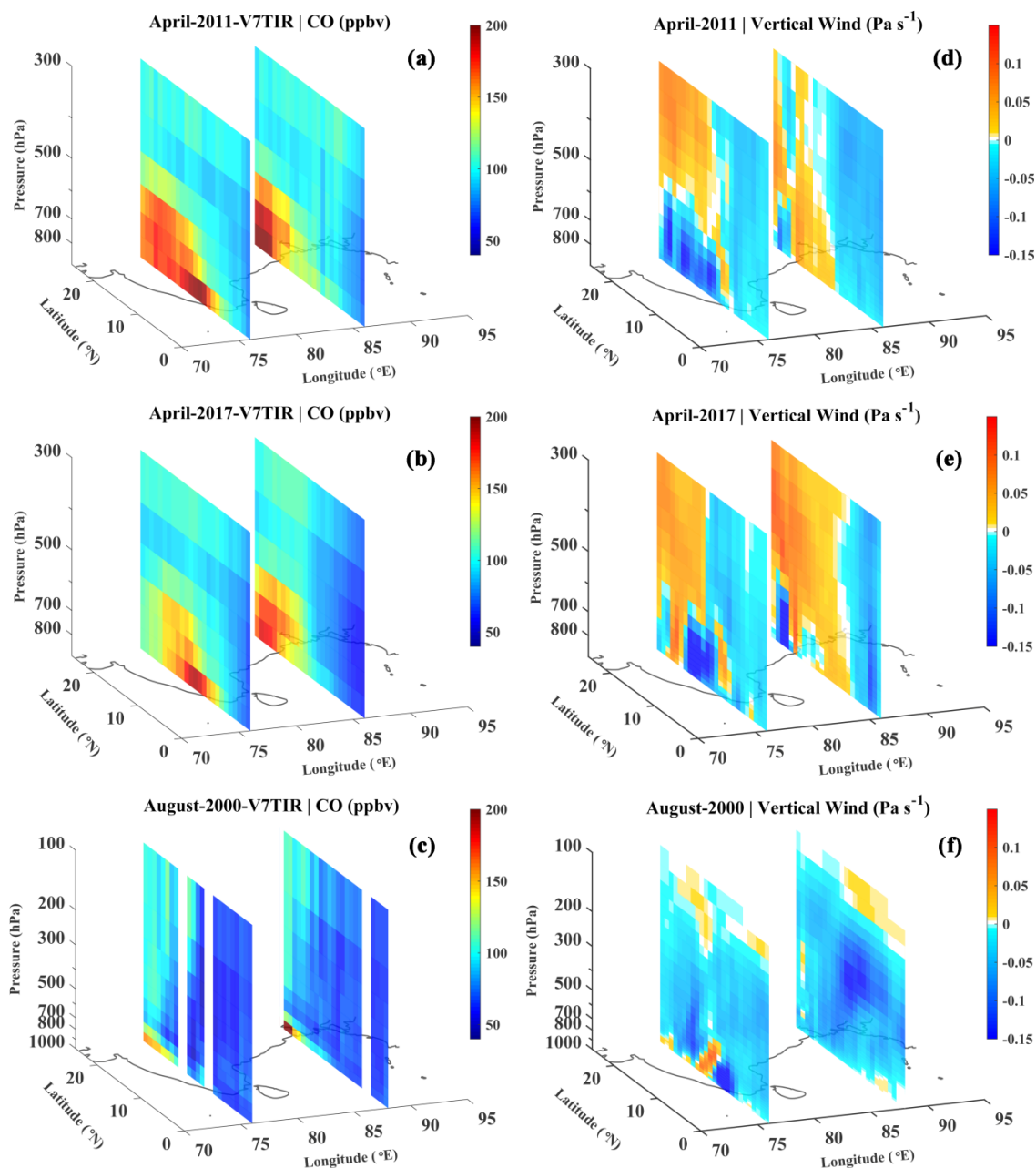
Figure 5.10: Pressure-latitude slices of CO and vertical wind for two representative longitudes over India during pre-monsoon month of April and summer-monsoon month of August 2000. White colour shows the absence of the data.

The regions of higher CO extending vertically up coincide with updrafts (cyan and blue colours) over the same regions. This shows clear one to one correspondence between convective activity and vertical distribution of CO. For longitude sector 76° E, strong updraft was seen over 10–22° N latitude which extended up to 500 hPa and uplifting of CO is also clearly seen upto 600 hPa. Similar feature is seen for the longitude sector, 86° E over 20–25° N latitude. However, in this region, the vertical updrafts are

confined to 650 hPa (figure 5.10d), but the spatial spread in CO is beyond the latitude range (20–25° N). This could be due to horizontal transport over the region. As discussed in Chapter - 3, the anti-cyclonic circulation extending upto 700 hPa over eastern IGP and northern BoB transport the vertically uplifted CO over to this region. Similar to pre-monsoon season, during monsoon season influence of convective updraft prevails up to tropopause (~100 hPa over tropics) and covers entire Indian region. As seen in the figure 5.10c, the higher CO mixing ratios is extended up to 100 hPa causing the upper-tropospheric high in the CO mixing ratios during summer-monsoon months.
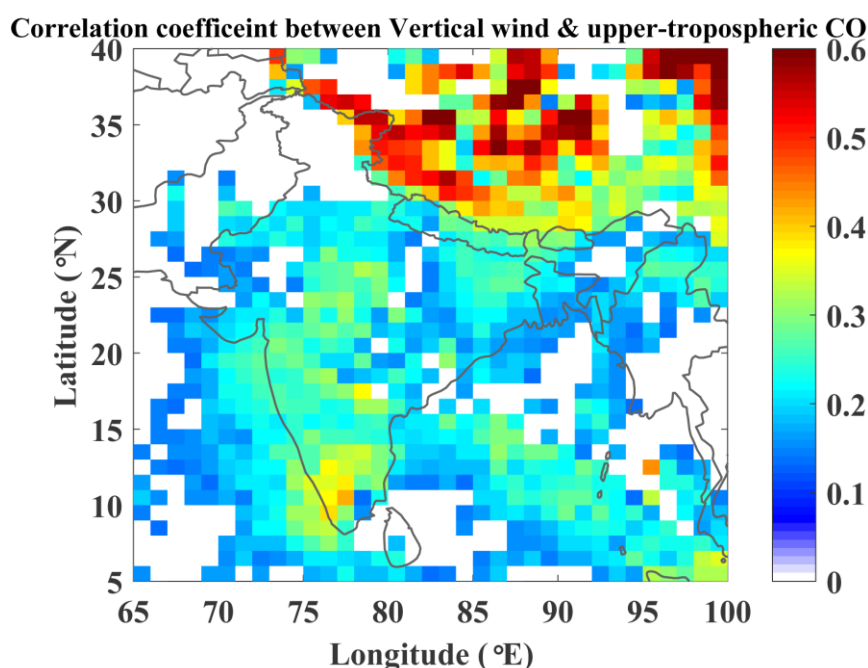
Figure 5.11: Spatial distribution of correlation coefficient (level of significant >95%) between upper-tropospheric vertical wind and MOPITT retrieved CO considering the monthly dataset over the period of ~18 years (2000–2018).

A correlation analysis was carried out between upper-tropospheric CO and vertical wind and the spatial distribution of correlation coefficient (level of significance >95%) is shown in figure 5.11. While the upper-tropospheric CO is considered at 200 hPa, the vertical wind is considered at 300 hPa, a level below. This is because when vertical wind varies around 300 hPa, its effect is clearly evident a layer above it. The increase in updraft or convection increases CO mixing ratios in the upper troposphere as it mixes lower-tropospheric air with upper-troposphere leading to positive correlation coefficient. The statistically significant correlation coefficient of magnitude around 0.1–0.4 is seen over the Indian region. It is important to note that higher magnitude of correlation coefficient is not expected due to following reasons. (1) The variation in the CO mixing ratios depends on many factors, like horizontal transport in the upper-

troposphere. (2) While CO gets vertically transported; it also undergoes reaction with OH and the variability of in the vertical profile of OH affects the CO reaching in the upper-troposphere. (3) The spatial heterogeneity in the lower-tropospheric CO also reduces the correlation probably due to mixing while getting transported in the upper-troposphere. This is in line with the higher correlation observed over Himalayan region where spatial heterogeneity in the lower-tropospheric CO is smaller as compared to other regions.

5.8   Long term trend in CO

5.8.1 Long term trend over India

Grid-by-grid trend analysis was carried out by utilising the monthly averaged MOPITT retrieved CO (level-3 V7-TIR daytime retrievals having DOF>1) over ~18 years (2000–2018) for lower-tropospheric, upper-tropospheric and columnar CO. Year 2015–2016 being El Niño year (MEI is 1 to 2.2; https://www.esrl.noaa.gov/psd/enso/mei/), CO mixing ratios were abnormally higher as can be seen in figure 5.7 and 5.8 and hence the data from post-monsoon 2015 to pre-monsoon 2016 were discounted in the trend analysis. In order to get realistic trend, time series of monthly CO values were de-seasonalised by subtracting the mean seasonal variation from monthly mean CO values. Linear regression analysis on the de-seasonalised CO versus time (in months) provides a quantitative estimate of the long term trend. Linear regression fit was carried out grid-by-grid weighing with the MOPITT retrieval uncertainty. The slope of linear fit provides the trend. The slope (i.e., trend) values corresponding to the level of significance greater than 95% (p-value less than 0.05) are only considered. Based on the trends, the percentage change per year has also been estimated.

The figure 5.12 shows the trend, (basically the slope of linear fit) along with percentage changes per year for the lower, upper and columnar CO (white color in the figure shows the regions where the trend is statistically insignificant). Figure 5.12 reveals the following features. (1) In general, there is a decreasing trend of -1 to -2.5 ppbv year^{-1} or -0.5 to -1.5% year^{-1} in the lower troposphere over India and surrounding oceanic regions. The trend is not significant over few locations in NE-I, central/southern India and AS. (2) Columnar CO also exhibits a decreasing trend of -0.5 to -2 molecules cm^{-2} year^{-1} or -0.1 to -1 % year^{-1}. While the decreasing trend is significant over W-I, W-IGP, E-IGP, surrounding oceans, it is not significant over central-I, S-I and E-I part of India. (3) The upper tropospheric CO shows increasing trend over most of the regions

(except northern India). However as discussed later in this chapter, the observed positive trend in upper troposphere needs further analysis to ensure this feature.
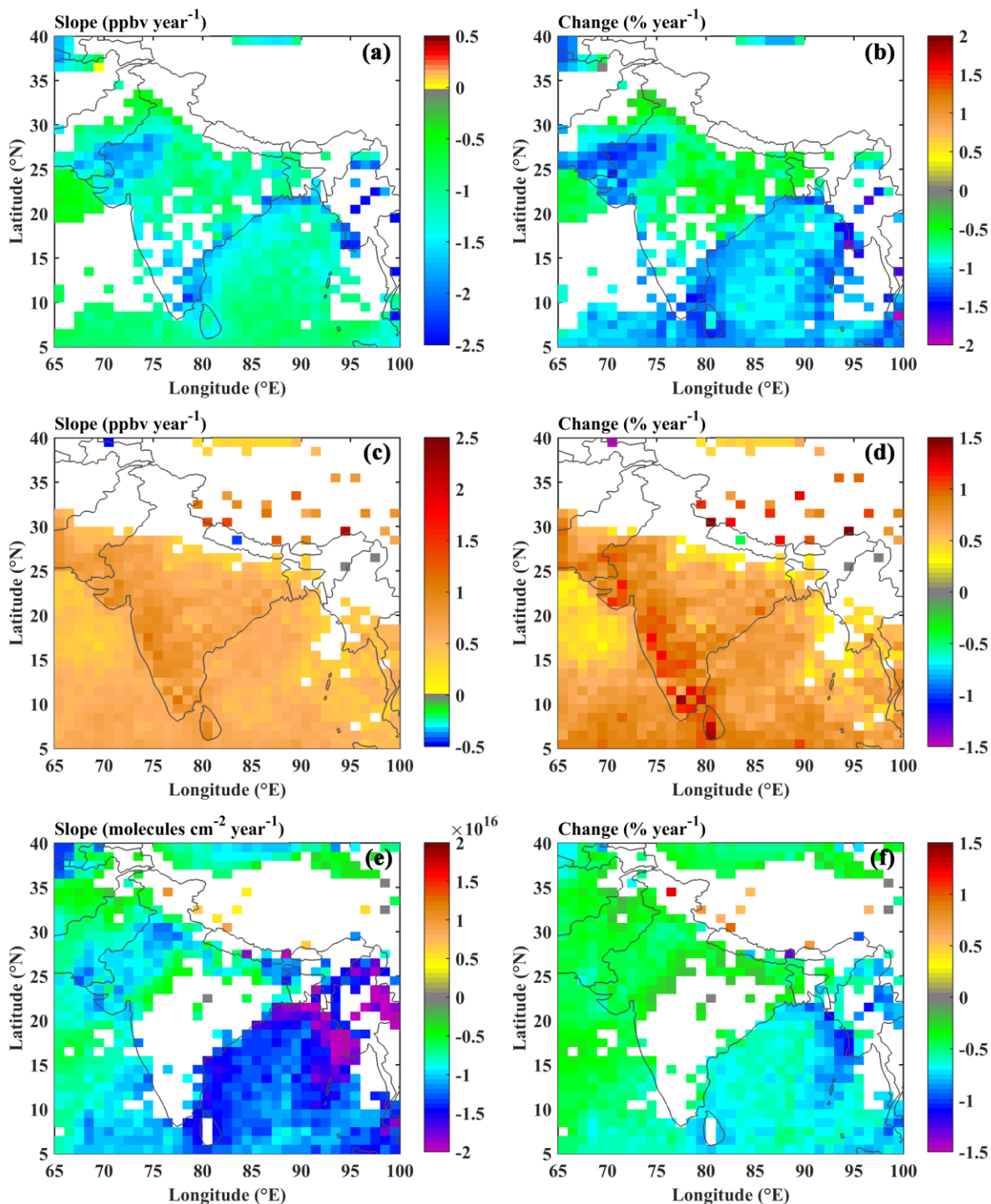
Figure 5.12: Trend (slope and percentage change corresponding to the linear fit) in the lower-tropospheric (at 900 hPa; a-b) upper-tropospheric (at 200 hPa; c-d) and columnar CO (e-f). White colour shows either absence of data or statistically insignificant trend. The trend values shown here are corresponding to the statistical significance greater than 95%. The percentage change is calculated with respect to mean value of year 2000 at respective grids.

5.8.1.1 Season-dependent trends
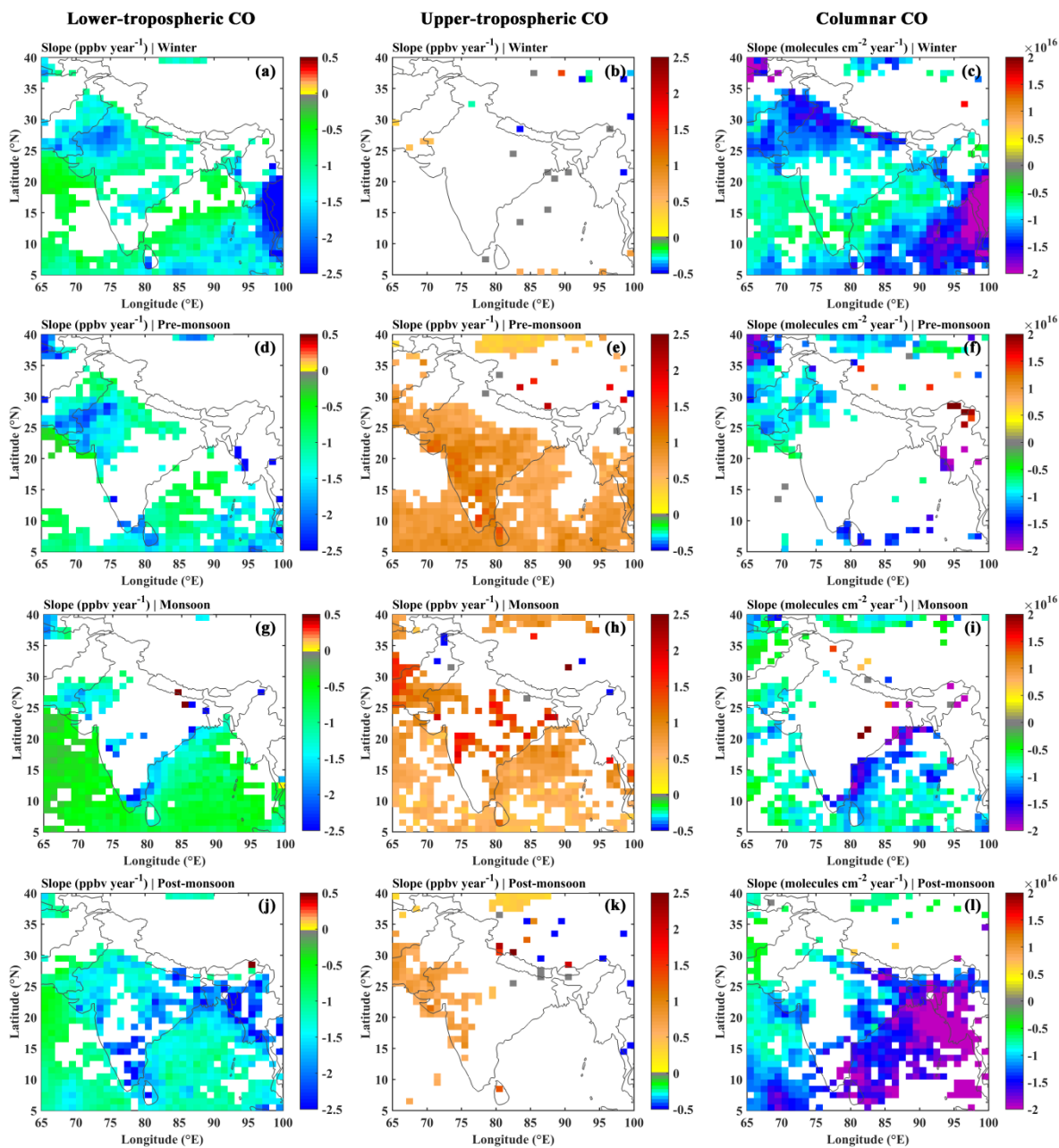
Figure 5.13: Trend (slope corresponding to the linear fit) in the lower-tropospheric (at 900 hPa; left panel), upper-tropospheric (at 200 hPa; middle panel) and columnar CO (right panel) for the four seasons. White colour shows either absence of data or statistically insignificant trend. The trend values shown here are corresponding to the statistical significance greater than 95%.

The magnitude of above discussed trend could be season dependent. Hence the datasets-lower tropospheric CO, upper tropospheric CO and columnar CO was divided into four seasons winter, pre-monsoon, monsoon and post-monsoon. The linear regression analysis on the seasonally averaged data was carried out estimating the seasonal trends.
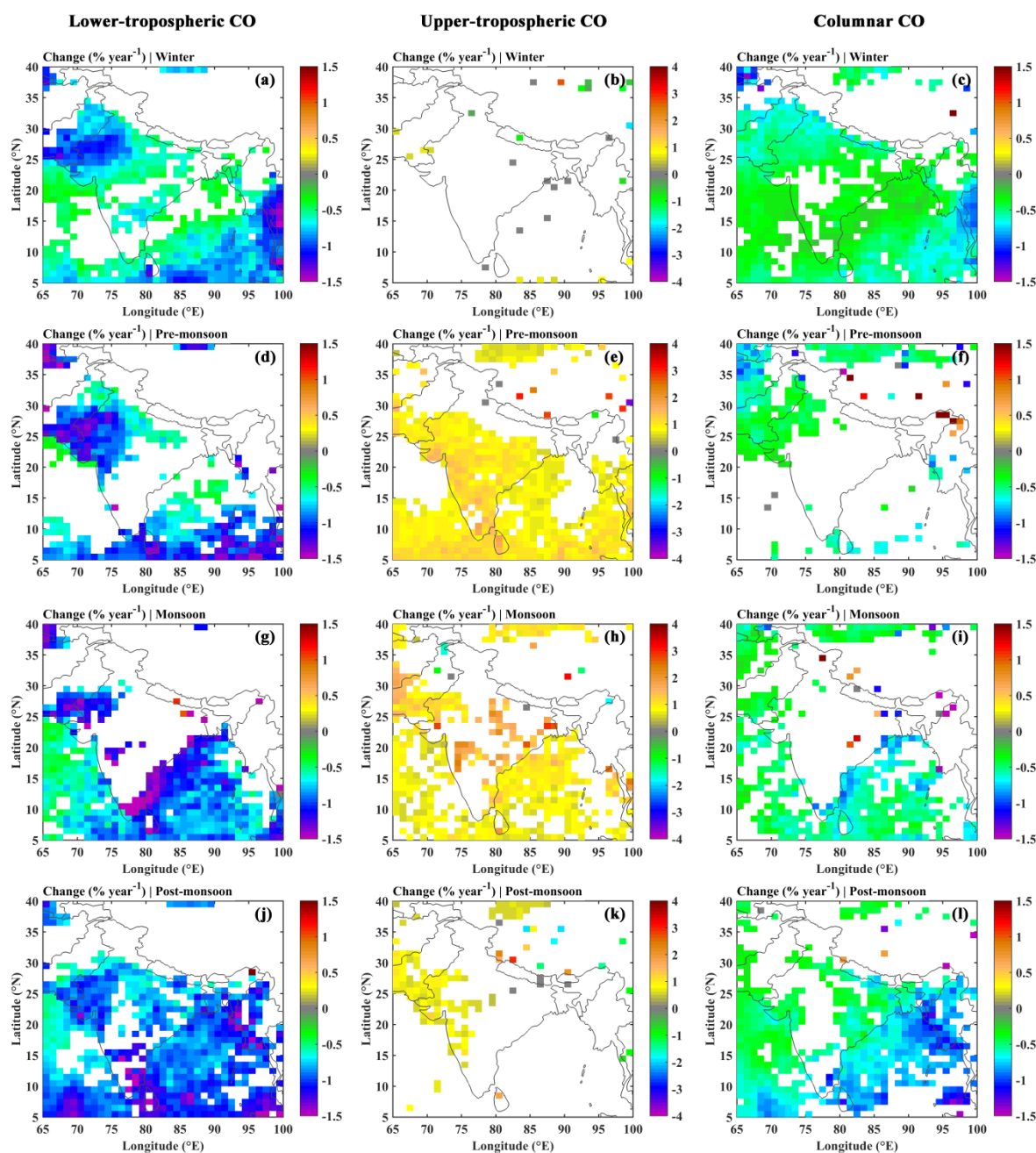
Figure 5.14: Same as figure 5.13 but in terms of percentage.

Figure 5.13 and 5.14 shows the spatial pattern of the trends (ppbv year^{-1} or molecules cm^{-2} year^{-1}) and percentage change per year for the four different seasons. In the lower troposphere, the decreasing trend is clearly evident over most of the regions during all the seasons except monsoon. The insignificant trend during monsoon can be partly attributed to less number of data points due to cloudy conditions and associated retrieval issues. It is also possible that CO does not exhibits significant changes during monsoon season. However, the surrounding oceanic regions show decreasing trend even during monsoon seasons. The columnar CO also shows decreasing trend during winter and post monsoon seasons. No significant trend is seen during pre-monsoon and

monsoon seasons. While, lower-tropospheric and columnar CO shows decreasing trend, the upper tropospheric CO shows increasing trend over Indian region during pre-monsoon and monsoon seasons. Though as mentioned before, increasing trend in upper-tropospheric CO needs further confirmation, there exist a possibility that the increasing trend observed in upper troposphere would compensate for the decreasing trend in lower troposphere leading no net decreasing trend in the columnar CO during pre-monsoon and monsoon seasons.

5.8.1.2 Observed trends and possible causes

Over the last few decades, the anthropogenic activity has increased as indicated by the increase in the population of India, motor vehicles, industrial activities, etc. (census, Ministry of Road Transport & Highways, Government of India Ministry of Finance, Government of India, Department of Industrial Policy & Promotion, Ministry of Commerce & Industry). The population of India was 1.028 billion in 2001, which increased by 181million reaching 1.210 billion in 2011 (as per census of 2001 and 2011 respectively). The increase in population indicates that CO emission from residential sector would have increased. The number of factories in India was 131,268 in 2000–2001 which has increased to 158,877 in 2009–2010 as per the report of Survey of Industries (http://data.gov.in/). In India, 68.19% of total electricity is produced from thermal power plants (http://powermin.nic.in) and electricity generation has increased to 112.8 GW in 2011 which was 74.4 GW in 2002 (Report on growth of electricity sector in India from 1947 to 2011, Ministry of Power, Government of India). The total number of motor vehicles was 55 million in 2001 which increased to 141.8 million in 2011 (Road Transport Year Book 2009–2010 and 2010–2011, Transport Research Wing, Ministry of Road Transport & Highways, Government of India). These vehicles (or the transport sector) are the major consumers of oil (~51% of total oil consumption) in India (Vehicular Pollution Control Programme, Central Pollution Control Board, Ministry of Environment & Forests, Government of India). The two-wheelers (or total number of vehicles) have increased almost by a factor of ~2.5 over 10 years. As per the norms of "Bharat stage emission standards" implemented by the Government for two-wheelers, CO emission has reduced to 1 g km^{-1} (BS-Bharat Stage- III norm) which was 2 g km^{-1} in 2000 (India Stage 2000 norm) (Central Pollution Control Board). While the number of vehicles has increased by a factor of ~2.5, the emission of CO (g km^{-1}) by the two-wheelers has reduced by a factor of 0.5 by the implementation of air pollution norms over the period of ~10 years. The recent implementation of BS IV standards further

reduces the emissions, and also sale of BS-III vehicles are banned since April 2017. Probably due to implementation of these norms, decreasing trends in surface SO_2 and BC concentration are observed in the cities (Gurjar et al., 2016; Manoj et al., 2019). Thus, the decreasing trend in lower tropospheric CO discussed above could be partially attributed to reduced CO emissions. However, the CO emission from EDGAR (Emissions Database for Global Atmospheric Research) version-4.3 inventory and REAS (Regional Emission inventory in ASia) version-2.1 inventory (Kurokawa et al., 2013) show increasing trend in total CO emission from India during period 2000–2008. Hence, removal/depletion mechanisms of CO should be active to cause decrease in lower-tropospheric and columnar CO. Increase in convective activity and consequent uplifting of CO to the upper-troposphere could be one reason for the decreasing trend in lower-tropospheric CO. Another factor which can deplete CO is the presence of water vapour (which is a source of OH radicals in the presence of ozone and solar radiation) and the subsequent photochemistry. So Increase in lower-tropospheric water vapour can lead to the decreasing trend. It is reported that the column water vapour over Arabian Sea and Bay of Bengal has increased at the rate of 0.5–2.5 g kg^{-1} per decade (IPCC, 2013). This magnitude is comparable or higher as compared to the other parts of the global ocean. Surface specific humidity shows increasing trend ($\sim$0.15 to 0.5 g kg^{-1} $decade^{-1}$) over the Indian (IPCC-2013, Jaswal and Koppar, 2011). Whether chemistry (or change observed in other trace gases) can account the observed decreased is discussed using box-model simulation in Chapter - 6.

Lower tropospheric CO contributes significantly to the columnar CO (molecules cm^{-2}) due to higher density (molecules cm^{-3}) in the lower troposphere. The decreasing trend in the lower part of troposphere is significantly stronger. Hence, the columnar CO showed decreasing trend over most of the regions over India and surrounding oceanic region. As discussed in the following section, the decreasing trend in lower and columnar CO is confirmed by utilising in-situ and multiple satellite observations. However, in the case of upper tropospheric CO, the trend estimated from different satellite retrievals is not consistent as discussed in the following section. Both increasing and decreasing trends are observed. This could be due to the artifact of changes in satellite instrument parameters over the decades as well as limitations in retrieval methodology. Hence full confidence is not attributed to the increasing trend in upper tropospheric CO. This needs further studies and improvement of retrieval algorithms for confirmation. In nutshell, while lower-tropospheric and columnar CO shows decreasing

trend over most of the regions including surrounding oceans, the upper-tropospheric CO shows an increasing trend for which full confidence cannot be attributed.

5.8.2 Global trends: comparison with in-situ measurements

However, in order to ensure that observed trend is realistic, the analysis was extended over the globe and compared with the trend estimated from in-situ measurements being carried out by the global network of NOAA which includes more than 85 stations spread all over the globe (figure 1.17). The details of this network are given in section 2.3.1. The trend in MOPITT retrieved CO at 900 hPa for 2000–2018 and the surface CO data of NOAA network were examined. Data from only those NOAA sites, over which measurements are available at least for a decade, are considered in this analysis.
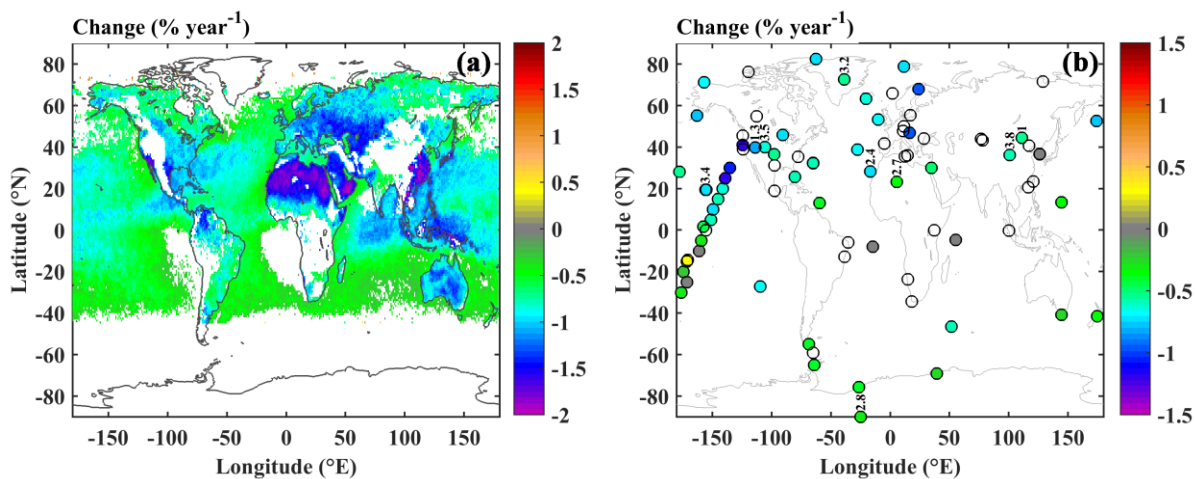
Figure 5.15: (a) Trend as percentage change per year, in lower tropospheric CO (at 900 hPa) as estimated using MOPITT data. White colour in shows either absence of data or statistically insignificant trend. (b) is same as (a) but in surface CO as estimated using in-situ measurements of NOAA-network. Unfilled circles represents statistically insignificant trend. The trend values shown here are corresponding to the statistical significance greater than 95%. In (b), the numbers mentioned above some of the circles represent the altitude (in km amsl) of station only if its altitude is greater than 1 km.

Figure 5.15 shows the trend in satellite retrieved CO at 900 hPa and the surface CO as obtained from MOPITT and NOAA network respectively. In case of MOPITT, the data availability is 70% (i.e., ~ 160 points over each grid cell) over the region between 60° N and 50° S (except for a few hilly regions like South America, South Asia, etc.) and hence it represents statistical robustness of the estimated trend. The MOPITT retrieved CO shows a decreasing trend of -0.77 ± 0.33 %year^{-1} (with minimum of -2.8 %year^{-1}) over the entire globe. Such a decreasing trend is observed in entire lower troposphere (1000–700 hPa) but here trend at 900 hPa is only shown as a representative of lower-

troposphere. Figure 5.15b reveals decreasing trend in the in-situ measured surface-CO at almost all the network stations except a few (unfilled circles) where the trends are not statistically significant. Over most of the locations, the decreasing trend in surface CO is $\sim 0.6 \pm 0.26$ %year^{-1} which is fairly consistent with the satellite based trend in the lower-tropospheric CO. This analysis confirms the observed decreasing trend in lower-tropospheric CO over the globe (as well as India) is realistic.
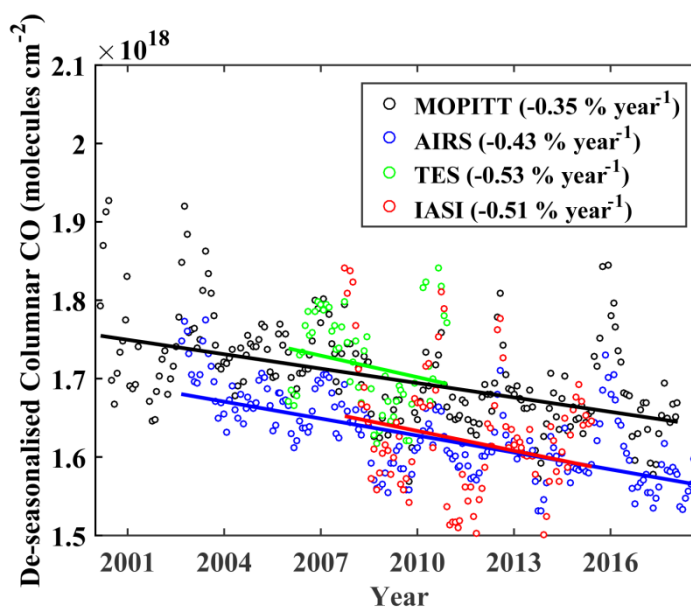
Figure 5.16: De-seasonalised globally averaged columnar CO as estimated using MOPITT, AIRS, TES and IASI data. The line shows the linear regression fit considering standard deviation and the slope of the linear fit (i.e., trend) is shown in terms of percentage change per year. The trend shown here is statistically significant (significance greater than 95%).

Since in-situ measurements for columnar CO for a long period are not available for such a comparison, the retrievals from multiple satellites namely MOPITT, AIRS, TES and IASI were utilised to confirm that MOPITT observed trend in columnar CO is realistic. In order to reduce the uncertainty in the estimation of trend, various data filtering procedures were applied depending on the satellite as described in section 2.5. Figure 5.16 shows the globally averaged de-seasonalised CO on monthly basis as obtained from the four different satellites. As evident from the figure 5.16, the time period of available data sets are 18 (2000–2017), 16 (2003–2018), 6 (2006–2011) and 9 (2007–2015) years for MOPITT, AIRS, TES and IASI respectively. The linear regression fit is carried out by weighing the standard deviation corresponding to the global variability. However, error bars corresponding to the standard deviations are not shown in the figure. The decreasing trend in globally averaged columnar CO is in the range of -0.35 to -0.53 % year^{-1} (-6.1 to -9.1 x 10^{15} molecules cm^{-2} year^{-1}) as obtained from MOPITT, AIRS, TES and IASI data. The estimated trend values are statistically significant

and comparable among themselves; however the differences among the estimated trends could be mainly due to different length of dataset, in addition to inherent uncertainty in the retrievals in the respective satellite. In spite of the differences in the magnitude of the trend, all the satellite datasets independently agree that columnar CO is decreasing over the globe. This feature of decreasing trend is reported by Girach and Nair, 2012; 2014; 2016 and Worden et al, 2013.

Similar to the trend analysis for columnar CO, discussed above, the trend analysis is carried out for the upper-tropospheric CO (200/215 hPa) over the globe using MOPITT, AIRS, MLS and TES retrievals and shown in figure 5.17. The magnitude of upper-tropospheric CO differs as retrieval at a given pressure level represents different thickness of atmospheric layer. As shown in figure 5.17, the trends observed by different satellites are not consistent. While AIRS shows close to zero trend, MOPITT as well as TES shows increasing trend and MLS shows decreasing trend. The temporal changes in averaging kernels could be a possible reason for the observed variations in trend. It can also be artifact of changes in the satellite parameters. Thus, the increasing trend in upper tropospheric CO needs to be confirmed by regular in-situ measurements and/or model simulations and needs further investigations.
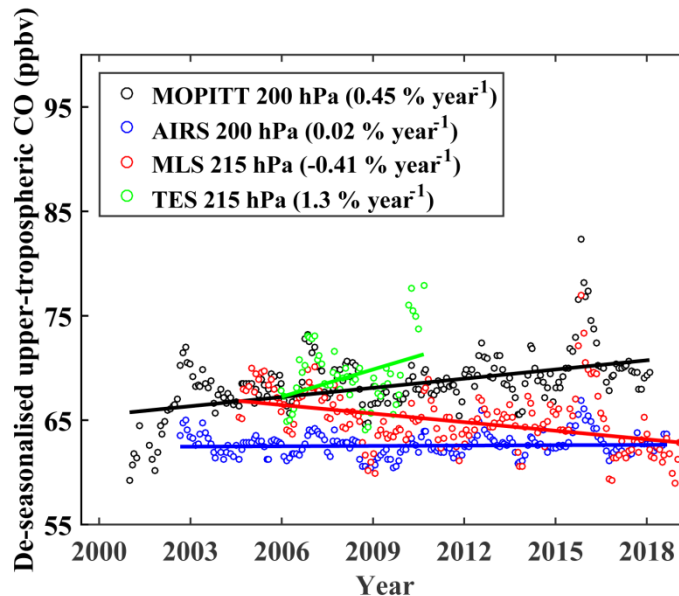
Figure 5.17: De-seasonalised globally averaged upper tropospheric CO (at 200/215 hPa) as estimated using MOPITT, AIRS, MLS, and TES data. The line shows the linear regression fit considering standard deviation and the slope of the linear fit (i.e., trend) is shown in terms of percentage change per year. The trend values shown here are corresponding to the statistical significance greater than 95%.

5.8.3 Possible reason for decreasing trend

The anthropogenic activity over the globe has increased as indicated by the increase of ~ 1 billion in population (http://www.census.gov) over the period of 2000–2013. Thus, decrease in emission of CO is not expected due to steadily increasing trend in anthropogenic activities. However, over certain regions like Europe and North America, reduction in CO emission has contributed to the observed negative trend in lower tropospheric/near-surface CO (Gratz et al., 2015). The decreasing trend in lower tropospheric CO and in columnar CO over entire globe could also be partially due to strengthening in chemical depletion of CO due to (1) Moistening of the troposphere (i.e. increase in tropospheric water vapour) and/or increasing trend in tropospheric O_3 and/or NO. The observations of tropospheric water vapour indicate an increase at near global scales since the 1970s occurring at a rate of about 7% per degree Celsius. The increasing trend in water vapour in turn could make increase in OH radical as reaction of $O(^1D)$ (which is produced by photolysis of ozone) with water vapour is a source of OH radicals. Increase in tropospheric ozone also can cause increase in OH radical. Thus, increasing trend in water vapour and/or tropospheric O_3 indicate the increasing trend in OH radical concentration which could cause decrease in tropospheric CO. However, there is no clear observational evidence of increasing trend in tropospheric OH radical due to scarcity of OH measurements and short lifetime of this species. (2) The increase in convective activity could partially explain the decreasing trend in lower-troposphere and increasing trend in upper-troposphere. However, trend in upper-tropospheric CO need to be confirmed. (3) Increase in the intrusion of CO into the stratosphere also could contribute for decreasing trend in tropospheric CO. The deep convective events penetrating 16 km (i.e. tropopause altitude over tropics) have increased over the years (Aumann et al., 2018) and moistening of stratosphere is evident in the IPCC-2013 report. This would indicate that CO would be getting intruded into the stratosphere from troposphere, thus contributing to the decrease in tropospheric CO.

5.8.4 Implications of decreasing trend in CO

The decreasing trend in tropospheric CO can be considered as a signature of changing climate of our globe. The major sources of greenhouse gases (which are responsible for climate change) are also emitters of trace gases which are precursors for ozone. Being a pollutant, decrease in lower-tropospheric CO is a good indication for air quality. But it could be associated with increase in tropospheric O_3 (which is a greenhouse gas) and NO, if decrease in CO is partly due to increase in OH. The both

increasing and decreasing trends are observed in surface and free tropospheric O_3 at various locations all over the globe. While surface O_3 has shown a decrease in several parts of eastern USA and Europe during past few decades mainly due to the control measures implemented on O_3 and its precursors (Logan et al., 2012; Parrish et al., 2012; Oltmans et al., 2013), increasing trend in O_3 and its precursors is observed over the Asian region (Munir et al., 2011; Akimoto et al., 2015; Xu et al., 2016). Surface O_3 recorded an overall increase of ~ 10 ppbv from 1973 to 2012, the rate of increase being 0.20 ppbv year^{-1} at coastal station Trivandrum, India with the fastest rate of increase since 2005 (1.05 ppbv year^{-1}). Thus, decreasing trend in lower-tropospheric CO would affect the concentration of other greenhouse gases which would have greater climatic implications. The annual average concentration of surface O_3 showed increasing trend 0.05, 0.04, and 0.04 ppbv year^{-1} at Delhi, Pune and Thiruvananthapuram respectively over the period of 1990–2013 (Saraf and Beig, 2004; Sinha et al., 2016).

The decreasing trend in columnar CO is in the range of 0.3–0.5 % year^{-1}. Globally, the major tropospheric sink of OH is CO, accounting for ~40% (Lelieveld et al., 2016). The decrease in CO could increase the concentration of OH. Globally, mean tropospheric OH is ~10^6 molecules cm^{-3} (Seinfeld and Pandis, 2006; Lelieveld et al., 2016). The quantification of possible increase in OH (due to decrease in CO) is complex due to non-linear chemistry and chemical feedback mechanisms. However, the increase in concentration of OH can affect the lifetime of methane, a major green house gas. The lifetime of methane turns out to be around 8.6 years, considering the OH concentration of ~10^6 molecules cm^{-3}. However, due to decreasing trend in CO as observed over period of ~2 decades, OH concentration would have risen. The simulations by Gaubert et al., 2017 has shown that mean OH would have increased by ~0.1 molecules cm^{-3} over a period of two decade due to decrease in CO. Considering the slight enhancement in OH concentration by ~0.1 molecules cm^{-3}, the lifetime of CH_4 reduces by 0.8 years (~9%), corresponding to the decrease in CO. The detailed simulations with chemical feedback also showed similar magnitude of decrease (i.e., 0.8 years) in the lifetime of CH_4 (Gaubert et al., 2017) due to increase in OH (which in turn due to decrease in CO).

5.9 Summary

The analysis of tropospheric CO is carried out on regional basis using MOPITT retrievals over the Indian landmass with the emphasis on lower-tropospheric, upper-tropospheric and columnar CO. The broad seasonal features, role of biomass burning, role of synoptic

meteorology, and long-term trends are analysed in detail and a comprehensive picture of the characteristics of tropospheric CO is brought out. The findings of the analysis and discussions could be summarised as followings.

- The in-situ observations of surface CO being made at Thiruvananthapuram and observations over various sites in India as available in the literature were analysed to understand the regional characteristics of near-surface CO. This analysis revealed the annual mean surface CO and its seasonal amplitude around 130–180 ppbv over the sites like Thiruvananthapuram, Cape Rama and Nainital (high altitude site), they are as high as 1600–1750 ppbv over the polluted regions like Mumbai and Delhi. Inter comparison of in-situ measure seasonal cycle with that from MOPITT shows that MOPITT surface retrievals could capture seasonal variations well.

- Seasonal variation of lower-tropospheric CO is characterised by a peak during winter over most of the Indian regions (except for few regions where is seen during pre-monsoon season) and a dip during summer-monsoon months. The winter peak is caused by stagnant meteorological conditions, higher emissions and weak chemical removal. On the other hand, the upper-tropospheric CO shows an opposite behaviour, peaking in summer-monsoon. The seasonal decrease in lower-tropospheric CO is attributed to the reduction in anthropogenic and biomass burning activity, monsoonal circulation and the presence of strong convective activity. The vertical updrafts lifting the CO to higher altitudes cause increase at higher altitudes as observed. The columnar CO exhibits similar variation as that of lower tropospheric CO, however, it peaks during pre-monsoon most of the regions or shows comparable levels as that of winter.

- The correlation analysis between columnar CO and fire counts show the stronger correlation coefficient positive (0.4–0.7) over NE-I, followed by E-I (0.3–0.6) indicate that biomass burning is a dominant controlling factor for the seasonal variation of CO over these regions. The biomass burning events over W-IGP (Haryana/Punjab region) corresponding to the crop residue burning enhances the columnar CO during pre-monsoon (May) as well as post-monsoon (October) over the region. The pre-monsoon peak in columnar CO over E-IGP has become prominent over the recent years (2009-2018).

- The grid-by-grid analysis of trend considering ~18 years of MOPITT data shows the decreasing trend of -1 to -2.5 ppbv year^{-1} (-0.5 to -1.5% year^{-1}) in the lower

troposphere over India and surrounding oceanic regions. While trend is significant over W-I, W-IGP, E-IGP, surrounding oceans, it is not significant over central-I, S-I and E-I part of India. Extending the analysis over the globe, the decreasing trend observed globally in lower-tropospheric CO is confirmed by in-situ surface CO observations from NOAA-network. The columnar CO also exhibits a decreasing trend of -0.5 to -2 molecules cm^{-2} $year^{-1}$ (-0.1 to -1 % $year^{-1}$). Using the multiple satellites, it is confirmed that decreasing trend in columnar CO is realistic. The upper-tropospheric CO shows increasing trend over India as well as over the globe, however, retrievals from multiple satellites are not consistent and hence full confidence could not be attributed to the increasing trend in upper-tropospheric CO, which needs further study. However, evidences of increase in the convective activity indicate the possibility of increasing trend in the upper-tropospheric CO.

- Though increase in anthropogenic activity over India (as well as over the globe) is evident, a decreasing trend is seen in the lower-tropospheric and columnar CO. The observed increase in water vapour, O_3 and/or NO could increase the OH levels leading to strengthening of sink mechanism of CO. This could be one of the reasons for the decreasing trend in CO, in addition to possible reduction in emissions due to implementation of vehicular pollution norms by the government. If the increasing trend in upper-tropospheric CO is realistic, the convective uplifting of the lower-tropospheric CO to the higher altitude could be a possible reason for increasing trend in upper-tropospheric CO which also partially explains the decreasing trend in lower-tropospheric CO.

- The decreasing trend in CO appears to be indicator of improvement in air quality, however, it points to the possible increase in O_3 or NO which are also air pollutants. One of the possible implications of decreasing trend in CO would be reduction in lifetime of methane.

<div align="center">***</div>

Chapter - 6

Model simulations of the near-surface CO: Comparison with observations

6.1   Introduction

There are various factors and processes controlling the mixing ratios and its variabilities (both temporal and spatial) in the tropospheric CO as discussed in the previous chapters. These factors include, (1) variabilities in the strength of emission (2) the distance from the source region to the point of observation or proximity to the source regions (3) synoptic and mesoscale meteorological conditions [e.g., winds, humidity, temperature, boundary layer or mixing height, and exchange between free-troposphere and boundary layer] and (4) chemical transformation (production of CO mainly from oxidation of methane and Isoprene; destruction of CO through OH radical; Seinfeld and Pandis, 2006). The delineation of contributions from various processes in the observed CO mixing ratios is very important. Some of the processes or the contributions can be delineated utilising the measurements of isotopes of CO. The ratio of $^{18}O/^{16}O$ in CO ($\delta^{18}O(CO)$) are being utilised to delineate contribution from fossil fuel combustion (high $\delta^{18}O(CO)$, biomass burning (less $\delta^{18}O(CO)$) and photo chemically generated CO (nearly zero $\delta^{18}O(CO)$) [Muhle et al., 2002]. In the absence of isotopic measurements, model simulations are considered as a potential tool for such estimations.

In this study, the photochemical box model and the Weather Research and Forecasting model coupled with Chemistry (WRF-chem) are utilised to understand the role of photochemistry, and to delineate the contribution of anthropogenic emission and transport to the total CO. In this chapter, photochemical box model is utilised to quantify the effect of water vapour, O_3, NO_2 and hydrocarbons on CO. The detailed description of the box model and WRF-Chem models are given in the following sections 6.2.1 and 6.2.2.

6.2 Model description and simulations

6.2.1 Box model simulations

The box model (or zero-dimensional model) is the simplest model, where the region of interest (or atmospheric domain) is represented by one box. When model is coupled with radiation (wavelength dependent flux), it is so-called photochemical box model. However, there exist options to simulate the effect of emission, dilution, boundary layer changes, etc. The photochemical box model, developed at National Center for Atmospheric Research, Boulder, USA, is known as NCAR's Master Mechanism (NCAR-MM) model [Madronich and Calvert, 1990; Madronich and Flocke, 1999; Saunders et al., 2003], which is used in this study. In this model, the atmospheric domain of interest is represented by a box and the chemical reaction rates are the backbone of the model. Concentration is same everywhere inside the box and hence it is a function of time only (Seinfeld and Pandis, 2006). As time advances, the concentration changes depending on the chemical reaction rates. One of the important inputs of the model is the initial concentration of species of interest. With the given initial concentrations, model calculates the concentrations at time step of a second based on reaction rate coefficients. In this temporal evolution, the species formed at any time step are considered and carried over to the next step of reaction/simulation. Since rate coefficients are temperature and pressure dependent, temperature and pressure are also necessary inputs. The box-model, by definition, does not account for transport (horizontal or vertical). The model being a photochemical box model, wavelength dependent flux (at given altitude) is needed for the simulation, which is estimated using the Tropospheric Ultraviolet Visible (TUV) radiative transfer model with a 4-stream discrete ordinate radiative transfer solver [Stamnes et al., 1988]. Various inputs like, Latitude, longitude, Date, Parcel elevation, Ozone column, Aerosol Optical Depth (AOD) at 550 nm, Aerosol Single Scattering Albedo (SSA), Aerosol Angstrom coefficient, Temperature, and Air density are essential for estimation of radiative fluxes. The estimation of photolysis rate coefficients is also done using the TUV model. In fact, the TUV model is a part of the MM model.

The model simulates chemical evolution of an air parcel taking into account gas phase chemistry among ~2000 gases involving ~5000 reactions. In this study, model is used for computation of time dependent chemical evolution of an air parcel initialised with known composition, assuming no additional emissions, no dilution, no boundary layer variation and no heterogeneous processes. Since no dynamical features

(horizontal or vertical transport) are included in the model, it investigates the effect of chemistry on the known concentration levels of various trace gases.

The recent version of model, version 2.5 downloaded from NCAR's website (https://www2.acom.ucar.edu/modeling/master-mechanism-download) has been made use for simulations on Linux platform using gfortran and C-shell scripts. Any input parameter may be constrained with respect to time, however, in the present study simulations are carried out with given initial conditions/concentration. More details of NCAR-MM are given by Madronich (2006).

6.2.1.1 Role of water vapour
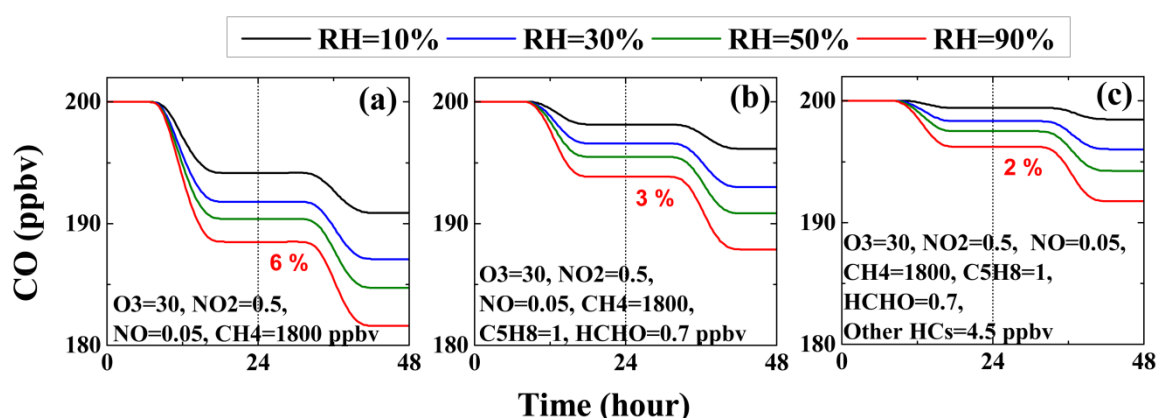
Figure 6.1: Box model simulations for temporal evolution of CO mixing ratio under different levels of water vapour (represented in terms of RH) for various initial conditions (a–c). Note that temperature is constant and increase in RH indeed represent the increase in water vapour content. The initial concentrations of the species are shown at left-bottom corners of each panel. The numbers shown in red colour are the percentage decrease in CO for 90% of RH (specific humidity = ~24 g/kg).

For a quantitative understanding of the role of water vapour in the destruction of CO, the temporal evolution of CO was simulated as a typical case using the NCAR-MM model, initializing with different initial concentrations of different species. The initial concentrations of various gases are so chosen that they represent the background conditions. These values were taken from our in-situ measurements over far oceanic region (equatorial IO) carried out during ICARB-2018. The geographical co-ordinates and the major environmental conditions used for the model simulation include latitude, longitude, date, parcel elevation, ozone column, NO_2 column, AOD at 550 nm, Aerosol SSA, Aerosol Angstrom coefficient, temperature and air density which were 0° N, 77° E, 21 March 2018 (i.e., spring equinox), 500 m, 255 DU, 2.727×10^{15} molecules cm^{-2}, 0.37, 0.73, 1.01, 30° C and 2.41×10^{19} molecules cm^{-2} respectively. The columnar ozone and

NO_2 were taken from OMI retrievals, aerosol parameters were chosen as the typical values over oceanic region (Moorthy et al., 2009).

The simulations were done for the four different levels of water vapour content which is function of temperature and relative humidity (RH). RH values of 10, 30, 50, and 90 % at fixed temperature of 30 °C are considered in this analysis. The estimated water vapour concentration corresponding to these RH values of 10, 30, 50, and 90 % are estimated to be 1.04×10^{17}, 3.12×10^{17}, 5.21×10^{17}, 9.37×10^{17} molecules cm^{-3} respectively and the specific humidity values are ~2.7, 8.0, 13.4, and 24.1 g kg^{-1} respectively. These simulations are carried out for three cases corresponding to three different initial concentrations. The temporal evolutions of CO for 48 h (i.e., 2 days) are shown in figure 6.1a to c for initial CO concentration of 200 ppbv (background values over oceanic region based on our in-situ measurements over the BoB and northern IO). In the case-1 (figure 6.1a), model was initialised with O_3=30 ppbv, NO_2=0.5 ppbv, NO=50 pptv, and CH_4=1800 ppbv; and NMHCs were not considered. The destruction of CO by water vapour is through OH radical. OH is mainly formed from two reactions: (1) $H_2O + O^1D \rightarrow 2\ OH$ and (2) $NO+HO_2 \rightarrow NO_2 + OH$ (Seinfeld and Pandis, 2006). Note that NO is the product of photolysis of NO_2. Lelieveld et al., 2018 has shown through model simulations that reaction (1) and (2) contributes ~35% and 39% (total of ~75%) respectively to the total OH concentration in the lower troposphere. Under this condition (i.e., case-1), the destruction of CO was ~3% for 10% of RH over a day. With the increase in RH up to 90%, reduction in CO increased to ~6% (11.5 ppbv) which is labelled in the figure 6.1a. It is to be noted that all of OH produced with aforementioned mixture of gases, is not used for destruction CO alone. The presence of methane takes its share from available OH concentration through reaction of $CH_4 + OH \rightarrow CH_3 + H_2O$. While Isoprene ($C_5H_8$) and formaldehyde ($CH_2O$) which are consumers of OH, are introduced in the system, the net reduction in CO over a day is reduced. As shown in figure 6.1b, increase in RH up to 90%, reduction in CO is up to ~3% (6.2 ppbv). Furthermore, in the presence of other hydrocarbons (HCs) like C_5H_8 = 1 ppbv, CH_2O = 0.7 ppbv, ethane = 1 ppbv, ethylene = 1 ppbv, propane = 0.3 ppbv, propylene = 0.1 ppbv, i-butane = 1 ppbv, n-butane = 1ppbv, the net reduction over a day reduced further to 2% for 90% RH (figure 6.1c). This is due to less availability of OH for destruction of CO because of the OH consumption by hydrocarbons. In short, for all the initial conditions, higher the water vapour, the stronger the decrease in CO. Moreover, the decrease in CO with the increase in water vapour depends on the concentration levels of precursor gases, particularly NOx and HCs. Here, it is emphasised that the model does not account for any diurnal

constraints, additional emissions, dilution, heterogeneous processes, transport/dynamics which play important role in controlling the observed variations of various species. Since the production/destruction of CO is controlled by inter-dependent reactions of multiple species and a set of meteorological parameters, these simulations can be considered only as approximate magnitude of chemical destruction of CO with increase in water vapour. Under the ambient conditions, realistic concentrations of species like, O_3, NOx, and HCs need to be considered get the actual variations.

6.2.1.2 Whether chemistry can account for decreasing trend in lower-tropospheric CO?
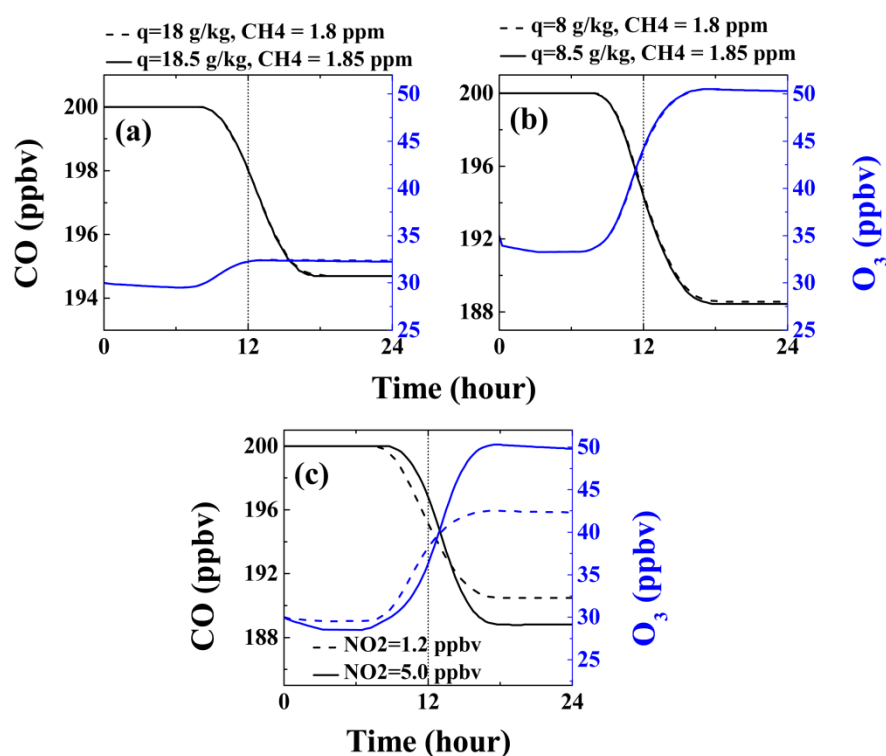
Figure 6.2: Box model simulations for temporal evolution of CO mixing ratio for various initial conditions (a–c; table 6.1) incorporating decadal change of H_2O, CH_4 and NO_2/O_3. While (a) is corresponding to cleaner moisture laden environment (e.g., tropics), (b) represents dry polluted environment, but both cases show the simulations under enhancement in water vapour by 0.5 g kg^{-1} and methane 0.05 ppmv. Figure (c) shows the simulations corresponding where enhancement in NO_2 is considered. The associated O_3 variations (blue curve) are also shown.

As discussed in section 5.8.1, lower-tropospheric CO exhibits decrease over the Indian region at the rate ranging from ~5 to 20 ppbv decade^{-1} (figure 5.12). There exist three possibilities which can explain the decreasing trend. (1) Increase in the strength of sink process. Since major sink for CO is its reaction with OH, increase in OH could cause decrease in CO. (2) Decrease in the CO emission. (3) Increase in convective activity

which could mix the lower tropospheric CO to higher altitude causing decrease in lower-troposphere. Since the measurement of OH is not available over long term, model simulations are used to infer whether OH-chemistry can explain the decreasing trend in CO.

Table 6.1: Initial conditions for the simulations shown in figure 6.2.

Initial conditions for (a)	Initial conditions for (b)	Initial conditions for (c)
CO=200 ppbv	CO=200 ppbv	CO=200 ppbv
O_3=30 ppbv	O_3=35 ppbv	O_3=30 ppbv
NO_2=0.5 ppbv	NO_2=1.5 ppbv	C_5H_8 = 0.01 ppbv
NO=50 pptv	NO=100 pptv	CH_2O=1 ppbv
C_5H_8 = 1 ppbv	C_5H_8 = 0.01 ppbv	H_2O =8 g kg^{-1} [6.98 x 10^{17} molecules cm^{-3}]
CH_2O=0.7 ppbv	CH_2O=1 ppbv	NO=100 ppt
CH_4=1800 ppbv for dashed curve (1830 ppbv for solid curve)	CH_4=1800 ppbv for dashed curve (1830 ppbv for solid curve)	CH_4=1800 ppbv for dashed curve (1830 ppbv for solid curve)
H2O =18 g kg^{-1} [6.98 x 10^{17} molecules cm^{-3}] for dashed curve (18.5 g kg^{-1} [7.18 x 10^{17} molecules cm^{-3}] for solid curve)	H_2O =18 g kg^{-1} [6.98 x 10^{17} molecules cm^{-3}] for dashed curve (18.5 g kg^{-1} [7.18 x 10^{17} molecules cm^{-3}] for solid curve)	NO_2=1.5 ppbv for dashed curve (5 ppbv for solid curve)

As mentioned before, OH is mainly formed from two reactions. (1) H_2O + O^1D → 2 OH and (2) NO+HO_2 → NO_2 + OH (Seinfeld and Pandis, 2006). Note that NO and O^1D are the product of photolysis of NO_2 and O_3 respectively. Thus, increase in OH could be due to increase in H_2O, O_3 and/or NO_2. Surface specific humidity shows increasing trend over the globe including Indian region. The magnitude of the increasing trend is in the range of ~0.15 to 0.5 g kg^{-1} decade^{-1} over Indian region (IPCC-2013, Jaswal and Koppar, 2011). The increasing trend in surface ozone is not linear and different trends are observed corresponding to different time period (Nair et al., 2018; Cooper et al., 2014). The increasing trend estimated based on annual mean of surface O_3 measured at Thumba, Thiruvananthapuram (2005–2014) shows ~7 ppbv decade^{-1}. Surface NO_2 as well as Tropospheric NO_2 showed increase over a decade 2004–2014 at Thumba, however, observed trend is not linear (Nair et al., 2018; David and Nair, 2013). Further,

CH_4 which is a significant consumer of OH (after CO) shows increasing trend (Kavitha and Nair, 2017). The annual mean surface CH_4 at Cape Rama, Goa (15.08° N, 73.83° E) showed trend of ~30 ppbv decade^{-1} over 2000–2012 (The trend is estimated based on in-situ observations obtained from https://gaw.kishou.go.jp/search). Based on the observed decadal changes in water vapour, O_3 (or NO_2) and CH_4, two sets of simulations were carried out.

In the first set of simulations, moisture laden cleaner environment (similar to the tropical oceanic region) and dry polluted environment (for example, desert or rural region) are considered and model was initialised with corresponding concentration levels as shown in the table 6.1. Keeping all conditions same, water vapour and CH_4 was increased by 0.5 g kg^{-1} and 30 ppbv respectively. The corresponding to this, figure 6.2a and b shows temporal evolution of CO for moisture laden cleaner environment and dry polluted environments with and without increase in water vapour and CH_4, respectively. The decrease of CO is due to destruction through OH, which is from the presence of NO_2 and formation of O_3. By introducing addition 0.5 g kg^{-1} water vapour (which is corresponding to decadal increase), CO did not reduce further significantly. Also note, along with additional water vapour, addition of 30 ppbv CH_4 reduces availability of OH for CO destruction. Thus, observed decadal increase of water vapour in the atmosphere could account the decrease in CO by <0.2 ppbv (negligible magnitude, as can be seen that continuous curve almost overlay the dashed curve in the figure 6.2). Thus, another simulation was carried out in which NO_2 and O_3 were increased and addition decrease in CO is seen.

Figure 6.2c shows the temporal evolution of CO for polluted environments corresponding to the initial conditions as shown in table 6.1. In this set of simulations, NO_2 was increased such that observed O_3 level increases by ~7–8 ppbv (similar to what is observed at Thumba). Also, similar to previous case, CH_4 was increased by 30 ppbv. As seen in the figure 6.3c, while O_3 level is risen by ~7 ppbv, reduction in CO is ~2 ppbv.

In nutshell, these simulations show that the observed decreasing trend in CO (5 to 20 ppbv over a decade) could be partly accounted by the chemistry due to the increase in water vapour and O_3 (and/or NO_2). However, It should also be noted that while CH_4, NO_2, O_3 have increased over a decade, VOCs also would have changed significantly (IPCC 2013). IPCC 2013 reports decrease of ethane and other VOCs over some parts of the globe. Satellite retrieved columnar formaldehyde shows significant positive trends (from 1997 to 2007) over China as well as India and negative trends

over Tokyo, Japan and the northeast USA (De Smedt et al., 2010). Global coverage of VOC measurements is poor, except for a few compounds (IPCC 2013). Unfortunately, long-term observations for the possible change in VOCs are not available and hence could not be accounted in the simulations. In addition to the chemistry (or increase in OH through NO_2 and O_3), the decrease in CO emission would also be partially responsible for the observed magnitude of decreasing trend. Here it may be noted that pollution control measures are being implemented strictly by the government to cut down the anthropogenic emissions, in particular the vehicular and industrial emissions. However, emission inventories (REAS, EDGAR, etc) shows increasing trend and multiple models (chemical transport model and chemistry climate model) using time dependent emission inventories could not reproduce the observed decreasing trend over Southeast Asia due to the positive emission trends (Strode et al., 2016). This raises enigma that trends seen in emission inventories are overestimated or chemistry simulations underestimate the decrease in CO simulated using box model with limited number of species.

6.2.1.3 Role of hydrocarbons
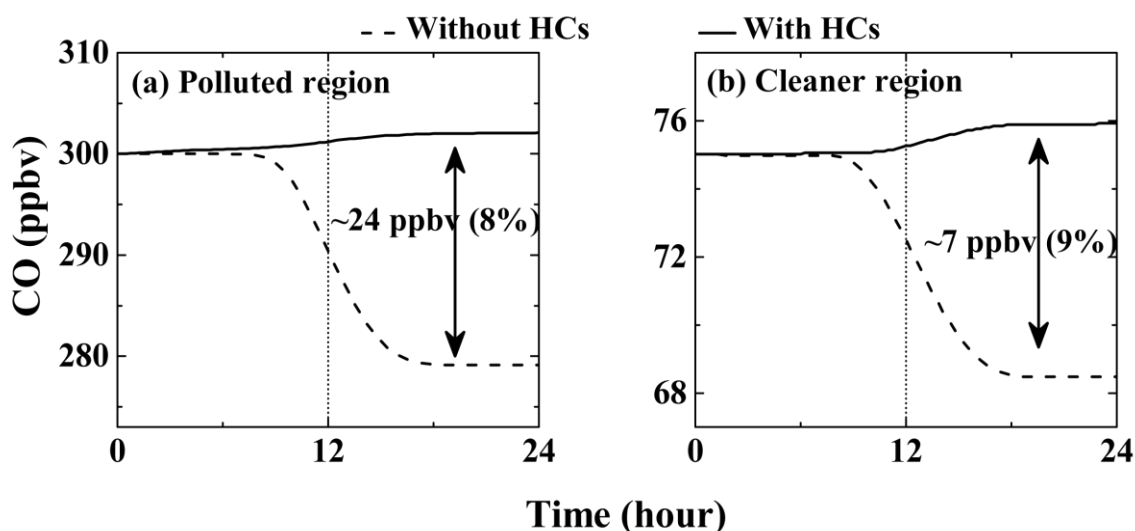
Figure 6.3: Box model simulations for temporal evolution of CO with and without hydrocarbons, for two different sets of initial conditions based on in-situ measurements over northern IO during ICARB-2018. While (a) is corresponding to polluted region, (b) represents cleaner region. The initial conditions are listed in the table 6.2.

Utilising the limited in-situ measurements of hydrocarbons made over northern IO during ICARB-2018, simulations were carried out for coastal polluted region of south-eastern AS and cleaner region of equatorial IO. These simulations were conducted

to estimate the contribution of hydrocarbons in the prevailing CO concentration. Two simulations were made with and without HCs. The initial conditions are set as given in the table 6.2 based on flask-based in-situ measurements over different regions (The measurements were made in collaboration with Physical Research Laboratory, Ahmedabad, India). Note that all the hydrocarbons/VOCs were not measured and limited number of species is included in the simulations as listed in the table 6.2.

Table 6.2: Initial conditions for the simulations shown in figure 6.3.

Initial conditions for (a): Polluted region (southeast coastal AS)	Initial conditions for (b): cleaner region (equatorial IO)
CO=300 ppbv	CO=75 ppbv
O_3=65 ppbv	O_3=15 ppbv
H_2O =75% RH (T=28° C)	H_2O =75% RH (T=28° C)
NO_2=1 ppbv	NO_2=0.1 ppbv
NO=0.1 ppbv	NO=0.001 ppbv
HCs:	HCs:
CH_4=2000 ppbv	CH_4=1870 ppbv
C_5H_8 = 1 ppbv	C_5H_8 = 0.05 ppbv
CH_2O=0.7 ppbv	CH_2O=0.1 ppbv
C_2H_6=2.5 ppbv	C_2H_6=1 ppbv
C_2H_4=6 ppbv	C_2H_4=3 ppbv
C_3H_8=1.3 ppbv	C_3H_8=0.3 ppbv
C_3H_6=3 ppbv	C_3H_6=1 ppbv
n-butane=30 ppbv	n-butane=10 ppbv

In figure 6.3a and b, temporal evaluation of CO is shown in presence and absence of HCs for polluted and cleaner regions, respectively. As seen in the figure 6.3, in the presence of HCs, daytime reduction of CO is vanished and slight enhancement is evident. This is mainly due to the fact that OH radicals are being utilised for oxidation of HCs and oxidation of some of HCs would produce CO (e.g., CH4 and Isoprene). The net enhancement in CO would be ~24 (8% with respect to 300 ppbv) and 7 (9% with respect to 75 ppbv) ppbv over polluted and cleaner environment, respectively, due to presence of HCs. In short, addition of HC enhances CO. These simulations could provide a broad idea on how photochemistry involving H_2O, NO, NO_2, CH_4 and VOCs control the time evolution of CO. But it could not provide an accurate quantitative estimate of the CO variations. In fact, the zero-dimensional model, the photochemical box model is the simplest one and capable for investigations on detailed chemistry involving ~2000

gases involving ~5000 reactions, it does not account for transport and dynamics showing the limitations while comparing with in-situ measurements. Also, in the present analysis, the box model estimations are limited for the initial concentrations shown in table 6.2 which corresponds to the observations during ICARB-2018 which may not be the true for all the scenarios. Moreover, the complicated inter-dependent chemistry coupled with changing meteorology makes it difficult to simulate the realistic observations in the ambient atmosphere. Hence, the photo chemical model cannot substitute for a three-dimensional chemistry-transport model, particularly for the spatial and temporal distribution of emissions, vertical as well as horizontal transport and dispersion. The three-dimensional models simulate the full concentration field, which is function of position (x, y, z) and time. In fact, the model complexity and accuracy increase with dimensionality. The simulations are carried out using the regional chemistry-transport model, i.e., Weather Research and Forecasting model coupled with Chemistry (WRF-Chem) which is a three dimensional model and it is one of the well-established models to study the regional scale changes in trace gases and aerosols.

6.2.2 WRF-Chem simulations

WRF-Chem is a three-dimensional chemistry-transport model and being used for investigation of variations in trace gases and aerosols and associated dynamical and chemical processes. The model simulates the emission, transport, mixing, and chemical transformation of trace gases and aerosols simultaneously with the meteorology (https://www2.acom.ucar.edu/wrf-chem). It is suitable for regional-scale studies. Various fields at the boundaries of study region (i.e., model domain) are being provided by global models like Model for Ozone and Related chemical Tracers-Version-4 (MOZART-4). The MOZART-4 is a global chemistry transport model developed by the NCAR, GFDL (NOAA Geophysical Fluid Dynamics Laboratory) and MPI-Met (Max Planck Institute for Meteorology). It contains comprehensive tropospheric chemistry including >130 chemical and aerosol species and associated chemical reactions (Emmons et al., 2010). The code of the WRF-Chem was developed, updated and maintained at the NOAA/ESRL/GSD in collaboration with other research groups at NOAA/ESRL, NCAR, PNNL, NASA and ERDC and many other institutes (https://ruc.noaa.gov/wrf/wrf-chem/support-team.htm). The user guide and related documents (https://ruc.noaa.gov/wrf/wrf-chem/model_info.htm), tutorials (https://ruc.noaa.gov/wrf/wrf-chem/Tutorial.html), various tools

(https://www2.acom.ucar.edu/wrf-chem/wrf-chem-tools-community) for installing, compiling and running the model are available from NOAA and NCAR websites. Two versions of WRF-Chem were used as available at the time of study. WRF-Chem (Grell et al., 2005) version 3.5.1 and 3.9.1 were used to simulate meteorological and chemical fields during the two different study periods (monsoon and winter seasons respectively).

Table 6.3: The WRF-Chem options used for parameterisation of atmospheric processes.

Atmospheric Process	Scheme used	Features of the scheme
Cloud microphysics	Lin et al., scheme (Lin et al., 1983)	Sophisticated parameterization including ice, snow and graupel processes, suitable for high-resolution simulations.
Longwave radiation	Rapid Radiative Transfer Model (RRTM; Mlawer et al., 1997)	Accurate scheme utilizes look-up tables for efficiency, accounts for multiple bands and microphysical properties.
Shortwave radiation	Goddard shortwave scheme (Chou and Suarez, 1994)	Two-stream multi-band scheme using O_3 from climatology and includes cloud effects
Surface Layer	Monin–Obukhov scheme (Janjic, 1996)	Based on Monin-Obukhov with Zilitinkevich thermal roughness length and standard similarity functions from look-up tables
Land surface option	Noah Land Surface Model (Chen and Dudhia, 2001)	Unified NCEP/NCAR/AFWA scheme with soil temperature and moisture in four layers, fractional snow cover and frozen soil physics. This includes the modifications for better representation of processes over ice sheets and snow covered areas.
Urban surface physics	Urban Canopy Model	3-category urban canopy model with surface effects for roofs, walls and streets.
Planetary boundary layer	Mellor–Yamada–Janjic scheme (Janjic, 2002)	One-dimensional prognostic turbulent kinetic energy scheme, local vertical mixing is included.
Cumulus parameterization	Grell 3D Ensemble scheme (Grell, 1993; Grell and Devenyi, 2002)	Improved version of the GD scheme suitable for coarse as well as high resolution simulations

The model domain is defined on the Mercator projection, at a spatial resolution of 15 km × 15 km. The model has 51 vertical levels from surface to 10 hPa. While the model domain was 65–95° E and 5–25° N for the simulations of CO during monsoon season corresponding to the observations during CTCZ campaign, it was 55–98° E,

13°S–40°N for winter seasons during ICARB-2018 experiment. The selection of domain size is based on the regions from which airmasses are reaching to the points of observations. The meteorological inputs have been adopted from ERA-Interim reanalysis by the ECMWF. Horizontal winds, temperature, and water vapour are nudged above the planetary boundary layer using a nudging coefficient of 0.0003 s^{-1} (Kumar et al., 2015), employing the four-dimensional data assimilation (FDDA) technique. The nudging with coefficient of 0.0003 s^{-1} is known as moderate nudging (Kumar et al., 2015). Anthropogenic emissions of CO, NOx, SO$_2$, and NMVOCs are provided by a regional emission inventory that was developed to support INTEX-B (Zhang et al., 2009; Kumar et al., 2012; Ojha et al., 2016). Aerosol emissions are provided by the Hemispheric Transport of Air Pollution (HTAP v2) inventory (Janssens-Maenhout et al., 2015). Anthropogenic emissions of gases were used from HTAP v2 for the simulations corresponding ICARB-2018 experiment. Biomass burning emissions from NCAR Fire Inventory (FINN; Wiedinmyer et al., 2011) and biogenic emissions calculated online using MEGAN (Guenther et al., 2006) were used in the simulations. Gas-phase chemistry in the model is represented by the second-generation Regional Acid Deposition Model (RADM2; Stockwell et al., 1990), and the aerosol module is based on MADE SORGAM (Binkowski and Shankar, 1995; Ackermann et al., 1998; Schell et al., 2001). Initial and boundary conditions for chemical fields are provided by the MOZART-4/GEOS5 data. The options used to parameterise different atmospheric processes are given in table 6.3. The information on evaluation of WRF-Chem simulations of CO over India and schemes used in the present simulations can be found elsewhere (e. g. Kumar et al., 2012; Ojha et al., 2016).

6.2.2.1 Simulations for marine boundary layer CO during monsoon season: Inter comparison and broad inferences

The spatial distribution of CO in the marine environment of BoB as measured during the CTCZ campaign conducted in the monsoon months (July 16–August 17, 2009) has been simulated using WRF-Chem. Simulations were conducted for the period from 29 June to 31 August 2009 and considering spin up time of 15 days, simulated output upto 15 July 2009 was discarded. Prior to analysing the chemical fields from WRF-Chem, meteorological fields need to be validated with in-situ measured parameters to ensuring that meteorology is correctly simulated. Figure 6.4 shows a comparison of WRF-Chem simulated meteorological parameters with the in-situ measurements along the cruise track during monsoon over the BoB. Model is seen to

simulate the temporal variations in meteorological parameters, with limitations in capturing sharp reduction in the air temperature and corresponding enhancements in relative humidity. The comparison shows the mean bias and correlation coefficient of -1.9 hPa, -0.6° C, and -1.1%; and 0.96, 0.4, and 0.6 in pressure, temperature and humidity respectively. This confirms that meteorology is well simulated and chemical fields can be simulated for further analysis.
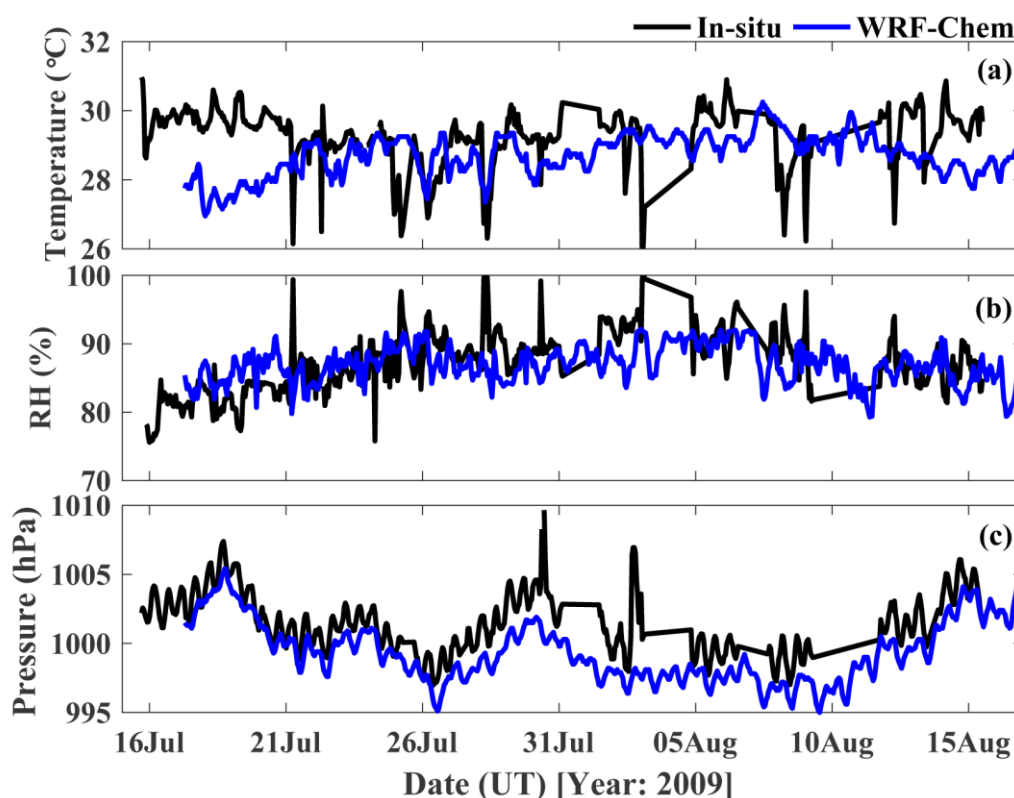
Figure 6.4: Comparison of WRF-chem simulated (blue curve) and in-situ measured (black curve) variations in surface temperature, relative humidity (RH) and pressure during the CTCZ campaign over the BoB.

Figure 6.5 shows the WRF-Chem simulated mean spatial distribution of surface CO averaged over the campaign period along with the in-situ measured surface CO mixing ratio along the cruise track during the CTCZ campaign. The characteristic of monsoonal CO distributions are discussed in detail in section 3.3. Even though the WRF-Chem simulated mean CO mixing ratio over the BoB and the in-situ measured CO do not match in terms of their magnitude, the distribution pattern exhibit more or less similar picture with more high values towards the coast and low towards east (i.e., central BoB). The mismatch could be due the fact that the in-situ measurements correspond to the particular location at a certain time, while the model simulation represents the mean picture over a month (i.e., July 16–August 17, 2009). The interesting features which could be inferred are: (1) The background surface CO over the oceanic regions is 60–75

ppbv, except over the regions closer to east coast of India. (2) The stronger westerlies bring pristine air from AS/IO and penetration of oceanic influence along west coast of India (blue contours) are clearly evident. The CO emitted over the Indian region outflows over to the BoB along with the prevailing westerlies. In other words, wind transports the CO emitted over the Indian region over to the BoB as can be seen as the high CO levels along the east coast over the BoB.
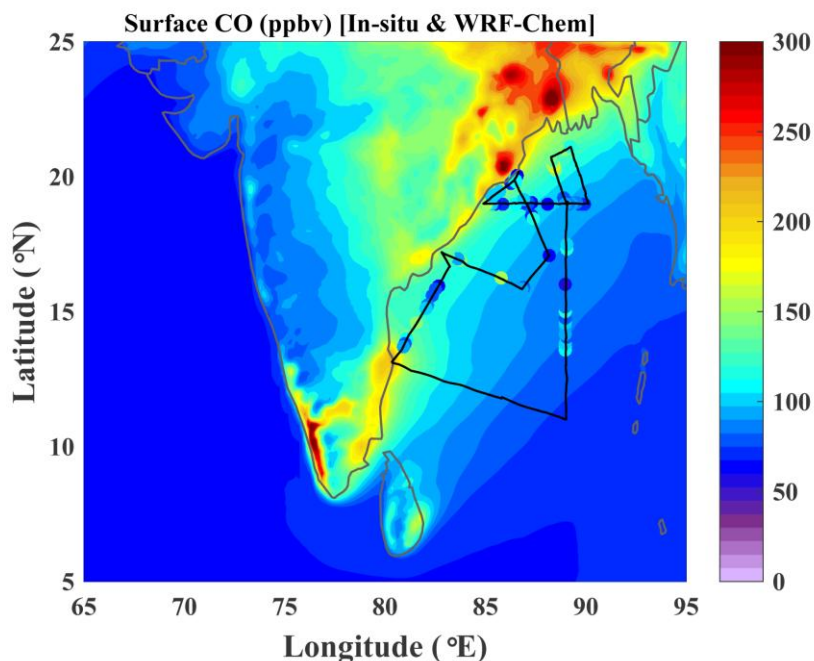
Figure 6.5: WRF-Chem-simulated mean spatial distribution of surface CO averaged during the CTCZ campaign period (July 16–August 17, 2009) is shown in as contour map. The in-situ measured surface CO mixing ratios along the cruise track (black line) during the campaign is superimposed on the contour map.

Figure 6.6a shows the one-to-one comparison of the WRF-Chem-simulated surface CO and the in-situ measurements taken along the cruise track. Figure 6.6b shows the variation of location (latitude and longitude) with time along the cruise track. WRF-Chem is found to reproduce the observed variations of CO over the BoB during the monsoon season with an overestimation of absolute CO levels by 18 ppbv (i.e. ~16% of averaged CO value, 96 ppbv) as calculated by taking difference between means of in-situ and simulated surface CO. Biases in the model simulations are attributed to the uncertainties in the emission datasets and in the simulated meteorology; however, in the present study, the model fields are used mainly to investigate temporal variations rather than absolute mixing ratios. The correlation coefficients between the daily averaged in-situ measured and simulated CO is ~0.4. To delineate the contribution of anthropogenic influence from Indian region, an additional simulation was conducted by

switching off the anthropogenic emissions over the model domain. The mean CO level is lower by 36 ppbv with smaller variability of 4.9 ppbv as seen in the figure 6.6a (dotted curve). This shows that enhanced levels and observed variability in CO mixing ratios over BoB are attributable to the anthropogenic emissions mostly from Indian landmass. Note that July–August being monsoon season, biomass burning events were negligible and hence the contribution of biomass burning to the observed variations in CO could be negligible. Also, note the transient enhancement in CO as marked by red arrow which is explained in the following section.
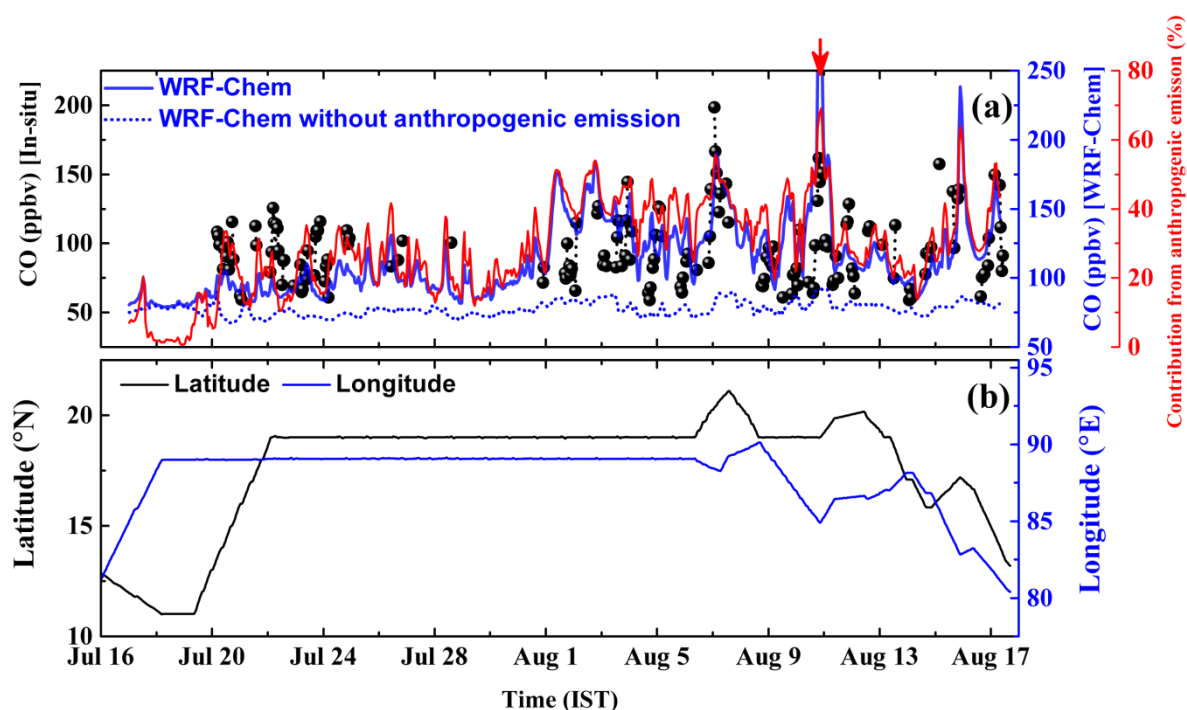
Figure 6.6: Variations in observed CO along with WRF-chem simulated CO (blue line) during the CTCZ campaign. Red arrow marks an event of CO enhancement which is corresponding to the spatial distributions shown in figure 6.7. Blue dotted curves shows WRF-Chem simulated CO without anthropogenic emissions within the model domain. Red curve shows percentage contribution from anthropogenic emissions. (b) shows the variations in measurement locations.

The enhancement in CO on 10 August 2009 as marked by red arrow in figure 6.6a is investigated further. The influence of horizontal advection on CO during this event is shown more clearly in figure 6.7, which shows the spatial distribution of CO from WRF-Chem. The white triangles show the two locations where the event was observed. A patch of higher levels of CO (~300 ppbv) is found to be distributed across the east coast of the Indian region. As time advanced, the patch of CO moved further over to the BoB along with dilution. Hence, under the prevailing synoptic winds (figure 3.16), the transport of CO patch along with dilution is clearly seen. Thus, in a nutshell, the horizontal advection played a key role in transporting CO-rich airmasses deeper into

the BoB region during the monsoon season. This feature is clearly seen in the mean distribution of CO (figure 6.5) also.
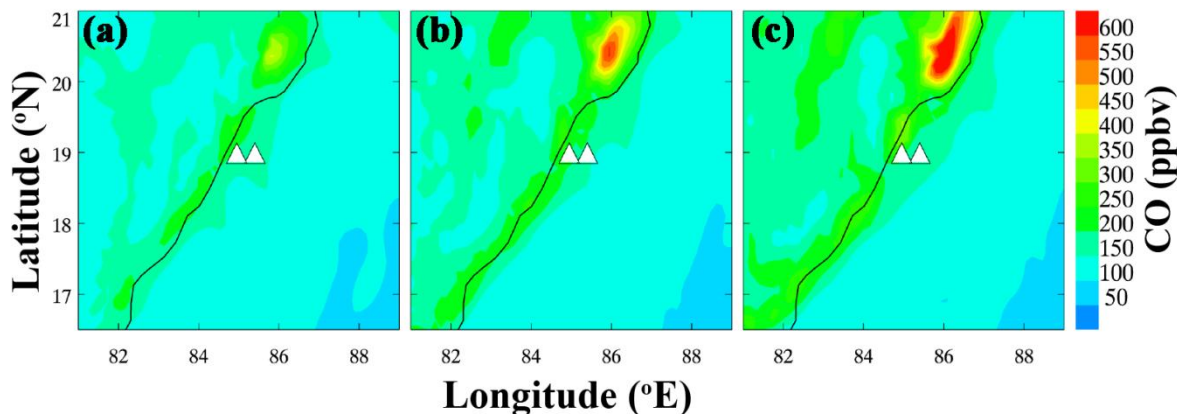
Figure 6.7: Spatial distribution of surface CO at (a) 16:00, (b) 19:00 and (c) 22:00 UT on 10 August 2009, during the CO enhancement event, as marked by red arrow in figure 6.6a. White triangles show two locations (85.40° E, 19.00° N; 84.95° E, 19.00° N) corresponding to the event.

6.2.2.2 Simulations of marine boundary layer CO for winter season (ICARB-2018 campaign)

Similar to the simulations done for monsoon season as discussed above, simulation was carried out for winter season, corresponding to the period of ICARB-2018 campaign (January 16–February 14, 2018). As discussed in section 6.2.2.1, meteorological fields simulated by WRF-Chem are compared with in-situ measurements. Figure 6.8 shows a comparison of WRF-Chem simulated meteorological parameters (temperature, relative humidity and pressure) with the in-situ measurements along the cruise track during ICARB-2018 campaign over the northern IO. This comparisons shows the WRF-Chem simulated the meteorological fields well with correlation coefficient of 0.5, 0.46, and 0.79 for temperature, relative humidity and pressure respectively. A fair agreement between in-situ measured and simulated meteorological parameters ensures that meteorology is simulated well in the model and simulated chemical fields can be used for further inferences on the regional scale.
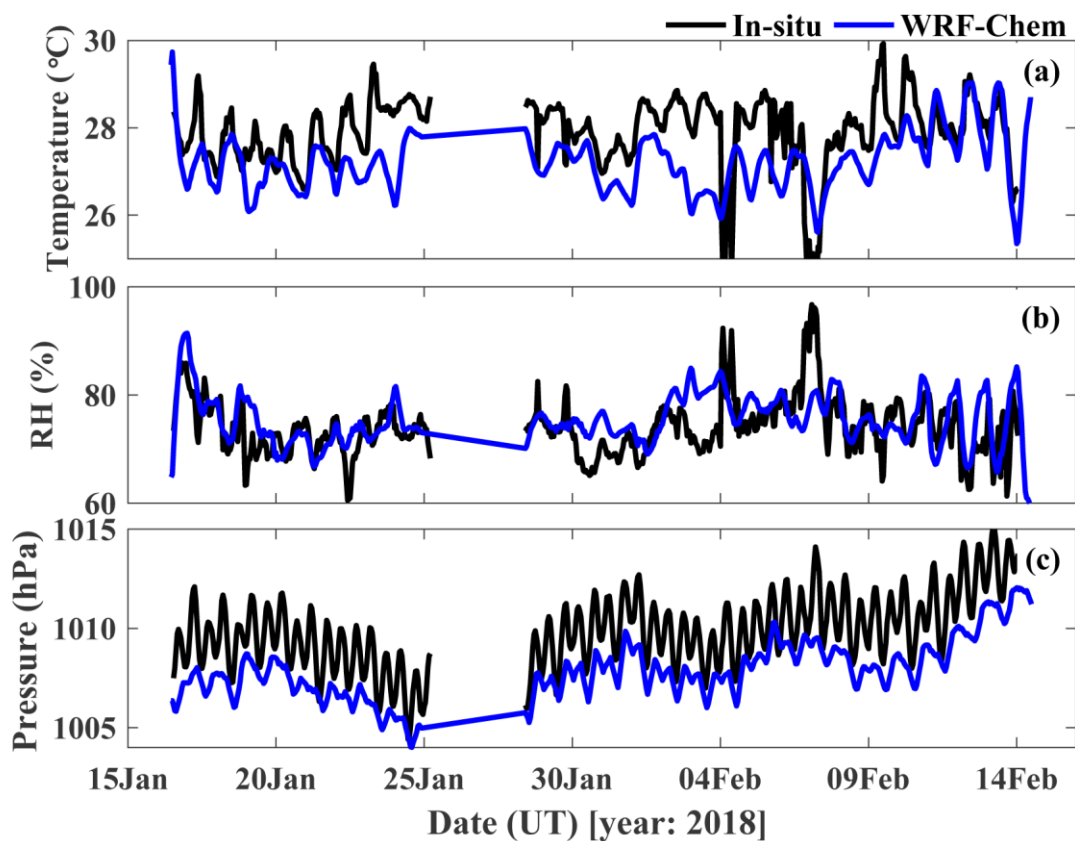
Figure 6.8: Comparison of WRF-chem simulated (blue curve) and in-situ measured (black curve) variations in surface temperature, relative humidity (RH) and pressure during ICARB-2018 campaign over the northern IO.
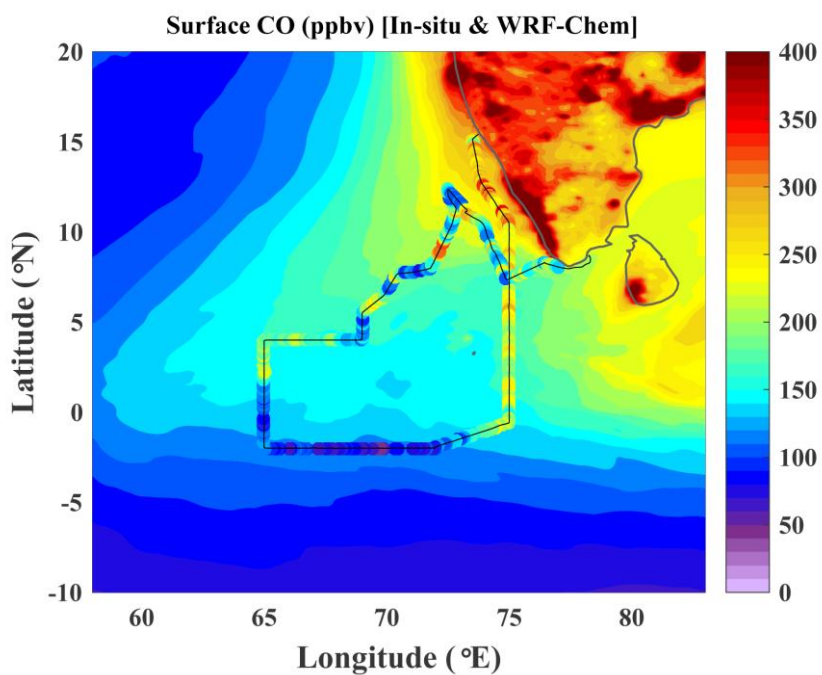
Figure 6.9: WRF-Chem-simulated mean spatial distribution of surface CO averaged during the ICARB-2018 (January 16 – February 14, 2018) is shown in as contour map. The in-situ measured surface CO mixing ratios along the cruise track (black line) during the campaign is superimposed on the contour map.

Figure 6.9 shows the mean spatial distribution of CO as simulated using WRF-Chem for the period of ICARB-2018 campaign. The in-situ measured surface CO mixing ratio along the cruise track is superimposed on the mean WRF-Chem simulated CO in figure 6.9. More details on the spatial distribution of CO over the northern IO as measured along the cruise track during the ICARB-2018 campaign are presented in Chapter 4. The higher CO mixing ratios (250–350 ppbv) over southeast AS and lower mixing ratios (50–100 ppbv) over equatorial IO are well reproduced. The synoptic winds during the winter seasons (figure 4.1) bring the pollutants from South Asian region to AS and then to IO, which is represented well by the model.

Figure 6.10a shows the variation of the model simulated values (blue line) along the cruise track on day to day basis along with the in-situ measured CO mixing ratio and (black dots). Most of the regions, the spatial pattern of model simulations match with the in-situ measurements. The correlation coefficient between in-situ measured CO and WRF-Chem simulated is 0.57 and the mean bias is +25 ppbv (~14% of its mean value, i.e., 174 ppbv). This shows that WRF-Chem simulation reproduced the variability with overestimation of mean CO levels. Figure 6.10b shows the variation of latitude and longitude with time. To delineate the contribution of biomass burning and anthropogenic activity from South Asian region (i.e., model domain), additional simulations were conducted by switching off the anthropogenic emissions (blue dotted line) within the model domain. By switching off the anthropogenic emissions in the model domain, CO levels reduced significantly over many regions. However, the reduction is negligible specifically over equatorial IO (where the ship was during 27 January to 01 February 2018). The contribution of anthropogenically emitted CO over the equatorial IO is ~5-15%, which is expected as airmass over this region is of marine origin. The CO mixing ratios seen in the absence of anthropogenic emissions is mainly due to the influx of CO at the boundary of the model domain (i.e., 55–98° E, 13° S–40° N). The red curve shows the percentage contribution of CO from anthropogenic emission to the total WRF-Chem simulated surface CO. This shows that enhanced levels and observed variability in CO mixing ratios over the southeast AS are attributable to the regional anthropogenic emissions up to 65%. In the absence of anthropogenic emissions within the model domain, the model simulated mean CO level is 128 ppbv with smaller variability of 62 ppbv.
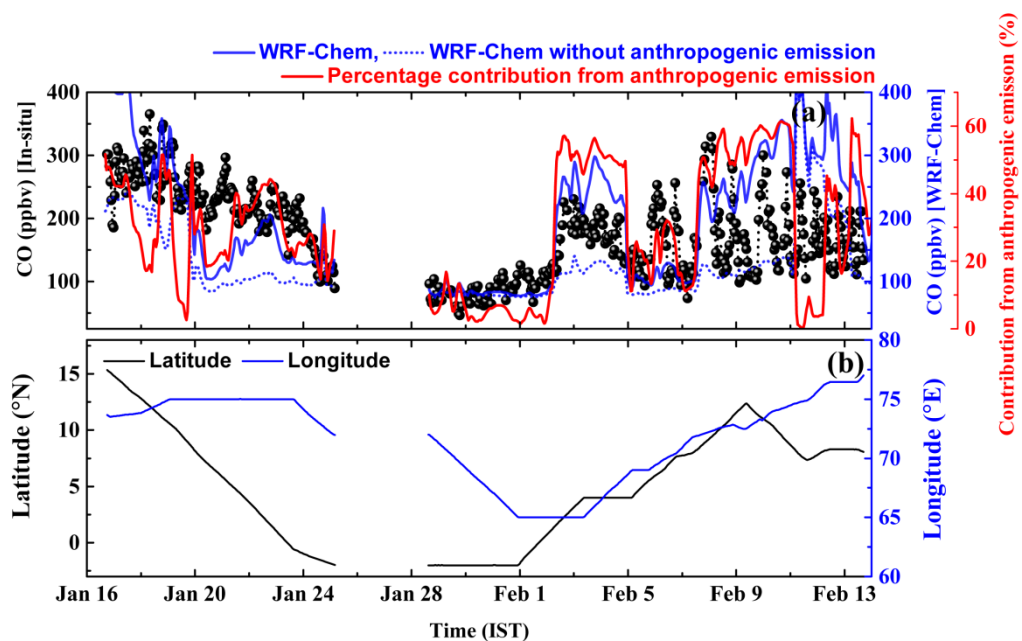
Figure 6.10: Variations in observed CO (black dots) along with WRF-Chem simulated CO (blue line) during the ICARB-2018 campaign. The dotted blue curve shows the WRF-Chem simulated CO without anthropogenic emission in the model domain. The red curve shows the percentage contribution from the anthropogenic emissions. Variations in the measurement locations along with time are shown in (b).

The mismatch between WRF-Chem simulated and in-situ measured surface CO could be due to uncertainties involved in the simulations as followings. (1) Uncertainty in the emission inventories (2) Though meteorological fields simulated well, there exist small biases and deviations over certain regions, which would contribute uncertainty in simulated surface CO.

6.3 Summary

The photochemical box model (NCAR-MM) and regional chemistry transport model (WRF-Chem) were utilised to understand the role of chemistry and to delineate the anthropogenic contributions to the surface CO over the oceanic regions respectively. In addition, inter-comparisons between the model simulated surface CO and in-situ observations were carried out to evaluate the model simulations. The results of the model simulations are summarised as followings.

- The increase in the water vapour causes the decrease in CO through its reaction with OH, the source of which is water vapour in the presence of sunlight and O_3 or NO_2. Under the different scenarios of combinations of trace gas concentrations; box model shows that when RH is increased to 90% (under constant temperature), 2−6% reduction in CO occurs over a day. It also shows

that amount of CO reduction due to water vapour depends on the concentration levels of gases like NO_2, CH_4, etc.

- Box-model simulations utilising the observations of hydrocarbons over polluted and cleaner oceanic regions shows that net effect of prevailing concentration level of hydrocarbons contributes ~8-9% of CO which is due to oxidation of hydrocarbons producing CO as well as due to reducing the availability of OH for destruction of CO.

- Based on observed decadal increase in water vapour, CH_4 and O_3 (or NO_2), box model simulations shows that chemistry (or CO +OH reaction) could account for the observed decreasing trend in CO only partially.

- The inter-comparisons of WRF-Chem simulated surface CO with the in-situ observations over the oceanic regions of BoB (during monsoon) and northern IO (during winter) shows that broader features of spatial and temporal variations are reproduced well by the WRF-Chem with slight overestimation of 18–25 ppbv in the absolute mean CO levels. The contributions of anthropogenic emissions to the surface CO over the oceanic regions were estimated by switching off the anthropogenic emissions within model domain. The anthropogenic emissions over the Indian region contributes 20 to 60% to the surface CO over the BoB during monsoons seasons and remaining percentage is due to influx at boundaries of model domain (i.e., Indian region) and biomass burning within the model domain. Similarly, 60% of CO over southeast AS is attributed to the anthropogenic emissions over model domain during winter; it is ~5-15% over the far oceanic region, the equatorial IO. The simulations also show that in absence of anthropogenic emissions variability in surface CO is significantly lower, apart from reduced CO level.

<div align="center">***</div>

Chapter - 7

Summary and Future Scope

The present study has brought out a comprehensive picture of three dimensional (latitude-longitude-altitude) distribution of tropospheric CO over India and surrounding oceanic regions utilising the in-situ measurements, satellite observations and modelling. The seasonal changes and governing various processes (dynamical, chemical) and role of biomass burning and anthropogenic activities are investigated in detail. The role of chemistry and delineation of the contributions of anthropogenically emitted CO over the marine region is studied using model simulations. In addition, using satellite observations of CO the long-term trend is investigated over the Indian region and compared with the global trends. The highlights of the major outcome of the present study and the future scope are presented in this chapter.

7.1 Summary

Chapter - 1 gives an introduction to the atmospheric CO. Following a brief description of the atmospheric structure in terms of pressure, temperature and composition, an overview of atmospheric CO in terms of its natural as well as anthropogenic sources and various sink mechanisms are discussed. The importance of CO in the troposphere in terms of its role in atmospheric chemistry involving OH radical, as precursor to ozone, as an air pollutant having impact on air quality, and as an indirect greenhouse gas having implications on radiative forcing and global warming is highlighted in the chapter. The tropospheric lifetime of CO and its altitude dependence is also presented in this Chapter. Different in-situ and remote sensing techniques used world-wide for the measurement of CO are also explained briefly. The network of ground based in-situ measurements, programs for aircraft based measurements and satellites in the orbit providing the CO measurements are also outlined in this chapter. The scenario of trace gas modelling is also touched upon briefly. Global scenario of its mean concentration levels, trend and literature survey of the scientific studies carried out all over the globe with emphasis on Indian region are also presented. This chapter concludes with the major objectives the present study.

Chapter - 2 describes the measurement technique of the CO analyser utilised for in-situ measurements of surface CO and the satellite based technique for retrieval of CO from the MOPITT. It also includes brief account of the calibration procedures and the uncertainties in the measurements. In addition, the chapter describes the various supporting data sets used in the study which includes in-situ observations of black carbon aerosol, surface ozone, CO observations from NOAA global network, remote sensing observations from various satellites; i.e., TES, AIRS, IASI, MLS, MODIS and OMI, and supplementary data of synoptic wind from ERA-Interim reanalysis; aimass back trajectories from HYSPLIT; and reanalysis/forecast data from MACC and CAMS.

Chapter - 3 presents the comprehensive investigations on tropospheric CO over the BoB making use of ship-based on in-situ measurements of surface CO during winter and monsoon seasons, the available in-situ measurements available during other seasons (from literature), and MOPITT retrievals of vertical profile of CO. CO levels and seasonal changes were quantified and associated atmospheric processes were analysed utilising the synoptic winds, airmass back trajectories, biomass burning activities, and MACC reanalysis data to bringing out the three dimensional distributions of CO over the BoB on seasonal scale. The major findings are summarized in the following.

- The surface CO over the BoB shows significant spatial heterogeneity and seasonal variation. Surface CO mixing ratios ranges from 80–480 ppbv being higher over northern (302±68 ppbv; east-IGP airmass) as well as eastern BoB (340±89 ppbv; Southeast Asian airmass) and lower over southern BoB (168±37 ppbv; marine airmass) during winter season. Lower mixing ratios are observed during monsoon season being 95±25 and 101±27 ppbv over northern (airmass from central/northern India) and central BoB (airmass from southern India) respectively. Combining the observations during other seasons, the seasonal amplitude is ~ 210 and 100 ppbv over northern and central BoB. The CO mixing ratios are higher over northern BoB as compared to the southern BoB, irrespective of the season.

- CO from the biomass burning and anthropogenic activities over landmass surrounding landmasses gets transported to the BoB depending upon the prevailing synoptic wind patterns. While the transport from eastern IGP during winter and pre-monsoon causes higher levels of surface CO over northern BoB, it is due to transport from central/northern India during monsoon season and from Myanmar, Bangladesh and northeast India during post-monsoon season. The central BoB experiences direct influence from eastern IGP, southern India, and

Southeast Asian courtiers during winter, monsoon and post-monsoon seasons. The highest surface CO observed over eastern BoB during winter season which is attributed to biomass burning over Thailand, Cambodia and eastern China, in addition to anthropogenic activities over these regions.

- The MOPITT retrieved surface CO was validated utilising in-situ measurements as available over the BoB during different campaigns and seasons. The correlation coefficient between MOPITT retrieved surface CO and in-situ measured surface CO is found to be around 0.7 which shows the potential of MOPITT surface retrievals to study the regional and seasonal changes in CO. The MOPITT retrieved vertical profiles of CO over the BoB are consistent with TES retrieved profiles.

- While MACC reanalysis shows good agreement with in-situ observations of surface CO (correlation coefficient of 0.6) during winter season, it could not reproduce the variations during monsoon season over the BoB.

- Analysis of vertical profiles over the BoB shows the CO mixing ratios are higher in the lower troposphere (below 700 hPa; ~2.5 km) as compared to that in the mid and upper troposphere during most of the seasons, except during monsoon (higher or comparable CO mixing ratios in the upper-troposphere). In addition, lower-tropospheric CO exhibits larger seasonal amplitudes as compared to upper troposphere.

- The vertical extent of CO is higher, upto 600 hPa (~ 4 km) during pre-monsoon season over the northern BoB. This is due to convective updraft over IGP and eastern India uplifts the CO to higher altitude and horizontal winds around 700−600 hPa transport it over to the northern BoB.

- The region under the influence of convection tends to show "C-shaped" profile. In other words, there exists enhancement in the upper-tropospheric CO around 300−200 hPa. The strong convective activity over the Indian region during summer monsoons seasons uplifts the lower tropospheric CO to higher altitude (upto 200−100 hPa) and synoptic winds (westerlies around 9−12 km) transport the CO over to the BoB. The influence of biomass burning and anthropogenic activities prevailing over the Southeast Asian region causes the enhancements in the upper-tropospheric CO over southern and central BoB due to convective uplifting over Indonesian region and associated outflows during post-monsoon and winter seasons.

- Utilising the CO observations as a tool to make inference about its companion species, Black carbon (BC), the BC emission from India is estimated to be in the range of 0.6–1.2 Tg year^{-1}.

Chapter - 4 deals with the winter-time shipborne measurements of surface CO conducted over the northern IO during ICARB-2018 complemented with MOPITT retrieved upper-tropospheric CO. The observed variability were analysed in the light of synoptic winds, airmass back-trajectories, CAMS reanalysis data and fire counts. The in-situ observations of surface O_3 and CO observations available in the literature are also utilised in the analysis. The major findings of this analysis are summarised as followings.

- The surface CO varied from <50 to 365 ppbv (mean=179 ppbv; standard deviation=67 ppbv) over the southeast AS and the equatorial IO during winter season. The study region encountered three different types of airmasses, from central/southern India, eastern IGP and marine region of AS. The higher mixing ratios over southeast AS close to the coastal region showed higher CO mixing ratios as high as 365 ppbv which is due to proximity to the source region.

- The comparison of MOPITT retrieved surface CO with the in-situ observations (including previous studies) shows good agreement with correlation coefficient of 0.76–0.8 indicating the potential of surface retrievals of MOPITT for its utilisation to make broader inferences on the variations of CO.

- The residence time of airmass over the land estimated based on HYSPLIT back trajectories showed positive correlation with CO variability (correlation coefficient of R=0.68) indicating the continental influences. This shows that the larger the airmass resides over the land (where CO sources exist) as compared to oceanic region, the higher the CO mixing ratios in the airmass.

- The comparison of surface CO observations with CAMS reanalysis data shows good agreement with correlation coefficient of 0.77. The analysis of CO from CAMS in conjunction with airmass back-trajectories and emission inventory shows that how CO mixing ratios gets reduced along the transport pathways due to dilution by mixing with oceanic airmass and removal by OH from its prominent source regions.

- The mean surface CO level during ICARB-2018 over the IO was lower by ~30 ppbv as compared to its level during INDOEX-1999, which was conducted 19 years before. This indicates the possibility of decreasing trend in surface CO (with probable rate of 0.7% year^{-1}).

- The MOPITT retrieved upper-tropospheric CO (at 300 hPa; ~9–12 km) shows enhancement which is in line with that observed during INDOEX-1999 in the in-situ measured profile of CO. Relatively higher CO mixing ratios (100–120 ppbv) was observed over southeast AS and the equatorial IO in the upper-troposphere during January 2018. This is attributed to long-range transport from the lower-troposphere of Southeast Asian region under the prevailing convective updrafts which outflow (easterlies) over the equatorial IO. The biomass burning and other anthropogenic emissions over Southeast Asia contribute to this.

- Upper-tropospheric CO showed an abnormal enhancement of ~ 40% (130–150 ppbv) over the equatorial IO during February 2018 as compared to the corresponding February values of previous 10 years. This enhancement coincided with unusually observed westerlies over the equatorial IO. The analysis of vertical as well as horizontal winds, along with fire counts reveals that usual "Indonesia-IO" walker circulation cell is disturbed during February 2018 and the combined effect of unusual convection (updrafts) over the equatorial IO and deeper penetration (up to the equator) of sub-tropical jet brought the influence of forest fire burning occurring over the African region. The westerlies over the equatorial IO were not observed during winter over a last decade, except during February 2018 which brought the influence of African forest fires.

Chapter - 5 presents the analysis of tropospheric CO on regional scale using MOPITT retrievals over the Indian landmass with emphasis on lower-tropospheric, upper-tropospheric and columnar CO. This analysis mainly used satellite-based MOPITT profiles, supported by limited in-situ measurements of near-surface CO. The broad seasonal features, role of biomass burning, role of synoptic meteorology, and long-term trends are analysed in detail and a comprehensive picture of the characteristics of tropospheric CO is brought out. The findings of this analysis are summarised as followings.

- The in-situ observations of surface CO being made at Thiruvananthapuram and available observations reported from few other locations in India were analysed to understand the regional characteristics of near-surface CO. This analysis revealed the annual mean surface CO and its seasonal amplitude around 130–180 ppbv over the sites like Thiruvananthapuram, Cape Rama and Nainital (high altitude site), they are as high as 1600–1750 ppbv over the polluted regions like Mumbai and Delhi. Inter comparison of in-situ measure seasonal cycle with that

from MOPITT shows that MOPITT surface retrievals could capture seasonal variations fairly well.

- Seasonal variation of lower-tropospheric CO is characterised by a peak during winter over most of the Indian regions (except for few regions where is seen during pre-monsoon season) and a dip during summer-monsoon months. The winter peak is caused by stagnant meteorological conditions, higher emissions and weak chemical removal. On the other hand, the upper-tropospheric CO shows an opposite behaviour, peaking in summer-monsoon. The seasonal decrease in lower-tropospheric CO is attributed to the reduction in anthropogenic and biomass burning activity, monsoonal circulation and the presence of strong convective activity. The vertical updrafts lifting the CO to higher altitudes cause increase at higher altitudes as observed. The columnar CO exhibits similar variation as that of lower tropospheric CO, however, it peaks during pre-monsoon most of the regions or shows comparable levels as that of winter.

- The columnar CO is found to be closely associated with the biomass burning events. The correlation analysis between satellite retrieved columnar CO and fire counts show stronger correlation coefficient positive (0.4–0.7) over Northeast-India (NE-I), followed by East-India (0.3–0.6) indicate that biomass burning is a dominant controlling factor for the seasonal variation of CO over these regions. The biomass burning events over West-IGP (Haryana/Punjab region) corresponding to the crop residue burning enhances the columnar CO during pre-monsoon (May) as well as post-monsoon (October) over the region. The pre-monsoon peak in columnar CO over East-IGP has become prominent over the recent years (2009-2018).

- The grid-by-grid analysis of trend considering ~18 years of MOPITT data shows the decreasing trend of -1 to -2.5 ppbv year^{-1} (-0.5 to -1.5% year^{-1}) in the lower troposphere over the Indian region. While trend is significant over W-I, W-IGP, E-IGP, surrounding oceans, it is not significant over central-I, S-I and E-I part of India. Extending the analysis over the globe, the decreasing trend observed globally in lower-tropospheric CO is confirmed by in-situ surface CO observations from NOAA-network. The columnar CO also exhibits a decreasing trend of -0.5 to -2 molecules cm^{-2} year^{-1} (-0.1 to -1 % year^{-1}). Using the multiple satellites, it is confirmed that decreasing trend in columnar CO is realistic. The upper-tropospheric CO shows increasing trend over India as well as over the globe,

however, retrievals from multiple satellites are not consistent and hence full confidence could not be attributed to the increasing trend in upper-tropospheric CO, which needs further study. However, evidences of increase in the convective activity indicate the possibility of increasing trend in the upper-tropospheric CO.

- Though increase in anthropogenic activity over India (as well as over the globe) is evident, a decreasing trend is seen in the lower-tropospheric and columnar CO. The observed increase in water vapour, O_3 or NO could increase the OH levels leading to strengthening of sink mechanism of CO. This could be one of the reasons for the decreasing trend in CO, in addition to possible reduction in emissions due to implementation of vehicular pollution norms by the government. If the increasing trend in upper-tropospheric CO is realistic, the convective uplifting of the lower-tropospheric CO to the higher altitude could be a possible reason for increasing trend in upper-tropospheric CO which also partially explains the decreasing trend in lower-tropospheric CO.

- The decreasing trend in CO appears to be indicator of improvement in air quality, however, it points to the possible increase in O_3 and/or NO which are also air pollutants. One of the possible implications of decreasing trend in CO would be reduction in lifetime of methane.

Chapter - 6 shows the result of simulations carried out using models, a photochemical box model (NCAR-MM) and the regional chemistry transport model WRF-Chem. Inter-comparisons between the model simulated surface CO and in-situ observations were carried out to evaluate the model simulations. While role of chemistry in the variation of CO is explored using box-model simulations, the anthropogenic contributions to the surface CO over the oceanic regions was estimated by WRF-Chem. The results of the model simulations are summarised as followings.

- The Box model simulations showed that increase in the water vapour causes the decrease in CO through its reaction with OH, the source of which is water vapour in the presence of sunlight and O_3 or NO_2. Under the different scenarios of combinations of trace gas concentrations; box model showed that when RH is increased to 90% (under constant temperature), 2–6% reduction in CO occurs over a day. It also showed that amount of CO reduction due to water vapour depends on the concentration levels of gases like NO_2, CH_4, etc.

- Box-model simulations utilising the observations of hydrocarbons over polluted and cleaner oceanic regions revealed that net effect of prevailing concentration level of hydrocarbons contributes ~8-9% of increase in CO which is due to

oxidation of hydrocarbons producing CO as well as due to reducing the availability of OH for destruction of CO.

- Based on observed decadal increase in water vapour, CH_4 and O_3 (or NO_2), box model simulations shows that chemistry (or CO +OH reaction) could account for the observed decreasing trend in CO only partially.

- The WRF-Chem simulated surface CO reproduced the broad features of spatial and temporal variations of near-surface CO measured over the oceanic regions of BoB (during monsoon) and northern IO (during winter) reasonably well, but with slight overestimation of 18–25 ppbv in the absolute CO levels. The contributions of anthropogenic emissions to the surface CO over the oceanic regions were estimated by switching off the anthropogenic emissions within model domain. The anthropogenic emissions over the Indian region contributes 20 to 60% to the surface CO over the BoB during monsoons seasons and remaining percentage is due to influx at boundaries of model domain (i.e., Indian region) and biomass burning within the study region. Similarly, 60% of CO over southeast AS is attributed to the anthropogenic emissions over model domain during winter; it is ~5-15% over the far oceanic region, the equatorial IO. The simulations also show that in absence of anthropogenic emissions variability in surface CO is significantly lower, apart from reduced CO level.

7.2 Future Scope

The present work has brought out several new results on three dimensional (latitude-longitude-altitude) distributions of tropospheric CO over Indian and surrounding marine environments, the BoB and the northern IO. This study has brought out the need of more in-situ observations on trace gases and opened up new topics for future research in the area of CO and other trace gases. The future directions in which the research activities can be taken up in the context of present work are given below.

There exist in-situ measurements for the surface CO, however, in-situ measurements of vertical profiles of CO (and other trace gases) are highly limited over the Indian region. Regular in-situ measurements on the vertical distribution of CO are essential to study the chemistry of upper-troposphere and dynamics. This is very important in the context of increasing aviation activities and the consequent increase in the emissions from aircraft. Of course, satellite measurements would complement the in-situ observations, but the in-situ observations become essential during the cloudy

conditions (where satellite fails to provide retrievals accurately). Moreover the in-situ measurements will provide CO profile with better altitude resolution and these profiles can be used to validate the satellite retrievals. Over many locations in India, monitoring of surface CO is going on; however, the isotopic measurements of CO are extremely limited. Measurements of isotopes of CO are essential to delineate the contributions of biomass burning and as discussed in the study, biomass burning significantly contributes to CO (and other trace constituents). The importance of CO measurement lies in its usefulness in validating model performance as well as quantifying the regional budget of CO. While megacities like Delhi experiences widespread pollution episodes which is frequently attributed to biomass (crop residue) burning, however, quantification of biomass burning contribution is lacking and the isotopic measurements of CO would be helpful for the same.

The tropospheric chemistry of CO, VOCs, and other trace gases involving OH is non-linear and measurements of hydrocarbons/VOCs are sparse over the Indian region. To understand the role of VOCs in the tropospheric chemistry, in-situ measurements complemented with satellite observation and regional scale modelling are essential over the Indian region.

Air quality related studies are limited and forecast of pollution levels over megacities is the need of hour. Assimilation of in-situ and remote sensing data along with air quality modelling is a thrust area in the present day of growing anthropogenic activity.

Deep convection during the monsoon season often penetrates the tropopause over the tropical region leading to the transport of CO and other trace gases to the stratosphere. The study addressing the changes in stratospheric chemistry and composition is another topic of research which needs to be taken up. The study of long-trend in the upper-troposphere and stratosphere would be of great interest in the context of climate change.

There exist several satellites in the orbit measuring the CO and other trace gases; however, India lacks such environmental satellite. The design and development of a payload and retrieval algorithm taking the legacy of existing satellites and their algorithms would be a challenging task to be taken up. The present study provides the necessary background information on CO for the design of the satellite payload.

***

References

Ackermann I. J., Hass H., Memmesheimer M., Ebel A., Binkowski F.S., Shankar U., 1998. Modal aerosol dynamics model for Europe: development and first applications, Atmos. Environ., 32, 2981–2999.

Ahammed Y.N., Reddy R.R., Gopal K.R., Narasimhulu K., Basha D.B., Reddy L.S.S., Rao T.V.R., 2006. Seasonal variation of the surface ozone and its precursor gases during 2001–2003, measured at Anantapur (14.62°N), a semi-arid site in India. Atmos. Res. 80(2–3), 151–164. doi: 10.1016/j.atmosres.2005.07.002.

Akimoto H., Mori Y., Sasaki K., Nakanishi H., Ohizumi T., Itano Y., 2015. Analysis of monitoring data of ground-level ozone in Japan for longterm trend during 1990–2010: causes of temporal and spatial variation, Atmos Environ 102:302–310, doi:10.1016/j.atmosenv.2014.12.001.

Andreae M.O. and Merlet P., 2001. Emission of trace gases and aerosols from biomass burning, Global Biogeochemical Cycles, 15, 4, 955–966.

Andreae M.O., 1983. Soot carbon and excess fine potassium: Long-range transport of combustion-derived aerosols, Science, 220, 1148 – 1151.

Aneesh V.R., Mohankumar G., Sampath S., 2008. Spatial distribution of atmospheric carbon monoxide over Bay of Bengal and Arabian Sea: Measurements during pre-monsoon period of 2006, J. Earth Syst. Sci., 117, 449–455.

Arnott W.P., Hamasha K., Moosmuller H., Sheridan P.J., Ogren J.A., 2005. Towards aerosol light-absorption measurements with a 7-wavelength aethalometer: evaluation with a photoacoustic instrument and 3-wavelength nephelometer, Aerosol. Sci. Technol. 39, 17-29, doi: 10.1080/027868290901972.

Aryasree S., Nair P.R., Girach I.A., Jacob S., 2015. Winter time chemical characteristics of aerosols over the Bay of Bengal: continental influence, Environmental Science and Pollution Research, 19, 14901-14918, doi: 10.1007/s11356-015-4700-7.

Asnani G.C., 2005. Tropical Meteorology, second edition, vol. 2, Pune, India.

Aumann H.H., Behrangi A., Wang Y., 2018. Increased frequency of extreme tropical deep convection: AIRS observations and climate model predictions. Geophysical Research Letters, 45, 13530–13537, doi: 10.1029/2018GL079423.

Aumann H.H., Chahine M.T., Gautier C., Goldberg M.D., Kalnay E., McMillin L.M., Revercomb H., Rosenkranz P.W., Smith W.L., Staelin D.H., Strow L. L., Susskind J., 2003. AIRS/AMSU/HSB on the Aqua mission: design, science objectives, data products, and processing systems," in IEEE Transactions on Geoscience and Remote Sensing, vol. 41, no. 2, pp. 253-264, doi: 10.1109/TGRS.2002.808356.

Babu S.S., Moorthy K.K., Satheesh S.K., 2004. Aerosol black carbon over Arabian Sea during inter monsoon and summer monsoon seasons, Geophys. Res. Lett. 31, L06104, doi: 10.1029/2003GL018716.

Badarinath K.V.S., Kharol S.K., Chand T.R.K., Parvathi Y.G., Anasuya T., Jyothsna A.N., 2007. Variations in black carbon aerosol, carbon monoxide and ozone over an urban area of Hyderabad, India, during the forest fire season, Atmos. Res., 85(1), 18–26.

Bartholomew G.W. and Alexander M., 1981. Soil as a sink for atmospheric carbon monoxide. Science, 212: 1389-1391.

Beer R., 2006. TES on the Aura mission: Scientific objectives, measurements, and analysis overview, IEEE Trans. Geosci. Remote Sens.,44,1102–1105, doi:10.1109/TGRS.2005.863716.

Beer R., Glavich T.A., Rider D.M., 2001. Tropospheric Emission Spectrometer for the Earth Observing System's Aura satellite," Appl. Opt., vol. 40, pp. 2356–2367.

Beig G., Gunthe S. Jadhav D.B., 2007. Simultaneous measurements of ozone and its precursors on a diurnal scale at a semi urban site in India, Journal of Atmospheric Chemistry, 57(3), 239-253, doi: 10.1007/s10874-007-9068-8.

Bergamaschi P., Hein R., Heimann M., Crutzen P. J., 2000. Inverse modeling of the global CO cycle 1. Inversion of CO mixing ratios, J. Geophys. Res., 105, 1909-1927.

Bhattacharya S.K., Borole D.V., Francey R.J., Allison C.E., Steele L.P., Krummel P., Langenfelds R., Masarie K.A., Tiwari Y.K. Patra P.K., 2009. Trace gases and CO2 isotope records from Cabo de Rama, India, current science, vol. 97, 9.

Bhattacharya S.K., Jani R.A., Borole D.V., Francey R.J., Allison C.E., and Masarie K.A., 2002. Monsoon signatures in trace gas records from Cape Rama, India, IAEA-TECDOC--1269, International Atomic Energy Agency (IAEA).

Bhuyan P.K., Bharali C., Pathak B., Kalita G., 2014. The role of precursor gases and meteorology on temporal evolution of O3 at a tropical location in northeast India, Environ Sci Pollut Res, doi: 10.1007/s11356-014-2587-3.

Binkowski F. S. and Shankar U., 1995. The regional particulate matter model: 1. Model description and preliminary results, J. Geophys. Res., 100, 26191–26209, doi:10.1029/95JD02093.

Boersma K.F., Eskes H.J., Brinksma E. J., 2004. Error analysis for tropospheric NO2 retrieval from space, J. Geophys. Res., 109, D04311, doi:10.1029/2003JD003962.

Bolin B. and Rodhe H., 1973. A note on the concepts of age distribution and transit time in natural reservoirs, Tellus, 25, 58-62.

Bovensmann H., Burrows J.P., Buchwitz M., Frerick J., Noël S., Rozanov V.V., Chance K.V., and Goede A.P.H., 1999. SCIAMACHY: Mission Objectives and Measurement Modes, Journal of the Atmospheric Sciences, 56, 2, 127–150, doi: 10.1175/1520-0469(1999)056<0127:SMOAMM>2.0.CO;2.

Brasseur G.P. and Jacob D.J., 2017. Modeling of atmospheric chemistry, Cambridge University Press, doi: 10.1017/9781316544754.

Brenninkmeijer C. A.M., Crutzen P., Boumard F., Dauer T., Dix B., Ebinghaus R., Filippi D., Fischer H., Franke H., Frieß U., Heintzenberg J., Helleis F., Hermann M., Kock H.H., Koeppel C., Lelieveld J., Leuenberger M., Martinsson B.G., Miemczyk S., Moret H.P., Nguyen H.N., Nyfeler P., Oram D., O'Sullivan D., Penkett S., Platt U., Pupek M., Ramonet M., Randa B., Reichelt M., Rhee T.S., Rohwer J., Rosenfeld K., Scharffe D., Schlager H., Schumann U., Slemr F., Sprung D., Stock P., Thaler R., Valentino F., van Velthoven P., Waibel A., Wandel A., Waschitschek K., Wiedensohler A., Xueref-Remy I., Zahn A., Zech U., Ziereis H., 2007. Civil Aircraft for the regular investigation of the atmosphere based on an instrumented container: The new CARIBIC system, Atmos. Chem. Phys., 7, 4953–4976, doi: 10.5194/acp-7-4953-2007.

Buchwitz M., de Beek R., Bramstedt K., Nöel S., Bovensmann H., Burrows J. P., 2004. Global carbon monoxide as retrieved from SCIAMACHY by WFM-DOAS, Atmos. Chem. Phys., 4, 1945–1960 , http://www.atmos-chem-phys.net/4/1945/2004/.

Burkert J., Andre´s-Herna´ndez M.D., Reichert L., Meyer-Arnek J., Doddridge B., Dickerson R.R., Muhle J., Zahn A., Carsey T., Burrows J.P., 2003. Trace gas and radical diurnal behavior in the marine boundary layer during INDOEX 1999, J. Geophys. Res., 108, D8, 8000, doi:10.1029/2002JD002790.

Caldwell D., Hackett J., Gibson A.S., Drummond J.R., Florian N., 2005. Proceedings of the 11th European Space Mechanisms and Tribology Symposium, ESMATS 2005, 21-23 September 2005, Lucerne, Switzerland. Edited by B. Warmbein. ESA SP-591, Noordwijk, Netherlands: ESA Publications Division, ISBN 92-9092-902-2, 2005, p. 99 – 106.

Chand D., Modh K.S., Naja M., Venkataramani S., Lal S., 2001. Latitudinal trends in O3, CO, CH4, and SF6 over the Indian Ocean during the INDOEX IFP-1999 ship cruise, Current Science, 80, 100–104.

Chandra N., Lal S., Venkataramani S., Patra P. K., and Sheel V., 2016. Temporal variations of atmospheric CO2 and CO at Ahmedabad in western India, Atmos. Chem. Phys., 16, 6153–6173, doi:10.5194/acp-16-6153-2016.

Chelani A.B., 2012. Persistence analysis of extreme CO, NO2 and O3 concentrations in ambient air of Delhi, Atmos. Res., 108, 128–134, doi:10.1016/j.atmosres.2012.02.001.

Chen F. and Dudhia J., 2001Coupling and advanced land surfacehydrology model with the Penn State-NCAR MM5 modeling system, Part I: Model implementation and sensitivity, Mon. Weather Rev., 129, 569–585.

Chou M.-D. and Suarez M.J., 1994, An effcient thermal infrared radiation parametrization for use in general circulation models, NASA Tech. Memo., 104606, 85 pp.

Clerbaux C., Boynard A., Clarisse L., George M., Hadji-Lazaro J., Herbin H., Hurtmans D., Pommier M., Razavi A., Turquety S., Wespes C., Coheur P.-F., 2009. Monitoring of atmospheric composition using the thermal infrared IASI/MetOp sounder, Atmos. Chem. Phys., 9, 6041–6054, doi:10.5194/acp-9-6041-2009.

Clerbaux C., Coheur P.-F., Hurtmans D., Barret B., Carleer M., Colin R., Semeniuk K., McConnell J. C., Boone C., Bernath P., 2005. Carbon monoxide distribution from the ACE-FTS solar occultation measurements, Geophys. Res. Lett., 32, L16S01, doi:10.1029/2005GL022394.

Coakley J.A.Jr. and Yang P., 2014. Atmospheric Radiation - A Primer with Illustrative Solutions, Wiley-VCH, Germany.

Cooper O.R., Parrish D., Ziemke J., Balashov N.V., Cupeiro M., Galbally I.E., Naik V., 2014. Global distribution and trends of tropospheric ozone: an observation-based review, Elementa Science of the Anthropocene, 2(1):000029.

Cristofanelli P., Fierli F., Marinoni A., Duchi R., Burkhart J., Stohl A., Maione M., Arduini J., Bonasoni P., 2012. Influence of biomass burning and anthropogenic emissions on ozone, carbon monoxide and black carbon concentrations at the Mt. Cimone GAW-WMO global station (Italy, 2165 ma.s.l.), Atmos. Chem. Phys. Discuss. 12, 21399-21435, doi: 10.5194/acpd-12-21399-2012.

Cros B., Delmas R., Nganga D., Clairac B., Fontan J., 1988. Seasonal trends of ozone in equatorial Africa: Experimental evidence of photochemical formation, J. Geophys. Res., 93(D7), 8355– 8366, doi:10.1029/JD093iD07p08355.

Cruickshank W., 1801.Some observations on different hydrocarbonates and combinations of carbone with oxygen, etc. in reply to some of Dr. Priestley's late objections to the new system of chemistry, Journal of Natural Philosophy, Chemistry and the Arts [a.k.a. Nicholson's Journal], 1st series, 5:1–9.

Crutzen P.J., and Zimmermann P.H., 1991. The changing photochemistry of the troposphere, Tellus,43AB, 136-151.

Dalvi M., Beig G., Patil U., Kaginalkar A., Sharma C., Mitra A.P., 2006. A GIS based methodology for gridding of large scale emission inventories: application to carbon-monoxide emissions over Indian region, Atmos. Environ. 40, 2995-3007, doi: 10.1016/j.atmosenv.2006.01.013.

Daniel J.S. and Solomon S., 1998. On the climate forcing of carbon monoxide. J. Geophys. Res., 103 (D11), 13249-13260.

David L.M. and Nair P.R. 2011. Diurnal and seasonal variability of surface ozone and NOx at a tropical coastal site: Association with mesoscale and synoptic meteorological conditions, J. Geophys. Res., 116, D10303, doi: 10.1029/2010JD015076.

David L.M. and Nair P.R., 2013. Tropospheric column O3 and NO2 over the Indian region observed by Ozone Monitoring Instrument (OMI): Seasonal changes and long-term trends, Atmospheric Environment, 65, 25-39. doi: 10.1016/j.atmosenv.2012.09.033.

de Gouw J.A., Warneke C., Scheeren H.A., van der Veen C., Bolder M., Scheele M.P., Williams J., Wong S., Lange L., Fischer H., Lelieveld J., 2001. Overview of the trace gas measurements on board the Citation aircraft during the intensive field phase of INDOEX, J. Geophys. Res.,106, D22, 28453-28467.

de Laat A.T.J., Lelieveld J., Roelofs G.J., Dickerson R.R., Lobert J.M., 2001. Source analysis of carbon monoxide pollution during INDOEX 1999, 106, 22, 28481-28495.

De Smedt I., Stavrakou T., Müller J.F., van der A R.J., Van Roozendael M., 2010. Trend detection in satellite observations of formaldehyde tropospheric columns, Geophys. Res. Lett., 37, L18808.

De Wachter E., Barret B., Le Flochmoën E., Pavelin E., Matricardi M., Clerbaux C., Hadji-Lazaro J., George M., Hurtmans D., Coheur P.-F., Nedelec P., Cammas J. P., 2012. Retrieval of MetOp-A/IASI CO profiles and validation with MOZAIC data, Atmos. Meas. Tech., 5, 2843-2857, doi: 10.5194/amt-5-2843-2012.

de Zafra R. L., and Muscari G., 2004. CO as an important high-altitude tracer of dynamics in the polar stratosphere and mesosphere, J. Geophys. Res., 109, D06105, doi: 10.1029/2003JD004099.

Dee D P., Uppala S. M., Simmons A.J., Berrisford P., Poli P. , Kobayashi S. , Andrae U., Balmaseda M. A., Balsamo G. , Bauer P., Bechtold P., Beljaars A.C., van de Berg L., Bidlot J., Bormann N. Delsol C., Dragani R., Fuentes M., Geer A.J., Haimberger L., Healy S.B., Hersbach H., Hólm E.V., Isaksen L., Kållberg P., Köhler M., Matricardi M., McNally A.P., Monge-Sanz B.M., Morcrette J., Park B., Peubey C., de Rosnay P., Tavolato C., Thépaut J., Vitart F., 2011. The ERA-Interim reanalysis: configuration and performance of the data assimilation system. Q.J.R. Meteorol. Soc., 137: 553-597. doi:10.1002/qj.828.

Deeter M.N., Edwards D.P., Francis G.L., Gille J.C., Martinez-Alonso S., Worden H.M., Sweeney C., 2017, A Climate-scale Satellite Record for Carbon Monoxide: The MOPITT Version 7 Product, Atmos. Meas. Tech. Discuss., 1–34, doi:10.5194/amt-2017-71.

Deeter M.N., Edwards D.P., Gille J.C., Drummond J.R., 2007. Sensitivity of MOPITT observations to carbon monoxide in the lower troposphere, J. Geophys. Res.112 (D24306), doi:10.1029/2007JD008929.

Deeter M.N., Emmons L.K., Edwards D.P., Gille J.C., Drummond J.R., 2004. Vertical resolution and information content of CO profiles retrieved by MOPITT, Geophys. Res. Lett., 31, L15112, doi:10.1029/2004GL020235.

Deeter M.N., Emmons L.K., Francis G.L., Edwards D.P., Gille J.C., Warner J.X., Khattatov B., Ziskin D., Lamarque J.-F., Ho S.-P., Yudin V., Atti J.-L., Packman D., Chen J., Mao D., Drummond J.R., 2003. Operational carbon monoxide retrieval algorithm and selected results for the MOPITT instrument, J. Geophys. Res., 108(D14), 4399–4410.

Deeter M.N., Martínez-Alonso S., Edwards D.P., Emmons L.K., Gille J.C., Worden H.M., Pittman J.V., Daube B.C., Wofsy S.C., 2013. Validation of MOPITT Version 5 thermal-infrared, near-infrared, and multispectral carbon monoxide profile retrievals for 2000–2011, J. Geophys. Res. Atmos., 118, doi:10.1002/jgrd.50272.

Deeter M.N., Martínez-Alonso S., Edwards D.P., Emmons L.K., Gille J.C., Worden H.M., Sweeney C., Pittman J.V., Daube B.C., Wofsy S.C., 2014. The MOPITT Version 6 product: algorithm enhancements and validation. Atmos. Meas. Tech., 7, 3623-3632, doi: 10.5194/amt-7-3623-2014.

Deeter M.N., Worden H.M., Edwards D.P., Gille J.C., Andrews A.E., 2012. Evalua- tion of MOPITT retrievals of lower-tropospheric carbon monoxide over the United States, J. Geophys. Res., 117, D13306, doi: 10.1029/2012JD017553.

Dessler A.E., 2000, The Chemistry and Physics of Stratospheric Ozone, Academic Press, UK.

Dickerson R., University of Maryland. 2007. Ron Brown Chemistry Carbon Monoxide. Version 1.0. UCAR/NCAR - Earth Observing Laboratory. https://data.eol.ucar.edu/dataset/22.022.

Dickerson R.R., Andreae M.O., Campos T., Mayol-Bracero O.L., Neusuess C., Streets D.G., 2002. Analysis of black carbon and carbon monoxide observed over the Indian Ocean: implications for emissions and photochemistry, J. Geophys. Res., 107 (D19), 8017 doi: 10.1029/2001JD000501.

Dlugokencky E.J., Dutton E.G., Novelli P.C., Tans P.P., Masarie K.A., Lantz K.O., Mardronich S., 1996. Changes in CH4 and CO growth rates after the eruption of Mt. Pinatubo and their link with changes in tropical tropospheric UV flux, Geophys. Res. Lett., 23, 2761–2764.

Draxler R.R., Taylor A.D., 1982. Horizontal dispersion parameters for long-range transport modeling, Jnl. appl. Met., 21, 367-372.

Drummond J.R. and Mand G.S., 1996, The Measurements of Pollution in the Troposphere (MOPITT) Instrument: Overall Performance and Calibration Requirements, Journal of Atmospheric and Oceanic Technology, 13(2), 314–320, doi:10.1175/1520-0426(1996)013<0314:TMOPIT>2.0.CO;2.

Drummond J.R., 1989. Novel correlation radiometer: the length modulated radiometer. Appl. Opt. 28, 2451,.

Drummond J.R., 1992, Measurements of Pollution in the Troposphere (MOPITT), in The use of EOS for Studies of Atmospheric Physics, edited by J. C. Gille and G. Visconti, North Holland, Amsterdam.

Drummond J.R., Zou J., Nichitiu F., Kar J., Deschambaut R., Hackett J., 2010. A review of 9-year performance and operation of the MOPITT instrument, Advances in Space Research, 45(6), 760–774, doi:10.1016/j.asr.2009.11.019.

Duncan B.N., Logan J.A., Bey I., Megretskaia I.A., Yantosca R.M., Novelli P.C., Jones N.B., and Rinsland C.P., 2007. Global budget of CO, 1988–1997: Source estimates and validation with a global model, J. Geophys. Res, VOL. 112, D22301, doi:10.1029/2007JD008459.

Edwards D.P., Halvorson C., Gille J. C., 1999. Radiative transfer modeling for the EOS Terra Satellite Measurement of Pollution in the Troposphere (MOPITT) instrument, J. Geophys. Res., 104, 16,755– 16,775.

Emmons L.K. et al., 2010. Description and evaluation of the Model for Ozone and Related chemical Tracers, version 4 (MOZART-4), Geosci. Model Dev., 3(1), 43–67, doi:10.5194/gmd-3-43-2010.

Emmons L.K., Deeter M.N., Gille J.C., Edwards D.P., Attie J.-L., Warner J., Ziskin D., Francis G., Khattatov B., Yudin V., Lamarque J.-F., Ho S.-P., Mao D., Chen J. S., Drummond J., Novelli P., Sachse G., Coffey M.T., Hannigan J.W., Gerbig C., Kawakami S., Kondo Y., Takegawa N., Schlager H., Baehr J., Ziereis H., 2004. Validation of Measurements of Pollution in the Troposphere (MOPITT) CO retrievals with aircraft in situ profiles, J. Geophys.Res., 109(D03), D03.1–D03.13.

Evans W.F.J. and Puckrin E., 1995. An observation of the greenhouse radiation associated with carbon monoxide, Geophys. Res. Lett., 22, 925-928.

Fadnavis S., Buchunde P., Ghude S.D., Kulkarni S.H., Beig G., 2011. Evidence of seasonal enhancement of CO in the upper troposphere over India, Int. J. Remote Sens. 32 (22), 7441-7452, doi: 10.1080/01431161.2010.523733.

Field R.D., van der Werf G.R., Fanin T., Fetzer E.J., Fuller R., Jethva H., Levy R., Livesey N.J., Luo M., Torres O., Worden H.M., 2016. Indonesian fire activity and smoke pollution in 2015 show persistent nonlinear sensitivity to El Niño-induced drought, PNAS, 9204–9209, 113, 33, doi: 10.1073/pnas.1524888113.

Finlayson-Pitts B.J. and Pitts Jr. J.N., 2000. Chemistry of the Upper and Lower Atmosphere: Theory, Experiments, and Applications. Academic, London.

Fishman J., and Seiler, W. (1983), Correlative nature of ozone and carbon monoxide in the troposphere: Implications for the tropospheric ozone budget, J. Geophys. Res., 88(C6), 3662– 3670, doi:10.1029/JC088iC06p03662.

Forkman P., Eriksson P., Murtagh D., and Espy P., 2005. Observing the vertical branch of the mesospheric circulation at latitude 60°N using ground-based measurements of CO and H2O, J. Geophys. Res., 110, D05107, doi: 10.1029/2004JD004916.

Francey R.J., Steele L.P., Langenfelds R.L., Lucarelli M.P., Allison C.E., Beardsmore D.J., Coram S.A., Derek N., de Silva F.R., Etheridge D.M., Fraser P.J., Henry R.J., Turner B., Welch E.D., Spencer D.A., Cooper L.N., 1996. Global Atmospheric Sampling Laboratory

(GASLAB): supporting and extending the Cape Grim trace gas programs. Baseline Atmospheric Program (Australia) 1993, edited by R.J. Francey, A.L. Dick and N. Derek, pp 8 - 29, Bureau of Meteorology and CSIRO Division of Atmospheric Research, Melbourne, Australia.

Gaubert B.,Worden H.M., Arellano A.F.J., Emmons L.K., Tilmes S., Barré J., Alonso S.M., Vitt F., Anderson J.L., Alkemade F., Houweling S., Edwards D.P., 2017. Chemical feedback from decreasing carbon monoxide emissions, Geophysical Research Letters, 44. doi: 10.1002/2017GL074987.

Gaudel A., Clark H., Thouret V., Jones L., Inness A., Flemming J., Stein O., Huijnen V., Eskes H., Nédélec P., Boulangerand D., 2015. On the use of MOZAIC-IAGOS data to assess the ability of the MACC reanalysis to reproduce the distribution of O3 and CO in the UTLS over Europe, Tellus B, 67, 27955, doi:10.3402/tellusb.v67.27955,.

Gaur A., Tripathi N., Kanawade V.P., Tare V., Shukla S.P., 2014. Four-year measurements of trace gases(SO2, NOx, CO, and O3) at an urban location, Kanpur, in Northern India, J AtmosChem, 71:283–301, doi: 10.1007/s10874-014-9295-8.

George M., Clerbaux C., Hurtmans D., Turquety S., Coheur P.-F., Pommier M., Hadji-Lazaro J., Edwards D.P., Worden H., Luo M., Rinsland C., McMillanW., 2009. Carbon monoxide distributions from the IASI/METOP mission: evaluation with other space-borne remote sensors, Atmos. Chem. Phys., 9, 8317–8330, doi:10.5194/acp-9-8317-2009.

Ghude S.D., Beig G., Kulkarni P.S., Kanawade V.P., Fadnavis S., Remedios J.J., Kulkarni S.H., 2011. Regional CO pollution over the Indian subcontinent and various transport pathways as observed by MOPITT, Int. J. Remote Sens. 32 (21), 6133-6148. doi: 10.1080/01431161.2010.507796.

Giglio L., Descloitres J., Justice C.O., Kaufman Y.J., 2003. An enhanced contextual fire detection algorithm for MODIS, Remote Sensing of Environment, 87:273-282.

Girach I.A. and Nair P.R., 2010. Spatial distribution of near-surface CO over Bay of Bengal during winter: role of transport. J. Atmos. Sol. Terr. Phys. 72, 1241-1250 doi: 10.1016/j.jastp.2010.07.02.

Girach I.A. and Nair P.R., 2012. Distribution of Carbon monoxide over Indian region as observed by Measurements of Pollution in the Troposphere (MOPITT)", A1.1-0026-12, 39th Committee on Space Research (COSPAR) - 2012.

Girach I.A. and Nair P.R., 2014.Carbon monoxide over Indian region as observed by MOPITT, Atmos. Environ., 99, 599-609., doi:10.1016/j.atmosenv.2014.10.019).

Girach I.A. and Nair P.R., 2016, Long-term trend in tropospheric carbon monoxide over the globe", Proc. SPIE 9876, Remote Sensing of the Atmosphere, Clouds, and Precipitation VI, 987624, doi: 10.1117/12.2223380

Goldstein M., 2008. Carbon monoxide poisoning, Journal of Emergency Nursing. 34 (6): 538–42. doi:10.1016/j.jen.2007.11.014.

Gordon I.E., Rothman L.S., Hill C., Kochanov R.V., Tan Y., Bernath P.F., Birk M., Boudon V., Campargue A., Chance K.V., Drouin B.J., Flaud J.-M., Gamache R.R., Hodges J.T., Jacquemart D., Perevalov V.I., Perrin A., Shine K.P., Smith M.-A.H., Tennyson J., Toon G.C., Tran H., Tyuterev V.G., Barbe A., Császár A.G., Devi V.M., Furtenbacher T., Harrison J.J., Hartmann J.-M., Jolly A., Johnson T.J., Karman T., Kleiner I., Kyuberis A.A., Loos J., Lyulin O.M., Massie S.T., Mikhailenko S.N., Moazzen-Ahmadi N., Müller H.S.P.,

Naumenko O.V., Nikitin A.V., Polyansky O.L., Rey M., Rotger M., Sharpe S.W., Sung K., Starikova E., Tashkun S.A., VanderAuwera J., Wagner G., Wilzewski J., Wcisło P., Yu S., Zak E.J., 2017. The HITRAN2016 molecular spectroscopic database, Journal of Quantitative Spectroscopy & Radiative Transfer203, 3–69, doi: 10.1016/j.jqsrt.2017.06.038.

Granier C., Bessagnet B., Bond T., D'Angiola A., Denier van der Gon H., Frost G.J., Heil A., Kaiser J.W., Kinne S., Klimont Z., Kloster S., Lamarque J.-F., Liousse C., Masui T., Meleux F., Mieville A., Ohara T., Raut J.-C., Riahi K., Schultz M.G., Smith S.J., Thompson A., van Aardenne J., van der Werf G.R., van Vuuren D.P., 2011. Evolution of anthropogenic and biomass burning emissions of air pollutants at global and regional scales during the 1980-2010 period. Clim. Change 109 (1-2), 163-190. doi: 10.1007/s10584-011-0154-1.

Gratz L.E., Jaffe D.A., Hee J.R., 2015. Causes of increasing ozone and decreasing carbon monoxide in springtime at the Mt. Bachelor Observatory from 2004 to 2013, Atmospheric Environment, 109, 323-330, doi: 10.1016/j.atmosenv.2014.05.076.

Grell G. A. and Devenyi D. 2002. A generalized approach to parameterizing convection combining ensemble and data assimilation techniques, Geophys. Res. Lett., 29, 38-1–38-4, doi:10.1029/2002GL015311,.

Grell G., 1993. Prognostic evaluation of assumptions used by cumulus parameterizations, Month. Weather Rev., 121, 764–787, doi:10.1175/1520-0493(1993)121<0764:PEOAUB>2.0.CO;2, 1993.

Grell G.A., Peckham S.E., Schmitz R., McKeen S.A., Frost G., Skamarock W.C., Eder B., 2005. Fully coupled "online" chemistrywithin the WRF model, Atmos. Environ., 39, 6957–6975.

Guenther A., Karl T., Harley P., Wiedinmyer C., Palmer P.I., Geron C., 2006. Estimates of global terrestrial isoprene emissions using MEGAN (Model of Emissions of Gases and Aerosols from Nature), Atmos. Chem. Phys., 6, 3181-3210, doi:10.5194/acp-6-3181-2006.

Gunson M.R., Abbas M., Abrams M.C., Allen M., Brown J.R., Brown T.L., et al., 1996. The Atmospheric Trace Molecule Spectroscopy (ATMOS) experiment: deployment on the ATLAS Space Shuttle missions. Geophys. Res. Lett. 23, 2333–2336, doi:10.1029/96GL01569.

Gurjar B.R., Ravindra K., Nagpure A.S., 2016. Air pollution trends over Indian megacities and their local-to-global implications, Atmospheric Environment, 142, 475–495, doi: 10.1016/j.atmosenv.2016.06.030.

Haan D. and Raynaud D., 1998. Ice core record of CO variations during the last two millennia: atmospheric implications and chemical interactions within the Greenland ice, Tellus, 50B, 253–262.

Hakim Z.Q., Archer-Nicholls S., Beig G., Folberth G.A., Sudo K., Abraham N.L., Ghude S., Henze D., Archibald A.T., 2018. Evaluation of tropospheric ozone and ozone precursors in simulations from the HTAPII and CCMI model intercomparisons – a focus on the Indian Subcontinent, Atmos. Chem. Phys. Discuss., doi: 10.5194/acp-2018-1235.

Hansen A.D.A., 1996. Magee Scientific Aethalometer User's Guide. Magee Sci., Berkely, Calif., p. 56.

Hauglustaine D.A., Brasseur G.P., Walters S., Rasch P.J., Müller J.-F., Emmons L.K., Carroll, M.A., 1998. MOZART, a global chemical transport model for ozone and related chemical tracers: 2. Model results and evaluation, J. Geophys. Res. 103, 28291-28335.

Hays P.B. and Olivero J. J., 1970. Carbon dioxide and monoxide above the troposphere, Planet. Space Sci., 18, 1729–1733.

Hollingsworth A., Engelen R. J., Textor C., Benedetti A., Boucher O., Chevallier F., Dethof, A., Elbern H., Eskes H., Flemming J., Granier C., Kaiser J.W., Morcrette J.-J., Rayner P., Peuch V.H., Rouil L., Schultz M.G.: Simmons A.J. and The GEMS Consortium: Toward a Monitoring and Forecasting System For Atmospheric Composition: The GEMS Project, B. Am. Meteorol. Soc., 89, 1147–1164, 2008.

Huijnen V., Wooster M.J., Kaiser J.W., Gaveau D.L.A., Flemming J., Parrington M., Inness A., Murdiyarso D., Main B., van Weele M., 2016. Fire carbon emissions over maritime southeast Asia in 2015 largest since 1997, Nature Scientific Reports, 6:26886, doi:10.1038/srep26886.

Hurtmans D., Coheur P.-F., Wespes C., Clarisse L., Scharf O., Clerbaux C., Hadji-Lazaro J., George M., Turquety S., 2012. FORLI radiative transfer and retrieval code for IASI. J Quant Spectrosc Radiat Transfer, 113, 1391–1408, doi:10.1016/j.jqsrt.2012.02.036,.

Inman R.E., Ingersoll R.B., Levy E.A., 1971. Soil: A Natural Sink for Carbon Monoxide, Science, Vol. 172, Issue 3989, pp. 1229-1231, doi: 10.1126/science.172.3989.1229.

Inness A., Baier F., Benedetti A., Bouarar I., Chabrillat S., Clark H., Clerbaux C., Coheur P., Engelen R.J., Errera Q., Flemming J., George M., Granier C., Hadji-Lazaro J., Huijnen V., Hurtmans D., Jones L., Kaiser J. W., Kapsomenakis J., Lefever K., Leitão J., Razinger M., Richter A., Schultz M.G., Simmons A.J., Suttie M., Stein O., Thépaut J.-N., Thouret V., Vrekoussis M., Zerefos C., the MACC team, 2013. The MACC reanalysis: an 8 yr data set of atmospheric composition, Atmos. Chem. Phys., 13, 4073–4109, doi:10.5194/acp-13-4073-2013.

Inness A., Blechschmidt A.-M., Bouarar I., Chabrillat S., Crepulja M., Engelen R.J., Eskes H., Flemming J., Gaudel A., Hendrick F., Huijnen V., Jones L., Kapsomenakis J., Katragkou E., Keppens A., Langerock B., de Mazière M., Melas D., Parrington M., Peuch V.H., Razinger M., Richter A., Schultz M. G., Suttie M., Thouret V., Vrekoussis M., Wagner A., Zerefos C., 2015. Data assimilation of satellite retrieved ozone, carbon monoxide and nitrogen dioxide with ECMWF's Composition-IFS, Atmos. Chem. Phys., 15, 5275–5303, doi:10.5194/acp-15-5275-2015.

IPCC, 1996. Intergovernmental Panel on Climate Change, Climate Change 1995: The Science of Climate Change, Cambridge Univ. Press, Cambridge, UK,.

IPCC, 2001. Intergovernmental Panel on Climate Change, Climate Change 2001: the scientific basis. Contribution of Working Group 1 to the Third Assessment Report of the Intergovernmental Panel on Climate Change, Cambridge University Press, Cambridge, UK, and New York, USA, 2001.

IPCC, 2013. Intergovernmental Panel on Climate Change,. Climate Change 2013: The Physical Science Basis, Report ofWorking Group I to the Fifth Assessment of the IPCC. Cambridge University Press, Cambridge, United Kingdom and New York, NY, USA.

Jacobson M.Z., 2005. Fundamentals of atmospheric modeling, Cambridge University Press, doi: 10.1017/CBO9781139165389.

Jaffe L.S., 1968. Ambient Carbon Monoxide And Its Fate in the Atmosphere, Journal of the Air Pollution Control Association, 18:8, 534-540, doi: 10.1080/00022470.1968.10469168.

Janjic Z.I., 2002. Nonsingular Implementation of the Mellor-Yamada Level 2.5 Scheme in the NCEP Meso Model, NCEP office Note, 437, 61.

Janssens-Maenhout, Crippa G., Guizzardi M., Dentener D., Muntean F., Pouliot M., Keating G., Zhang T., Kurokawa Q., Wankmuller J., Denier van der Gon R., Klimont H., Frost Z., Darras G. S. and Koffi B., 2015. HTAP_v2: a mosaic of regional and global emission gridmaps for 2008 and 2010 to study hemispheric transport of air pollution, Atmos. Chem. Phys. Discuss., 15, 12867-12909, doi:10.5194/acpd-15-12867-2015,.

Jaswal A.K. and Koppar A.L., 2011. Recent climatology and trends in surface humidity over India for 1969-2007, MAUSAM, 62, 2, 145-162.

Jiang Z., Jones D.B.A., Worden H.M., Deeter M.N., Henze D.K., Worden J., Bowman K.W., Brenninkmeijer C.A.M., and Schuck T. J., 2013. Impact of model errors in convective transport on CO source estimates inferred from MOPITT CO retrievals, J. Geophys. Res. Atmos., 118, 2073–2083, doi:10.1002/jgrd.50216.

Jöckel P., 2012. Book chapter: Chapter-35: Earth system modeling in Book: Atmospheric Physics: Background-Methods-Trends edited by U. Schumann, Springer, pp.577–589, doi: 10.1007/978-3-642-30183-4.

Kanawade V.P., 2010. Doctoral thesis on "The Sensitivity of The Measurement Of Pollution In The Troposphere (MOPITT) Retrievals of Carbon Monoxide to the Lowermost Troposphere", University of Leicester, UK.

Kar J., Bremer H., Drummond J.R., Rochon Y.J., Jones D.B.A., Nichitiu F., Zou J., Liu J., Gille J.C., Edwards D.P., Deeter M.N., Francis G., Ziskin D., Warner J., 2004. Evidence of vertical transport of carbon monoxide from Measurements of Pollution in the Troposphere (MOPITT). Geophys. Res. Lett. 31, L23105, doi: 10.1029/2004GL021128.

Kar J., Deeter M.N., Fishman J., Liu Z., Omar A., Creilson J.K., Trepte C.R., Vaughan M.A., Winker D.M., 2010. Wintertime pollution over the Eastern Indo-Gangetic Plains as observed from MOPITT, CALIPSO and tropospheric ozone residual data. Atmos. Chem. Phys. 10, 12273e12283, doi: 10.5194/acp-10-12273-2010.

Kar J., Jones D.B.A., Drummond J.R., Attie J.L., Liu J., Zou J., Nichitiu F., Seymour M.D., Edwards D.P., Deeter M.N., Gille J.C., Richter A., 2008. Measurement of low-altitude CO over the Indian subcontinent by MOPITT. J. Geophys. Res. 113, D16307. doi:10.1029/2007JD009362.

Kavitha M. and Nair P. R., 2017. SCIAMACHY observed changes in the column mixing ratio of methane over the Indian region and a comparison with global scenario, Atmospheric Environment, doi: 10.1016/j.atmosenv.2017.07.044.

Kerzenmacher T., Dils B., Kumps N., Blumenstock T., Clerbaux C., Coheur P.-F., Demoulin P., Garcıa O., George M., Griffith D.W.T., Hase F., Hadji-Lazaro J., Hurtmans D., Jones N., Mahieu E., Notholt J., Paton-Walsh C., Raffalski U., Ridder T., Schneider M., Servais C.,

De Maziere M., 2012. Validation of IASI FORLI carbon monoxide retrievals using FTIR data from NDACC, Atmos. Meas. Tech., 5, 2751–2761, doi:10.5194/amt-5-2751-2012.

Khalil M.A.K. and Rasmussen R.A., 1990. The global cycle of carbon monoxide: trends and mass balance. Chemosphere, 20: 227-242.

Khalil M.A.K. and Rasmussen R.A., 1994. Global decrease in atmospheric carbon monoxide concentration, Nature (Lond), 370: 639-641.

Khalil M.A.K. and Rasmussen R.A.,1988. Carbon monoxide in the earth's atmosphere: indications of a global increase. Nature (Lond), 332: 242-245.

Kobayashi H., Shimota A., Kondo K., Okumura E., Kameda Y., Shimoda H., Ogawa T., 1999. Development and evaluation of the interferometric monitor for greenhouse gases: a high throughout Fourier transform infrared radiometer for nadir Earth observation. Appl. Opt. 38, 6801–6807.

Kreyszig E., 1968. Advanced Engineering Mathematics. 2nd Ed., J. Wiley and Sons, New York, 898.

Krotkov N.A., Lamsal L.N., Celarier E.A., Swartz W.H., Marchenko S.V., Bucsela E.J., Chan, K.L., Wenig M., Zara M., 2017. The version 3 OMI NO2 standard product, Atmos. Meas. Tech., 10, 3133-3149, doi: 10.5194/amt-10-3133-2017.

Kumar G.M., Jeena V.S., Sampath S., 2006. Features of atmospheric Carbon Monoxide at two different coastal environments, J. Ind. Geophys. Union.,10, 4, 279-284.

Kumar G.M., Sampath S., Jeena V.S., Anjali R., 2008, Carbon Monoxide Pollution Levels at Environmentally Different Sites, J. Ind. Geophys. Union.12, 1, 31-40.

Kumar R., Barth M.C., Pfister G.G., Nair V.S., Ghude S.D., Ojha N., 2015. What controls the seasonal cycle of black carbon aerosols in India?, J. Geophys. Res. Atmos., 120, doi:10.1002/2015JD023298,.

Kumar R., Naja M., Pfister G.G., Barth M.C., Wiedinmyer C., Brasseur G.P., 2012. Simulations over South Asia using theWeather Research and Forecasting model with Chemistry (WRFChem): chemistry evaluation and initial results, Geosci. ModelDev., 5, 619–648, doi:10.5194/gmd-5-619-2012,.

Kumar R., Naja M., Satheesh S. K., Ojha N., Joshi H., Sarangi T., Pant P., Dumka U.C., Hegde, P., and Venkataramani S., 2011. Influences of the springtime northern Indian biomass burning over the central Himalayas, J. Geophys. Res., 116, D19302, doi: 10.1029/2010JD015509.

Kurokawa J., Ohara T., Morikawa T., Hanayama S., Greet J.-M., Fukui T., Kawashima K., Akimoto H., 2013. Emissions of air pollutants and greenhouse gases over Asian regions during 2000-2008: Regional Emission inventory in ASia (REAS) version 2. Atmos. Chem. Phys. 13, 11019-11058, doi:10.5194/acp-13-11019-2013.

Laing A. and Evans J-L., 2011. Introduction to Tropical Meteorology, 2nd Edition, A Comprehensive Online & Print Textbook, The COMET Program.

Lal S., Chand D., Sahu L.K., Venkataramani S., Brasseur G., Schultz M.G., 2006. High levels of ozone and related gases over the Bay of Bengal during winter and early spring of 2001. Atmos. Environ. 40, 1633-1644.

Lal S., Naja M., and Jayaraman A., 1998. Ozone in the marine boundary layer over the tropical Indian Ocean, J. Geophys. Res., 103(D15), 18907–18917, doi: 10.1029/98JD01566.

Lal S., Naja M., Subbaraya B.H., 2000. Seasonal variations in surface ozone and its precursors over an urban site in India, Atmos. Environ., 34, 2713–2724.

Lal S., Sahu L. K., Venkataramani S., 2007. Impact of transport from the surrounding continental regions on the distributions of ozone and related trace gases over the Bay of Bengal during February 2003, J. Geophys. Res., 112, D14302, doi: 10.1029/2006JD008023,.

Lal S., Sahu L.K., Venkataramani S., Mallik C., 2012. Light non-methane hydrocarbons at two sites in the Indo-Gangetic Plain. J. Environ. Monit., 14, 1159. doi: 10.1039/c2em10682e.

Lal S., Sahu L.K., Venkataramani S., Rajesh T.A., Modh K.S., 2008. Distributions of O3, CO and NMHCs over the rural sites in central India, J. Atmos. Chem., 61:73–84, doi: 10.1007/s10874-009-9126-5

Latha K.M. and Badarinath K.V.S., 2004. Correlation between black carbon aerosols, carbon monoxide and tropospheric ozone over a tropical urban site, Atmos. Res., 71, 265–274.

Lau K.-M. and S.Yang, 2015. Tropical Meteorology & Climate, Encyclopedia of Atmospheric Sciences (Second Edition), 177-181, doi:10.1016/B978-0-12-382225-3.00450-3.

Lawrence M.G. and Crutzen P.J., 1999. Influence of NOx emissions from ships on tropospheric photochemistry and climate, Nature, 402, 167–170.

Lawrence M.G. and Lelieveld J., 2010. Atmospheric pollutant outflow from southern Asia: a review, Atmos. Chem. Phys., 10, 11017–11096, doi:10.5194/acp-10-11017-2010,.

Lawrence M.G., 1996. Photochemistry in the Tropical Pacific Troposphere: Studies with a Global 3D Chemistry-Meteorology Model, Ph.D. thesis, Georgia Institute of Technology.

Lawrence M.G., Jockel P., von Kuhlmann R., 2001. What does the global mean OH concentration tell us?, Atmos. Chem. Phys., 1, 37–49, www.atmos-chem-phys.org/acp/1/37/.

Lelieveld J., Bourtsoukidis E., Brühl C., Fischer H., Fuchs H., Harder H., Hofzumahaus A., Holland F., Marno D., Neumaier M., Pozzer A., Schlager H., Williams J., Zahn A., Ziereis H., 2018. The South Asian monsoon—pollution pump and purifier, Science, 10.1126/science.aar2501 (2018).

Lelieveld J., Crutzen P.J., Ramanathan V., Andreae M.O., Brenninkmeijer C.A.M., Campos T., Cass G.R., Dickerson R.R., Fischer H., de Gouw J.A., Hansel A., Jefferson A., Kley D., de Laat A.T.J., Lal S., Lawrence M.G., Lobert J.M., Mayol-Bracero O.L., Mitra A.P., Novakov T., Oltmans S.J., Prather K.A., Reiner T., Rodhe H., Scheeren H.A., Sikka D., Williams J., 2001. The Indian Ocean Experiment: Widespread Air Pollution from South and Southeast Asia, Science, 291.

Lelieveld J., Gromov S., Pozzer A., Taraborrelli D., 2016. Global tropospheric hydroxyl distribution, budget and reactivity, Atmos. Chem. Phys., 16, 12477–12493, doi:10.5194/acp-16-12477-2016.

Li Qian, Hua-Feng S., Ai-Mei S., Jian-Chun B. & Da-Ren L., 2014. Distribution and Variation of Carbon Monoxide in the Tropical Troposphere and Lower Stratosphere, Atmospheric and Oceanic Science Letters, 7:3, 218-223, doi: 10.3878/j.issn.1674-2834.13.0111.

Lin Y.-L., Farley R.D., Orville H. D. 1983, Bulk Parameterization of the Snow Field in a Cloud Model, J. Clim. Appl. Meteorol., 22, 1065–1092.

Liu X., Murcray F.J., Murcray D.G., and Russell J.M., 1996. Comparison of HF and HC1 vertical profiles from ground-based high resolution infrared solar spectra with Halogen Occultation Experiment observations, J. Geophys. Res.,101, 10,175-10,181.

Livesey N.J., Filipiak M.J., Froidevaux L., Read W.G., Lambert A., Santee M.L., Jiang J.H., Pumphrey H.C., Waters J.W., Cofield R.E., Cuddy D.T., Daffer W.H., Drouin B.J., Fuller R.A., Jarnot R.F., Jiang Y.B., Knosp B.W., Li Q.B., Perun V.S., Schwartz M.J., Snyder W.V., Stek P.C., Thurstans R.P., Wagner P.A., Avery M., Browell E.V., Cammas J.-P., Christensen L.E., Diskin G.S., Gao R.-S., Jost H.-J., Loewenstein M., Lopez J.D., Nedelec P., Osterman G.B., Sachse G.W., Webster C.R., 2008. Validation of Aura Microwave Limb Sounder O3 and CO observations in the upper troposphere and lower stratosphere, J. Geophys. Res., 113, D15S02, doi: 10.1029/2007JD008805.

Livesey N.J., Snyder W.V., Read W.G., Wagner P.A., 2006. Retrieval algorithms for the EOS Microwave Limb Sounder (MLS) instrument, IEEE Trans. Geosci. Remote Sens., 44(5), 1144– 1155.

Lobert J. and Harris J.M., 2002. Trace gases and air mass origin at Kaashidhoo, Indian Ocean, J. Geophys. Res., 107, NO. D19, 8013, doi:10.1029/2001JD000731.

Logan J.A., Prather M.J., Wofsy S.C., McElroy M.B., 1981. Tropospheric chemistry: a global perspective. J Geophys Res Oceans Atmos, C86: 7210-7254.

Logan J.A., Staehelin J, Megretskaia I.A., Cammas J.P., Thouret V., Claude H., Fröhlich M., 2012. Changes in ozone over Europe: analysis of ozone measurements from Sondes, regular aircraft (MOZAIC) and alpine surface sites. J. Geophys. Res. Atmos., 117(D9).

Lopez J.P., Luo M., Christensen L.E., Loewenstein M., Jost H., Webster C.R., Osterman G., 2008. TES carbon monoxide validation during two AVE campaigns using the Argus and ALIAS instruments on NASA's WB-57F, J. Geophys. Res., 113, D16S47, doi:10.1029/2007JD008811.

Luo M., Rinsland C.P., Rodgers C.D., Logan J.A., Worden H., Kulawik S., Eldering A., Goldman A., Shephard M.W., Gunson M., Lampel M., 2007a. Comparison of carbon monoxide measurements by TES and MOPITT: the influence of a priori data and instrument characteristics on nadir atmospheric species retrievals, J. Geophys. Res., 112, D09303, doi:101029/2006JD007663.

Luo M., Rinsland C., Fisher B., Sachse G., Diskin G., Logan J., Worden H., Kulawik S., Osterman G., Eldering A., Herman R., Shephard M., 2007b. TES carbon monoxide validation with DACOM aircraft measurements during INTEX-B 2006, J. Geophys. Res., 112, D24S48, doi:10.1029/2007JD008803.

Madronich S. and Calvert J.G., 1990. Permutation reactions of organic peroxy radicals in the troposphere. J. Geophys. Res., 95(D5), 5697–5715, doi:10.1029/JD095iD05p05697.

Madronich S. and Flocke S., 1999. The role of solar radiation in atmospheric chemistry, in Handbook of Environmental Chemistry, edited by P. Boule, pp. 1–26, Springer, Heidelberg, Germany.

Madronich S., 2006. Chemical evolution of gaseous air pollutants down-wind of tropical megacities: Mexico city case study. Atmos. Environ. 40, 6012-6018.

Mahapatra P.S., Panda S., Walvekar P.P., Kumar R., Das T., Gurjar B.R., 2014. Seasonal trends, meteorological impacts, and associated health risks with atmospheric concentrations of gaseous pollutants at an Indian coastal city, Environ SciPollut Res, doi: 10.1007/s11356-014-3078-2.

Mallik C., Ghosh D., Ghosh D., Sarkar U., Lal S., Venkataramani S., 2014. Variability of SO2, CO, and light hydrocarbons over a megacity in Eastern India: effects of emissions and transport, Environ Sci Pollut Res (2014) 21:8692–8706, doi: 10.1007/s11356-014-2795-x.

Mallik C., Lal S., Venkataramani S., Naja M., Ojha N., 2013. Variability in ozone and its precursors over the Bay of Bengal during post monsoon: Transport and emission effects, J. Geophys. Res.-Atmos., 118, 10190–10209, doi:10.1002/jgrd.50764.

Mandal T.K., Khan A., Ahammed Y.N., Tanwar R.S., Parmar R.S., Zalpuri K.S., Gupta P.K., Jain S.L., Singh R., Mitra A.P., Garg S.C., Suryanarayana A., Murty V.S.N, Kumar M.D., Shepherd A.J., 2006. Observations of trace gases and aerosols over the Indian Ocean during the monsoon transition period, J. Earth Syst. Sci., 115, 4, 473–484.

Manoj M.R., Satheesh S.K., Moorthy K.K., Gogoi M.M., Babu S.S., 2019. Decreasing trend in black carbon aerosols over the Indian region. Geophysical Research Letters, 46, doi: 10.1029/2018GL081666.

Marathe S.A. and Murthy S., 2015. Seasonal variation in surface ozone concentrations, meteorology and primary pollutants in coastal mega city of Mumbai, India, Journal of Climatology & Weather Forecasting, doi: 10.4172/2332-2594.1000149.

Marenco A., Thouret V., Nédélec P., Smit H., Helten M., Kley D., Karcher F., Simon P., Law K., Pyle J., Poschmann G., Von Wrede R., Hume C., Cook T., 1998. Measurement of ozone and water vapor by Airbus in-service aircraft: The MOZAIC airborne program, an overview, J. Geophys. Res.-Atmos., 103, 25631–25642, doi: 10.1029/98JD00977.

Masarie K.A., Langenfelds R.L., Allison C.E., Conway T.J., Dlugokencky E.J., Francey R.J., Novelli P.C., Steele L.P., Tans P.P., Vaughn B., White J.W.C., 2001. NOAA/CSIRO Flask Air Intercomparison Experiment: A strategy for directly assessing consistency among atmospheric measurements made by independent laboratories, J. Geophys. Res., 106(D17), 20445–20464, doi: 10.1029/2000JD000023.

Matsui H., Kondo Y., Moteki N., Takegawa N., Sahu L.K., Zhao Y., Fuelberg H.E., Sessions W.R., Diskin G., Blake D.R., Wisthaler A., Koike M., 2011. Seasonal variation of the transport of black carbon aerosol from the Asian continent to the Arctic during the ARCTAS aircraft campaign. J. Geophys. Res. 116, D05202, doi: 10.1029/2010JD015067.

McMillan W.W., Barnet C., Strow L., Chahine M.T., McCourt M.L., Warner J.X., Novelli P.C., Korontzi S., Maddy E.S., Datta S., 2005. Daily global maps of carbon monoxide from NASA's Atmospheric Infrared Sounder, Geophys. Res. Lett., 32, L11801, doi:10.1029/2004GL021821.

McMillan W.W., Evans K.D., Barnet C.D., Maddy E.S., Sachse G.W., Diskin G.S., 2011. Validating the AIRS Version 5 CO Retrieval With DACOM In Situ Measurements During INTEX-A and -B, IEEE Transactions On Geoscience And Remote Sensing, 49, 710.1109/TGRS.2011.2106505

Minschwaner K., Manney G.L., Livesey N.J., Pumphrey H.C., Pickett H.M., Froidevaux L., Lambert A., Schwartz M.J., Bernath P.F., Walker K.A., Boone C.D., 2010. The photochemistry of carbon monoxide in the stratosphere and mesosphere evaluated from observations by the Microwave Limb Sounder on the Aura satellite, J. Geophys. Res., 115, D13303, doi:10.1029/2009JD012654.

Mlawer E.J., Taubman S.J., Brown P.D., Iacono M.J., Clough S. A., 1997. Radiative transfer for inhomogeneous atmospheres: RRTM, a validated correlated-k model for the longwave, J. Geophys. Res.-Atmos., 102, 16663–16682, doi:10.1029/97JD00237.

Mohanakumar K., 2008. Stratosphere Troposphere Interactions – An Introduction, Springer, India.

Moorthy K.K., Nair V.S., Babu S.S., Satheesh S.K., 2009. Spatial and vertical heterogeneities in aerosol properties over oceanic regions around India: implications for radiative forcing. Quarterly Journal of the Royal Meteorological Society 135, 2131-2145.

Muhle J., Zahn A., Brenninkmeijer C.A.M., GrosV., Crutzen P.J., 2002. Airmass classification during the INDOEX R/V cruise using measurements of non-methane hydrocarbons, CH, CO2, CO, 14CO, and d18O(CO). J.Geophys.Res.107 (D19), 8021.

Munir S., Chen H., Ropkins K., 2011. Non-parametric nature of groundlevel ozone and its dependence on nitrogen oxides (NOx): a view point of vehicular emissions.WIT Trans Ecol Environ 147:93–104, doi:10.2495/AIR110091.

Nair P.R., David L.M., Aryasree S., George K.S., 2013. Distribution of ozone in the marine boundary layer of Arabian Sea prior to monsoon: Prevailing airmass and effect of aerosols, Atmospheric Environment, 74, 18-28, doi: 10.1016/j.atmosenv.2013.02.049.

Nair P.R., David L.M., Girach I.A., George K.S., 2011. Ozone in the marine boundary layer of Bay of Bengal during post-winter period: Spatial pattern and role of meteorology, Atmos. Environ., 45, 4671-4681, doi:10.1016/j.atmosenv.2011.05.040.

Nair P.R., Revathy S.A., David L.M., Girach I.A., Kavitha M., 2018. Decadal changes in surface ozone at the tropical station Thiruvananthapuram (8.542° N, 76.858° E), India: effects of anthropogenic activities and meteorological variability, Environmental Science and Pollution Research, doi:10.1007/s11356-018-1695-x.

Nair V.S., Babu S.S., Moorthy K.K., 2008. Aerosol characteristics in the marine atmospheric boundary layer over the Bay of Bengal and Arabian Sea during ICARB: spatial distribution and latitudinal and longitudinal gradients, J. Geophys. Res. 113, D15208, doi: 10.1029/2008JD009823.

Nair V.S., Moorthy K.K., Alappattu D.P., Kunhikrishnan P.K., George S., Nair P.R., Babu S.S., Abish B., Satheesh S.K., Tripathi S.N., Niranjan K., Madhavan B.L., Srikant V., Dutt C.B.S., Badarinath K.V.S., Reddy R.R., 2007. Wintertime aerosol characteristics over the Indo Gangetic Plain (IGP): impacts of local boundary layer processes and long-range transport. J. Geophys. Res. 112, D13205, doi: 10.1029/2006JD008099.

Naja M. and Lal S., 2002. Surface ozone and precursor gases at Gadanki (13.5 N, 79.2 E), a tropical rural site in India, J. Geophys. Res., 107, 4197, doi: 10.1029/2001JD000357.

Naja M., Chand D., Sahu L., Lal S., 2004. Trace gases over marine regions around India; Ind. J. Mar. Sci. 33(1) 95–106.

Naja M., Lal S., Chand D., 2003. Diurnal and Seasonal variabilities in surface ozone at a high altitude site Mt Abu (24.6N, 72.7E, 1680 m asl) in India, Atmospheric Environment, 37, 4205-4215.

Narayanan V., 1967, An observational study of sea breeze at an equatorial coastal station, Indian J. Meteorol. Geophys., 18, 497–504.

Novelli P.C., Masarie K.A., Lang P.M., 1998. Distributions and recent changes of carbon monoxide in the lower troposphere, J. Geophys. Res., 103(D15), 19015–19033, doi: 10.1029/98JD01366.

Novelli P.C., Masarie K.A., Lang P.M., Hall B.D., Myers R.C., Elkins J.W., 2003. Re-analysis of tropospheric CO trends: Effects of the 1997-1998 wild fires, J. Geophys. Res., 108, D15 : 4464, doi:10.1029/2002JD003031.

Novelli P.C., Massarie K.A., Tans P.T., and Lang P.A., 1994. Recent changes in atmospheric carbon monoxide, Science, 263: 1587-1590.

Novelli P.C., Steele P., Tans P.P., 1992. Mixing ratios of carbon monoxide in the troposphere, J. Geophys. Res., 97, 20731–20750, doi:10.1029/92JD02010.

Ohta K., 1997. Diurnal variation of carbon monoxide concentration in the Equatorial Pacific upwelling region, J. Oceanogr, 53, 173–178.

Ojha N., Naja M., Singh K.P., Sarangi T., Kumar R., Lal S., Lawrence M.G., Butler T.M., Chandola H.C., 2012. Variabilities in ozone at a semi-urban site in the Indo-Gangetic Plain region: Association with the meteorology and regional processes, J. Geophys. Res., 117, D20301, doi:10.1029/2012JD017716.

Ojha N., Pozzer A., Rauthe-Schöch A., Baker A.K., Yoon J., Brenninkmeijer C.A.M., Lelieveld J., 2016. Ozone and carbon monoxide over India during the summer monsoon: regional emissions and transport, Atmos. Chem. Phys., 16, 3013–3032, doi:10.5194/acp-16-3013-2016.

Oltmans S.J., Lefohn A.S, Shadwick D., Harris J.M., Scheel H.E., Galbally I., Zeng G., 2013. Recent tropospheric ozone changes—a pattern dominated by slow or no growth, Atmos Environ 67:331–351

Palmer P. I., Suntharalingam P., Jones D.B.A., Jacob D.J., Streets D.G., Fu Q., Vay S.A., Sachse G.W., 2006. Using CO2:CO correlations to improve inverse analyses of carbon fluxes, J. Geophys. Res., 111, D12318, doi:10.1029/2005JD006697.

Pan L., Gille J.C., Edwards D.P., Bailey P.L., Rodgers C.D., 1998. Retrieval of tropospheric carbon monoxide for the MOPITT experiment, J. Geophys. Res., 103(D24), 32277–32290, doi:10.1029/98JD01828.

Parrish D. D., M. Trainer, J. S. Holloway, J. E. Yee, M. S. Warshawsky, F. C. Fehsenfeld, G. L. Forbes, and J. L. Moody, Relationships between ozone and carbon monoxide at surface sites in the North Atlantic region, J. Geophys. Res., 103(D11), 13,357– 13,376, 1998.

Parrish D.D., Law K.S., Staehelin J., Derwent R., Cooper O.R., Tanimoto H., Volz-Thomas A., Gilge S., Scheel H.E., Steinbacher M., Chan E., 2012. Long-term changes in lower tropospheric baseline ozone concentrations at northern mid-latitudes. Atmos Chem Phys 12:11485–11504, doi: 10.5194/acp-12-11485-2012

Peshin S.K., Sharma A., Sharma S.K., Mandal T.K., 2014. Seasonal variability of trace gases (O3, NO, NO2 and CO) and particulate matter (PM10 and PM2.5) over Delhi, India. Vayu Mandal. 40(1-4), 61-73.

Peshin S.K., Sharma A., Sharma S.K., Naja M., Mandal T.K., 2017. Spatio-temporal variation of air pollutants and the impact of anthropogenic effects on the photochemical buildup of ozone across Delhi-NCR, Sustainable Cities and Society, doi: 10.1016/j.scs.2017.09.024.2017

Petron G., Crotwell A.M., Lang P.M., Dlugokencky E., 2018. Atmospheric Carbon Monoxide Dry Air Mole Fractions from the NOAA ESRL Carbon Cycle Cooperative Global Air Sampling Network, 1988-2017, Version: 2018-10-17, Path: ftp://aftp.cmdl.noaa.gov/data/trace_gases/co/flask/surface/.

Petzold A., Thouret V., Gerbig C., Zahn A., Brenninkmeijer C.A.M., Gallagher M., Hermann, M., Pontaud M., Ziereis H., Boulanger D., Marshall J., Nédélec P., Smit H.G.J., Friess U., Flaud J.-M., Wahner A., Cammas J.-P., Volz-Thomas A., 2015, Global-scale atmosphere monitoring by in-service aircraft – current achievements and future prospects of the European Research Infrastructure IAGOS, Tellus B, 67, 1–24, doi:10.3402/tellusb.v67.28452.

Platt U., 1994. Differential Optical Absorption Spectroscopy (DOAS), in Air Monitoring by Spectroscopic Techniques, Chem. Anal., 127, edited by M. W. Sigrist, pp. 27– 76, Wiley-Interscience.

Pommier M., Law K.S., Clerbaux C., Turquety S., Hurtmans D., Hadji-Lazaro J., Coheur P.-F., Schlager H., Ancellet G., Paris J.-D., Nedelec P., Diskin G.S., Podolske J.R., Holloway J.S., Bernath P., 2010. IASI carbon monoxide validation over the Arctic during POLARCAT spring and summer campaigns, Atmos. Chem. Phys., 10, 10655–10678, doi:10.5194/acp-10-10655-2010.

Pressman J. and Warneck P, 1970. The stratosphere as a chemical sink for Carbon monoxide, Journal of the Atmospheric Sciences, 27, 155-163.

Pumphrey H.C., Filipiak M.J., Livesey N.J., Schwartz M.J., Boone C., Walker K.A., Bernath P., Ricaud P., Barret B., Clerbaux C., Jarnot R.F., Manney G.L., Waters J.W., 2007. Validation of middle-atmosphere carbon monoxide retrievals from the Microwave Limb Sounder on Aura, J. Geophys. Res., 112, D24S38, doi:10.1029/2007JD008723.

Reddy R.R., RamaGopal K., Narasimhulu K.L., Reddy S.S., Kumar K.R., Ahammed Y.N., Rao T.V.R., Azeem P.A., 2008. Diurnal and seasonal variabilities in surface ozone and its precursor gases at a semi-arid site Anantapur (14.62°N, 77.65°E, 331 m asl) in India, International Journal of Environmental Studies, 65:2, 247-265, doi: 10.1080/00207230701844379.

Reichle H.G., Anderson B.E., Connors V.S., Denkins T.C., Forbes D.A., Gormsen B.B., Langenfelds R.L., Neil D.O., Nolf S.R., Novelli P.C., Pougatchev N.S., Roell M.M., Steele L.P., 1999. Space shuttle based global CO measurements during April and October 1994, MAPS instrument, data reduction and data validation. J. Geophys. Res. 104 (D17), 21,443–21454.

Rinsland C.P., Luo M., Logan J.A., Beer R., Worden H.M., Kulawik S.S., Rider D., Osterman G., Gunson M., Eldering A., Goldman A., Shephard M.W., Clough S.A., Rodgers C., Lampel, M.C., Chiou L., 2006. Nadir measurements of carbon monoxide distributions by the Tropospheric Emission Spectrometer instrument onboard the Aura Spacecraft: Overview of analysis approach and examples of initial results, Geophys. Res. Lett., 33, L22806, doi:10.1029/2006GL027000.

Rodgers C.D., 1990. Characterization and error analysis of profiles retrieved from remote sounding measurements, J. Geophys. Res., 95, 5587-5595.

Rodgers C.D., 2000. Inverse Methods for Atmospheric Sounding,World Scientific Publishing Co. Pte. Ltd, Tokyo.

Rolph G., Stein A., Stunder B., 2017. Real-time Environmental Applications and Display sYstem: READY. Environmental Modelling & Software, 95, 210-228, doi: 10.1016/j.envsoft.2017.06.025

Rothman L.S., Gordon I.E., Babikov Y., Barbe A., Benner D.C, Bernath P.F., Birk M., Bizzocchi L., Boudon V., Brown L.R., Campargue A., Chance K., Cohen E.A., Coudert L.H., Devi V.M., Drouin B.J., Fayt A., Flaud J.-M., Gamache R.R., Harrison J.J., Hartmann J.-M., Hill C., Hodges J.T., Jacquemart D., Jolly A., Lamouroux J., Le Roy R.J., Li G., Long D.A., Lyulin O.M., Mackie C.J., Massie S.T., Mikhailenko S., Müller H.S.P., Naumenko O.V., Nikitin A.V., Orphal J., Perevalov V., Perrin A., Polovtseva E.R., Richard C., Smith M.A.H., Starikova E., Sung K., Tashkun S., Tennyson J., Toon G.C., Tyuterev Vl.G., Wagner G., 2013. The HITRAN2012 Molecular Spectroscopic Database // J.Quant. Spectrosc. Radiat. Transfer, 130, 4-50, doi: 10.1016/j.jqsrt.2013.07.002.

Sahu L.K. and Lal S., 2006. Distributions of C2-C5 NMHCs and related trace gases at a tropical urban site in India. Atmos. Environ. 40, 880-891.

Sahu L.K., Lal S., Venkataramani S., 2006. Distributions of O3, CO and hydrocarbons over the Bay of Bengal: a study to assess the role of transport from southern India and marine regions during September-October 2002. Atmos. Environ. 40, 4633-4645.

Sahu L.K., Sheel V., Kajino M., Deushi M., Gunthe S.S., Sinha P.R., Yadav R., Pal D., Nedelec P., Thouret V., Smit H.G., Impact of tropical convection and ENSO variability in vertical, distributions of CO and O3 over an urban site of India, Clim Dyn, doi: 10.1007/s00382-016-3353-7, 2016

Sahu S.K., Beig G., Sharma C., 2008. Decadal growth of black carbon emissions in India. Geophys. Res. Lett. 35, L02807, doi: 10.1029/2007GL032333.

Saini R., Masih A., Satsangi P.G., Taneja A., 2009. Seasonal and diurnal characteristics of surface level O3 and its precursors in the North Central part of India. International Journal of Environment and Waste Management 4, 126–139.

Saini R., Singh P., Awasthi B.B., Kumar K., Taneja A., 2014. Ozone distributions and urban air quality during summer in Agra – a world heritage site, Atmospheric Pollution Research, 5, 796-804.

Saraf N., and Beig G., 2004. Long-term trends in tropospheric ozone over the Indian tropical region, Geophys. Res. Lett., 31, L05101, doi:10.1029/2003GL018516.

Sarangi T., Naja M., Ojha N., Kumar R., Lal S., Venkataramani S., Kumar A., Sagar R., Chandola H.C., 2014. First simultaneous measurements of ozone, CO, and NOy at a

high-altitude regional representative site in the central Himalayas, J. Geophys. Res. Atmos., 119, 1592–1611, doi: 10.1002/2013JD020631.

Saunders S.M., Pascoe S., Johnson A.P., Pilling M.J., Jenkin M.E., 2003. Development and preliminary test results of an expert system for the automatic generation of tropospheric VOC degradation mechanisms, Atmospheric Environment 37, 1723–1735.

Schell B., Ackermann I. J., Hass H., Binkowski F.S., Ebel A., 2001. Modeling the formation of secondary organic aerosol within a comprehensive air quality model system, J. Geophys. Res., 106, 28275–28293.

Seinfeld J.H. and Pandis S.N., 2006. Atmospheric Chemistry and Physics: from air pollution to climate change, 2nd Edn., Wiley-Interscience publication, USA.

Sharma A., Mandal T.K., Sharma S.K., Shukla D.K., Singh S., 2016. Relationships of surface ozone with its precursors, particulate matter and meteorology over Delhi. Journal of Atmospheric Chemistry, 1-24.

Siegel S.M., Renwick G., Rosen L.A., 1962. Formation of carbon monoxide during seed germination and seedling growth, Science, 137, 683-684.

Singh N., Solanki R., Ojha N., Janssen R.H.H., Pozzer A., Dhaka S.K., 2016. Boundary layer evolution over the central Himalayas from radio wind profiler and model simulations, Atmos. Chem. Phys., 16, 10559-10572, doi:10.5194/acp-16-10559-2016.

Sinha A. and Toumi R., 1996. A Comparison of climate forcings due to chlorofluorocarbons and carbon monoxide, Geophys. Res. Lett., 23, 65-68.

Sinha P.R. Bisht A., Peshin S., 2016. Long term trend in surface ozone over Indian stations, Mausam, 67, 887-896.

Spackman J.R., Schwarz J.P., Gao R.S., Watts L.A., Thomson D.S., Fahey D.W., Holloway J.S., de Gouw J.A., Trainer M., Ryerson T.B., 2008. Empirical correlations between black carbon aerosol and carbon monoxide in the lower and middle troposphere, Geophys. Res. Lett. 35 (19), L19816, doi: 10.1029/2008GL035237.

Spivakovsky C.M., Logan J.A., Montzka S.A., Balkanski Y.J., Foreman-Fowler M., Jones D.B.A., Horowitz L.W., Fusco A.C., Brenninkmeijer C.A.M., Prather M.J., Wofsy S.C., McElroy M.B., 2000. Three-dimensional climatological distribution of tropospheric OH: Update and evaluation, J. Geophys. Res., 105, 8931–8980.

Srivastava S. and Sheel V., 2013. Study of tropospheric CO and O3 enhancement episode over Indonesia during Autumn 2006 using the Model for Ozone and Related chemical Tracers (MOZART-4), Atmospheric Environment, 67, 53-62, doi:10.1016/j.atmosenv.2012.09.067.

Srivastava S., Lal S., Venkataramani S., Gupta S., Sheel V., 2012. Surface distributions of O3, CO and hydrocarbons over the Bay of Bengal and the Arabian Sea during pre-monsoon season, Atmos. Environ., 47, 459–467, doi:10.1016/j.atmosenv.2011.10.023.

Stamnes K., Tsay S.-C., Wiscombe W.J., Jayaweera K., 1988. Numerically stable algorithm for discrete-ordinate-method radiative transfer in multiple scattering and emitting layered media, Appl. Opt., 27, 2502–2509, doi:10.1364/AO.27.002502.

Stehr J.W., Ball W.P., Dickerson R.R., Doddridge B.G., Piety C.A., Johnson J.E., 2002. Latitudinal gradients in O3 and CO during INDOEX 1999, J. Geophys. Res., 107(D19), 8015, doi:10.1029/2001JD000446

Stein A.F., Draxler R.R, Rolph G.D., Stunder B.J.B., Cohen M.D., Ngan F., 2015. NOAA's HYSPLIT atmospheric transport and dispersion modeling system, Bull. Amer. Meteor. Soc., 96, 2059-2077, doi:10.1175/BAMS-D-14-00110.1

Stockwell W.R., Middleton P., Chang J.S., Tang X., 1990. The second generation regional acid deposition model chemical mechanism for regional air quality modeling, J. Geophys. Res., 95(D10), 16343–16367, doi:10.1029/JD095iD10p16343.

Streets D.G., Bond T.C., Carmichael G.R., Fernandes S.D., Fu Q., He D., Klimont Z., Nelson S.M., Tsai N.Y., Wang M.Q., Woo J.-H., Yarber K.F., 2003. An inventory of gaseous and primary aerosol emissions in Asia in the year 2000, J. Geophys. Res., 108 (D21), 8809 doi: 10.1029/2002JD003093.

Strode S.A., Worden H.M., Damon M., Douglass A.R., Duncan B.N., Emmons L.K., Lamarque J.-F., Manyin M., Oman L.D., Rodriguez J.M., Strahan S.E., Tilmes S., 2016. Interpreting space-based trends in carbon monoxide with multiple models, Atmos. Chem. Phys., 16, 7285–7294, doi:10.5194/acp-16-7285-2016.

Stubbins A.P., Uher G., Law C.S., Mopper K., Robinson C., Upstill-Goddard R.C., 2006. Open-Ocean Carbon Monoxide Photoproduction, Deep-Sea Research II 53, 1695-1705, doi:10.1016/j.dsr2.2006.05.011.

Su L., Yuan Z., Fung J.C.H., Lau A.K.H., A comparison of HYSPLIT backward trajectories generated from two GDAS datasets, Science of the Total Environment 506–507, 527–537, 2015, doi: 10.1016/j.scitotenv.2014.11.072.

Susskind J., Barnet C.D., Blaisdell J.M., 2003. Retrieval of atmospheric and surface parameters from AIRS/AMSU/HSB data in the presence of clouds, IEEE T. Geosci. Remote., 41(2), 390– 409.

Sze N.D., 1977. Anthropogenic CO emissions: Implications for the atmospheric CO-OH-CH4 cycle,Science,195, 673-675,.

Takegawa N., Kondo Y., Ko M., Koike M., Kita K., Blake D.R., Hu W., Scott C., Kawakami S., Miyazaki Y., Russell-Smith J., Ogawa T., 2003. Photochemical production of O3 in biomass burning plumes in the boundary layer over northern Australia, Geophys. Res. Lett., 30(10), 1500, doi:10.1029/2003GL017017.

Tanimoto H., Sawa Y., Matsueda H., Yonemura S., Wada A., Mukai H., Wang T., Poon S., Wong A., Lee G., Jung J.-Y., Kim K.-R., Lee M., Lin N.-H., Wang J.-L., Ou-Yang C.-F., Wu C.-F., 2007. Evaluation of standards and methods for continuous measurements of carbon monoxide at ground-based sites in Asia, Pap. Meteorol. Geophys. 58, 85-93 doi:10.2467/mripapers.58.85.

Thompson A.M., 1992. The oxidizing capacity of the Earth's atmosphere: probable past and future changes, Science 256, 1157–1165.

Tiwari S., Dahiya A., Kumar N., 2015. Investigation into relationships among NO, NO2, NOx, O3, and CO at an urban background site in Delhi, India, Atmospheric Research, 157, 119-126.

Tyagi S., Tiwari S., Mishra A., Hopke P.K., Attri S.D., Srivastava A.K., Bisht D.S., 2016. Spatial variability of concentrations of gaseous pollutants across the National Capital Region of Delhi, India, Atmospheric Pollution Research, 7(5), 808-816.

van der Werf, G.R., Randerson J.T., Giglio L., van Leeuwen T.T., Chen Y., Rogers B.M., Mu M., van Marle M.J.E., Morton D.C., Collatz G.J., Yokelson R.J., Kasibhatla P.S., 2017. Global fire emissions estimates during 1997–2016, Earth Syst. Sci. Data, 9, 697-720, doi:10.5194/essd-9-697-2017.

Venkataraman C., Habib G., Kadamba D., Shrivastava M., Leon J.-F., Crouzille B., Boucher O., Streets D.G., 2006. Emissions from open biomass burning in India: integrating the inventory approach with high-resolution Moderate Resolution Imaging Spectroradiometer (MODIS) active-fire and land cover data, Glob. Biogeochem. Cycles 20, GB2013, doi: 10.1029/2005GB002547.

Verma N., Satsangi A., Lakhani A., Kumari K.M., Lal S., 2017. Diurnal, Seasonal, and Vertical Variability in Carbon Monoxide Levels at a Semi-Urban Site in India, Clean – Soil, Air, Water 2017, 45 (9999) 1600432, 10.1002/clen.201600432.

Von Kuhlmann R., 2001. Photochemistry of Tropospheric Ozone, its Precursors and the Hydroxyl Radical: A 3D-Modeling Study Considering Non-Methane Hydrocarbons, Ph.D. thesis, Johannes Gutenberg-Universität Mainz, Mainz, Germany,

Wagner A., Blechschmidt A.-M., Bouarar I., Brunke E.-G., Clerbaux C., Cupeiro M., Cristofanelli P., Eskes H., Flemming J., Flentje H., George M., Gilge S., Hilboll A., Inness A., Kapsomenakis J., Richter A., Ries L., Spangl W., Stein O., Weller R., Zerefos C., 2015. Evaluation of the MACC operational forecast system – potential and challenges of global near-real-time modelling with respect to reactive gases in the troposphere, Atmos. Chem. Phys., 15, 14005-14030, doi: 10.5194/acp-15-14005-2015, 2015.

Wallace J.M. and Hobbs P.V., 2006. Atmospheric Science - An Introductory Survey, Second Edition, Academic Press, Elsevier Inc., USA.

Wang J., Deeter M.N., Gille J.C., Bailey P.L., 1999. Retrieval of tropospheric carbon monxide profiles from MOPITT: algorithm description and retrieval simulation, Proc. SPIE 3756, Optical Spectroscopic Techniques and Instrumentation for Atmospheric and Space Research III.

Warner J.X., Comer M.M., Barnet C.D., McMillan W.W., Wolf W., Maddy E., Sachse G., 2007. A Comparison of Satellite Tropospheric Carbon Monoxide Measurements from AIRS and MOPITT During INTEX-A, J. Geophys. Res., 112, D12S17, doi:10.1029/2006JD007925,.

Waters J.W, Froidevaux L., Harwood R.S., Jarnot R.F., Pickett H.M., Read W.G., Siegel P.H., Cofield R.E., Filipiak M.J., Flower D.A., Holden J.R., Lau G.K., Livesey N.J., Manney G.L., Pumphrey H.C., Santee M.L., Wu D.L., Cuddy D.T., Lay R.R., Loo M.S., Perun V.S., Schwartz M.J., Stek P.C., Thurstans R.P., Boyles M.A., Chandra K.M., Chavez M.C., Chen G.-S., Chudasama B.V., Dodge R., Fuller R.A., Girard M.A., Jiang J.H., Jiang Y., Knosp B.W., LaBelle R.C., Lam J.C., Lee K.A., Miller D., Oswald J.E., Patel N.C., Pukala D.M., Quintero O., Scaff D.M., Snyder W.V., Tope M.C., Wagner P.A., Walch M.J., 2006. The Earth Observing System Microwave Limb Sounder (EOS MLS) on the Aura satellite, IEEE Trans. Geosci. Remote Sens., 44(5), 1106– 1121.

Weinstock B., 1972, Carbon Monoxide Balance in Nature, Science 176.

WHO, 2004. Report on Environmental Health Criteria 213, Carbon Monoxide (Second Edition), World Health Organization, Geneva.

Wiedinmyer C., Akagi S.K., Yokelson R.J., Emmons L.K., Al-Saadi J.A., Orlando J.J., Soja A.J., 2011. The Fire Inventory from NCAR (FINN): a high resolution global model to estimate the emissions from open burning, Geosci. Model Dev., 4, 625–641, doi:10.5194/gmd-4-625-2011.

Wienhold F.G., Fischer H., Hoor P., Wagner V., Konigstedt R., Harris G.W., Anders J., Grisar R., Knothe M., Riedel W.J., 1998. Tristar--A tracer in situ TDLAS for atmospheric research, Appl. Phys. B Lasers and Optics, 67, 411.

WMO, 2018. WDCGG Data Summary No. 42, Global Atmosphere Watch, Japan Meteorological Agency In Co-Operation With World Meteorological Organization (https://gaw.kishou.go.jp/publications/summary)

Worden H.M., Deeter M.N., Frankenberg C., George M., Nichitiu F., Worden J., Aben I., Bowman K.W., Clerbaux C., Coheur P.F., de Laat A.T.J., Detweiler R., Drummond J.R., Edwards D.P., Gille J.C., Hurtmans D., Luo M., Martínez-Alonso S., Massie S., Pfister G., Warner J.X., 2013. Decadal record of satellite carbon monoxide observations. Atmos. Chem. Phys. 13, 837-850, doi:10.5194/acp-13-837-2013.

Worden J., Kulawik S.S., Shephard M.W., Clough S.A., Worden H., Bowman K., Goldman A., 2004. Predicted errors of tropospheric emission spectrometer nadir retrievals from spectral window selection, J. Geophys. Res., 109, D09308, doi:10.1029/2004JD004522.

Xu W., LinW., Xu X., Tang J., Huang J.,Wu H., Zhang X., 2016. Long-term trends of surface ozone and its influencing factors at the Mt Waliguan GAW station, China–part 1: overall trends and characteristics. Atmos Chem Phys 16(10):6191–6205

Yadav R., Sahu L.K., Jaaffrey SNA, Beig G., 2014. Temporal Variation of Particulate Matter (PM) and Potential Sources at an Urban Site of Udaipur in Western India, Aerosol and Air Quality Research, 14: 1613–1629, doi: 10.4209/aaqr.2013.10.0310.

Yin Y., Chevallier F., Ciais P., Broquet G., Fortems-Cheiney A., Pison I., Saunois M., 2015, Decadal trends in global CO emissions as seen by MOPITT, Atmos. Chem. Phys., 15, 13433–13451, doi:10.5194/acp-15-13433-2015.

Yurganov L. N., Rakitin V., Dzhola A., August T., Fokeeva E., George M., Gorchakov G., Grechko E., Hannon S., Karpov A., Ott L., Semutnikova E., Shumsky R., Strow L., 2011. Satellite- and ground-based CO total column observations over 2010 Russian fires: accuracy of top-down estimates based on thermal IR satellite data, Atmos. Chem. Phys., 11, 7925–7942, doi: 10.5194/acp-11-7925-2011.

Zellweger C., uglin C.H., Klausen J., Steinbacher M., Vollmer M., Buchmann B., 2009. Inter-comparison of four different carbon monoxide measurement techniques and evaluation of the long-term carbon monoxide time series of Jungfraujoch, Atmos. Chem. Phys., 9, 3491–3503, www.atmos-chem-phys.net/9/3491/2009/.

Zhang Q., Streets D.G., Carmichael G.R., He K.B., Huo H., Kannari A., Klimont Z., Park I.S., Reddy S., Fu J.S., Chen D., Duan L., Lei Y., Wang L.T., Yao Z.L., 2009, Asian emissions in 2006 for the NASA INTEX-B mission, Atmos. Chem. Phys., 9, 5131–5153, doi:10.5194/acp-9-5131-2009.

Zhao Y., Kondo Y., Murcray F.J., Liu X., Koike M., Kita K., Nakajima H., Murata I., Suzuki K., 1997. Carbon monoxide column abundances and tropospheric concentrations retrieved from high resolution ground based infrared solar spectra at 43.5°N over Japan, Journal of Geophysical Research, 102, D19, 23,403-23,411.

Journal Publications

1. **Girach I. A.**, Ojha N., Nair P. R., Tiwari Y. K., Ravi Kumar K., **2018**, "Variations of trace gases over the Bay of Bengal during the summer monsoon", **Journal of Earth System Science**, 127, 15. (http://dx.doi.org/10.1007/s12040-017-0915-y).

2. **Girach I. A.**, Ojha N., Nair P. R., Pozzer A., Tiwari Y. K., Ravi Kumar K., Lelieveld J., **2017**, "Variations in O_3, CO, and CH_4 over the Bay of Bengal during the summer monsoon season: shipborne measurements and model simulations", **Atmospheric Chemistry and Physics**, 17, 257-275. (http://dx.doi.org/10.5194/acp-17-257-2017)

3. **Girach I. A.** and Nair P. R., **2014**, On the vertical distribution of Carbon monoxide over Bay of Bengal during winter: Role of water vapour and vertical updrafts, **Journal of Atmospheric and Solar-Terrestrial Physics**, 117, 31–47. (http://dx.doi.org/10.1016/j.jastp.2014.05.003)

4. **Girach I. A.**, Nair V. S., Babu S. S., Nair P. R., **2014**, Black Carbon and Carbon Monoxide over Bay of Bengal during W_ICARB: Source characteristics, **Atmospheric Environment**, 94, 508-517. (http://dx.doi.org/10.1016/j.atmosenv.2014.05.054)

5. **Girach I. A.** and Nair P. R., **2014**, Carbon monoxide over Indian region as observed by MOPITT, **Atmospheric Environment**, 99, 599-609. (http://dx.doi.org/10.1016/j.atmosenv.2014.10.019)